

**INVESTIGATION OF BOILING PROCESS IN
WATER EVAPORATOR WITH INTERNAL
CAPILLARY STRUCTURE**

By
Y. B. M. Elhag

A thesis submitted to the requirements for the degree of
Doctoral of Philosophy (PhD) in Mechanical Engineering

**Kingston University
Faculty of Engineering**

May 2006

Supervisor
Dr. H. M. Sabir
Senior Lecturer
Faculty of Engineering

Please do **not** digitise the following figures:

Figure 1.2	p.18
Figure 1.3	p.19
Figure 1.4	p.19
Figure 1.5	p.19
Figure 1.6	p.20
Figure 1.7	p.20
Figure 1.8	p.21
Figure 1.9	p.21
Figure 1.10	p.21

Acknowledgment

I would like to express my profound gratitude to my supervisor Dr. H. Sabir for giving me the chance to do this research and trusting me to do this difficult work the outcome of which I very much hope has pleased him. However, I will remain deeply indebted to him. His guidance, valuable advice and encouragement throughout this research enabled me to finish the work.

My sincere gratitude is also extended to my wife and two children for their persistent support, tolerance and understanding during the preparation of this work. I am also very grateful to my mother, brother and sisters as well as to all relatives and friends who have been encouraging me during the course of this work.

I wish to thank Mr. R. McCoy for the great efforts he made to manufacture the evaporators tested in this research. Thanks are also extended to Mr. D. Wells for his great assistance in manufacturing these evaporators and to all the technical staff in Roehampton Vale Campus of Kingston University, particularly Mr. G. Venables and Mr. W. Prophet, for their assistance during the course of the experimental work.

I wish to thank Kingston University very much for funding this research and the government of the Sudan for assisting me financially with my living expenses.

In this research, boiling inside an evaporator whose tubes are lined with internal circumferential layer of sintered metal powder was investigated analytically and experimentally. This is done in an attempt to overcome the problems associated with water boiling at low temperature inside the evaporators of absorption air conditioners which use water as a refrigerant. This would eventually enable the use of a single heat exchanger in such refrigeration cycles to cool the air instead of using two heat exchangers as is currently done. That, in turn, would reduce the cost and improve the thermal efficiency.

A theoretical background to help understand the mechanisms of boiling in porous structures was first introduced and then the literature on boiling in capillary structures; both porous and grooved structures was critically reviewed.

In the analytical phase of this research a mathematical model was built incorporating the heat transfer processes that take place when hot load air flows across a two-row staggered sintered tube evaporator of an absorption lithium bromide/water cycle. This model was then used in an iterative computational scheme, using FORTRAN 95 language to simulate boiling performance of the modified tubes. Results were obtained for boiling heat rates and boiling heat transfer coefficients and plotted against particle size and layer thickness. The heat transfer limits were determined analytically using heat pipe theory.

In the experimental work, sixteen evaporators differing in particles size and layer thickness were tested. Four particle sizes; 50, 100, 200 and 300 μm , and four layer thicknesses for each particle size; 1.0, 1.5, 2.0 and 2.5 mm, were tested at different load air velocities and temperatures. The obtained results were plotted against particle size and layer thickness. Wall superheats as low as 0.77 $^{\circ}\text{C}$ and boiling heat transfer coefficients as high as 6890 were achieved experimentally.

Good agreement was found between the experimental boiling heat rate and the analytical one when using O'Neil's [35] boiling formula. Both results showed that the boiling heat rate increases gradually to a maximum with increase in particle size and then decreases.

Abstract

However, the experimental boiling heat rate is found to be slightly higher than the analytical one. On average, the analytical heat rate was about 74% of the experimental one. The analytical boiling heat rate obtained using Rao and Balkrishnan [32] boiling formula, was found to monotonically increase with increase in particle size. However, it was smaller than the experimental one as it only mounted to 30% of the experimental one on average. The experimental boiling heat transfer coefficient's trend was found to be similar to that of the experimental boiling heat rate, i.e. increases slowly to a maximum and then decreases. The effect of varying the sintered layer thickness on the boiling performance of the evaporators is found to be relatively mild compared to that of the particle size. This trend showed varying effects of the layer thickness on boiling performance. Some of the curves showed mild monotonous decrease in performance with increasing layer thickness while others showed monotonous increase in performance for both, boiling heat rate and boiling heat transfer coefficient.

The discrepancy between the analytical and experimental results was explained in terms of the inaccuracies resulting from underestimating flooding boiling nucleation sites for the large particle size evaporators and from using Darcy's law and Clapeyron equations in deriving the analytical models.

Contents

Acknowledgement	i
Abstract	ii
Contents	iv
Nomenclature	viii
CHAPTER 1: Introduction	
1.1 Introduction	1
1.2 Background on Conventional Lithium Bromide Refrigeration Cycle	1
1.3 Statement of the Problem	2
1.4 Objectives	2
1.5 Boiling in Porous Surfaces	3
1.5.1 Porous Structure	3
1.5.2 Surface Tension	3
1.5.3 Contact Angle	4
1.5.4 Capillary Pressure and Hydraulic Radius	5
1.5.5 Capillary Rise	7
1.5.6 Liquid-vapour Interface Regions	7
1.5.7 Disjoining Pressure	8
1.5.8 Effect of Temperature and Contaminants on Interfacial Behaviour	8
1.5.9 Thermo physical Properties	8
1.5.10 Effect of Effective Capillary/pore Radius on Mass Flow Rate Through a Wick Structure	9
1.5.11 Boiling Heat Transfer and Vapour Formation Modes	10
1.5.11.1 Boiling Modes in Plane Surfaces	11
1.5.11.2 Boiling Modes in Porous Wicked Surfaces	12
1.5.12 Critical Temperature Difference	13
1.5.13 Heat Pipes	13
1.5.14 Heat Transfer Limitation in Heat Pipes	14
1.5.14.1 Capillary Limit	14
1.5.14.2 Boiling Limit	15
1.5.14.3 Sonic Limit	16
1.5.14.4 Viscous Limit	16
1.5.14.5 Entrainment Limit	17
1.6 Summary of Chapter One	17
CHAPTER 2: Literature Review	22
2.1 Introduction	22
2.2 Boiling in Porous Media	22
2.2.1 Boiling Enhancement	22
2.2.2 Mechanism of Boiling	29
2.2.3 Effect of Layer Geometry	32
2.2.4 Effect of Thermophysical Properties	37
2.2.5 Effect of Fluid Flow	39
2.3 Boiling in Grooved Surfaces	40
2.3.1 Boiling Enhancement	40
2.3.2 Mechanisms of Boiling	45
2.3.3 Effect of Grooved Geometry	46
2.3.4 Fluid Flow Effects	49
2.4 Capillary Pumped Loops	50
2.4.1 Heat Transport Capacity	50
2.4.2 Effect of Thermal Conductivity	52
2.4.3 Hydrodynamic Aspects	53
2.4.4 Advances in CPLs	53
2.5 Combined Wick Structures	54

2.6 Conclusion	55
CHAPTER 3: Analytical Work	58
3.1 Introduction	58
3.2 Physical Description of the Evaporators	58
3.3 Description of Heat Rate Transfer Model	58
3.4 Boiling Heat Rate	59
3.4.1 O'Neil et al. Equation	60
3.4.2 Rao and Balkrishnan Equation	61
3.4.3 Nishikawa et al. Equation	62
3.4.4 Fukusako et al. Equation	62
3.4.5 Zhang and Zhang Equation	63
3.4.6 Cornwell et al. Equation	64
3.5 Convection outside the Tubes	64
3.6 Condensation on the Evaporator Tubes	65
3.7 The Minimum Limit Heat Rate Q_{min}	66
3.7.1 Adaptation of Heat Transfer Limitation Equations of Conventional Heat Pipes to Suit a Capillary-Assisted Evaporator of an Absorption Refrigeration Cycle	67
3.7.1.1 Vapour Pressure Drop	67
3.7.1.1.1 Vapour Pressure Drop in the Wick and Adiabatic Sections	67
3.7.1.1.2 Normal Hydrostatic Vapour Pressure Drop	68
3.7.1.1.3 Vapour Pressure Drop at the Elbows	69
3.7.1.1.4 Vapour Pressure Drop at the Expansions of the Vapour outlet Pipe	69
3.7.1.2 Liquid Pressure Drop	70
3.7.1.3 Normal and Axial Hydrostatic Pressure drops	71
3.7.1.4 Inertial Pressure Gradient	71
3.7.1.5 Other Heat Transfer Limitations	72
3.8 Algorithms Description	72
3.9 Sample Calculation	75
3.9.1 Dimensions & Sintered Material Properties	75
3.9.2 Thermo physical Properties	76
3.9.3 Capillary Limit Calculation	76
3.9.4 Sonic Limit	84
3.9.5 Viscous Limit Heat Rate	84
3.9.6 Boiling Limit Heat Rate	84
3.10 Analytical Results	85
3.10.1 Effect of Particle Size on Boiling Heat Rate	85
3.10.1.1 Boiling Heat Rates Obtained Using O'Neil's Formula	86
3.10.1.1 Boiling Heat Rates Obtained Using Rao and Balkrishnan's Formula	86
3.10.2 Effect of Particle Size on Boiling Heat Transfer Coefficient	87
3.10.3 Effect of Layer Thickness on Boiling Heat Rate	87
3.10.4 Effect of Layer Thickness on Boiling Heat Transfer Coefficient	87
3.11 Summary of Chapter Three	88
CHAPTER 4: Experimental Work	121
4.1 Introduction	121
4.2 Test-ring Description	121
4.2.1 General Function	122
4.2.2 Test-rig Components	122
4.2.2.1 Absorber	122
4.2.2.2 Generator	123
4.2.2.3 The Condenser	123

4.2.2.4 Evaporator	123
4.2.2.5 Water Tank	124
4.2.2.6 Diaphragm Pumps	124
4.2.2.7 Load Air System	124
4.2.2.8 Vacuum Pumps	124
4.2.2.9 Cooling Water	124
4.2.3 Evaporator Manufacturing & Production	125
4.3 Test Measurements & Measuring Devices	125
4.3.1 Air Velocity Measurements	125
4.3.2 Temperature Measurements	126
4.3.2.1 Primary Temperature Measurements	126
4.3.2.2 Secondary Temperature Measurements	127
4.3.3 Pressure Measurements	127
4.3.4 Flow Measurements	127
4.3.5 Data Logging	127
4.3.6 Test Execution Stages	127
4.3.6.1 Stability Maintaining Stages	128
4.3.7.2 Measurements taking Stages	128
4.4 Problems and Trouble Shootings	128
4.4.1 Air Ingress	128
4.4.2 Entrainment to The Condenser	129
4.4.3 Flow Meters Sensitivity	129
4.4.4 Adequacy of Absorbent Concentration in the Absorber	129
4.4.5 Crystallisation	130
4.4.6 Degradation of Absorbent	130
4.4.7 Blockage of Nozzles	131
4.4.8 Frequent Breakdown of Joints on the Solution Lines	131
4.5 Calculations	131
4.5.1 Boiling Heat Rate	131
4.5.2 Boiling Heat Transfer Coefficient	132
4.6 Results	133
4.6.1 Effect of Varying Particle Size	133
4.6.2 Effect of Varying Layer Thickness	134
4.7 Summary of Chapter Four	134
CHAPTER 5: Discussion	160
5.1 Introduction	160
5.2 Effects of Varying Particle Size	160
5.2.1 Experimental Boiling Heat Rates Compared to O'Neil's Analytical Results	161
5.2.1.1 Reasons for Decrease in Boiling Performance after Reaching a Maximum	163
5.2.1.2 Discrepancies between O'Neil's Analytical Results and the Experimental Ones	165
5.2.2 Experimental Boiling Heat Rates Compared to Rao and Balkrishnan's Analytical Results	167
5.2.3 Experimental Boiling Heat Transfer Coefficient Compared to O'Neil's Analytical Results	168
5.2.4 Experimental Boiling Heat Transfer Coefficient Compared to Rao & Balkrishnan's Analytical Results	170
5.3 Effect of Varying Layer Thickness	171
5.3.1 Experimental Boiling Heat Rates Compared to O'Neil's Analytical Results	171
5.3.2 Experimental Boiling Heat Rates Compared to Rao and Balkrishnan's Analytical Results	172

5.3.3 Experimental Boiling Heat Transfer Coefficient Compared to O'Neil's Analytical Results	173
5.3.4 Experimental Boiling Heat Transfer Coefficient Compared to Rao & Balkrishnan's Analytical Results	173
5.4 Effect of Air Inlet Conditions	174
5.4.1 Effect of Air Inlet Temperature & Velocity	174
5.4.2 Effect of Air Inlet Relative Humidity	174
CHAPTER 6: Conclusion	212
CHAPTER 7: Recommendations for future Work	215
APPENDICES	
Appendix A : Iterative Computational Programme Algorithm	216
Appendix B1: Main Programme Flow Chart	226
Appendix B2: Flow Chart for a Subroutine to Calculate the Minimum Limit Heat Rate	227
Appendix C: FORTRAN Programme	228
Appendix D: Flow Chart for an Iterative Computational Scheme Incorporating Inlet Relative Humidity	243
Appendix E: Tables of Experimental Results	244
REFERENCES	248

Nomenclature

Symbols	Description	SI Unit
ΔP_{II}	Axial hydrostatic pressure drop	Pa
ΔP_+	Normal hydrostatic pressure drop	Pa
ΔP_i	Inertial pressure drop	Pa
ΔP_{l_1}	Liquid pressure drop	Pa
ΔP_{v_1}	vapour pressure drop due to friction in the wick and adiabatic	Pa
ΔP_{v_2}	normal hydrostatic vapour pressure drop	Pa
ΔP_{v_3}	The vapour pressure drop at elbows	Pa
ΔP_{v_4}	pressure drop due to these expansions	Pa
$\Delta P_{v_{4-1}}$	Vapour pressure drop at expansion 1	Pa
$\Delta P_{v_{4-2}}$	Vapour pressure drop at expansion 2	Pa
$\Delta P_{v_{4-3}}$	Vapour pressure drop at expansion 3	Pa
A	Cross-sectional area	m^2
A_T	Surface area of evaporator tubes	m^2
HTC/BHTC	Boiling heat transfer coefficient	W/m^2K
c	Coefficient in equation (3.23)	-
c_0	Initial value of the constant c (3.23)	-
C_p	Specific heat	kJ/kgK
d	Diameter	m
D_p	Pore diameter	m
g	Gravity acceleration	m/s^2
Gr	Grashof number	-
H	Height/Enthalpy	m
h	Heat transfer coefficient	W/m^2K
h_{f_3}	Friction head loss at 90 ° angle elbows	m
$h_{f_{4-1}}$	Friction head loss at expansion 1	m
$h_{f_{4-2}}$	Friction head loss at expansion 2	m
$h_{f_{4-3}}$	Friction head loss at expansion 2	m
h_{fg}	Latent heat of vaporisation	$J/kg K$
Ja	Jacob number	-
K	Permeability	m^2
k	Thermal conductivity	$W/m K$
K	Permeability	m^2
K_f	Friction coefficient	-
L	Length	m
\dot{m}	Mass flow rate	kg/s
n	Number of evaporator tubes	-
Nu	Nusselt number	-

Nomenclature

Symbols	Description	SI Unit
$P_{c,m}$	Max capillary pressure	Pa
Pr	Prandtl number	-
q	Heat flux	W/m ²
Q	Heat Rate	W
Q_{bl}	Boiling limit heat rate	W
r	Radius	m
R	Specific gas constant	kJ/kgK
Re	Reynolds number	-
R_{th}	Thermal resistance	K/W
S_L	Longitudinal pitch	m
S_T	Transverse pitch	m
T	Temperature	K
$Re_{d,max}$	Maximum Reynolds number	-
V	Velocity	m/s
z	Index in equation (3.23)	-
ΔT_s	Wall superheat temperatures	°C
Greek letters		
Symbol	Description	SI Unit
δ	Porous layer thickness	m
ψ	Angle of inclination between pipe and horizontal level	°
μ	Dynamic viscosity	Ns/m
ϵ	Porosity	-
σ	Surface tension	N/m
γ	Specific heat ratios	-
ρ	Density	Kg/m ³
θ	Contact angle	°
v	Specific volume	m ³ /kg

Nomenclature

	Subscripts
Symbol	Description
b	Boiling
ℓ	Liquid
v	Vapour/viscous
s	Sonic/saturation/solid/superheat
c	capillary
min	minimum
w	Wick/wall/Water
cond	Condensation
conv	Convection
s	Solid
db	Dry bulb
m	Maximum
o	outer
p	Particle
1	Inlet/section of the vapour pipe after expansion 1
2	Outlet/the section of vapour pipe after expansion 2
eff	Effective
e	Equivalent/experimental
in	Inlet
out	outlet
c,m	Capillary maximum
a	Air/adiabatic/analytical
max	maximum
bl	Boiling limit
i	Interfacial
rem	Removed
D	Diameter/Darcy
ana	Analytical
exp	Experimental
h	Hydraulic
w	Wick

Nomenclature of the FORTRAN 95 Programme Algorithm

Symbol	Description	Unit
a	Coefficient of the quadratic equation	-
A _i	Cross-sectional area of the evaporator based on inner diameter	m ²
A _o	Cross-sectional area based on outside diameter	m ²
A _v	Cross-sectional area of vapour core	m ²
A _w	Cross-sectional area of the wick section	m ²
A1	Cross-sectional area of the vapour outlet pipe after expansion 2	m ²

Nomenclature

Symbol	Description	Unit
A2	Cross-sectional area of the vapour outlet pipe after expansion 3	m ²
b	Coefficient of the quadratic equation	-
c	Coefficient of the quadratic equation	-
D _p	Particle diameter	m
d _v	Diameter of vapour core	m
Delta	Porous layer thickness	m
Delta_P_i	Factor of Vapour pressure gradient due to inertia	N/m ² W
Delta_P_L	Total liquid pressure drop	Pa
Delta_P_L_Lam	Liquid pressure drop in case of laminar flow	N/m ²
Delta_P_L1	Factor of liquid pressure drop	N/m ² W
Delta_P_L2	Factor of hydrostatic liquid pressure drop	N/m ² W
Delta_P_v	Factor of the sum of vapour pressure drops at elbows and expansions / Total vapour pressure drop	N/m ² W ²
Delta_P_v_Lam	Vapour pressure drop in case of laminar flow	N/m ²
Delta_P_v1	Factor of vapour pressure drop due to friction	N/m ² W
Delta_P_v2	Hydrostatic vapour pressure drop	N/m ²
Delta_P_v3	Factor of vapour pressure drop at the 90 ° angle	N/m ² W ²
Delta_P_v4_2	Factor of vapour pressure drop at expansion 2 on vapour outlet pipe.	N/m ² W ²
Delta_P_v4_2	Coefficient of vapour pressure drop at expansion 2 of the vapour outlet pipe	N/m ² W ²
Delta_P_v4_3	Coefficient of vapour pressure drop at expansion 3 of the vapour outlet pipe	N/m ² W ²
DELTA_T	Temperature difference (T _w - T _{sat})	K
Fx	Function used for iteration	-
Fx_dash	First derivative of the function used for iteration	-
h _{cond}	Condensation heat transfer coefficient	W/m ² K
h _{conv}	Convective heat transfer coefficient	W/m ² K
h _{f3}	Factor of friction head loss at 90 ° angle elbows	m/W ²
h _{f4_1}	Factor of friction head loss at expansion 2 on vapour outlet pipe.	m/W ²
h _{f4_2}	Factor of friction head loss at expansion 1 on vapour outlet pipe.	m/W ²

Nomenclature

Symbol	Description	Unit
H_{fg}	Latent heat of vaporisation	KJ/kg
BHTC	Boiling heat transfer coefficient	$Wm^2 K$
Ja	Jacob number	-
K	Permeability	m^2
k_{eff}	Effective thermal conductivity	W/mK
k_L	Thermal conductivity of liquid	W/mK
L_e	Evaporator length	m
M_{Dot_w}	Liquid mass flow rate	Kg/s
μ_L	Dynamic viscosity	Kg/ms
μ_v	Dynamic viscosity of vapour	Kg/ms
NU_boil	Boiling Nusselt number	-
NUAIR_max	Maximum Nusselt number	-
P_{c_max}	Maximum capillary pressure	N/m^2
P_{sat}	Saturation pressure	N/m^2
Pr_L	Prandtl number	-
PRSA	Prandtl number for air on the tube surface	-
Q_b	Boiling limit heat rate	W
Q_{boil}	Boiling heat rate	W
$q_{boiling}$	Boiling heat flux	W/m^2
Q_c	Capillary limit heat rate	W
Q_{cond}	Condensation heat rate	W
Q_{conv}	Convective heat rate	W
Q_{min}	The smallest limit heat rate	W
Q_{new}	Iteration factor	-
Q_{out}	Heat rate on the exterior side of the evaporator tubes	W
Q_s	Sonic limit heat rate	W
Q_v	Viscous limit heat rate	W
Q1	Root for the quadratic equation in Q_c	W
Q2	Root for the quadratic equation in Q_c	W
R_{eff}	Effective capillary radius	m
R_v	Reynolds number	-
Re_v	Reynolds number	-
REAIR_max	Maximum Reynolds number	-

Nomenclature

Symbol	Description	Unit
ROH_L	Density of liquid	Kg/m ³
ROH_v	Density of vapour	Kg/m ³
SIGMA	Surface tension	N/m
T_sat	Saturation temperature	K
T_w	Tube wall temperature	K
V_v	Factor of vapour velocity inside the vapour core	m/sW
V_v1	Factor of Vapour velocity after expansion 1	m/sW
VAIR_max	Maximum air velocity	m/s

Order of Presentation

The figures of each chapter are presented at its end

Chapter One

Introduction

1.1 Introduction:

A major advantage of lithium bromide/water absorption refrigerator over conventional vapour compression one is that the former one uses low temperature heat source as its main driving power while the latter uses electricity from the mains. Thus, a lithium bromide refrigerator is more environmentally friendly, in terms of CO₂ emissions, as it can be powered by low grade heat; e.g. from domestic waste incinerators, solar energy etc. In addition, lithium bromide/water cycle refrigerators use water as their refrigerant which has a number of environmental advantages. However, as refrigerant, water has the disadvantage of having a low vapour pressure, which hampers its boiling in conventional flooded evaporators.

1.2 Background on Conventional Lithium Bromide/Water Refrigeration Cycle:

Because of the relatively high temperature of evaporation of water (>0), the use of lithium bromide/water cycles is generally restricted to air conditioning applications. This is accomplished in the manner described below:

The main components of a lithium bromide/water refrigeration cycle are absorber, generator, condenser and evaporator; see Fig (1.1). The components are maintained under low pressure. In a conventional air cooling system, due to the heating of lithium bromide solution in the generator, pure water vapour is generated and driven to the condenser leaving the remaining solution in the generator more concentrated. The concentrated solution returns by gravity to the absorber. In the condenser the vapour loses its latent heat to the cooling medium flowing through the coil inside the condenser. The water then passes through a throttle valve to the evaporator where it is sprayed over the outside of a coil through which water flows. Since the evaporator is at low pressure (8.7 mbar), then the water spray evaporates absorbing its latent heat of vaporisation from the water flowing through the coil hence producing chilled water inside the coil. This water is then circulated

Chapter 1: Introduction

through fan-coil units to cool the air, which, in turn, cools a building. The vapour is then absorbed by lithium bromide solution in the absorber and produces a weaker solution which is pumped back to the generator. A heat exchanger is used to exchange heat between the strong and weak solution to minimise the heating required in the generator and the cooling required in the absorber.

1.3 Statement of the Problem:

Using water as a refrigerant has a distinct disadvantage which is its low vapour pressure. This means that liquid hydrostatic heads can suppress boiling. For example in a conventional flooded evaporator one meter high, water at the bottom of the coil will not boil until it reaches 46 °C – hardly suitable for air conditioning purposes. This necessitates the use of two heat exchange coils, where refrigerant water boils externally in the first one producing chilled water. The latter is then transferred to a second coil to cool air. The use of two heat exchangers increases the cost and decreases efficiency.

1.4 Objectives:

The main objective of this research is to use one direct heat exchanger in a lithium bromide refrigeration system to cool the air, instead of using two heat exchangers as done in conventional systems. This will increase the thermal efficiency of the cycle and reduce the capital cost of the system. To do this a modified-tube evaporator, in which the liquid is caused to flow only over the inner surface of the tube in an evaporating film, leaving the centre of the tube open for the passage of vapour, is proposed. This is necessary to overcome the problems associated with water boiling at low temperatures, namely suppression of boiling by the hydrostatic head of water. The cooled air would flow across the outside of the evaporator coil exchanging heat directly with the refrigerant water. A good way of creating a uniform layer of evaporating liquid inside the evaporator tube, without flooding it, is to use capillary effects to draw the liquid across the inner surface of the tube. This could be accomplished by, for example, engraving capillary grooves on the

inner surface of the tube or adding a wick to it, such as a layer of sintered metal powder. A previous research [1] in this field showed that an evaporator coated with sintered metal powder layer outperforms an internally grooved tube evaporator. In this research, therefore, further investigation is carried out to study the effects of the sintered powder layer geometry (particle size and layer thickness) on the boiling performance of such evaporators. However, this requires good understanding of the mechanisms of boiling in porous media which is done in the following sections.

1.5 Boiling in Porous Structures:

To have good understanding how capillary effects help forming a uniform thin layer of evaporating liquid inside the evaporator tube and how that could lead to improved boiling inside the layer of the sintered metal powder that covers the inner surface of the evaporators tested in this research, it is essential to define terms and properties associated with boiling in porous media. This is important because the removal of heat from the hot air in the absorption refrigeration cycle in this research is believed to occur due to the phase change that the water refrigerant undergoes inside the evaporator tubes.

1.5.1 Porous Structure:

A porous medium is a solid matrix made of consolidated or non-consolidated particles with voids between them. A porous media can be naturally formed (e.g. rocks, sand, beds, sponges, wood) or fabricated (e.g. catalytic pellets, wicks, insulation). The particle sizes that form a porous media range from molecular size, micrometres to large sizes.

1.5.2 Surface Tension:

When a liquid is in contact with another medium, whether it is liquid, vapour or solid, then it will be subjected to force imbalance between its boundaries. A liquid molecule near or at liquid vapour interface will experience a resultant force in the direction of the liquid, since forces between the interacting gas and liquid molecules are less than the forces between the liquid molecules. However, a liquid molecule surrounded by other liquid molecules will not experience any resultant force since it will be attracted equally in all directions. The

Chapter 1: Introduction

surface layer of a liquid surrounded by its own vapour will act like a rubber membrane under tension since the force in the surface layer is directed towards the liquid which tends toward the shape of minimum surface area. Therefore, if the surface area of the liquid is to be increased, then negative work must be done on the liquid against the liquid-to-liquid molecular forces. This shows that any increase in the surface area will require movement of molecules from the interior of the liquid out to surface. The work or energy required to increase the surface area can be obtained from the following relation [2]

$$\sigma = \frac{dE}{dS} \dots\dots\dots (1.1)$$

The surface tension σ , which is referred to as free energy per unit area or as force per unit length, exists at all phase interfaces i.e., solid, liquid and vapour. Therefore, the shape that the liquid takes is determined by the combination of the interfacial forces of the three phases. The surface in which interfacial tension exists is not two-dimensional, but three-dimensional with very small thickness. In this very thin region, properties differ from the bordering bulk phases.

1.5.3 Contact Angle:

Fig (1.2a) & Fig (1.2b) [2] show concave and convex surfaces, which result from a wetting fluid and a non-wetting fluid respectively. Media interactions result in surface tensions that are denoted by $\sigma_{\ell,v}$, $\sigma_{s,\ell}$ & $\sigma_{s,v}$ where s, ℓ & v corresponds to solid, liquid & vapour phases respectively. The surface forces act tangentially at the interface between each two phases. i.e. solid-liquid, liquid-vapour & vapour-solid interfaces. The angle between the solid-liquid (s, ℓ) interface and the vapour-liquid (ℓ, v) interface, denoted by θ , is known as the angle of contact. This angle is acute for wetting liquids (e.g. water) and obtuse for non-wetting liquids (e.g. mercury).

The balance of forces at equilibrium conditions gives

$$\sigma_{s,v} = \sigma_{s,\ell} + \sigma_{\ell,v} \cos \theta \dots\dots\dots (1.2)$$

This shows that the angle of contact could also be given as [2]

$$\theta = \cos^{-1} \left(\frac{\sigma_{s,v} - \sigma_{s,\ell}}{\sigma_{\ell,v}} \right) \dots\dots\dots (1.3)$$

1.5.4 Capillary Pressure and Hydraulic Radius:

In applications of wick structures (e.g. heat pipe) the flow of a liquid under the influence of its own surface and interfacial forces is known as capillarity. The differences in curvature along the liquid vapour interface and the existence of surface tension generates capillary pressure difference that causes the liquid to flow. Faghri [2] determined the capillary pressure, P_{cap} , by examining the radii of curvature of a liquid menisci in a porous wick. In Fig (1.3) an arbitrary curved surface is described by the two radii R_I & R_{II} . The curved surface is small enough that R_I & R_{II} are approximately constant.

If the surface is displaced outward by a small distance, the change in area is

$$\Delta S = (x + dx)(y + dy) - xy \dots\dots\dots (1.4)$$

If $dx \approx 0$, then

$$\Delta S = ydx + x dy \dots\dots\dots (1.5)$$

The energy required to displace the surface is

$$dE = \sigma (x dy + y dx) \dots\dots\dots (1.6)$$

There is also a pressure difference ΔP across the surface due to the displacement, which acts on the area xy over the distance dz . The work or energy attributed to generation of this pressure difference is

$$dE = \Delta P xy dz = P_{cap} xy dz \dots\dots\dots (1.7)$$

From the geometry of Fig (1.3), it follows that

$$\frac{x + dx}{R_I + dz} = \frac{x}{R_I} \dots\dots\dots (1.8)$$

$$dx = \frac{xdz}{R_I} \dots\dots\dots (1.9)$$

And similarly

$$dy = \frac{ydz}{R_{II}} \dots\dots\dots (1.10)$$

For the two surfaces to be in equilibrium, the two expressions for energy E must be equal

$$\sigma (x dy + y dx) = \Delta P xy dz \dots\dots\dots (1.11)$$

$$\sigma \left(\frac{xydz}{R_I} + \frac{xydz}{R_{II}} \right) = \Delta P xy dz \dots\dots\dots (1.12)$$

$$P_{cap} = \Delta P = \sigma \left(\frac{1}{R_I} + \frac{1}{R_{II}} \right) \dots\dots\dots (1.13)$$

This expression is called the Young-Laplace equation [2] and is the fundamental equation for capillary pressure. For constant surface tension, σ , along the liquid-vapour line (assuming no significant temperature change), P_{cap} is a function of curvature only. Therefore, P_{cap} depends mainly on the geometry of the interface.

It is possible to derive the theoretical maximum capillary pressure, $P_{c,m}$, for wick structures and geometries with constant cross-sectional flow area, e.g. in the case of a circular capillary, the minimum Radii are; see Fig (1.4):

$$(R_I)_{min} = (R_{II})_{min} = \frac{r}{\cos \theta} \dots\dots\dots (1.14)$$

Substituting this expression into the Young-Laplace equation, the capillary pressure is [2]:

$$P_c = \frac{2\sigma \cos \theta}{r} \dots\dots\dots (1.15)$$

For this expression to be maximum value, the contact angle, θ , must be zero; i.e. perfectly wetting fluid. Thus

$$P_{c,m} = \frac{2\sigma}{r} \dots\dots\dots (1.16)$$

For a rectangular channel; see Fig (1.4b), $R_I = \infty$ and

$$(R_{II})_{min} = \frac{W}{2 \cos \theta} \dots\dots\dots (1.17)$$

Thus,

$$P_c = \frac{2\sigma \cos\theta}{W} \dots\dots\dots (1.18)$$

For this expression to be a maximum value, the contact angle must be zero, i.e.

$$P_{c,m} = \frac{2\sigma}{W} \dots\dots\dots (1.19)$$

Faghri [2] explained that from these and other cases, the Young-Laplace equation can be generalized as:

$$P_{c,m} = \frac{2\sigma}{r_{eff}} \dots\dots\dots (1.20)$$

Where r_{eff} is the effective pore radius¹.

1.5.5 Capillary Rise:

If a wetting liquid is placed in a vertical tube of inner radius r , the liquid will rise to height H above the plane surface of the liquid; see Fig (1.5)

Pressure balance between the hydrostatic and capillary pressure gives [3]:

$$\rho g H = \frac{2\sigma \cos\theta}{r} \dots\dots\dots (1.21)$$

The distance H is known as the capillary rise and it is a measure of the height to which a liquid will rise in porous structure. Capillary rise, H , is inversely proportional to the effective radius of a porous structure.

1.5.6 Liquid-Vapour Interface Regions:

Faghri [2] explained that the actual liquid-vapour interface is conventionally divided into three regions, as shown in Fig (1.6). The intrinsic meniscus, which is the region governed by Young-Laplace equation and where disjoining² pressure effects are negligible; the thin-film region, or that region above the intrinsic meniscus where the disjoining pressure are important; and the extended meniscus, which typically describes the entire meniscus.

¹ The effective pore radius for sintered spherical particles is given in section 1.5.9.

² Disjoing pressure is explained in section (1.5.7)

1.5.7 Disjoining Pressure:

The pressure losses due to the attraction of the liquid phase by the solid are known as the disjoining pressure. This pressure gradient is generated within the thin film of liquid; see Fig (1.6) [2]. There is a significant difference between the properties of a liquid in the thin film and the properties of the bulk of liquid. The disjoining pressure is a product of long range intermolecular forces composed of molecular and electrostatic interactions. Since the properties and chemical potentials of the bulk liquid and liquid thin film are not the same, an additional pressure difference arises. This pressure is described by [2] as

$$P_d = -\frac{A}{\delta^3} - \frac{B}{\delta^2} \dots\dots\dots(1.22)$$

Where A and B are constants that describe the molecular and electrostatic interactions, and δ is the film thickness. The disjoining pressure produces increasing negative pressure with decreasing film thickness. The transport of liquid in ultra-thin thin films is highly affected by the disjoining pressure, which has essential role in evaporation especially for low temperature fluids. The disjoining pressure is one of the fundamental phenomena, which affect the formation of thin evaporating films and the magnitude of the contact angle.

1.5.8 Effect of temperature and contaminants on Interfacial Behaviour:

Surface tension is to some extent determined by the density gradients that exist at the three phase common line between a liquid in contact with a solid surface and the liquid's vapour. Increases in the temperature of a liquid in contact with a heated solid will result in increases in density difference and decreases in surface tension.

The presence of dissolved contaminants in a liquid can have significant effect on the surface tension. Faghri [2] explained that the surface tension decreases as the concentration of the contaminant increases in a liquid.

1.5.9 Thermo Physical Properties:

Here the main thermo physical properties of a porous media are explained, namely porosity, permeability and thermal conductivity. Porosity, ϵ , is defined as the volume

fraction occupied by voids, i.e. the total void volume divided by the total volume occupied by the solid matrix and void volume [4]. If a series of adjacent voids are connected to each other, then the porosity is said to be interconnected porosity. Typically, the porosity is said to be unconnected or isolated when a void is connected only to one other void/pore. The volume fraction of the inter-connected pores is called effective porosity. Due to irregularity of void shape, an average/effective pore diameter is defined as [2]

$$D_p = 0.41 d_p \dots \dots \dots (1.23)$$

The ability of the porous material to transmit the liquid under some applied pressure gradient is described by a term known as Permeability, K. This term is introduced to account for the fact that the pores in porous media may not be contiguous [5]. Mathematically, K, is defined as [4]:

$$K = \frac{\varepsilon D_p^2}{32} \dots \dots \dots (1.24)$$

Another important thermophysical property of porous wick is the effective thermal conductivity, which is given by [2]:

$$k_w = \frac{k_s [2k_s + k_t - 2\varepsilon(k_s - k_t)]}{2k_s + k_t + \varepsilon(k_s - k_t)} \dots \dots \dots (1.25)$$

1.5.10 Effect of Effective Capillary/Pore Radius on Mass Flow Rate Through a Wick

Structure:

For a steady state laminar flow of an incompressible fluid at constant viscosity μ , flowing through a tube of circular cross-section of radius a , the flow is described by Hagen-Poiseuille equation below [3]

$$V_r = \frac{a^2}{4\mu} \left[1 - \left(\frac{r}{a} \right)^2 \right] \frac{P_2 - P_1}{\ell} \dots \dots \dots (1.26)$$

Where V_r is the velocity at radius r and $P_2 - P_1$ is the pressure difference across the tube length ℓ .

Chapter 1: Introduction

The maximum velocity at the tube axis (where $r=0$) and the average velocity are given by equation (1.27) & (1.26) below

$$V_{\max} = \frac{a^2}{4\mu_1} \frac{p_2 - p_1}{\ell} \dots\dots\dots (1.27)$$

$$\bar{V} = \frac{a^2}{8\mu_1} \frac{p_2 - p_1}{\ell} \dots\dots\dots (1.28)$$

The volume flowing per second is given by:

$$\dot{V} = \pi a^2 \bar{V} = \frac{\pi a^4}{8\mu_t} \frac{p_2 - p_1}{\ell} \dots\dots\dots (1.29)$$

And the mass flow rate, \dot{m} is given by

$$\dot{m} = \rho \dot{V} = \rho \frac{\pi a^4}{8\mu_t} \frac{p_2 - p_1}{\ell} \dots\dots\dots (1.30)$$

The total flow through cross-sectional area A of a tube covered with a porous wick on its inner surface is

$$A = \pi(r_w^2 - r_v^2) \varepsilon \dots\dots\dots (1.31)$$

Substituting equation (1.31) in equation (1.30) the mass flow rate, \dot{m} , in a tube covered with a wick structure on its inner surface is [3]:

$$\dot{m} = \frac{\pi (r_w^2 - r_v^2) \varepsilon r_{\text{eff}}^2 \rho_t \Delta P_t}{8 \mu_t \ell_{\text{eff}}} \dots\dots\dots (1.32)$$

Equation (1.32) shows that the mass flow rate in a wick structure is directly proportional to the square of the effective pore radius of the wick.

1.5.11 Boiling Heat Transfer and Vapour Formation Models:

Boiling heat transfer from porous wicked surfaces is more complicated than from plain surfaces. Fig (1.7) shows the boiling curve for water on a plane surface [6] while Fig (1.8) show different heat transfer modes during boiling in a porous wick [2]. To better understand the underlying boiling mechanisms in wick structures, a brief summary is first presented for the regimes of boiling on plane surfaces [6-8]:

1.5.11.1 Boiling Modes in Plane Surfaces:

Boiling in plane surfaces is mainly divided into two modes; pool boiling and convection boiling. The only difference mainly stems from the influence of flow effect [6]. In pool boiling the bouncy effect is significant and the liquid motion is due to free convection and mixing induced by bubble growth and detachment. In forced convection boiling, fluid motion is induced by external means as well as by free convection and bubble-induced mixing. Boiling may also be classified according to whether it is subcooled or saturated. To understand the underlying physical mechanisms of boiling, Fig (1.7) shows the boiling modes of saturated pool boiling for water at 1 atm in plane surfaces, although similar trend characterises the behaviour of other fluids. These modes could be described briefly as follows [6] & [7]:

Free Convection Boiling:

In this regime (range A-B) there is insufficient vapour in contact with the liquid phase to cause boiling at the saturation temperature. Bubble inception will eventually occur with increasing wall superheat temperatures.

Nucleate Boiling:

In this regime (range B-C), which is characterised by a very high heat transfer rate for only a small temperature difference, the liquid near the wall is superheated and tends to evaporate, wherever there are nucleation sites such as tiny pits or scratches on the surface. The bubbles transport the latent heat of phase change and also increase the convective heat transfer by inducing considerable fluid mixing near the surface. There are two main regions in nucleate boiling: local boiling and bulk boiling. In the former the liquid is subcooled and the bubbles formed at the heating surface tend to condense locally. In the latter the liquid is saturated and the bubbles do not collapse. In this regime vapour escapes as jets or columns forming slugs of vapour which, at sufficiently high heat fluxes, prevents the incoming liquid from reaching the heating surface. When the heating surface is

blanketed with vapour, boiling crisis is said to be reached (point C) and the heat flux before reaching this crisis is the critical heat flux (CHF).

Transition Boiling:

In this regime (range C-D), which is also known as partial film boiling, boiling becomes unstable. The surface is alternately covered with a vapour blanket and a liquid layer, resulting in oscillating surface temperatures. If the power input is maintained, the surface temperature increases rapidly to point D due to the low thermal conductivity in the vapour blanket.

Film Boiling:

In this regime (range D-E), a stable vapour film is formed on the heating surface and the heat transfer reaches a minimum. Further increase in heat flux corresponds to abrupt increase in the tube wall temperature which may lead to exceeding the melting temperature of the tube material.

1.5.11.2 Boiling Modes in Porous Wicked Surfaces:

In the following section the regimes of boiling in porous wicked surfaces is presented:

Mode 1, Conduction-Convection:

The whole wick is filled with liquid. Conduction occurs across the liquid layer and vaporisation takes place from the surface. Natural convection may take place within the wick for some thick wicks under gravitational force. This mode is common under a low or moderate heat flux; see Fig (1.8a).

Mode 2, Receding Liquid:

With the increase in heat flux, evaporation at the liquid surface intensifies and the liquid layer begins to recede into the wick structure if the capillary force available is not enough to drive sufficient liquid to the heated surface. In this mode heat transfer across the liquid layer by conduction and vaporisation takes place at the liquid-vapour interface; see Fig (1.8b)

Mode 3, Nucleate Boiling:

When the temperature difference across the wick is large, nucleate boiling may take place within the wick. Bubbles grow at the heated wall, escape to the liquid surface and burst rapidly. Nucleate boiling within the wick does not necessarily represent a heat transfer limit unless bubbles can't escape from the wick; see Fig (1.8c).

Mode 4, Film Boiling:

This is characterised by the generation of a large quantity of bubbles at the heated wall. The bubbles coalesce together before escaping to the surface forming a layer of vapour adjacent to the heated wall, which prevents the liquid from reaching the wall surface. This causes the wall temperature to increase rapidly which will finally lead to the burn out condition. See Fig (1.8d)

1.5.12 Critical Temperature Difference:

The temperature difference at which burn out occurs due to the formation of a film of vapour on the heating surface to the extent that the liquid is prevented from reaching the wall surface is known as the critical temperature difference ΔT_{crit} . Faghri [2] showed that this critical temperature difference for boiling in wick structures is given by:

$$\Delta T_{crit} = \frac{2\sigma T_v}{h_{fg} \rho_v} \left(\frac{1}{R_b} - \frac{1}{R_{men}} \right) \dots\dots\dots(1.33)$$

Furthermore Faghri [2] explained that the meniscus radius, R_{men} , can be taken to be approximately the effective pore radius, r_{eff} . When R_{men} is very small or very close to the bubble radius, R_b , then ΔT_{crit} is very small too. See Fig (1.9)

1.5.13 Heat Pipes:

Heat pipes are one of the major applications that use capillary assisted evaporation. Therefore defining and understanding the theory behind them is of great importance in evaluating the performance of the capillary assisted evaporators tested in this research. A heat pipe is a device that is used to transfer heat through phase change by making use of

Chapter 1: Introduction

the capillary pumping effect. A heat pipe is made of three sections: evaporator, adiabatic section and condenser; See Fig (1.10) [2].

Heat is applied to the evaporator section by an external source. This heat is conducted through the pipe wall and wick structure to vaporise the working fluid. The resulting vapour pressure drives the vapour through the adiabatic section to the condenser where it condenses releasing its latent heat of vaporisation to the provided heat sink. The capillary pressure is created by the menisci in the wick pumps the condensed fluid back to the evaporator section. Later, in this thesis, analogy will be drawn between a heat pipe and the capillary assisted evaporators tested in this research.

1.5.14 Heat Transfer Limitations in Heat Pipes:

The maximum heat rate that can be achieved by a particular heat pipe under certain working conditions is determined by a number of heat transfer limitations. These are: Continuum flow limit, frozen start-up limit, viscous limit, sonic limit and boiling limit [2]. Brief summary is given below for the heat transfer limitations that are envisaged to be encountered in the capillary evaporators tested in this research.

1.5.14.1 Capillary Limit:

Capillary pressure is the main driving force of circulation of the working fluid between the evaporator and condenser. Therefore, the magnitude of this pressure should be equal to or greater than the pressure drops encountered. Peterson [5] showed that this relationship can be expressed mathematically as follows:

$$\Delta P_{c,m} \geq \Delta P_v + \Delta P_f + \Delta P_{f_i} + \Delta P_{+} + \Delta P_{\Pi} \dots\dots\dots (1.34)$$

Where the vapour pressure drop, ΔP_v , for laminar and turbulent flows is given by equation (1.35) and (1.36) below; [5]:

$$(\Delta P_v)_{laminar} = \frac{16\mu_v L_{eff} Q_c}{2r_v^2 A_v \rho_v h_{fg}} \dots\dots\dots (1.35)$$

$$(\Delta P_v)_{turbulent} = 0.038 \left(\frac{d_v Q_c}{A_v u_v h_{fg}} \right)^{\frac{3}{4}} \frac{2 \mu_v L_{eff} Q_c}{d_v^2 A_v \rho_v h_{fg}} \dots\dots\dots (1.36)$$

The liquid pressure drop, ΔP_t , across a porous body is given by [5]:

$$\Delta P_t = \frac{\mu_t L_{eff} Q_c}{K A_w h_{fg} \rho_t} \dots\dots\dots (1.37)$$

Where the effective capillary length, L_{eff} , in equations (1.35) to (1.37) is given by [5]:

$$L_{eff} = L_a + \frac{L_e + L_c}{2} \dots\dots\dots (1.38)$$

The inertial pressure gradient due to liquid flow in most heat pipe applications is small because of the small liquid velocity and is, therefore, ignored. However, the inertial pressure gradient in the vapour phase is more significant. Busse [9], suggested that for laminar flow of an incompressible vapour stream in a cylindrical heat pipe with uniform heat addition and rejection the inertial pressure gradient, ΔP_i , could be given by:

$$\Delta P_i = \frac{\rho_v V_v^2}{2g} \left[\frac{28}{9} - \frac{0.68 \text{ Re}}{\left(\frac{29 L_e}{d_v} \right) - \text{Re}} \text{EXP} \left(-\frac{60 L_a}{\text{Re} d_v} \right) \right] \dots\dots (1.39)$$

Peterson [5] showed that the above expression provides a reasonably accurate estimation of inertial effects of vapour turbulent flows in heat pipes.

The last two terms in equation (1.34) are the normal and axial hydrostatic liquid pressure drops; ΔP_+ & ΔP_{Π} respectively. These two pressure drops are given by:

$$\Delta P_+ = \rho_t g d_v \cos \psi \dots\dots\dots (1.40)$$

$$\Delta P_{\Pi} = \rho_t g L \sin \psi \dots\dots\dots (1.41)$$

Where ψ is the angle of inclination between the heat pipe and the horizontal level.

1.5.14.2 Boiling Limit:

This heat transfer limit occurs in heat pipes when the liquid return to the evaporator is blocked by bubbles in the wick. This happens when the input heat flux is large. Chi [10]

gave an expression for the heat flux beyond which such bubble growth that could lead to boiling limitation is reached:

$$Q_{bl} = \left(\frac{2 \pi L_e k_{eff} T_v}{h_{fg} \ell n \left(\frac{r_i}{r_v} \right)} \right) \left(\frac{2 \sigma}{r_n} - P_{c,m} \right) \dots (1.42)$$

Where r_n is the critical nucleation site radius, which according to Dunn and Reay [3], can be assumed to be from 2.54×10^{-5} to 2.54×10^{-7} m for conventional metallic heat pipe case materials.

1.5.14.3 Sonic Limit:

In a heat pipe the vapour velocity increases as the vapour travels along the evaporator and reaches a maximum at the end of the evaporator section. When the vapour velocity reaches that of sound (sonic velocity) the flow becomes choked and a sonic limit is reached. In literature, resemblance is drawn between a heat pipe and a converging-diverging nozzle. The evaporator and condenser section of a heat pipe represent a vapour flow channel with mass addition and extraction due to evaporation and condensation, respectively. In a converging-diverging nozzle the mass flow rate is constant whilst the cross-sectional area of the pipe changes. The similarity is in the change of the fluid velocity. As the fluid travels along the heat pipe, its velocity changes due to evaporation & condensation. Typically, the fluid velocity changes as it travels along a converging-diverging nozzle due to the change in the cross-sectional area of the pipe. Peterson [5] explained that the sonic limit is given by:

$$Q_s = 0.47 h_{fg} A_v (\rho_v P_v)^{\frac{1}{2}} \dots (1.43)$$

1.5.14.4 Viscous Limit:

For heat pipes operating at low temperatures, the vapour pressure difference between the evaporator and condenser regions may be very small. This could lead, in some cases, to a

situation where the viscous forces within the vapour region may actually be larger than the pressure gradients resulting from the imposed temperature field. This, in turn, may cause the vapour to stagnate since the pressure gradients within the vapour region may not be sufficient to generate vapour flow. The maximum heat rate a heat pipe could transport before reaching this limit is given by [5]:

$$Q_v = \frac{A_v r_v^2 h_{fv} \rho_v P_v}{16 \mu L_e} \dots\dots\dots (1.44)$$

1.5.14.5 Entrainment Limit:

At high relative velocity in a heat pipe, liquid droplets may be torn from the wick surface and entrained into the flowing vapour by the shear force that exists at the liquid-vapour interface.

The entrained water droplets will be carried back to the condenser. If the entrainment becomes too great, the evaporator will dry out.

The maximum heat transported based on entrainment is given by Peterson [5]:

$$Q_t = A_v h_{fg} \left(\frac{\sigma \rho_v}{2 r_{h,w}} \right)^{\frac{1}{2}} \dots\dots\dots (1.45)$$

1.6 Summary of Chapter One:

In this chapter the problem of using a single heat exchanger for cooling the air in a lithium bromide system has been introduced. Overcoming the hydrostatic head of water by using an evaporator of modified tubes lined with a layer of sintered metal powder leaving the centre of the tube empty for the passage of vapour has been proposed as a solution to this problem. Basic theory on boiling in porous media has also been presented which will be used as a major tool for investigating this problem analytically in chapter 3. However, a body of literature on capillary-assisted boiling has been reviewed before hand as presented in chapter 2.

Fig (1.2) Meniscus Shape at a Solid Wall [3]

Fig (1.3) Arbitrary Curved Surface with Two Radii of Curvature R_I and R_{II} [3]

Fig (1.4) Effective Pumping Radius [3]

Fig (1.5) Capillary Rise in a Tube [6]

Fig (1.6) Interfacial Regions [6]

Fig (1.7) Pool Boiling Curve for Water on a Plane Surface [6]

Fig (1.8) Modes of Heat Transfer and Vapour Formation in Wicks [3]

Fig (1.9) Bubble Formation at the Wall-wick Interface [3]

Fig (1.10) Heat Pipe [3]

Chapter Two

Literature Review

2.1 Introduction

Boiling in capillary structures is an important phenomenon that has found application in many thermal engineering systems, most notably heat pipe technology. The technology of capillary assisted boiling has also found application in recent efforts to develop evaporators of low vapour pressure fluids. In boiling such fluids small hydrostatic liquid heads become significant in suppressing nucleation. This eliminates the possibility of using conventional flooded evaporators. In such cases, evaporator tubes, lined with a capillary structure, can help spread a thin layer of boiling liquid over the internal surface, without the need for flooding the tube. This chapter offers a review of relevant research work. The review looks into two distinct capillary structures, namely porous media and open grooves as they are more relevant to thermal applications. The review also notes development in Capillary Pumped Loops (CPL) as being an established and efficient heat pipe technology.

2.2 Boiling in Porous Media:

Porous structures have proven to be an important means in improving boiling performance. The formation of a thin film of liquid inside the pores of a porous structure greatly improves boiling on these surfaces. Below is a review of some research work on this field.

2.2.1 Boiling Enhancement:

A number of reports on boiling enhancement in porous media were found in the literature. Ponzyak et al. [11] found that boiling heat transfer in porous media increases 8 to 10 times when boiling nitrogen and 2.4 to 3 times when boiling oxygen. Their figures suggest a strong relationship between the enhancement and the working fluid. A finding that is echoed in other reports.

Kovalev and Len'kov [12] found that a porous coating significantly intensifies performance at low heat fluxes. Moreover, they found that boiling started at temperature heads as low as 1 to 2 °C. Their statement on boiling intensification was not quantified. However, the reduction of the boiling temperature head is significant and is repeated elsewhere in the literature.

Bergles and Chyu [13], who investigated experimentally pool boiling from commercial porous metallic surfaces, showed that improvements in boiling heat transfer coefficients, if evaluated at constant heat flux, were 250% for water and 400% to 800% for R-113. Again their figures suggest Variation of enhancement with working fluid, similar to Poznyak et al's [11] report.

Afgan et al [14] investigated experimentally boiling heat transfer of water, ethyl alcohol and Freon-114 at atmospheric pressure in Cr-Ni stainless steel tubes internally covered with sintered porous layer. They found that bubble boiling commenced at small temperature differences of 1 to 1.5 K. The critical heat flux for porous surfaces was found to be 2 to 3 times greater than that for smooth surfaces. The Decrease of superheat reported by these researchers agrees well with that of Kovalev & Len'kov [12].

Zhao and Zhang [15] studied experimentally the performance of boiling heat transfer at higher heat fluxes of distilled water, ethyl alcohol and F-113 on a sintered bronze powder surface at atmosphere pressure. They found that the performance of this surface was 5 to 10 times better than that of smooth surfaces. Their figures of boiling enhancement imply that enhancement varies with working fluid type.

Zhang and Zhao [16] investigated experimentally the performance of nucleate boiling heat transfer on a sprayed porous surface with ethyl alcohol, R-113 and water. They found that the superheat required to initiate boiling was low, the boiling heat transfer coefficient was high, and the range of heat fluxes of enhancement was wide. However,

the lack of figures in their reports doesn't enable the comparison of their work with other researcher's work.

In an experimental work, Tekhver et al. [17] boiled Freon F-113 on the horizontal upper surfaces of an aluminium copper plate with plasma sprayed coating at atmospheric pressure. They found that the burnout heat flux was 1.3 to 2.0 times larger on porous coating surfaces than on surfaces without coating. Although their figures show relatively low enhancement compared to other researchers' work, however, it confirms the superiority of boiling on porous surfaces over plain surfaces.

Pasek [18] studied experimentally boiling of cryogenic and refrigerant liquids on plasma sprayed porous surfaces made of pure aluminium or aluminium/silicon. He found that the heat transfer coefficients of nucleate boiling were 3 to 10 times higher than on smooth surfaces. In addition he also found that the heat transfer coefficients and critical heat fluxes in film boiling regime were larger than those of smooth surfaces. However, his work did not indicate whether the enhancement of the film boiling matched that of the nucleate boiling.

Marto and Lepere [19] conducted pool boiling heat-transfer measurements on two tubes, one with a smooth surface, the other was internally powder coated. When boiling Freon-113 at low heat flux of 4 kW/m^2 , they reported a heat transfer coefficient, which was 10 times that of the plain tube. This enhancement tapered off to a factor slightly above 3 as heat flux was increased to 100 kW/m^2 . When boiling FC-72 the enhanced tube exhibited a heat transfer coefficient from between four to five times that of the plain tube as the heat flux was gradually increased. This paper seems to suggest that improvement to boiling performance at low heat fluxes is much better than that at high ones for porous coated surfaces.

Yilmaz and Westwater [20] tested a tube with internal porous coating with two pure hydrocarbons (isopropyl alcohol and p-xylene). The tube had 0.43 mm thick coating. They

reported that this enhanced tube improved nucleate boiling heat transfer coefficient by shifting the boiling curve to lower boiling temperatures compared with a plain copper tube. Again the non-quantified improvement to the boiling performance in this report doesn't allow comparison of his work to other researchers work.

Zuo et al. [21] tested an advanced heat pipe mechanism which combines the capillary effect of sintered metal powder wicks with the pulsating motion of the working fluid for cooling high heat flux electronics. The heat pipes showed significantly better performance than that of equivalent pure copper pipes by four folds. It was not clear from the report whether the pulsating motion of the working fluid had the same intensifying effect on both pipes. Chang and You [22] tested the boiling of FC-72 at atmospheric pressure on five different micro-porous coated surfaces (made of aluminium, copper, silver and two diamond surfaces that differ in the type of binder used). The micro-porous enhanced surfaces showed about 80-90 % reduction in incipience superheat, about 330% enhancement of the nucleate boiling heat-transfer coefficient and about 100% enhancement in critical heat flux. Many researchers reported that for boiling in a porous media, the heat transfer coefficients increase to a maximum, with increasing heat flux, and then drop after the critical heat flux is reached. However, Fujii et al. [23] who tested five samples of a porous structure reported that two samples out of the five have shown a different trend. For the other three samples they reported that the heat transfer coefficient increased with increasing heat flux without mentioning whether this increase goes through maximum. A heat transfer coefficient of $57,000 \text{ W/m}^2 \text{ } ^\circ\text{C}$ at a heat flux of $116,300 \text{ W/m}^2$ was obtained by them for R-113. This paper shows that the evidence on the behaviour of the heat transfer coefficient seems to be inconclusive, as the samples showed opposite trends. However, the total picture (of the five samples) seems to suggest the existence of an optimum coefficient, and that the trend is not monotonous.

Ivanovskii et al. [24] recorded a heat transfer coefficient of $1.2 \times 10^4 \text{ W/m}^2\text{K}$ for a corrugated nickel mesh of thickness 0.12 mm and an effective pore radius of 18 μm . They found that by setting up a thin layer of brass mesh of square weave between the corrugated structure and heating surface, the heat transfer coefficient and heat flux increased by 30 – 40%. Their work didn't include comparison to boiling in smooth surfaces.

Udell [25] & [26] recorded a dry out heat flux of 3.25 kW/m^2 when sand grain in a tube is heated from top as well as from bottom. This work didn't include comparison with boiling in smooth surfaces; however, the value of the dry out heat flux recorded is relatively low compared to other researchers' work.

Kovalev et al. [27] predicted a maximum heat transfer coefficient at a critical heat flux of $1.0 \times 10^6 \text{ W/m}^2$ for water boiling on 1 mm thick porous coating made of sintered stainless steel particles of 300 – 400 μm diameter. Their work did not include comparison with boiling in a non-porous media. However, the high value of the critical heat flux indicates improved performance.

Eames et al. [28] recorded a heat transfer coefficient of $140 \text{ W/m}^2 \text{ }^\circ\text{C}$ for a water tube evaporator coated with porous structure in its interior. The relatively low value of heat transfer coefficient appears to be due to the low heat fluxes used in their experiments. No comparison with smooth surface boiling was reported.

Liao and Zhao [29] recorded a critical heat flux of 268.9 kW/m^2 when they tested experimentally heat and mass transfer in a capillary-driven vertical rectangular capillary porous structure with water heated from top by a grooved block. The high value of critical heat flux recorded in this work is very notable.

Zhao and Liao [30] tested experimentally boiling in a vertical porous structure made of a number of staggered miniature silver-copper circular cylinders and heated from top by a grooved copper block. They plotted heat transfer coefficient against heat flux. They reached a heat transfer coefficient of $10750 \text{ W/m}^2 \text{ }^\circ\text{C}$ at a critical heat flux of 264.81

kW/m^2 . This heat transfer coefficient agreed with a modelled one within 11.2%. Again the high value of critical heat flux recorded in this work is very notable.

Sabir and Bwalya [1] obtained a heat flux of 2.75 kW/m^2 for an internally power coated tube. Judging by the value of their heat flux, it is reasonable to assume that it was no where close to the critical heat flux. No comparison with smooth surface performance was given in their work.

Raiff and Wayner [31] carried out experimental and theoretical investigation to study the evaporation from a microporous flow control element (MPFCE) on a porous heat source. In this study a porous structure was heated from below using porous structure disks. The liquid (either water or methanol) was fed to the MPFCE from above. Comparison between theoretical results obtained from the analytical model developed in this study and the experimental results showed that: for pore diameter of $10 \text{ }\mu\text{m}$, the theoretical and experimental heat transfers coefficients were $6530 \text{ W/ m}^2\text{K}$ and $6439 \text{ W/ m}^2\text{K}$, respectively. For pore diameter of $2 \text{ }\mu\text{m}$ these theoretical and experimental coefficients were $8347 \text{ W/m}^2\text{K}$ and $6882 \text{ W/ m}^2\text{K}$ respectively. For pore diameters of $0.25 \text{ }\mu\text{m}$ the theoretical coefficient was $11357 \text{ W/m}^2\text{K}$ whereas experimental one could not be obtained due to extremely low values of critical heat flux for $0.25 \text{ }\mu\text{m}$ element. The authors explained that examination of the heat flux distribution revealed that approximately 50% of the energy was removed in 20% of the vapour exhaust channels adjacent to the heat source. It is interesting to note the wide range of heat transfer coefficients and fluxes reported in this section. Although they used two working fluids, the authors did not report variation of heat transfer coefficient with the fluid used, in contradiction to other workers. Madhusudana and Balakrishnan [32] found that the burnout heat flux was purely a geometrical constraint. However, no values or trends for thermal performance were given in their paper.

Tekhver and Sui [33] suggested that the value of the critical heat flux depended on the previous history of the process (boiling curve process), however, no values or trends for thermal performance were given in their paper too.

Brautsh and Kew [34] investigated experimentally the heat transfer process in wire mesh wicks. They found that the formation and entrapment of vapour within the wick is a factor in the dry out of the wick and in disruption of the liquid supply to areas above the trapped vapour bubble. They also found that for a given wicking height the heat flux prior to that required to initiate dry out increased with increasing mesh number and increasing number of layers. Up to the dry out heat flux, the heat transfer coefficient increased with heat flux, and for a given heat flux, increased with mesh number and decreased with increasing number of layers. The authors seem to suggest monotonous increase of heat transfer coefficient with heat flux up to the burn-out point.

O'Neil et al [35] compared experimentally pool boiling in porous surfaces to boiling on smooth surfaces for propylene, ethanol, and R11. They found that at constant heat flux the boiling superheat is reduced by over a factor of ten for the porous surfaces. They also found that the critical heat flux for a horizontal disc covered by porous surface is raised by a factor of 1.8 and concluded that the behaviour of a porous surface near the critical value tend to be more stable than that of smooth surfaces. The reduction in boiling superheat and enhancement in critical heat flux they found are notable and comparable with other researchers work.

Vasiliev et al [36] investigated experimentally pool boiling on single horizontal stainless steel pipes with smooth and porous surfaces for a range of heat flux densities of 0.1 to 100 kW/m² and saturation temperatures T_s -10 to +40 °C which corresponds to saturation pressure range of 3.45 to 13.8 bar. They found that application of porous coatings led to increase in heat transfer coefficients in pool boiling of propane on a horizontal pipe by a factor of 3 to 5 in the region of low heat loads ($q < 8$ kW/m²) and by a factor of 2.5 to 3 in

the region of high heat fluxes ($q > 8 \text{ kW/m}^2$). Their finding agrees with that of Marto and Lepere [19] in that enhancement to boiling heat transfer at higher heat fluxes is less than that at lower heat fluxes, however, the reduction in performance noted here is less than that noted by Marto and Lepere [19]. This difference might be because of different fluids tested in the two researches.

2.2.2 Mechanism of Boiling:

A number of researchers attempted to explain the mechanisms by which boiling in porous media occurs.

Orlov and Savel'ev [37] assumed that the porous coating has communicating open capillaries, the majority of which are of relatively small cross-sectional size and a minority of larger size channels. They explained that boiling heat transfer takes place predominantly in the capillaries (channel) of large cross-sectional area and the capillaries of small cross-sectional area act as feeders. However, this physical model, though logical, was assumed, rather than observed.

Afgan et al. [14] stated that a nucleation centre in a porous structure functioned as a small heat pipe i.e. the cavities between particles of a porous structure constituted small heat pipes. Thus, intensive feeding of the growing bubble with vapour through the channel of the "heat pipe" would take place until its separation from the heated wall. They explained that this is why the bubble generated on a surface with a porous surface, in relatively cold liquid, grows without the difficulties which usually accompany boiling on smooth surfaces where the growth of the bubble ceases or slows down as soon as the top of the bubble leaves the superheated boundary layer adjacent to the tube wall and touches the bulk of the cold liquid. The model of Afgan et al. [14] could be described as a model that established the capillary effect as a sole mechanism of liquid circulation.

Zhang and Zhao [16], in their study of nucleate boiling heat transfer on spraying porous surface, noted that there are a lot of cavities with different shapes in a spraying porous

layer. These pores and cavities form a series of entrant or re-entrant cavities with quite well gas-entrapping ability. Therefore, such cavities would retain and gather vapour or non-condensable gases and become stable nucleation centres. They explained that the liquid can penetrate into the layer fully and re-flow to the heating surface by the capillary force and the suction force induced by the vapour escaping thin jets. Moreover, the thin vapour jets hardly coalesce with one another, thus the liquid supplement to the heating surface would not be obstructed. The authors suggested that the vapour jets hardly coalesce. However, it is almost certain that with increased heat flux and number of active nucleation sites, these jets would eventually start to coalesce and a dry-out flux will be reached.

In a similar explanation, Zhang and Zhang [38] described a model for boiling heat transfer in a thin porous layer of sintered bronze powder at low and moderate heat fluxes. They noted that there are a lot of inter-connected entrant and re-entrant cavities. On one hand, these cavities can retain gas (or vapour) to form activated nuclei, and on the other hand, they can promote vapour-liquid two-phase flow. The researchers stated that at low and moderate heat fluxes, only some of the cavities in the layer are active. For simplicity, they assumed that every active cavity is surrounded by inactive ones which represent a simplified model of a porous-wall capillary pipe. Furthermore, they stated that in a steady state boiling, the vapour resulting from the evaporation of the thin liquid film adheres to the powder surfaces in the cavity channel and ejects from the channel in the form of a thin jet. Under the action of the capillary force and the suction force caused by vapour ejection, part of the pool liquid is supplied from inactive cavities into the active cavity through the porous wall, and the other part of the liquid would re-flow into the active cavity along the channel itself. The two supplements of liquid flow down the inner wall of capillary channel and evaporate gradually, and a two-phase re-circulation heat transfer is consequently established. With increasing heat flux, the former supplement decreases and the latter increases. Finally, Zhang and Zhang explained that the process of two-phase flow and heat

transfer in the porous wall capillary pipe could be considered to be a combination of two simpler processes. The first one is similar to the process in the evaporation section of a micro-thermosyphon pipe, and the second is similar to micro-porous-wall pipe only with liquid radial permeating. It has to be re-iterated here that this model is similar to that of Zhang and Zhao [16], whoever, the assumption of active sites surrounded by inactive ones in this model was adopted for simplicity.

Ma and Pan [39] discussed the idea of a thin liquid on a thermo-capillary driven flow. They defined a macro layer as a thin liquid film between the heating surface and hovering bubbles that were nourished by the evaporation of vapour at the interface of the liquid film (the vapour-liquid interface). They explained that this liquid film is penetrated by the surface of vapour stem and covered by the hovering bubbles, which provide a very efficient heat transfer mechanism. This model ignores liquid ejection, although describes rising columns of vapour.

Chang and You [40] reported the identification of the heat-transfer mechanisms responsible for augmenting the boiling process from porous metallic surfaces given by Thome [41]. The latter explained that latent heat is transported by three types of evaporation mechanisms: thin film, capillary and external evaporation. He added that additional convection mechanisms are generated as well on the exterior surface.

Nakayama et al. [42] developed an analytical model of the dynamic cycle of bubble formation. The cycle consisted of a waiting period and a bubble growth period; in the former the pressure in the tunnel (cavity) was increased due to evaporation from internally held menisci and in the latter a certain amount of pool liquid was sucked in the tunnel (by capillary forces) to be subsequently evaporated. The model was intended for a class of porous layers that have a relatively large volume of interconnected cavities and narrow openings on the exterior surface. This cyclic model is unique in the literature, but needs experimental validation.

Hanlon and Ma [43] developed two-dimensional model based on the fact that on a sintered metal layer the bulk of evaporation occurs on the thin film region on the top surface of the fluid saturating the sintered layer which provides a higher thermal conductivity medium transferring heat to the surface. This model is unique in focusing on thin film evaporation as having a major role in enhancing boiling in porous structures although other researchers e.g. Chang and Yu [40] and Thome [41] have considered that but with less emphasis. However, the role of thin film in enhancing evaporation in capillary assisted-boiling is much echoed in grooved capillary structures.

2.2.3 Effect of Layer Geometry:

Researchers have studied the effect of porous material geometry (particle size/diameter¹, pore diameter, and layer thickness) on the boiling heat transfer performance. Different results are obtained.

Fujii et al [23] studied experimentally the boiling of saturated R-11 on a porous surface made by fixing copper particles on a smooth flat surface by plating with copper. The diameters of the tested copper particles were in the range of 115 to 530 μm and each sample tested had 2 to 4 layers of porous particles. They found that the ratio of heat transfer coefficient of a micro porous surface to the heat transfer coefficient of a smooth surface increased as the copper particles forming the micro-porous heating surface were reduced in size and the number of micro-porous layers increased.

Pikhlak and Tekhver [44] investigated experimentally the effects of the principal parameters of a porous coating on heat transfer during the boiling of F-113. They found that the curve of the temperature rise against the pore size showed that for a given heat load there exists an optimum powder grain size. As the heat density increased, the optimal shifted toward larger dimensions. Similarly, the temperature rise of the surface

¹ The terms particle size and particle diameter are used to indicate the same parameter in porous layer literature, however, in this thesis the term 'particle size' is widely used.

with respect to the boiling liquid for a given heat load had a minimum that corresponded to optimal coating thickness. This seems more logical than the findings of Orlov and Savel'ev [37], who suggested monotonous improvement with layer thickness. However, the contradiction between the findings of Pikhvak & Tekhver [44] and Orlov & Savel'ev [37] might be due to limited range of layer thicknesses and/or conditions tested.

Zhao and Zhang [15], who found that a sintered powder surface had excellent enhanced boiling performance at moderate and low heat fluxes, remarked that the porous layer thickness inversely affected the performance of the porous surface at high heat fluxes. The experiments of Zhao and Zhang [15] were carried out using sintered bronze powder as a porous material having pore range of 161.3 to 370.4 μm and a porous layer thickness range of 1.0 to 2.65 mm. They used distilled water, ethyl alcohol and F-113 as working fluids. Their finding about the effect of layer thickness seems to contradict all previously reported findings. This might be due to their seemingly small range of thicknesses (1.0 – 2.65 mm).

In a conclusion similar to that of Fujii et al. [23], Tung and Dhir [45], who seem to suggest insignificant effect of particle size on the performance, found that film heat transfer coefficient increased slightly with decreasing particle size when a stainless steel sphere was embedded in a porous medium composed of glass particles. The size of the glass particle was varied from 19 to 2.9 mm. It is worth noting that the difference in particle diameter tested by Fujii et al. (115 to 530 μm) and those tested by Tung and Dhir [45] (19 to 2.9 mm) is large.

Zhang and Zhang [38] obtained experimentally, graphs for the influence of particle diameter and porous layer thickness on boiling heat transfer. They tested distilled water and F-113 on a bronze sintered powder with pore diameters from 0.529 to 0.106 mm and layer thickness from 2.63 to 0.94 mm. Their results showed that an optimum pore existed for minimum superheat.

Tekhver et al. [17] tested experimentally F-113 on plasma sprayed porous coating deposited on aluminium and copper surfaces. The mean pore radius of the porous coating ranged between 1 to 20 μm and the layer thickness ranged between 0.03 to 0.06 mm. They explained that a minimum superheat existed for a certain pore diameter and for a certain porous layer thickness. Moreover, Tekhver et al. [17] found that the optimum value of the porous layer thickness decreased as the heat flux increased and increased as the pore diameter decreased. It is to be noted that the latter of these two effects is uniquely reported by them. The findings of Tekhver et al. [17] agreed with those of Pikhlak and Tekhver [44] and partially agreed with Zhang and Zhang [38].

Pasek [18], who only tested the effect of layer thickness on boiling performance, carried out experimental work on plasma sprayed porous surfaces of pure aluminium and aluminium/silicon with various thicknesses starting from 0.13 mm. He stated that for low heat fluxes, the influence of the coating thickness is not significant when boiling cryogenic liquids. For high heat fluxes, He stated that there is an optimum coating thickness which gives the maximum heat transfer coefficient for a given heat flux. It has to be noted here that limiting the existence of an optimum layer thickness to high heat fluxes is unique to this report.

Liao and Zhao [46] studied experimentally a vertical rectangular capillary porous structure saturated with water and heated from a grooved block placed on the top. They concluded that there existed an optimum pore diameter for the maximum heat transfer coefficient. This conclusion agrees with many previous findings. They also explained that the critical heat flux is inversely proportional to the pore diameter. They found that the maximum value of the heat transfer coefficient is not affected by the thickness of the porous material. This finding looks to be in agreement with that of Pasek [18] at low heat fluxes. The difference is that the finding of Pasek is limited to low heat fluxes only. However, Liao and Zhao [46] stated that the thickness of the material directly affected

the critical heat flux. This contradicts that of Zhang and Zhao [16] who believed that the thickness of the porous material has no effect on the critical heat flux.

O'Neil et al [35] found that there is an optimum pore radius which varies with the fluid properties, heat flux, and type of porous packing. For instance, if the liquid has high surface tension and high thermal conductivity, such as water, a relatively coarse matrix is required. For a low-surface tension, low thermal conductivity liquid such as light hydrocarbons, fluorocarbons, and cryogenics, a fine matrix is optimum. The link between the value of optimum pore radius and heat flux is much echoed elsewhere in the literature of boiling in porous media e.g. Phikhlak and Tekhever [44], Zhang and Zhang [38], Tekhver et al. [17] and Pasek [18]. However, the link between fluid properties and the value of optimum pore radius is emphasised here.

Vasiliev et al. [36] investigated experimentally pool boiling on single horizontal stainless steel pipes with smooth and porous surfaces for a range of heat flux densities of 0.1 to 100 kW/m² and saturation temperatures T_{sat} -10 to +40 °C which corresponds to saturation pressure range of 3.45 to 13.8 bar. At a porosity of 12% they found that the heat flux decreases to a minimum and then increases with increase in layer thickness for the thickness range tested; 0.1 to 0.3 mm. The notably high values of working fluid pressure, relatively small range of layer thickness and small value of layer porosity have probably affected the finding of this work.

Wang and Peterson [48] developed analytically a two-dimensional model in which mass and momentum conservation equations are applied to predict the heat transfer performance of the thin porous layer and the capillary evaporation limitation. The model investigates the effects of thickness, porosity, and permeability of the porous layer on the maximum heat transport capacity and wall superheats. They tested two types of porous materials; sintered powder and layers of screen mesh. The results indicated that the maximum capillary evaporation heat transfer is proportional to the thickness and the

permeability of the thin porous layer and that increasing the thickness of the porous layer can result in higher superheat. It is also found that while the heat flux increases with increasing particle size, the maximum capillary evaporation capacity decreases. What characterises this model over other models is that it applied the momentum conservation principle which is overlooked in many ones.

Pogorelova and Kiselev [49] tested experimentally the effect of layer thickness on boiling of water at 0.1 MPa saturation pressure on fine-porous copper powder of 10 μm diameter and 0.61-0.68 porosity and on highly porous cellular material of 0.6 mm particle diameter and 0.87-0.91 porosity. For the fine porous material they tested three layer thicknesses 0.5, 1.0 and 2.0 mm and for the highly porous material they tested five layer thicknesses 16, 13, 10, 6, and 2 mm. For the fine porous material they found that the heat transfer coefficient increases to a maximum with the increase in layer. The relatively large difference in particle size between the fine porous material (10 μm) and the highly cellular material (0.6 mm) possibly makes it difficult to compare the results of the two porous materials.

Hanlon and Ma [43] developed two-dimensional analytical model incorporating the capillary limitation and the onset of nucleate boiling to predict the overall heat transfer capability in the sintered wick structure. The porous wick tested was made of pure copper particles. They found that by decreasing the average particle radius, the evaporation heat transfer coefficient can be enhanced and that there exist an optimum layer thickness for maximum heat removal. They did not specify whether this enhancement will persist for no matter how small the particle size is. However, it seems logical that there is a certain limit for the particle size below which the trend changes.

2.2.4 Effect of Thermophysical Properties:

Reports on this topic are relatively few in number. Mustafa and Duwari [47] defined porosity as a measure of the pore space and hence of the fluid capacity of the medium.

Meanwhile, they defined permeability as a measure of the ease with which fluids may traverse the medium under the influence of a driving pressure.

Pikhlak and Tekhver [44], who studied boiling in a porous structure using F-113, reported that the surface super heat decreased monotonically as the thermal conductivity of the porous layer increased. They also found that there is an optimal porosity (in the range of 0.2 to 0.3) that gives minimum surface temperature rise. Furthermore, they reported that this optimum porosity increases with the increase of heat flux and porous layer thickness. It has to be mentioned here the above findings regarding thermal conductivity are logical as high conductivity improves the heat transfer coefficient and decreases super heat temperatures.

Udell [25] and [26] studied boiling heat transfer in a porous media composed of sand grain in a tube heated from both ends. He found that the temperature difference across the two-phase zone increases as the permeability decreases. He attributed this to the decreased thermal conductivity at low permeability resulting in high thermal resistance. This is to be expected as liquids moving under capillary effect through the pores will improve the effective conductivity of the porous layer.

Tekhver et al. [17] reported the existence of an optimum porosity, which is directly proportional to the heat flux, and indirectly proportional to the pore diameter. The direct proportionality with heat flux is in line with the findings of Pikhlak & Tekhver [44]. Pasek [18] found that permeability does not significantly affect conductivity and hence does not influence the heat transfer coefficient. His findings contradict other workers and it seems inconceivable that resistance to liquid flow will have little or no effect on the effective conductivity of the porous layer.

Zhang and Zhang [38] found that for low and moderate heat fluxes the smaller the permeability the better boiling heat transfer. Their findings supports Udell's [25] and [26] report.

Chang and You [40], related porosity to pore size and defined an Effective Volume Ratio (EVR) as the ratio of effective volume of powder to that of the binding material. They found that reduced porosity may lead to reduced evaporation rates. They also measured 3 – 4.5 times enhancement of heat transfer coefficient at $EVR > 1.1$ compared with bare surfaces. They found that boiling curves were found to be largely scattered as the EVR decreases. Comparing their work with other researcher's work it could be mentioned that greater EVR means greater powder volume, i.e., larger particles and pores. Their findings of improved performance with increased EVR, therefore, seem in contradiction with other workers.

Vasiliev et al. [36] who investigated experimentally pool boiling on single horizontal stainless steel pipes with smooth and porous surfaces for a range of heat flux densities of 0.1 to 100 kW/m² and saturation temperatures of -10 to +40 °C. They found that increase in porous coating porosity favours heat transfer enhancement. This finding agrees with that of Chang and You [40], however, the low range of porosity tested here should be noted (4 – 17%).

Wang and Peterson [48] who tested two types of porous materials; sintered powder and layers of screen mesh, found that the heat flux increases rapidly with increasing bond number, Bo (The Bond number is a number that defines the characteristics of the porous layer and it is given by:

$$Bo = \frac{g (\rho_l - \rho_v) K}{\sigma \epsilon} \dots\dots\dots(2.1)$$

They also found that larger permeability and smaller porosity increase the heat flux. The notion of introducing Bond number to show the effect of layer characteristics on boiling seems to be more practicable than dealing with the porosity and permeability individually because of the confusing similarities in the concepts of the two parameters. However, the findings of this research agree with other researcher's findings regarding

the porosity and permeability e.g. Udell [25], Chang and You [40] and Vasiliev et al [36].

Hanlon and Ma [43] who tested analytically a porous wick made of pure copper particles found that for a wick made of 0.635 mm radius copper particles and 10 mm layer thickness, the dry-out heat flux decreases with increasing layer porosity. Their finding agrees with other researchers work.

Pogorelova and Kiselev [49] tested experimentally fine-porous copper powder of 10 μm diameter and 0.61-0.68 porosity and highly porous cellular material of 0.6 mm particle diameter and 0.87-0.91 porosity. Although they noted difference in trend in the performance of the two types of porous materials as explained earlier in section 2.1.3, but the relatively large difference in particle size between the two porous materials (10 μm & 0.6 mm) and possibly makes it difficult to compare the performance on the basis of porosity.

2.2.5 Effect of fluid Flow:

Khrustalev and Faghri [50] developed a physical and mathematical model to investigate whether the high-velocity vapour flows could explain the existence of extended thick liquid films attached to evaporating meniscus ending with the liquid microfilm. They obtained numerical results for water evaporating from a cylindrical pore with inner radius of 20 μm . They found that high vapour velocities during evaporation of pure liquids in micropores can, in principle, make possible existence of thick liquid films attached to a hemispherical evaporating meniscus. They also found that thick-film evaporation from micropores could occur at lower rates, compared to the case of hemispherical meniscus ending with the microfilms. However, it has to be mentioned here there was no experimental validation of their model was conducted.

Zhu & Vafai [51] developed an analytical model, which incorporated liquid-vapour interfacial hydrodynamic transport through a porous wick, for predicting the vapour and

liquid flow and the maximum heat transfer capability of a heat pipe. A closed-form solution was obtained for the vapour and wall temperatures as well as the vapour and liquid velocity and pressure distributions for a convective cooling condition in the condenser region. The results showed that the interfacial effects were small and could be neglected. It has to be mentioned here that it is difficult to accept that interfacial forces can be neglected even at high vapour velocities. It may be that the range of velocities studied was too low to have an effect.

2.3 Boiling in Grooved Surfaces:

Boiling in grooved structure is very similar to boiling in porous structures. In grooved structures, the capillary effect also plays an essential role in promoting boiling performance through the formation of a meniscus on the groove's wall.

2.3.1 Boiling Enhancement:

Wayner et al. [52] developed a formula for calculating the average evaporation heat transfer-coefficient for the interline region of an adsorption controlled wetting film of non-polar liquids. The formula was obtained in terms of the ideal liquid-vapour interfacial heat-transfer coefficient and the physical properties of the system. The coefficient varied from zero, at the interline, to a value equal to liquid-vapour interfacial heat-transfer coefficient over a relatively short distance. However, their model lacks experimental validation.

Stephan and Busse [53] presented an analytical model for the radial heat transfer of an open grooved heat pipe evaporator. The model took into account the influence of meniscus curvature and adhesion forces on the volatility of the liquid. The model was used for computing radial heat transfer coefficient at the evaporator of an aluminium/ammonia heat pipe. This showed that assuming saturation temperature at the meniscus surface introduced an artificial cooling to the top of the groove and led to a large over prediction of the radial heat transfer coefficient.

Schonberg and Wayner [54] studied analytically the heat transfer by evaporation from a thin film. Their study was an extension to that of Wayner et al. [52] in which the capillary and conductivity effects had been neglected. In the study, the researchers presented an analytical solution for the 'integral contact-line evaporative heat sink' including film conductivity effects as well as presenting analytical film profile for the case of strong conductivity effects. They explained that 'contact-line' refers to the junction of a meniscus and non-evaporating thin film. The 'integral contact-line evaporating heat sink' was defined as the total power per unit length of the contact line.

Khrustalev et al. [55] and Khrustalev and Fagrhi [56] developed a mathematical model in which the heat and mass transfer processes in an axially grooved heat pipe (AGHP) were examined. The model described heat transfer through thin liquid films accounting for the effects of interfacial thermal resistance, disjoining pressure and surface roughness. The main findings of this mathematical model were:

Accounting for the roughness of the solid surface in the thin evaporating film region resulted in a decrease of the heat transfer coefficient by 30 % in comparison to that obtained for smooth surface. However, this finding disagrees with that of Wang and Catton [57] who found that evaporation heat transfer is significantly improved when a triangular grooved is covered by a thin porous layer. Heat transfer coefficients calculated taking account of curvature variation along the film were 5% higher than those calculated assuming no curvature variation. The value of the local evaporative heat transfer coefficient (for a fixed contact angle) was nearly independent of the external evaporator wall heat flux.

Ha and Peterson [58] developed an analytical method to understand the vaporisation occurring in the interline region of a thin liquid film on a V-shape groove wall. The method allowed the determination of the average heat transfer coefficient and the effective evaporating length of a given set of parameters such as groove geometry,

working fluid properties, heat flux variation along the plate, and vapour and groove wall temperatures. They found that the average and local heat transfer coefficients were sensitive to the characteristic thermal resistance ratio. Both coefficients increased sharply in a very short term of the thin film thickness in the interline region and after reaching a maximum value, decreased slowly.

Höhmnn and Stephan [59] carried out experimental work to study the wetting and heat transfer characteristics in close proximity of an evaporating liquid meniscus in the micro region. Thermodynamic liquid crystals (TLCs) were used to measure temperature distribution underneath the evaporating meniscus. The colour play of the TLCs was recorded with a long- working-distance microscope and a CCD-camera. A plot was drawn for the temperature against the meniscus length. The researchers divided the temperature plot to three regions: macro region, micro region and adsorbed film region. It was found that macro region showed constant temperature. This corresponded to the convection region in the fluid bulk. Adjacent to this section was a strong temperature drop in the micro region. This was caused by the local cooling due to evaporation in the micro region. The temperature then rose, as the heat transfer in the third region (adsorbed film region) was small. The finding of Hohmann and Stephan [59] about the strong temperature drop in the micro region interprets that of Ha and Peterson [58] about sharp increase in the average and local heat transfer coefficients of the thin film (occurring in the interline region on a V-shape groove wall) in a very short term of the thin film thickness.

Khrustalev & Faghri [60] developed a mathematical model of the evaporating liquid meniscus in a capillary slot to investigate the influence of the liquid and vapour flows on evaporation from the liquid-vapour meniscus and to numerically evaluate the vapour flow patterns in a narrow passage over the curved interface. This model assumed a constant wall temperature and constant liquid-vapour interface curvature. The model

included two-dimensional steady-state momentum conservation and energy equations for both vapour and liquid phases. It was shown that the fluid flow effect on the heat transfer during evaporation from the liquid-vapour meniscus resulted in increasing the effective heat transfer coefficient by up to 30%.

Peterson and Ma [61] developed a mathematical model to predict the minimum meniscus radius and the maximum heat transport in triangular grooves, as a function of the physical characteristics and geometry. The calculated results, using methanol, indicated that the heat transport capacity of a micro heat pipe was dependent on: the channel angle of grooves, the contact angle of the liquid, the length of the micro heat pipe, the vapour flow characteristics, and the tilt angle. It was shown that neglecting the effects of the frictional interaction between the liquid and vapour flow could result in significant errors in predicting the maximum heat transport capacity. A maximum capillary heat transport capability of 6.7 W/cm^2 was recorded in this calculation.

Plesch et al. [62] studied experimentally the performance of two types of copper miniature heat pipes of rectangular cross section for the purpose of cooling electronic devices. The first type had transverse grooves and capillary supply channels for liquid transport in the longitudinal direction on the small faces of the heat pipe. The second type had longitudinal grooves on its entire pipe length. Axial liquid transport as well as evaporation and condensation could take place in these grooves. The two plates were charged with clean water. A maximum heat flux of 14 W and a minimum thermal resistance of 0.6 K/W were registered for the first type. A maximum heat flux of 60 W/cm^2 at surface temperature of $125 \text{ }^\circ\text{C}$ and a minimum thermal resistance of 0.4 K/W were registered for the second type on the vertical position with the condenser of the heat pipe on the upper end. The heat transport capability of the first type was found to be 28 times better than an equivalent solid copper bar whereas the heat transport capability of the second type was found to be 40 times better.

Krustalev and Faghri [63] presented a mathematical model of low-temperature miniature axially grooved heat pipes in which the fluid circulation was considered along with heat and mass transfer processes during evaporation and condensation. The model was developed for rectangular and triangular grooves in circular or flat tubes. Maximum heat fluxes in the evaporator of 25 and 40 W/cm² for the horizontal and vertical orientations, respectively, at operating temperature of 90 to 120 °C were achieved.

Schonberg et al. [64] modelled high heat flux evaporation from steady meniscus formed in a 2 µm channel using kinetic theory and the augmented Young-Laplace equation of capillarity. Heat fluxes of 1.3-1.6 x 10⁶ W/m² based on the width of the channel were obtained for heptane completely wetting the substrate at 100 °C. It can be said here that the high value of heat flux achieved by these researchers is remarkable.

Cao and Goa [65] tested two flat copper axially grooved miniature heat pipes. The two plates were tested under different heat inputs, cooling water temperatures and orientations. The maximum power input and heat flux at the evaporator were about 31 W and 20.6 W/cm², respectively, for the horizontal arrangement. The effective thermal conductance of the heat pipe was about 40 times that of copper based on the external cross-sectional area of the miniature heat pipe.

Cao et al. [66] studied experimentally an air-cooled system employing longitudinally grooved miniature heat pipes as thermal spreaders for cooling Metal oxide semiconductors Controlled Thyristors (MCTs). The maximum heat transfer rate obtained from this heat pipe was about 40 W and the maximum heat flux was 18.3 W/cm².

Hopkins et al. [67] investigated experimentally and analytically the maximum heat transfer capabilities of three copper-water Flat Miniature Heat Pipes (FMHP): two with diagonal trapezoidal capillary grooves (at slight angle to longitudinal axis) and one with rectangular axial (longitudinal) micro capillary grooves, for a range of operating

temperatures, orientations and heating configurations. It was found that the heat pipes with axial capillary grooves, for which the maximum heat flux on the evaporator wall exceeded 90 W/cm^2 in the horizontal orientation and 150 W/cm^2 in the vertical orientation, were more promising than the heat pipes with trapezoidal grooves. The high values of heat fluxes, given here by Hopkins et al. are also remarkable.

2.3.2 Mechanisms of Boiling:

Holm and Goplen [68] showed experimentally that the extended meniscus formed on the heated wall of a capillary groove is characterised by three regions: an equilibrium thin film region (formed at the upper extent of the meniscus and in which no evaporation occurred), an evaporating thin film region (formed just below the equilibrium thin film and in which the film thickness increased and the adhesion forces diminished causing evaporation), and an intrinsic meniscus region (formed at the bottom of the extended meniscus and in which the film thickness is sufficiently large i.e. significant thermal resistances). It was found that more than 80% of the total heat dissipation occurred in a region that was 0.127 to 0.152 mm high in the meniscus thin transition region. It was also found that less 10% of the total heat dissipation occurred in the evaporative film region. This finding of Holm and Goplen agrees well with temperature distribution plot drawn by Ha and Peterson [58].

Ha and Peterson [69] carried out an analytical study of axial flow evaporating thin film through a V-shaped micro channel for the case of a grooved plate inclined with a very small tilt angle. They tried to identify the end point of the wetted region for a given uniform heat flux applied on one end of a grooved plate immersed in a pool of liquid and held stationary at a small inclination angle, while heat is applied to a portion of the underside of the plate. A generalised graph of the non-dimensional radius of curvature with respect to the non-dimensionalised axial length was obtained.

Ha and Peterson [70] developed an analytical method for predicting the axial dry out location for a V-shaped microgrooved plate immersed in a pool of liquid and held stationary at an inclination. In this model, an axial adiabatic region was included between the origin point where the plate emerged from the liquid pool and the junction point from which a uniform heat flux was applied. It was found that, for the isothermal case, the non-dimensionalized wetted length was twice the inverse of the Bond number multiplied by the sine of the angle of inclination of the grooved plate. For the evaporating non-isothermal case with uniform heat flux, the non-dimensionalized wetted length of the evaporating liquid film was approximately proportional to the inverse of the square root of the applied heat flux.

Ha and Peterson [58] developed an analytical method to understand the vaporisation occurring in the interline region of a thin liquid film of a V-shape groove wall. They found that when the film superheat was constant, the primary factor affecting the length of the evaporating interline region was the heat supplied from the bottom plate.

Belonogov and Kiseev [71] investigated experimentally the process of evaporation from wetting meniscus in a capillary glass. They found that during intensive evaporation the shape of the wetting film changed as, consequently, did the wetting angle. It is worth noting here that this shape change of the meniscus and the subsequent reduction of the wetting angle is the driving force in heat pipes, where the difference in meniscus profile between the evaporator and condenser sections drives the liquid circulation.

2.3.3 Effect of Groove Geometry:

Stores and Catton [72] investigated experimentally the performance of two axially grooved capillary stainless steel flat plates; one plate with sinusoidal channels and the other with triangular ones. The channels had identical cross sectional areas. Thermal load was applied in steps (up to 22 W) from below and the wetted length was registered. The researchers concluded that for equivalent cross sectional area, angle of inclination,

and heat input from below, a triangular groove geometry sustained a larger wetted area while a sinusoidal groove supported a greater average heat flux. However, they didn't give any explanation for the improved performance in the sinusoidal grooves.

Sabir and Bwalya [1] developed and tested three water evaporators with internal capillary structure. Two evaporators had internal open grooves (IOG), one with deep grooves (DG) and the other with shallow grooves (SG). The third had internal powder coating (IPC) on its surface. The evaporators were fitted to lithium bromide/water vapour absorption refrigeration system. The evaporators load was provided by hot air of controlled temperature and velocity. The IPC evaporator was found to outperform the IOG evaporators and it achieved the highest evaporation capacity and boiling heat transfer coefficient under the same test conditions. DG evaporator performed better than SG evaporator. Evaporation capacities averaged about 500 and 300 W for DG and SG, respectively. IPC achieved an average boiling heat transfer coefficient of about $2.75 \text{ kW/m}^2\text{K}$ compared to about $1 \text{ kW/m}^2\text{K}$ for the IOG evaporators. Perhaps the difference in the two groove sizes was not large enough to affect measurable performance difference. However, the difference in heat capacity and, consequently, heat flux can be attributed to the larger mass flow rate sustained by the deeper grooves.

Hopkins et al. [67], who investigated experimentally and analytically the maximum heat transfer capabilities of two copper-water Flat Miniature Heat Pipes (FMHP) with diagonal trapezoidal (at slight angle to longitudinal axis) micro capillary grooves and one FMHP with axial (longitudinal) rectangular micro capillary grooves, found that the plate with axial grooves outperformed that with trapezoidal grooves. Goto et al. [73] experimentally studied the heat transfer coefficient and pressure drop of condensation and evaporation of R410A and HCFC22 inside two internally grooved tubes. One tube had conventional spiral groove and the other with herring-bone grooves. The obtained

heat transfer data indicated that the evaporation local coefficients were found to be only slightly larger in the herring bone grooves than the spiral ones.

Ayyaswamy et al. [74] studied analytically the capillary flow in triangular grooves. The two parameters, which characterised the flow configuration, were the half angle of the liquid-filled triangular groove and the contact angle of the shear-free meniscus. Results were reported for channel half angles from 5-60 degree and contact angles from 0.1 degree to complementary angle. It was found that with increasing groove half angle, the variation of the friction coefficient and the contact angle increased while the magnitude of the friction coefficient experienced crossover behaviour. For contact angles less than 15 degree the friction coefficient was higher for smaller half groove angle values while it increased with increasing half groove angle beyond that range. Their findings suggest that the performance improved with decreasing half angle.

Ma and Peterson [75] developed analytical expressions for predicting the minimum meniscus radius and the maximum capillary heat transport in micro heat pipes with longitudinal grooves. These expressions verified that there existed an optimum hydraulic radius for the grooves associated with maximum capillary heat-transport capability. They explained that when the hydraulic radius was less than the optimum, the groove dimension would directly limit the capillary heat transport capability occurring in the triangular grooves. Furthermore, they explained that no increase in the capillary pumping occurred when the hydraulic radius of the grooves was much larger than optimum.

Stepanov et al. [76] determined experimentally the wetting contact angle of a number of systems (solid, liquid and gas). The measurements were carried out in the air at temperatures of 20-70 °C. A table showing the inflow and the outflow contact angles for systems frequently encountered in practice was given. The researchers also showed

graphically the dependence of the contact angle on the concentration of aqueous solutions of ethyl alcohol and glycerine.

In their study to develop a model for the liquid pressure drop occurring in triangular grooves with vapour flow occurring across a free surface, Ma et al. [77] found that the friction factor-Reynolds number product was strongly dependent upon the channel angle, contact angle, and dimensionless vapour-liquid flow number.

Ha and Peterson [69] carried out an analytical study of axial flow evaporating thin film through a V-shaped micro channel for the case of a grooved plate inclined with a very small tilt angle. A generalised graph of the non-dimensional radius of curvature with respect to the non-dimensionalised axial length was obtained. The gravity term resulting from the tilt angle variation had changed the form of the governing equation of the wetted length from linear to non-linear.

Cao et al. [66] studied experimentally an air-cooled system employing longitudinally grooved miniature heat pipes. They found that a positive tilt angle of 20 degree of the heat pipe has a significant effect on the performance. The tilt resulted in a reflux operation mode, which helped to increase the maximum heat transfer rate, compared to the results of horizontal positions.

2.3.4 Fluid Flow Effects:

Khrustalev and Faghri [60] explained that the fluid flow effect on the heat transfer during evaporation from the liquid-vapour meniscus resulted in the increase of the evaporation heat transfer coefficient by up to 30%. It was also shown that, for large temperature drops, a re-circulation zone appears in the vapour over the interline, which could be important for some applications including evaporation from capillary structures. Additionally, it was shown that the vapour exiting a capillary slot or pore could be significantly superheated over the saturation temperature. The heat transfer

between the vapour and the heated wall was most extensive at a distance from the interline of about one slot width along the longitudinal direction (y-coordinate).

2.4 Capillary Pumped Loops:

A body of literature exists on Capillary Pumped Loops, or CPLs. These are the most advanced of all heat pipes, and are capable of transferring high heat fluxes. In addition, CPLs are able to benefit from a joint mode of operation combining capillary and mechanically assisted pumping modes. CPLs are widely used for cooling space crafts. They are composed of a capillary evaporator and condenser (usually made of a porous wick). They are different from conventional heat pipes in that the evaporator and condenser do not share the same pipe, but are interconnected by two tubes; one for each of the two phases.

2.4.1 Heat Transport Capacity:

Wulz and Embacher [78] presented the performance characteristics of different capillary evaporator design. Their study was part of the German Program for the Development of Capillary-Pumped Loops for Space Applications. The evaporators were tested with different working fluids. The heat transfer coefficients and the available capillary-pumping head, both were shown as functions of heat flux density. Among the five evaporators tested two were shown to have outstanding performance. The two designs were a flat plate porous wick evaporator and a tubular porous wick one. It was shown that the advantages of plate-type evaporator were: having a low temperature difference between the evaporator surface and vapour, insensitive to drying out, and having a high transferable heat flux density. The greater wall thickness of the plate-type evaporator, which was required on account of the ammonia pressure, represented a disadvantage. The advantages of the tubular evaporator type were: the heat transfer rate was approximately twice that of the plate-type evaporator and the capillary head achieved was high due to low pressure losses at the evaporator entry and exit. The disadvantage

was that it was more susceptible to drying out when it was overloaded. The comparison between a tubular and a plate evaporator, made in this study, is almost unique in the literature.

Jentung [79] described the development of CPL technology since 1970s. The paper explained that in 1986, a CPL capable of transporting a heat load of 70 kW-m with high heat fluxes up to 15 W/cm² and using ammonia as the working fluid was introduced. To meet the ever-increasing heat transport demands, a High Power Spacecraft Thermal Management system (HPSTM) was introduced in 1988 and 1989. Test results verified that the HPSTM system could transport 25 kW in the capillary mode and over 50 kW in the mechanical pump assisted mode using ammonia as working fluid. Porous wicks used in CPL evaporator pumps were made of ultra high molecular weight polyethylene with 15 μ m typical pore size and permeability of 10⁻² m².

Zuo et al. [21] conducted analytical and experimental investigation of an advanced heat pipe mechanism which combined the capillary effect of sintered metal powder wicks with the pulsating motion of the working fluid (Combined Pulsating and Capillary Transport, CPCT) for cooling high heat flux electronics. The theoretical model developed showed that with the right amount of fluid in the heat pipes (fluid fill ratio), steady state oscillation could be achieved and consequently steady state heat pipe performance. The CPCT heat pipes showed significantly better performance than the pure copper pipes by dissipating over 200 W/cm² heat fluxes at 0.16 °C/W thermal resistance - a four fold improvement over the pure copper pipes. The measured optimum fill ratio was found to be in reasonable agreement with the predicted value with a deviation of $\pm 10\%$.

Zuo et al [21] and Chen and Lin [80] are among the very few researchers who offer discussion on the significance of the fill ratio.

Chen and Lin [80] carried out experimental study to investigate the parameters affecting the performance of a CPL used for cooling electronic equipment. A porous material of 1.05×10^{-5} m radius was inserted into the evaporator. The working fluid was FC-72. The experiments were conducted with different power inputs, inventories, and relative heights. The study showed that the surface temperature of the evaporator decreased with increasing inventory especially for inventories less than 40%. However, the trend reversed when the inventory was increased from 50% to 80%. The paper concluded that the tested capillary pumped loop had the capability of removing up to 40 W of heat, keeping the chip temperature under 100 °C.

2.4.2 Effect of Thermal Conductivity:

Li and Ochterbeck [81] carried out numerical and experimental investigation to study the effects of wick thermal conductivity on the evaporator performance of a CPL. The evaporator studied in this investigation had a porous wick rounded by a grooved metallic cylinder. Two different wick materials (polyethylene and nickel) with different thicknesses were tested. It was found that the temperature gradient in the radial direction in the polyethylene wick was much greater than in the nickel wick. At the same time, the maximum temperature difference for the polyethylene wick was 35 °C, compared with 2.5 °C for nickel. In the experiments, two polyethylene wicks with different thicknesses were used (6.35 and 12.7 mm). Reducing the wick thickness was considered to have a similar effect on the wick's effective thermal conductivity, as using a material with higher thermal conductivity. It was found that the thicker wick operated in a much more stable condition than the thinner wick. Thus, the researchers concluded that the lower wick thermal conductivity, the better the wick would perform at start-up to avoid deprime. The findings of Pikhlik and Tekhver [44] and Pasek [18] seem to be different from that of Li and Ochterbeck [81] regarding the effect of thermal conductivity.

2.4.3 Hydrodynamic Aspects:

Hoang & Ku [82] explained in an analytical and experimental work the hydrodynamics aspects of CPL that led to CPL deprime. These aspects were pressure spikes, pressure surge, and pressure oscillation. The pressure spike was defined as the large pressure differential measured between the loop and the reservoir at the onset of nucleate boiling. During start-ups, the generated vapour purges liquid from the vapour line into the reservoir creating a high mass flow rate of liquid flow in the transport lines. This short period of vapour line clearing process was known as the pressure surge. Hoang & Ku [82] explained that the theory of hydrodynamic stability for CPL pointed out that the CPL fluid behaved in the same manner as a simple spring-mass-damper dynamical system susceptible to the modulation of external disturbances. The amplitude of the pressure oscillation generally increases with power and maximises at some intermediate power level beyond which it decreased to almost zero. If the peak of the pressure oscillation exceeds the capillary limit of the wick, vapour would be able to penetrate the largest pores of the pump wick creating an intermitted injection of vapour from the vapour grooves into the liquid core. The authors explained that with the design of CPL with three-port capillary pump, the pressure spike and pressure surge became less of a nuisance.

2.4.4 Advances in CPLs:

Development efforts in the field of CPLs were focused on component design improvements and overall system performance enhancements. Hoang [83] developed and tested an advanced capillary pumped loop (A-CPL). The A-CPL had the ability to avoid the major shortcomings of the traditional CPL, such as the inability to tolerate vapour and/or non-condensable gas (NCG) bubbles in liquid side of the loop. These vapour/NCG bubble ultimately cause capillary pumps to fail (deprime). Dickey and Peterson [84] carried out an analytical investigation of a CPL at various power inputs

and adverse heights. The condenser and evaporator of this A-CPL were housed in aluminium saddles and were separated by two stainless steel-tubes, one for vapour and one for liquid return. The evaporator consisted of a cylindrical metal wick, of sintered nickel powder with an average pore radius 1-1.5 μm , inserted into stainless steel tube housing. The working fluid was ammonia. It was found that the CPL was capable of continuous operation at adverse height of 0.61 m when it was operating at a condenser temperature of 30 °C, which represented substantial wicking height when compared to conventional heat pipes. The effective thermal resistance was found to be relatively constant, at 0.15 °C/W, over much of the tested performance domain and had only slight dependence on power input or orientation. Wulz and Embacher [78] explained that modern capillary wick materials have running age of 8500 hrs in continuous operation.

2.5 Combined Wick Structures:

Khurstalev and Faghri [85] & [86] determined experimentally the maximum heat transfer capability of a copper-water flat miniature Axially Grooved Heat Pipe (AGHP) with the same characteristics as the prototype tested by Plesch et al. [62] except that a porous coating, of thermal conductivity of 100 W/m K, was added to the land area between the grooves. The enhanced AGHP with porous coating was found to be superior to the AGHP with plain axial grooves. The enhanced AGHP operate at a maximum heat flux in the evaporator of 80 W/cm² in the horizontal orientation at an evaporation temperature of 110 °C, and about 100 W/cm² in the vertical orientation with elevated condenser end at an evaporation temperature of 105 °C. A maximum heat flux of 60 W/cm² at an evaporation temperature of 125 °C were registered for the original AGHP on the vertical position with the condenser of the heat pipe on the upper end. It was also found that the enhanced AGHP could effectively perform in the vertical orientation when its evaporator end was elevated.

Wang and Catton [57] studied analytically the enhancement of evaporation heat transfer when a triangular groove formed by trapezoidal fins is covered by a thin fine porous layer. The enhancement mechanisms were explained and an analytical model to predict evaporation heat transfer performance was developed. The calculations performed, for different geometrical parameters of grooves and menisci, indicated that the thin porous layer significantly improved evaporation heat transfer in triangular grooves (by three to six times). This was especially so at situations of low meniscus radii when the heat fluxes were high. The calculations also revealed that the total heat transfer coefficient decreases with increasing liquid meniscus radii. For example, when the liquid meniscus in the groove decreased from 1.5 to 0.5 mm, the heat flow rose from 0.56 to 1.04 W. Their model further showed that the heat transfer coefficient increased with increasing the half groove angle and half top fin width. Comparison of the evaporation heat transfer in triangular grooves with and without a thin porous layer showed that the former is much better, although the latter has a small area with heat transfer coefficients as high as $108 \text{ W/m}^2 \text{ K}$.

Generally speaking, the combined wick structures showed better results than plain-grooved surfaces.

2.6 Conclusion:

1. The reviewed literature shows that boiling in porous structure is enhanced compared to that on smooth surface. It's been shown that boiling starts at low temperature heads and that higher heat fluxes and heat transfer coefficients could be achieved.
2. Different explanations are given in the reviewed literature for mechanisms of boiling in porous structure. Most of these explanations agree on the following points:
 - The series of small cavities in a porous structure help feed liquid to the evaporating centres.

- The cavities entrap the vapour and non-condensable gases and this activates the evaporating centres.
 - The liquid is supplied to the evaporating centres by capillary force and suction force due to ejection of vapour.
3. There are apparent discrepancies in the findings of researchers as to the effect of particles' diameter, porous layer thickness and the thermophysical properties of the porous structure on boiling.
 4. Most of the researchers agree that for boiling in a porous structure, the heat transfer coefficient increases to a maximum with increasing heat flux and then drop after the critical heat flux is reached.
 5. The reviewed literature showed that boiling in grooved surfaces outperforms that on plain surfaces. Furthermore, applying a porous layer on the grooved surface led to further enhancement.
 6. The meniscus that forms inside the pores of a porous layer or on the wall of the groove has an important role in enhancing boiling performance.
 7. The high values of heat fluxes achieved by the capillary pumped loops (CPLs), show the extent of improvement that capillary force could have on boiling performance.

2.7 Summary of Chapter two:

In this chapter a body of literature on capillary-assisted boiling has been critically reviewed. The review included boiling on porous structures, grooved surfaces and on combined wick structures. The main issues looked at in this review were:

1. Enhancements in boiling performance on capillary structures to boiling on smooth surfaces.
2. Mechanisms of boiling in porous structures.

Chapter 2: Literature Review

3. The effect of porous structure geometry on boiling performance, particularly the effect of sintered powder geometry on boiling (particle size/diameter and layer thickness).
4. Effect of thermophysical properties of the porous structure on boiling.
5. Effect of liquid and vapour flow on boiling performance.

Chapter Three

Analytical Work

3.1 Introduction:

In this chapter a mathematical model incorporating heat transfer processes occurring inside and around the tubes of an evaporator whose inner surfaces are lined with a layer made of sintered metal powder, is built. This evaporator is required to replace the two heat exchangers used in a conventional lithium/bromide water refrigeration cycle for cooling the air as explained earlier in section (1.4). This mathematical model is then used in a computer programme simulating heat transfer processes occurring inside and around the evaporator tubes in order to study the effect of particle size and layer thickness on evaporators' performance as well as other parameters such as load air inlet velocity and temperature.

3.2 Physical Description of the Evaporator:

The evaporator consists of nine copper pipes, arranged in staggered tube bank configuration of two rows; see Fig (3.1). Each tube is 0.3 m long and 25.3 and 28.6 mm inner and outer diameters respectively. The longitudinal and transverse pitches of the staggered tube bank arrangement are 84 and 56.4 mm respectively. Fig (3.2a) to (3.2c) is an engineering drawing for the three sides of this evaporator which is designed to fit in a single-effect lithium bromide/water absorption system test-rig. This configuration of the evaporator is chosen in such a way so as to provide sufficient size for achieving the designed cooling effect of the absorption cycle.

3.3 Description of the Heat Transfer Model:

In this model it is assumed that the heat removed from the air, through convection and condensation of some of the moisture content of the air, induces boiling of the refrigerant water inside the evaporator tubes. This is expressed mathematically by:

$$Q_b = Q_{conv} + Q_{cond} \dots\dots\dots(3.1)$$

Fig (3.3) shows the thermal circuit of the heat transfer processes involved when hot air flows across this evaporator.

The similarity of design between the evaporator tubes and heat pipes allows the analysis of the boiling to be carried out according to the theory of heat pipes. From heat pipe theory, it is known that the maximum heat rate transported by a heat pipe is always bounded by the minimum heat transfer limitation encountered by that heat pipe. These heat transfer limitations are discussed in section 1.5.14. Mathematically, this could be expressed by:

$$Q_b \leq Q_{\min} \dots\dots\dots(3.2)$$

Equation (3.1) involves calculating the heat transfer coefficients/rates associated with convection and condensation. Equation (3.2) enables the calculation of the heat transfer rate, Q_b , through calculating the minimum heat transport limit based on heat pipe theory.

Equations (3.1) & (3.2) are used as the principal equations of an iterative computational scheme, using computer programme written in FORTRAN 95 language. In this iterative scheme, the water saturation temperature inside the evaporator's tubes and tubes' wall temperature are logically adjusted until values are reached at which equations (3.1) & (3.2) are satisfied. This program is described in section (3.8). Algorithms and flow charts of this program are given in appendix A & B respectively and the programme itself is given in appendix C.

In the flowing sections the heat rates of equations (3.1) & (3.2) are further explained and the equations used for their calculations are derived.

3.4 Boiling Heat Rate:

Several formulae for boiling in porous media were found in the literature and were used in this model. Each formula was combined with formulae describing convective and condensation heat transfer to give a computational scheme as described above. Each scheme is different from the others in the equation used to evaluate the boiling heat rate. Some of the schemes achieved meaningful results and some gave trivial solutions.

Furthermore, some schemes failed to give a continuous range of solution. The trivial and intermittent solutions are believed to be due to incompatibilities between the various formulae of the schemes in terms of conditions of applications, accuracies, etc. This is to be expected, as these formulae are predominantly empirical and were developed independently of one another. A brief summary of each of these formulae is given below:

3.4.1 O'Neill et al. [35]:

O'Neill et al. [35] developed a model for boiling in porous surfaces¹. They assumed that vapour bubbles exist inside the pores between particles and each bubble is surrounded by thin liquid film. Evaporation takes place on the liquid-vapour interface. The pores are assumed to be interconnected, so that liquid can be supplied to the pores and the generated vapour can pass through the porous layer to the liquid bulk. Their model is given by:

$$q = \left(\Delta T_s - \frac{9.66 \sigma T_s}{\rho_v h_{fg} d_p} \right) \frac{k_t \delta}{0.044 d_p^2} \dots\dots\dots(3.3)$$

The following assumptions also apply to their model:

- All the particles are spherical and uniform in diameter,
- All pores are uniform size,
- The geometrical packing arrangement of particles is known, hence, the pore diameter is calculable
- Each pore is active,
- The matrix is a perfect heat conductor; hence, there is no temperature drop within the porous layer.

When they compared their equation with that of Nishikawa et al. [87], which is given in section (3.4.3), they found that the latter gave better predictions. However, when the equation of Nishikawa et al. [87] was used in the iterative computational scheme of this research it gave trivial solutions.

¹ Reported by Pasek [18], page 26.

3.4.2 Rao and Blakrishnan [32]:

Rao & Blakrishnan [32] developed an analytical model, which incorporated bubble dynamics for boiling in porous surfaces. They explained that previous correlations in the literature for boiling in porous surfaces were specific to particular systems for which they were developed, and could not be safely extrapolated to other systems. The assumptions they adopted for developing their model were: uniform diameter for the particles of the porous matrix, interconnected porous particles such that vapour could flow between them, constant porous matrix temperature over its thickness, activity of all pores on the surface at the burn out heat flux, saturation temperature for the boiling liquid, and neglecting the coalescence of bubbles. They presented an expression, shown by equation (3.4) below, for the total heat flux in terms of the wall superheat, pore geometry and the physical properties of the liquid.

$$q = 2.4 \times 10^{-4} \frac{\rho_l \rho_v^2 K h_{fg}^2 \Delta T_s \left(\delta / D_p \right)^{0.8} ja^{0.22}}{\mu_v \delta T_s (\rho_l - \rho_v) \varepsilon^{1.23}} \dots\dots\dots(3.4)$$

Where the permeability, K , is given by Kaviany [4]:

$$K = \frac{\varepsilon D_p^2}{32} \dots\dots\dots(3.5)$$

The pore diameter, D_p , is given by Afgan et al. [14]:

$$D_p = 0.414 d_p \dots\dots\dots(3.6)$$

And Jacob number, Ja , is given by [32]:

$$Ja = \rho_l c_{p_l} \Delta T_s / \rho_v h_{fg} \dots\dots\dots(3.7)$$

Using this model, they found that nucleation sites density at any heat flux had definite relation with the maximum number of pores available for a given matrix geometry.

3.4.3 Nishikawa et al. [87]:

Nishikawa et al. [87] proposed the following correlation for porous surfaces with spherical particles

$$\frac{q \delta}{k_{eff}(T_w - T_s)} = 0.001 \left(\frac{\sigma^2 h_{fg}}{q^2 \delta^2} \right)^{0.0284} \left(\frac{\delta}{d_p} \right)^{0.56} \left(\frac{q d_p}{\varepsilon h_{fg} \mu_v} \right)^{0.593} \left(\frac{k_t}{k_e} \right) \left(\frac{\rho_t}{\rho_v} \right)^{1.67} \dots (3.8)$$

Where k_{eff} is given by [87]:

$$k_{eff} = k_t + (1 - \varepsilon)k_{pr} \dots (3.9)$$

3.4.4 Fukusako et al. [88]:

Fukusako et al. [88] developed two relations to fit the results of their experimental work on studying boiling performance in porous media. The porous material they used was composed of packed spherical beads whose diameters ranged from 1.0 to 16.5 mm with a layer thickness that varied between 10 to 300 mm and a porosity range of 0.39 – 0.5. They proposed equation (3.10) for transitional boiling and equation (3.11) for film boiling

$$Nu_t = 7.5 \times 10^{-2} \left[\frac{d_p}{\sqrt{\sigma/g(\rho_t - \rho_v)}} \right]^{0.9} \left[\frac{h_{fg}}{c_{p_{t_e}} \Delta T_s} \right]^m \rho_r^{2.37} (k_{t_e}/k_t)^* \dots (3.10)$$

$$Nu = 4.10 (G_r P_{r_v})^{0.25} \left(\frac{h_{fg}}{C_{p_{v_e}} \Delta T_s} \right)^{0.4} \left(\frac{k_{v_e}}{k_v} \right)^{-0.95} \left(\frac{d_p}{\delta} \right)^{0.15} \dots (3.11)$$

Where

$$m = \left[\frac{d_p}{\sqrt{\sigma/g(\rho_t - \rho_v)}} \right]^{0.6} P_{r_t}^{-0.8} \dots (3.12)$$

$$n = -0.5 P_{r_t}^{0.3} \dots (3.13)$$

$$c_{p_{t_e}} = \varepsilon c_{p_t} + (1 - \varepsilon) c_{p_{pr}} \dots (3.14)$$

$$k_{t_e} = \varepsilon k_t + (1 - \varepsilon) k_{pr} \dots (3.15)$$

$$c_{p_{v_e}} = \varepsilon c_{p_v} + (1 - \varepsilon) c_{p_{pr}} \dots (3.16)$$

$$k_{t_e} = \varepsilon k_v + (1 - \varepsilon) k_{pr} \dots\dots\dots(3.17)$$

3.4.5 Zhang and Zhang [38]:

Zhang & Zhang [38] developed an empirical model describing boiling in porous layers at low and moderate heat fluxes, using dimensionless parameter groups affecting the two-phase flow and boiling heat transfer. By synthesising a large number of experimental data, they obtained the following correlation by regression:

$$N_u = 1.6746 \times 10^{-5} \left(F_r / We \right)^{0.4254} \left(Re_t \rho_t / \rho_v \right)^{-0.6032} We_1^{1.1605} We_2^{-0.811} \left[\frac{\delta^2 \varepsilon^3}{4d_p^2} \right]^{0.2626} \left(\nu_t / \nu_v \right)^{0.2999} \dots(3.18)$$

Where

$$F_r / We = \frac{q^2 d_p}{\sigma \rho_v h_{fg}} \dots\dots\dots(3.19)$$

representing the ratio of inertial force to surface tension.

$$We_1 = \frac{\sigma}{d_p (\rho_t - \rho_v) g} \dots\dots\dots(3.20)$$

representing the ratio of surface tension to gravity difference between liquid and vapour.

$$We_2 = \frac{\sigma}{d_p \rho_t g} \dots\dots\dots(3.21)$$

reflecting the effect of tension and gravity on liquid permeating flow in porous wall cavities.

$$Re_t \rho_t / \rho_v = \frac{(\rho_t / \rho_v) q K}{\rho_v h_{fg} \nu_t \delta} \dots\dots\dots(3.22)$$

is the modified Reynolds number

$\delta \varepsilon / d_p$ reflects the effects of geometry of porous layer and ν_t / ν_v is the kinetic viscosity ratio of liquid and vapour.

3.4.6 Cornwell et al [89]:

Cornwell et al. [89] undertook an experimental investigation to study the evaporative process in a thin porous medium. They developed a correlation for boiling heat flux in terms of the ratio of the vapour covered area to the total area of the wick and the vapour pressure drop across the wick as shown in equation (3.23) below:

$$q = c h_{fg} \left(\frac{A_v}{A_w} \right) \left(\frac{\Delta P_{v,wick}}{\delta} \right)^{1/(2+z)} \dots\dots\dots(3.23)$$

Where c is a constant involving ρ , μ , d_p , z and c_o .

3.5 Convection Outside The Tubes:

To obtain the external convective heat rate on the exterior of the evaporator tubes, modified Zhukauskas equation is used [92]:

$$Nu_{d,conv} = 0.76 * 0.35 \left(\frac{S_T}{S_L} \right)^{0.2} * Re_{d,max}^{0.6} * Pr^{0.36} * \left(\frac{Pr}{Pr_s} \right)^{0.25} \dots\dots\dots(3.24)$$

Equation (3.24) includes a correction factor of 0.76 to account for the fact that the number of tubes in the longitudinal direction of the tested evaporator is less than 20. The Reynolds number, $Re_{d,max}$, is based on the maximum velocity, V_{max} , occurring within the tube bank. This maximum velocity is given by; [92]:

$$V_{max} = \frac{S_T}{S_T - d_o} V_a \dots\dots\dots(3.25)$$

Thus, $Re_{d,max}$ is given by; [92]:

$$Re_{d,max} = \frac{\rho_a V_{max} d_o}{\mu_a} \dots\dots\dots(3.26)$$

The properties of equation (3.24) and (3.26) are evaluated at the air inlet temperature instead of the average of inlet and outlet temperatures. This was dictated by the fact that the outlet temperature is unknown. However, the drop in air temperature at exit is not large

(as will be shown by the experimental work) and the simplification is, therefore, justified [92].

The Nusselt number, calculated by equation (3.24), is then used to calculate the convective heat transfer coefficient as shown by:

$$h_{conv} = \frac{Nu_{d,conv} k_a}{d_o} \dots\dots\dots(3.27)$$

Then, outside convective heat rate is then given by:

$$Q_{conv} = h_{conv} A_T (T_a - T_w) \dots\dots\dots(3.28)$$

3.6 Condensation On The Evaporator Tubes:

Some of the air's moisture content will condense as the air flows across the evaporator tube bank. This is due to the fact that the tubes' temperature is below the dew point of the air. The literature was searched for formulae that describe condensation from humid air on the external surface of a staggered tube bank. Many difficulties were encountered in this search such as that almost all the condensation formulae in the literature are based on limited amount of entrained air and on the conditions of downward flow.

The condensation formula, found in the literature, and used in the heat transfer model described in section 3.3 to calculate the condensation heat rate, Q_{cond} , is given by Bryan [93] who tested the heat transfer from humid air flowing across a six-row deep-staggered bare coil. He proposed the following correlation for calculating the condensation heat transfer coefficient² on the exterior of the coil:

$$h_{cond} = \frac{\dot{m}_a c_{p_a}}{A} \ln \frac{(T_{db_{in}} - T_w)}{(T_{db_{out}} - T_w)} \dots\dots\dots (3.29)$$

² The parameters appearing in equation (3.29) & (3.30) are in British Units. The appropriate conversion factors to SI Unit were used before using equation (3.30) in the model.

Moreover, he explained that the heat transfer coefficient for the data he used could be statistically correlated as a function of the coil face velocity, with an error of $\pm 6\%$, as shown below:

$$h_{cond} = 0.616 V_a^{0.5} \dots\dots\dots (3.30)$$

For the purposes of the computational scheme of this research, equation (3.30) was used. Equation (3.29) gave intermittent solution. This is believed to be due to incompatibilities between the various formulae of the schemes, in terms of conditions of applications, accuracies, etc. This is to be expected as mentioned earlier since these formulae are predominantly empirical and were developed independently of one another.

The condensation heat rate, Q_{cond} , is then calculated as follows:

$$Q_{cond} = h_{cond} A_T (T_a - T_w) \dots\dots\dots (3.31)$$

3.7 The Minimum Limit Heat Rate, Q_{min} :

The maximum heat rate that could be transported by the capillary-assisted evaporators tested in this research can be calculated in a similar way to that of calculating heat transfer limitations of conventional heat pipes. This is because analogy can be drawn between the two systems. An absorption refrigeration cycle using a capillary-assisted evaporator represents a heat pipe whose condenser is the absorber. However, a major difference that distinguishes the absorption refrigeration cycle using a capillary-assisted evaporator from a conventional heat pipe is that the liquid doesn't return from the absorber directly to the evaporator via the wick. Instead, it is transferred to the generator and then to the condenser of the refrigeration cycle before being delivered to the evaporator. Thus, the capillary pressure generated by the wick is solely used in distributing the water along the evaporator tubes' inner circumference and in overcoming the vapour pressure drop encountered before the vapour reaches the absorber.

3.7.1 Adaptation of Heat Transfer Limitation Equations of Conventional Heat Pipes

to Suit a Capillary-Assisted Evaporator of an Absorption Refrigeration Cycle:

The heat transfer limitation equations of a conventional heat pipe could be used to find out the heat transfer limits of the capillary-assisted evaporators tested in this research provided that simple changes are made on these equations to compensate for the differences between the two systems mentioned in section (3.7) above. Thus, the following changes are suggested:

3.7.1.1 Vapour Pressure Drop:

The vapour pressure drop in a capillary-assisted evaporator is composed of four major components:

1. Vapour pressure drop in the wick and adiabatic pipes, ΔP_{v_1} .
2. Normal hydrostatic vapour pressure drop, ΔP_{v_2} .
3. Vapour pressure drop at elbows, ΔP_{v_3} .
4. Vapour pressure drop at the expansions of the vapour outlet pipe diameter, ΔP_{v_4} .

3.7.1.1 .1 Vapour Pressure Drop in the Wick and Adiabatic Sections:

For a laminar incompressible vapour flow in the evaporator, the vapour pressure drop due to friction in the wick and adiabatic sections is given by [5]:

$$(\Delta P_{v_1})_{laminar} = \frac{16\mu_v L_{eff} Q_c}{2r_v^2 A_v \rho_v h_{fg}} \dots\dots\dots(3.32)$$

Typically, for a turbulent incompressible vapour flow, the vapour pressure drop is given by [5]:

$$(\Delta P_{v_1})_{turbulent} = 0.038 \left(\frac{d_v Q_c}{A_v u_v h_{fg}} \right)^{\frac{3}{4}} \frac{2\mu_v L_{eff} Q_c}{d_v^2 A_v \rho_v h_{fg}} \dots\dots\dots(3.33)$$

Equations (3.32) and (3.33) are similar to equations (1.35) and (1.36) except that the effective capillary length is shorter. In this case the vapour pressure drop in the condenser is eliminated since, as explained before, a capillary-assisted evaporator of an absorption

refrigeration cycle represents a heat pipe with an evaporator and adiabatic sections only. Hence, the component which accounts for the vapour pressure drop in the condenser of a normal heat pipe is eliminated here. However, a component that accounts for vapour pressure drop due to the sudden expansion in cross-sectional area when the vapour enters the absorber section is added. This component is given by equation (3.43) below. Thus, the effective capillary length in equations (3.32) & (3.33) is given by:

$$L_{eff_v} = L_e + L_a \dots\dots\dots(3.34)$$

It should be noted that the internal diameter of the pipe in the evaporator length, L_e , is different from that on the adiabatic length, L_a , for the evaporators tested in this research.

Reynolds Number³ is evaluated using the following equation to determine whether the flow is laminar or turbulent:

$$Re = \frac{2 r_v Q_c}{A_v \mu_v h_{fg}} \dots\dots\dots(3.35)$$

Mach Number⁴ is evaluated using the following equation to assess whether the flow is compressible or incompressible [5]:

$$Ma = \frac{(4 Q_c / h_{fg} \pi d_v^2)}{\sqrt{\gamma R T_v}} \dots\dots\dots(3.36)$$

3.7.1.1.2 Normal Hydrostatic Vapour Pressure Drop:

Since the evaporator is placed at a level slightly below that of absorber, then the vapour has to travel a vertical distance upwards before reaching the absorber's level. Thus, a normal hydrostatic vapour pressure component should be considered. The vapour should rise from where it is generated into the sintered tubes up to the absorber level; see Fig (3.4).

Thus, the normal hydrostatic vapour pressure drop is evaluated, ΔP_{v_2} , as:

³ If Re No. is less than 2300, then the flow is laminar.

⁴ If Mach No. is much less than 0.3, then the flow is incompressible.

$$\Delta P_{v_2} = \rho_v g H \dots\dots\dots (3.37)$$

Where H is given by; see Fig (3.4):

$$H = L_1 + L_2 \dots\dots\dots (3.38)$$

3.7.1.1.3 Vapour Pressure Drop at the Elbows:

The vapour generated into the evaporator will experience pressure drop at a number of 90 ° angle elbows along its path to the absorber, see Fig (3.4). The vapour pressure drop at these elbows, ΔP_{v_3} , is given by:

$$\Delta P_{v_3} = h_{f_3} \rho_v g \dots\dots\dots (3.39)$$

Where the friction head loss h_{f_3} , is given by [92]:

$$h_{f_3} = K_f \frac{V_{v_i}^2}{2g} \dots\dots\dots (3.40)$$

The vapour V_{v_i} could be obtained from:

$$V_{v_i} = V_v \frac{A_v}{A_i} \dots\dots\dots (3.41)$$

Where

$$V_v = \frac{Q}{\rho_v A_v h_{fg}} \dots\dots\dots (3.42)$$

3.7.1.1.4 Vapour Pressure Drop at the Expansions of the Vapour outlet Pipe:

The vapour outlet pipe expands at three positions. Firstly, it expands when the vapour leaves the sintered tubes and enters the smooth pipes in the adiabatic section. The second expansion is shortly before the end of the adiabatic length and the third one is at entry to the absorber; see Fig (3.4). The pressure drop due to these expansions, ΔP_{v_4} could be evaluated as follows:

Vapour pressure drop at expansion 1, $\Delta P_{v_{4-1}}$:

$$\Delta P_{v_{4-1}} = h_{f_{4-1}} \rho_v g \dots\dots\dots (3.43)$$

Vapour pressure drop at expansion 2, $\Delta P_{v_{4-2}}$; (see Fig 3.3):

$$\Delta P_{v_{4-2}} = h_{f_{4-2}} \rho_v g \dots\dots\dots(3.44)$$

Vapour pressure drop at expansion 3, $\Delta P_{v_{4-3}}$; (see Fig 3.3):

$$\Delta P_{v_{4-3}} = h_{f_{4-3}} \rho_v g \dots\dots\dots(3.45)$$

The friction head loss, $h_{f_{4-1}}$, $h_{f_{4-2}}$ & $h_{f_{4-3}}$, are given by; [92]:

$$h_{f_{4-1}} = \frac{V_v^2}{2g} \left(1 - \frac{A_v}{A_i} \right)^2 \dots\dots\dots(3.46)$$

$$h_{f_{4-2}} = \frac{V_{v_1}^2}{2g} \left(1 - \frac{A_i}{A_1} \right)^2 \dots\dots\dots(3.47)$$

$$h_{f_{4-3}} = \frac{V_{v_1}^2}{2g} \left(1 - \frac{A_1}{A_2} \right)^2 \dots\dots\dots(3.48)$$

Where

$$V_{v_1} = V_v \left(\frac{A_i}{A_1} \right) \dots\dots\dots(3.49)$$

V_{v_1} is the vapour velocity after expansion 2 of vapour outlet pipe.

3.7.1.2 Liquid Pressure Drop:

The liquid pressure drop in a capillary-assisted evaporator is evaluated by [5]:

$$\Delta P_{\ell_1} = \frac{\mu_{\ell} L_{eff} Q_c}{K A_w h_{fg} \rho_{\ell}} \dots\dots\dots(3.50)$$

Again, equation (3.50) is similar to equation (1.37) except that the effective capillary length, L_{eff} , in equation (3.50) is given by:

$$L_{eff_{\ell}} = \pi d_i / 2 \dots\dots\dots(3.51)$$

This is because in a capillary-assisted evaporator the only distance that the liquid has to travel under capillary effect is to rise from bottom of the tube, along the tubes inner circumference, up to the tube's top i.e. it travels a distance $\pi d_i/2$. Due to this up rise a normal hydrostatic liquid pressure drop, on which further explanation is given in section (3.7.1.3), will be encountered. Furthermore, in a capillary-assisted evaporator, the liquid passes neither through an adiabatic length nor through a condenser length as it does in a normal heat pipe. Therefore, liquid pressure drops over these two lengths shouldn't be considered. It should be mentioned here that the axial flow of the liquid inside the tubes is maintained by gravity force as the liquid will flow downwards to the bottom of the evaporator and then to the excess water tank. However, the velocity of water inside the evaporator's tubes is very low.

3.7.1.3 Normal and Axial Hydrostatic Pressure drops:

Due to the fact that the liquid should rise from the bottom of the tube up to the tube's top, a normal hydrostatic liquid pressure drop, ΔP_+ , should be accounted for. This is given by [5]:

$$\Delta P_+ = \rho_l g d_v \dots\dots\dots(3.52)$$

Equation (3.52) is similar to equation (1.41) except that $\cos\psi = 1$, because the angle between the evaporator's tubes and the horizontal is zero.

The axial liquid hydrostatic pressure drop, ΔP_{II} , which might be evaluated using equation (1.42), is zero for these capillary-assisted evaporators because ψ , which is the angle between the evaporator's tubes and the horizontal, is zero.

3.7.1.4 Inertial Pressure Gradient:

Due to small liquid velocities in capillary-assisted evaporators the inertial pressure gradient due to liquid flow is small and therefore, ignored. However, the inertial pressure gradient in the vapour phase is more significant. This pressure gradient, ΔP_i , could be calculated

using equation (3.50) which is suggested by Busse [9], for laminar flow of an incompressible vapour stream in a cylindrical heat pipe.

$$\Delta P_i = \frac{\rho_v V_v^2}{2g} \left[\frac{28}{9} - \frac{0.68 \text{ Re}}{\left(\frac{29 L_e}{d_v} \right) + \text{Re}} \text{EXP} \left(- \frac{60 L_e}{\text{Re} d_v} \right) \right] \dots\dots\dots (3.53)$$

Peterson [5] showed that the above expression provides a reasonably accurate estimation of inertial effects of vapour turbulent flows in heat pipes.

3.7.1.5 Other Heat Transfer Limitations:

The sonic, viscous and boiling heat transfer limits in the capillary-assisted evaporators are evaluated using the following equations [5]:

$$Q_s = 0.47 h_{fg} A_v (\rho_v P_v)^{\frac{1}{2}} \dots\dots\dots (3.54)$$

$$Q_v = \frac{A_v r_v^2 h_{fg} \rho_v P_v}{16 \mu L_e} \dots\dots\dots (3.55)$$

$$Q_{bl} = \left(\frac{2 \pi L_e k_{eff} T_v}{h_{fg} \ell n \left(\frac{r_i}{r_v} \right)} \right) \left(\frac{2 \sigma}{r_n} - P_{c,m} \right) \dots\dots\dots (3.56)$$

The effective thermal conductivity, k_{eff} , is given by equation (1.25).

The entrainment limit and other heat transfer limits applicable to heat pipes are not applicable here to the capillary-assisted evaporators tested in this research. However, further discussion regarding these heat transfer limits is given in chapter 5.

3.8 Algorithms Description

The aim of this programme as explained earlier in section (3.1) is to look for the values of the tube wall temperature, T_w , and the water saturation temperature, T_s , that satisfy equations (3.1) and (3.2). It is known that the tube wall temperature, T_w , lies between the

water saturation temperature, T_s , and the air temperature, T_a , and the water saturation temperature, T_s , lies between zero and the tube wall temperature, T_w . Use is made of this fact to write a programme in FORTRAN 95 computer language that is made up mainly of two DO LOOPS⁵. One loop is for finding the tube wall temperature T_w and the other is for finding the water saturation temperature T_s . The latter DO LOOP is inside the former one, i.e each time the external DO LOOP (the one for finding temperature T_w) is executed, the inner DO LOOP (the one for finding T_s), is executed too. The initial guesses of T_w and T_s are chosen to be as small as possible. Each time the inner DO LOOP is executed, the water saturation temperature guess, T_s , is increased by an incremental amount. This is repeated until one of two things happen; either equations (3.1) and (3.2) are satisfied or the water saturation temperature, T_s , reaches the tube wall temperature, T_w . When the latter happens, whilst equations (3.1) and (3.2) are not satisfied, the tube wall temperature, T_w , guess is increased by an incremental amount. For this new value of T_w , the inner loop is re-executed many times until the water saturation temperature, T_s , reaches that of the new tube wall temperature, T_w . If the value of the tube wall temperature reaches the air temperature, T_a , whilst no solution to satisfy equations (3.1) and (3.2) is found, then a message saying that “Both ranges of temperature were checked and no solution is found” is written on the screen. The programme contains many subroutines. The major subroutine is the one for calculating the minimum heat rate, Q_{\min} . This is because the value of Q_{\min} changes with the change of water saturation temperature’s value. Typically, due to the change of water saturation temperature and the tube wall temperature guesses, the working fluid properties and some of the air properties required for the calculation of various equations used in this model should be changed correspondingly. This is done by using

⁵ A DO LOOP is a repetition construct inside a computer programme. Statements inside a DO LOOP are executed repeatedly until a certain condition is satisfied.

various subroutines for interpolating. The correlations used in the interpolating subroutines are obtained from excel fitted relationships to the plots of these properties against temperature. Below is a brief summary of the main steps of this programme⁶:

1. The programme begins with declaring the different parameters and opening input and output files. The input data are the particle size and layer thickness for the sixteen evaporators to be tested in this research.
2. Initial guesses for the water saturation temperature, T_s , and the tube wall temperature, T_w , are made as follows:
 - i. $T_s = 273.16$
 - ii. $T_w = 1.0001 \times T_s$
3. Start the external DO LOOP for finding the tube wall temperature.
4. Interpolating subroutines are called to calculate the working fluid properties at T_s & T_w .
5. Using heat pipe theory the minimum heat rate limit, Q_{\min} , is calculated. A special subroutine is used for calculating this minimum heat rate limit, Q_{\min} , which is then called each time the external/internal DO LOOP is executed.
6. Calculate the boiling, convection & condensation heat rates Q_b , Q_{conv} & Q_{cond} respectively.
7. If equations (3.1) & (3.2) are satisfied or $T_w = T_a$ then exit the external DO LOOP.
8. Start the internal DO LOOP for finding the water saturation temperature.
9. Re-calculate the minimum heat rate, Q_{\min} , and the boiling heat rate, Q_b . Interpolating subroutines should be called before calculating Q_{\min} & Q_b .

⁶ For detailed information on the steps of the full programme refer to appendix A, B & C.

10. If equations (3.1) & (3.2) are satisfied or $T_s = T_w$ then exit the external DO LOOP.

Otherwise incrementally increase T_s and re-execute the internal DO LOOP

11. If equations (3.1) & (3.2) are satisfied or $T_w = T_a$ then exit the external DO LOOP.

Otherwise increase T_w incrementally, reset the value of T_s to 273.16 ° K, and re-execute the external DO LOOP.

12. Write the output values to the output file.

3.9 Sample Calculation

In this section a sample of the calculation to get Q_{\min} is given. The capillary limit heat rate, Q_c , sonic limit heat rate, Q_s , viscous limit heat rate, Q_v , and boiling limit heat rates, Q_{bl} , will also be calculated. The smallest one of these four limits will be taken as the minimum limit heat rate to be used in equations (3.2). This is because this part of calculation in the iterative computational scheme is the most complicated part. In this calculation sample an initial guess of 5 °C is made for water saturation temperature inside the evaporator tubes. In the real iterative scheme the initial guess for the saturation temperature inside the tubes is less than 5 °C. However, this guess is chosen here so as to avoid interpolations for assessing fluid properties. This calculation is made for the evaporator with a sintered layer made of bronze particles of 300 µm particle size and 1.0 mm layer thickness.

3.9.1 Dimensions and Sintered Material Properties:

Particle size/diameter, $d_p = 300 \mu\text{m}$

Sintered layer thickness= 1.0 mm

Evaporator tube's internal diameter, $d_i = 25.3 \text{ mm}$

Evaporator tube's outer diameter, $d_o = 28.6 \text{ mm}$

Average vertical distance between evaporator tubes and absorber level, $H = 0.57 \text{ m}$

Evaporator tubes length, $L_T = 0.3 \text{ m}$

Adiabatic length of evaporator, $L_a = 2.235 \text{ m}$

Sintered layer porosity, $\varepsilon = 0.48$

Chapter 3: Analytical Work

Commercial bronze thermal conductivity, $k_s = 52 \text{ W/mK}$

Number of evaporator tubes, $n = 9$

3.9.2 Thermo Physical Properties

The thermophysical properties of the working fluid @ 5°C are:

Dynamic viscosity of water, $\mu_l = 1506 \times 10^{-6} \text{ kg/ms}$

Dynamic viscosity of vapour, $\mu_v = 8.66 \times 10^{-6} \text{ kg/ms}$

Density of water, $\rho_l = 1000 \text{ kg/m}^3$

Density of vapour, $\rho_v = 0.007 \text{ kg/m}^3$

Thermal conductivity of water, $k_l = 578 \times 10^{-3} \text{ W/mK}$

Surface tension, $\sigma = 74.8 \times 10^{-3} \text{ N/m}$

Saturation pressure, $P_{\text{sat}} = 871.9 \text{ Pa}$

Latent heat of vaporisation, $h_{fg} = 2488.9 \text{ kJ/kg}$

3.9.3 Capillary Limit Calculation

The maximum capillary pressure generated by the porous layer should be greater than or equal to the summation of all pressure losses occurring throughout the liquid and vapour flow paths [5] i.e.

$$P_{c,m} \geq (\Delta P_v)_{\text{total}} + (\Delta P_l)_{\text{total}} \dots\dots\dots(3.57)$$

The total vapour pressure $(\Delta P_v)_{\text{total}}$ is given by:

$$(\Delta P_v)_{\text{total}} = \Delta P_{v_1} + \Delta P_{v_2} + \Delta P_{v_3} + \Delta P_{v_4}$$

To get ΔP_{v_1} , equations (3.32) or equations (3.33) could be used depending on whether the vapour flow is laminar or turbulent. At the moment, assume that the flow is laminar and incompressible. Later on these assumptions will be verified; if they are not true, then necessary changes will be made.

$$(\Delta P_{v_1})_{\text{laminar}} = \frac{16\mu_v L_{\text{eff}} Q_c}{2r_v^2 A_v \rho_v h_{fg}} \dots\dots\dots(3.32)$$

Chapter 3: Analytical Work

To account for the fact that the inner diameter of the evaporator's sintered tube and that of the adiabatic section are different⁷:

$$(\Delta P_{v_1})_{la \min ar} = \frac{16\mu_v Q_c}{2\rho_v h_{fg}} \left[\frac{nL_T}{r_v^2 A_v} + \frac{L_a}{r_i^2 A_i} \right] \dots\dots\dots(3.58)$$

$$d_v = d_i - 2\delta$$

$$d_v = 25.3 - 2 \times 1 = 23.3 \text{ mm}$$

$$A_v = \frac{\pi}{4} (0.0233)^2 = 4.26 \times 10^{-4} \text{ m}^2$$

$$A_i = \frac{\pi}{4} (0.0253)^2 = 5.03 \times 10^{-4} \text{ m}^2$$

$$\Delta P_{v_1} = \frac{16 (8.66 \times 10^{-6}) Q_c}{2 (0.007) (2488.9 \times 10^3)} \left[\frac{\frac{9 \times 0.3}{\left(\frac{0.0233}{2}\right)^2 (4.26 \times 10^{-4})}}{+ \frac{2.235}{\left(\frac{0.0253}{2}\right)^2 (5.03 \times 10^{-4})}} \right]$$

$$\Delta P_{v_1} = 0.30 Q_c \text{ Pa}$$

The normal hydrostatic vapour pressure drop is given by equation (3.37):

$$\Delta P_{v_2} = \rho_v g H = 0.007 \times 9.81 \times 0.57 = 0.039 \text{ Pa}$$

To get vapour pressure drop at the right angle elbows (5 off), first get the vapour velocity from equation (3.41):

$$V_v = \frac{Q_c}{\rho_v A_v h_{fg}}$$

$$V_v = \frac{Q_c}{(0.007) (4.26 \times 10^{-4}) (2488.9 \times 10^3)} = 0.135 Q_c \text{ m/s}$$

$$V_{v_i} = V_v \left(\frac{A_v}{A_i} \right)$$

⁷ Actually the adiabatic section expands from 25.3 mm to 76 mm over a short length before entering the absorber. The calculation here is based on a constant diameter of 25.3 mm. However, the pressure drop due to this expansion has been considered.

$$V_{v_i} = 0.135 Q_c \times \frac{4.26 \times 10^{-4}}{5.03 \times 10^{-4}} = 0.114 Q_c$$

Using equation (3.40), the friction coefficient, h_{f_3} , is:

$$h_{f_3} = K_f \frac{V_{v_i}^2}{2g} = 0.9 \frac{(0.114 Q_c)^2}{2 \times 9.81} = 0.000596 Q_c^2 \text{ m}$$

Hence the vapour pressure drop at the right angle elbows (5 off) is:

$$\Delta P_{v_3} = 5 \times h_{f_3} \rho_v g = 5 (0.000596 Q_c^2) (0.007) (9.81) = 2.05 \times 10^{-4} Q_c^2 \text{ Pa}$$

Now get vapour pressure drop at the 3 expansions on the vapour line (see Fig. 3.3), use equations (3.46) to (3.48) to get the friction coefficient first.

1- Expansion 1; from d_v to d_i :

$$\begin{aligned} h_{f_{1-1}} &= \frac{V_v^2}{2g} \left(1 - \frac{A_v}{A_i} \right)^2 \\ &= \frac{(0.135 Q_c)^2}{2 \times 9.81} \left(1 - \frac{4.26 \times 10^{-4}}{5.03 \times 10^{-4}} \right)^2 \\ &= 5.5 \times 10^{-4} Q_c^2 \text{ m} \end{aligned}$$

Hence, vapour pressure drop at expansion 1, is:

$$\begin{aligned} \Delta P_{v_{1-1}} &= h_{f_{1-1}} \rho_v g \\ &= (5.5 \times 10^{-4} Q_c^2) (0.007) (9.81) \\ &= 3.78 \times 10^{-5} Q_c^2 \text{ Pa} \end{aligned}$$

2- Expansion 2; from d_i to d_1 :

$$\begin{aligned} h_{f_{1-2}} &= \frac{V_{v_i}^2}{2g} \left(1 - \frac{A_i}{A_1} \right)^2 \\ &= \frac{(0.114 Q_c)^2}{2 \times 9.81} \left(1 - \frac{\frac{\pi}{4} (0.0253)^2}{\frac{\pi}{4} (0.076)^2} \right)^2 \end{aligned}$$

$$= 5.24 \times 10^{-4} Q_c^2 \text{ m}$$

Equation (3.43) gives vapour pressure drop at expansion 2

$$\begin{aligned} \Delta P_{v_{4-2}} &= h_{f_{4-2}} \rho_v g \\ &= 5.24 \times 10^{-4} Q_c^2 (0.007)(9.81) \\ &= 3.6 \times 10^{-5} Q_c^2 \text{ Pa} \end{aligned}$$

3- Expansion 3; from d_1 to d_2 :

$$h_{f_{4-3}} = \frac{V_{v_1}^2}{2g} \left(1 - \frac{A_1}{A_2} \right)^2$$

Vapour velocity before expansion 3 is:

$$\begin{aligned} V_{v_1} &= V_{v_i} \left(\frac{A_i}{A_1} \right) \\ V_{v_1} &= 0.114 Q_c \times \frac{\frac{\pi}{4} (0.0253)^2}{\frac{\pi}{4} (0.076)^2} \\ &= 0.0126 Q_c \text{ m/s} \end{aligned}$$

$$\begin{aligned} &= \frac{(0.114 Q_c)^2}{2 \times 9.81} \left(1 - \frac{\frac{\pi}{4} (0.0253)^2}{\frac{\pi}{4} (0.076)^2} \right)^2 \\ &= 5.24 \times 10^{-4} Q_c^2 \text{ m} \end{aligned}$$

Equation (3.44) gives vapour pressure drop at expansion 3:

$$\begin{aligned} \Delta P_{v_{4-3}} &= h_{f_{4-3}} \rho_v g \\ &= 5.62 \times 10^{-4} Q_c^2 (0.007)(9.81) \\ &= 3.86 \times 10^{-5} Q_c^2 \text{ Pa} \end{aligned}$$

Vapour pressure drop in all the expansions resulting from vapour flow of 9 tubes is:

$$\Delta P_{v_4} = (\Delta P_{v_{4-1}} + \Delta P_{v_{4-2}} + \Delta P_{v_{4-3}}) Q_c^2$$

$$\begin{aligned} \Delta P_{v_4} &= (3.78 \times 10^{-5} + 3.6 \times 10^{-5} + 3.86 \times 10^{-5}) Q_c^2 \\ &= 1.12 \times 10^{-4} Q_c^2 \end{aligned}$$

Substituting the values of ΔP_{v_1} , ΔP_{v_2} , ΔP_{v_3} & ΔP_{v_4} on equation (3.57) gives:

$$\begin{aligned} \Delta P_{v_{total}} &= \Delta P_{v_1} + \Delta P_{v_2} + \Delta P_{v_3} + \Delta P_{v_4} \\ &= 0.30 Q_c + 0.039 + 2.05 \times 10^{-4} Q_c^2 + 1.12 \times 10^{-4} Q_c^2 \\ \Delta P_{v_{total}} &= 3.17 \times 10^{-4} Q_c^2 + 0.30 Q_c + 0.039 \end{aligned}$$

The liquid pressure drop, $\Delta P_{\ell_{total}}$, is given by:

$$\Delta P_{\ell_{total}} = \Delta P_{\ell} + \Delta P_{+}$$

Taking into account the number of evaporator's tubes, and using equation (3.50), the liquid pressure drop due to friction with the porous layer is evaluated as follows:

$$\Delta P_{\ell} = \frac{\mu_{\ell} \left(\pi \frac{d_{\ell}}{2} \right) Q_c}{K A_w h_{fg} \rho_{\ell}}$$

The permeability, K, is given by:

$$\begin{aligned} K &= \frac{\varepsilon d_p^2}{32} \\ &= \frac{0.48 (0.41 \times 300 \times 10^{-6})^2}{32} \\ &= 2.27 \times 10^{-10} \text{ m}^2 \end{aligned}$$

The wick cross-sectional area, A_w is given by:

$$\begin{aligned} A_w &= n L_r \delta = 9 * 0.3 * 0.001 \\ &= 2.7 \times 10^{-3} \text{ m}^2 \end{aligned}$$

Thus,

$$\Delta P_t = \frac{(1506 \times 10^{-6}) \left(\pi \frac{0.0253}{2} \right) Q_c}{(2.27 \times 10^{-10}) (2.7 \times 10^{-3}) (2488.9 \times 10^3) (1000)}$$

$$= 0.04 Q_c \text{ Pa}$$

The normal hydrostatic liquid pressure drop ΔP_+ is given by:

$$\Delta P_+ = \rho_l g d_v$$

$$= (1000)(9.81)(0.0233)$$

$$= 228.57 \text{ Pa}$$

Hence the total liquid pressure drop $\Delta P_{t_{total}}$ is:

$$\Delta P_{t_{total}} = 0.04 Q_c + 228.57 \text{ Pa}$$

The maximum capillary pressure for the evaporator is given by:

$$\Delta P_{c,m} = \frac{2\sigma}{r_{eff}}$$

$$= \frac{2 \times 74.8 \times 10^{-3}}{0.41 \left(\frac{300 \times 10^{-6}}{2} \right)}$$

$$= 2432.52 \text{ Pa}$$

Substituting the values of $\Delta P_{v_{total}}$, $\Delta P_{t_{total}}$ & $\Delta P_{c,m}$ in equation (3.57) gives:

$$2432.52 = 3.17 \times 10^{-4} Q_c^2 + 0.30 Q_c + 0.039 + 0.04 Q_c + 228.57$$

Re-arranging, a quadratic equation is obtained

$$3.17 \times 10^{-4} Q_c^2 + 0.34 Q_c - 2203.91 = 0$$

Solving the quadratic equation gives:

$$Q_c = \frac{-0.34 \pm \sqrt{(0.34)^2 - 4(3.17 \times 10^{-4} \times (-2203.91))}}{2 \times (-2203.91)}$$

$$Q_c = 2154.45 \text{ W}$$

Calculate Reynolds number and Mach number using the above value of Q_c to verify the assumption of laminar incompressible flow made earlier:

$$\begin{aligned}
 Re_v &= \frac{4Q_c}{\pi d_v \mu_v h_{fg}} \\
 &= \frac{4(2154.45)}{\pi(0.0233)(8.66 \times 10^{-6})(2488.9 \times 10^3)} \\
 &= 5462.17 \Rightarrow \text{Turbulent flow} \\
 Ma &= \frac{(4 Q_c / h_{fg} \pi d_v^2)}{\sqrt{\gamma R T_v}} \\
 Ma &= \frac{4 \times 2154.45 / ((2488.9 \times 10^3) \pi (0.0233)^2)}{\sqrt{1.33 \times 461.89 \times 278}} \\
 &= 0.005 < 0.3 \Rightarrow \text{incompressible flow}
 \end{aligned}$$

For turbulent vapour flow, ΔP_{v_1} is given by equation (3.33):

$$(\Delta P_{v_1})_{turbulent} = 0.038 \left(\frac{d_v Q_c}{A_v u_v h_{fg}} \right)^{\frac{3}{4}} \frac{2 \mu_v L_{eff} Q_c}{d_v^2 A_v \rho_v h_{fg}}$$

To account for the fact that the internal diameter of the evaporator and adiabatic tubes are different, the above equation becomes:

$$\begin{aligned}
 (\Delta P_{v_1})_{turbulent} &= 0.038 \left(\frac{Q_c}{u_v h_{fg}} \right)^{\frac{3}{4}} \frac{2 \mu_v Q_c}{\rho_v h_{fg}} \left[\left(\frac{d_v}{A_v} \right)^{\frac{3}{4}} \left(\frac{L_e}{d_v^2 A_v} \right) + \left(\frac{d_i}{A_i} \right)^{\frac{3}{4}} \left(\frac{L_a}{d_i^2 A_i} \right) \right] \\
 \Delta P_{v_1} &= 0.038 \left(\frac{Q_c}{(8.66 \times 10^{-6})(24889 \times 10^3)} \right)^{\frac{3}{4}} \left(\frac{2(8.66 \times 10^{-6}) Q_c}{(0.007)(24889 \times 10^3)} \right) \\
 &\quad \left[\left(\frac{0.0233}{\frac{\pi}{4} (0.0233)^2} \right)^{\frac{3}{4}} \left(\frac{9 \times 0.3}{(0.0233)^2 \frac{\pi}{4} (0.0233)^2} \right) + \left(\frac{0.0233}{\frac{\pi}{4} (0.0233)^2} \right)^{\frac{3}{4}} \left(\frac{2.235}{(0.0253)^2 \frac{\pi}{4} (0.0253)^2} \right) \right] \\
 &= 1.4 \times 10^{-3} Q_c^{\frac{7}{4}} \text{ Pa}
 \end{aligned}$$

Use equation (3.50) to calculate the inertial pressure gradient, ΔP_i :

$$\Delta P_i = \frac{\rho_v V_v^2}{2g} \left[\frac{28}{9} - \frac{0.68 \text{Re}}{\left[\frac{29L_e}{d_v} \right] + \text{Re}} \text{Exp} \left(-\frac{60L_a}{\text{Re} d_v} \right) \right]$$

Again, accounting for different inner diameters (the inner diameter of the evaporator's sintered tube is different from that of the adiabatic section), equation (3.53) becomes:

$$\Delta P_i = \frac{\rho_v V_v^2}{2g} \left[\frac{28}{9} - \frac{0.68 \text{Re}}{\left[29L_e/d_v \right] + \text{Re}} \right]$$

For the evaporator section, i.e. when $L_a=0$, and

$$\Delta P_i = \frac{\rho_v V_{v_i}^2}{2g} \left[\frac{28}{9} - 0.68 \times \text{Exp} \left(-\frac{60L_a}{\text{Re} d_i} \right) \right]$$

For the adiabatic section, i.e. when $L_e=0$.

Then the total inertial pressure drop is given by:

$$\Delta P_i = \frac{\rho_v}{2g} \left[V_v^2 \left(\frac{28}{9} - \frac{0.68 \text{Re}}{\left[29L_e/d_v \right] + \text{Re}} \right) + V_i^2 \left(\frac{28}{9} - 0.68 \text{Exp} \left(-\frac{60L_a}{\text{Re} d_i} \right) \right) \right]$$

$$\Delta P_i = 2.7 \times 10^{-5} Q_c^2 \text{ Pa}$$

Now, the total vapours pressure becomes,

$$\Delta P_{v_{total}} = \Delta P_{v_1} + \Delta P_{v_2} + \Delta P_{v_3} + \Delta P_{v_4} + \Delta P_i$$

$$\Delta P_{v_{total}} = 1.4 \times 10^{-3} Q_c^{\frac{7}{4}} + 0.039 + 2.05 \times 10^{-4} Q_c^2 + 1.12 \times 10^{-4} Q_c^2 + 2.7 \times 10^{-5} Q_c^2$$

$$\Delta P_{v_{total}} = 3.44 \times 10^{-4} Q_c^2 + 1.4 \times 10^{-3} Q_c^{\frac{7}{4}} + 0.039$$

Re-substitute the values of $\Delta P_{v_{total}}$, $\Delta P_{t_{total}}$ & $\Delta P_{c,m}$ in equation (3.57). This gives:

$$2432.52 = 3.44 \times 10^{-4} Q_c^2 + 1.4 \times 10^{-3} Q_c^{\frac{7}{4}} + 0.039 + 0.34 Q_c + 228.57$$

$$3.44 \times 10^{-4} Q_c^2 + 1.4 \times 10^{-3} Q_c^{\frac{7}{4}} + 0.34 Q_c - 2203.91 = 0$$

Chapter 3: Analytical Work

Solving the above equation by iteration⁸, gives:

$$Q_c = 1700.76 \text{ W}$$

The above value of Q_c is the capillary limit heat rate for this evaporator under the specified test conditions.

3.9.4 Sonic Limit:

Equation (3.54) can be used to obtain the sonic limit:

$$\begin{aligned} Q_s &= 0.47 h_{fg} A_v (\rho_v P_v)^{1/2} \\ &= 0.47 * 2488.9 \times 10^3 * (4.2 \times 10^{-4}) [(0.007)(8.719 \times 10^{-4})]^{1/2} \\ &= 1242.71 \text{ W} \end{aligned}$$

3.9.5 Viscous Limit Heat Rate:

Equation (3.55) can be used to obtain the viscous limit:

$$\begin{aligned} Q_v &= \frac{A_v r_v^2 h_{fg} \rho_v P_v}{16 \mu L_e} \\ &= 2349.76 \text{ W} \end{aligned}$$

3.9.6 Boiling Limit Heat Rate:

It is given by equation (3.56) as follows:

$$Q_{bl} = \left(\frac{2\pi L_e k_{eff} T_v}{h_{fg} \ln\left(\frac{r_i}{r_v}\right)} \right) \left(\frac{2\sigma}{r_n} - P_{c,m} \right)$$

Where k_{eff} is given by equation (1.26)

$$\begin{aligned} k_w &= \frac{k_s [2k_s + k_t - 2\varepsilon(k_s - k_t)]}{2k_s + k_t + \varepsilon(k_s - k_t)} \\ k_w &= \frac{52 [2 \times 52 + 578 \times 10^{-3} - 2 \times 0.48(52 - 578 \times 10^{-3})]}{2 \times 52 + 578 \times 10^{-3} + 0.48(52 - 578 \times 10^{-3})} = 22.2 \text{ W/m K} \end{aligned}$$

⁸ The iteration in this sample calculation is done using excel spread sheet while the one used in the iterative computational scheme is done using Newton-Raphson method.

$$Q_{bl} = \left(\frac{2\pi (9 \times 0.3) (22.2) (278)}{(2488.9 \times 10^3) \ln \left(\frac{0.5 \times 0.0253}{0.5 \times 0.0233} \right)} \right) \left(\frac{2 \times 74.8 \times 10^{-3}}{2.54 \times 10^{-6}} - 2432.52 \right)$$

$$= 285363.780 \text{ W}$$

Summarising the results:

Capillary limit heat rate, $Q_c = 1700.76 \text{ W}$

Sonic limit heat rate, $Q_s = 1242.71 \text{ W}$

Viscous limit heat rate, $Q_v = 2349.76 \text{ W}$

Boiling limit heat rate, $Q_{bl} = 28973.23 \text{ W}$

Hence the minimum limit heat rate is:

$$Q_{min} = Q_s = 1242.71 \text{ W}$$

3.10 Analytical Results:

In this section the results obtained when running the iterative computational scheme described in the section (3.1) are presented. The programme was run several times using different boiling formulae. Some of the results are trivial and, as such are not presentable, however, those obtained using O'Neil's [35] and Rao & Balkrishnan [32] boiling formulae are shown in Fig (3.5) to (3.76). The capillary, sonic and viscous limit heat rates are shown in Fig (3.77). The figures show the variation of the boiling heat rates and boiling heat transfer coefficients with the particle size and layer thickness for different air inlet temperatures (25, 30 & 35 °C) and velocities (1.0, 2.0 & 3.0 m/s). Further explanation of these curves is given below but detailed discussion of these results is carried out in chapter five where analytical results are compared with experimental ones.

3.10.1 Effect of Particle Size on Boiling Heat Rate:

The effect of varying particle size on boiling heat rate is shown in Fig (3.5) to (3.22). Results obtained using O'Neil boiling formula are shown in Fig (3.5) to (3.13) and those obtained using Rao and Balkrishnan boiling formula are shown in Fig (3.14) to (3.22).

3.10.1.1 Boiling Heat Rates Obtained Using O'Neil's Formula:

Generally speaking, the boiling heat rate increases with increased particle size to a maximum and then either decreases slowly or remains constant at this maximum value; see Fig (3.5) to (3.13). However, in few cases the boiling heat rate increases monotonically, as it appears in Fig (3.5), (3.6), (3.9) & (3.11). It is not known whether the heat rate will reach a maximum at larger particle size ranges. For particular points where no solution was obtained for the 50 μm or 100 μm particle size the boiling heat rate is seen to decrease monotonically; see Fig (3.5), (3.7) & (3.13). It might be reasonable to assume that the trend appearing in these three figures would have been more or less one of an increasing-decreasing nature had the programme converged to a solution for these evaporators. Some of the boiling heat rates are seen to increase monotonically. The capillary, sonic and viscous limit heat rates are found to be monotonically decreasing with increase in particle size for the tested range of particle size. The fact that the limit heat rate curves are falling suggests that the heat rate transported by the evaporators tested in this research should have a pattern that either decreases monotonically with increasing particle size or increases to a maximum before decreasing again. The results show that the heat rate curves of various particle sizes follow a path parallel to the lowest of the three limits after increasing to a maximum. In chapter five explanations will be given for the restrictions that possibly prevented achieving higher heat rates for small particle size evaporators such that the trend for this part of the tested particle size range is one of increasing nature. In Fig (3.77) to (3.79) average limit heat rates are shown for all layer thicknesses' curves. Actually, for each layer thickness, three limit heat rate curves were obtained analytically i.e. a number of twelve curves just for the limit heat rates. The average curves were presented rather than the real values to improve clarity of the graphs.

3.10.1.2 Boiling Heat Rates Obtained Using Rao and Balkrishnan's Formula:

These are shown in Fig (3.14) to (3.22). The boiling heat rate increases monotonically with increasing particle size for the particle size range tested. It is not known whether the heat

rate will reach a maximum at larger particle size ranges. However, the values of heat rates obtained using this formula are less than the values obtained using O'Neil's formula for the same particle size. The capillary, sonic and viscous limit heat rates are found to be monotonically decreasing with increase in particle size for the tested range of particle size.

3.10.2 Effect of Particle Size on Boiling Heat Transfer Coefficient:

The effect of varying particle size on boiling heat transfer coefficient is shown in Fig (3.23) to (3.40). Results obtained using O'Neil's boiling formula are shown in Fig (3.23) to (3.31) and those obtained using Rao and Balkrishnan's boiling formula are shown in Fig (3.32) to (3.40).

The heat transfer coefficient increases monotonically with increase in particle size when Using O'Neil's Formula, see Fig (3.23) to (3.31). It is not known whether the heat rate will reach a maximum at larger particle size ranges.

The heat transfer coefficient Obtained Using Rao and Balkrishnan's Formula increases monotonically with increase in particle size; see Fig (3.32) to (3.40). However, the value of heat transfer coefficient obtained using this formula is much less compared to that obtained using O'Neil's formula.

3.10.3 Effect of Layer Thickness on Boiling Heat Rate:

Figs (3.41) to (3.58) show the variation of the boiling heat rate with increasing layer thickness. The figures show that the heat rate varies slightly with increase in layer thickness. However, the results obtained from O'Neil boiling formula show varying effects of layer thickness on boiling performance. Whilst the heat rate increases slightly with layer thickness in some cases, it acts differently in others as it decreases with increasing layer thickness.

3.10.4 Effect of Layer Thickness on Boiling Heat Transfer Coefficient:

Figs (3.59) to (3.76) show the variation of the boiling heat transfer coefficient with layer thickness. The figures show that the boiling heat transfer coefficient varies slightly with layer thickness. However, the heat transfer coefficient obtained using O'Neil's boiling

formula is evidently much higher than that obtained using Rao and Balkrishnan formula. It is also remarkable that the results obtained using O'Neil boiling formula showed varying effects of layer thickness on boiling heat transfer coefficient (i.e. it increases with layer thickness in some cases and decreases in others).

3.11 Summary of Chapter 3:

In this chapter complete description of the analytical model used in this research for calculating the boiling heat rate transported by the sintered tube evaporators tested in this research was given. Sample of the calculation used for determining the limit heat rates that bound the increase of boiling heat rate, sustained by these evaporators, was also presented. An iterative computational scheme based on the analytical model was built and used to calculate boiling heat rates and heat transfer coefficients. This iterative computational scheme, which is shown in the appendices along with its algorithm and flow charts, was written using a computer programme in FORTRAN 95 language.

Finally, analytical results were obtained from the iterative computational scheme on the effect of varying particle size and layer thickness on boiling heat rate and boiling heat transfer coefficient, and presented but detailed discussion of the results is made in chapter 5.

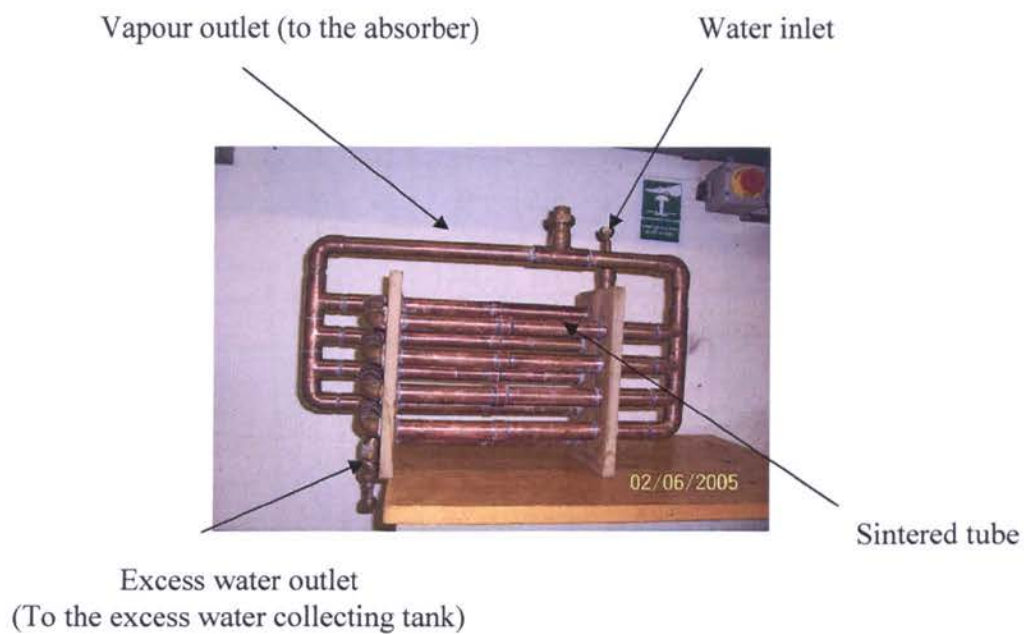


Fig (3.1a) Sintered tubes Evaporator

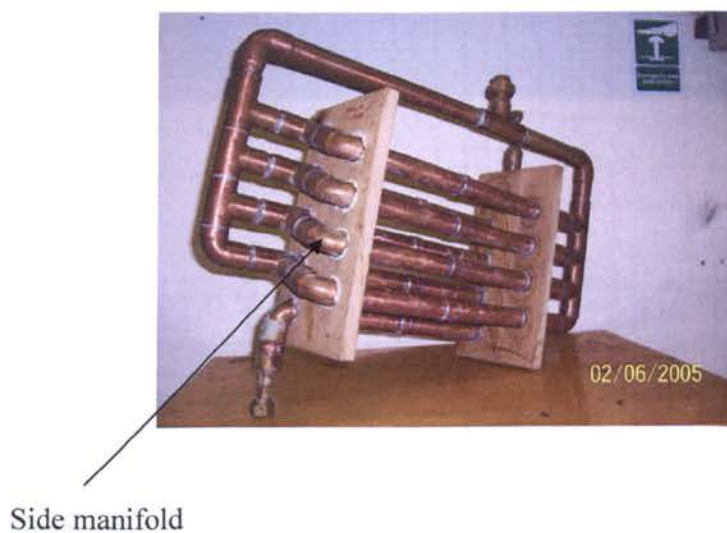


Fig (3.1b) Sintered Tubes Evaporator

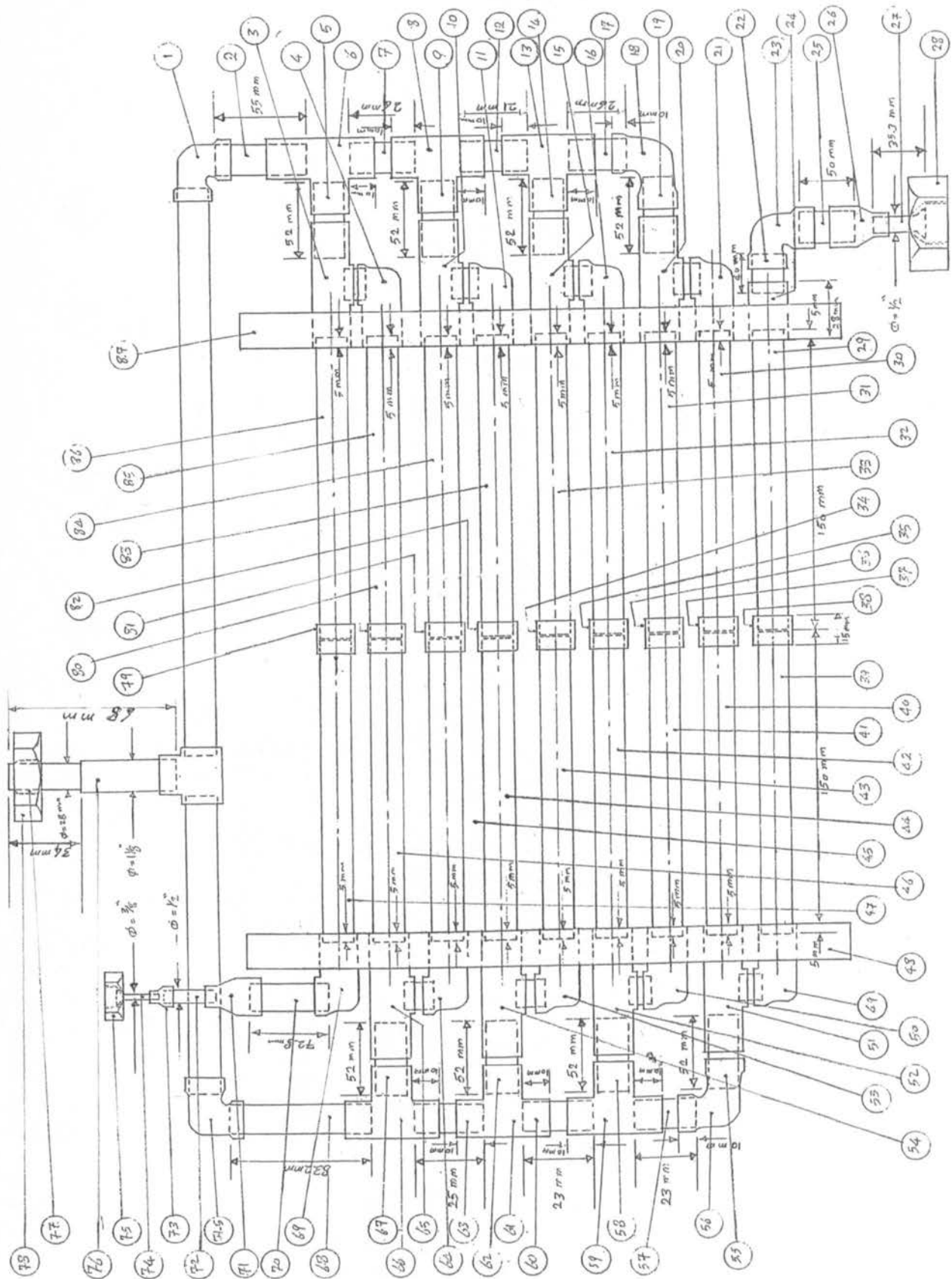


Fig (3.2a) Front View of the Evaporator

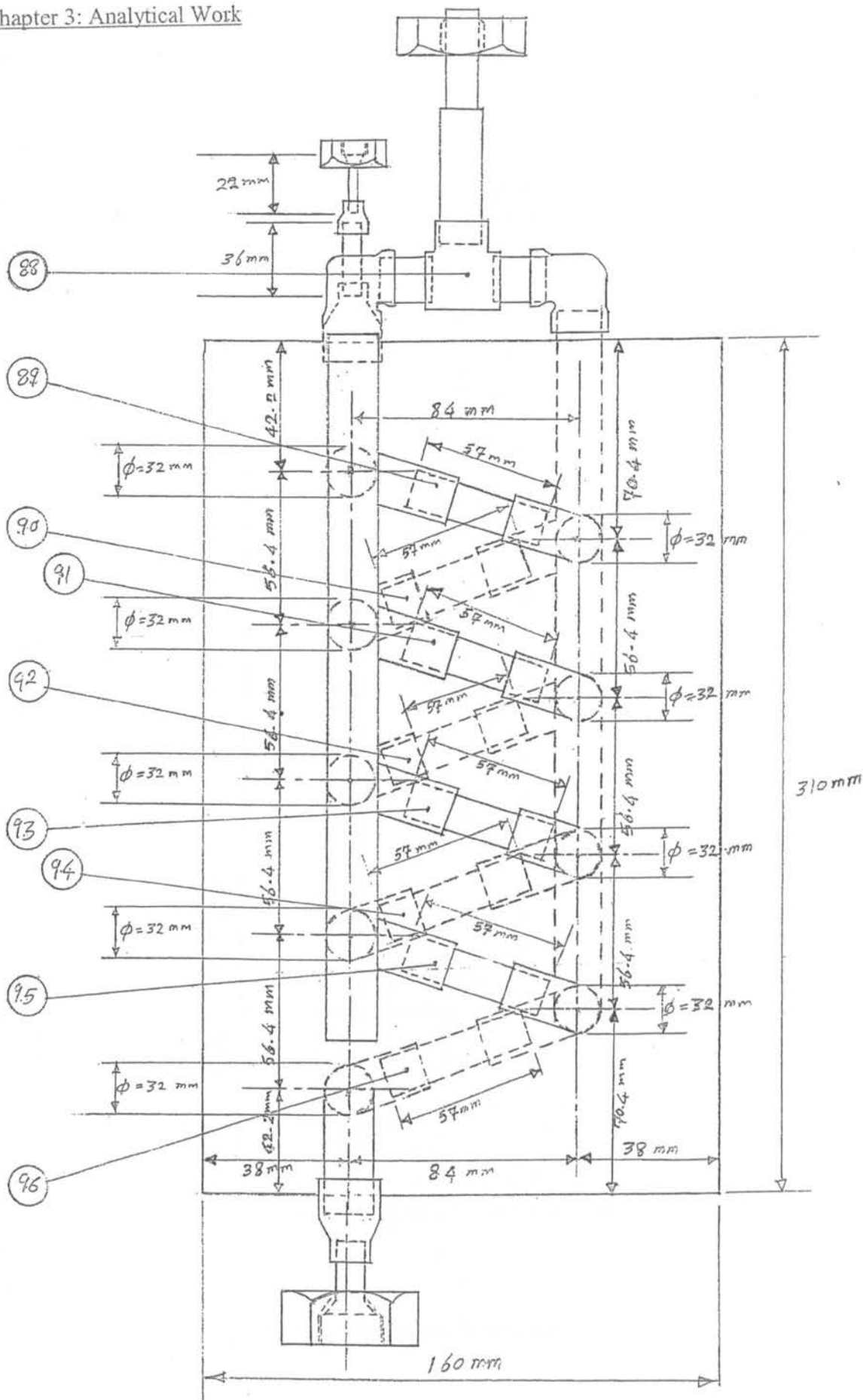


Fig (3.2b) Side View of the Evaporator

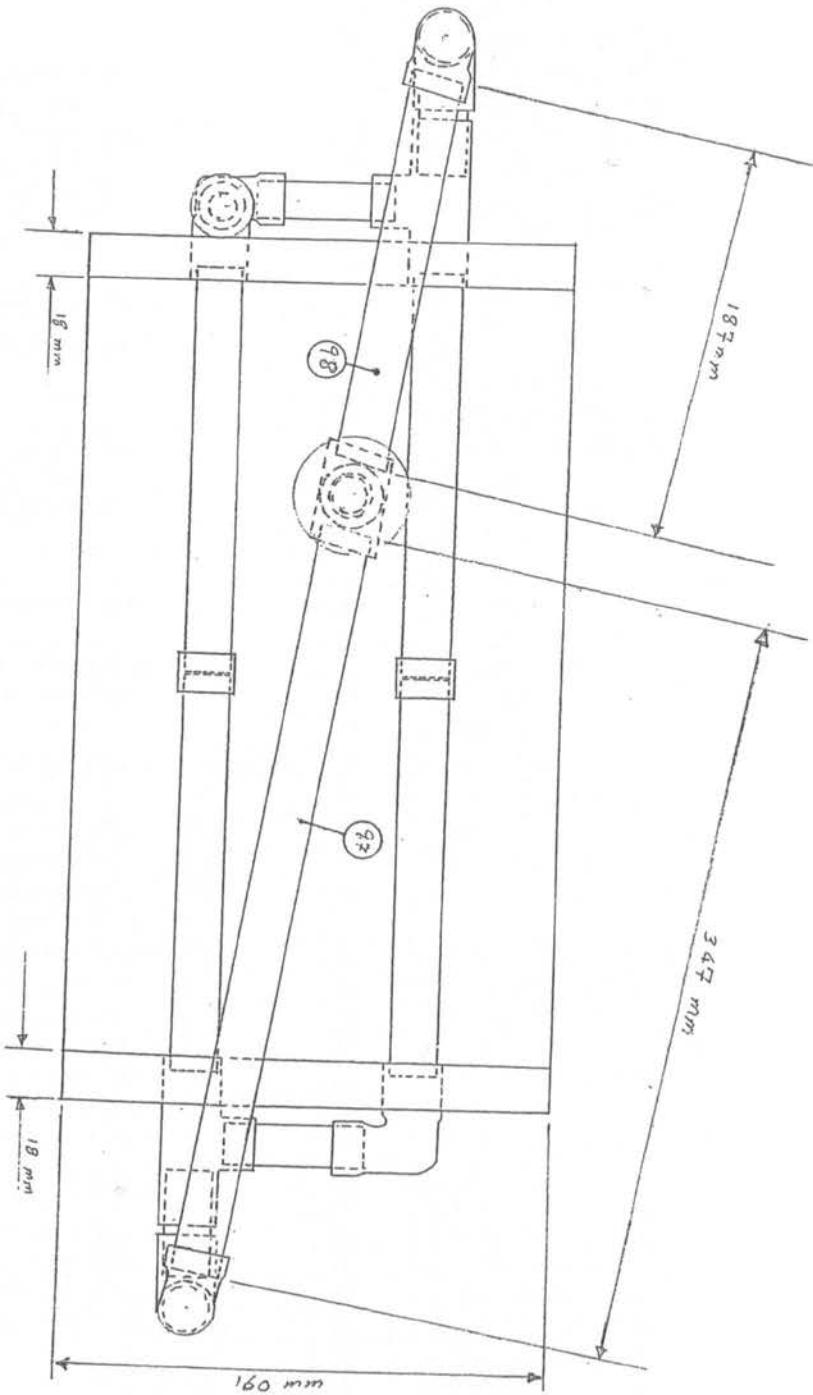


Fig (3.2c) Top View of the Evaporator

Legend for Figs (3.2a) to (3.2c)

N0.	items	N0.	items
1	1½' Elbow	52	1½' Tee
2	1½' Outer diameter pipe	53	1½' Elbow
3	1½' Tee	54	1½' Tee
4	1½' Elbow	55	1½' Outer diameter pipe
5	1½' Outer diameter pipe	56	1½' Elbow (Shortened)
6	1½' Tee (shortened)	57	1½' Outer diameter pipe
7	1½' Outer diameter pipe	58	1½' Outer diameter pipe
8	1½' Tee (shortened)	59	1½' Tee (Shortened)
9	1½' Outer diameter pipe	60	1½' Outer diameter pipe
10	1½' Tee	61	1½' Tee (Shortened)
11	1½' Elbow	62	1½' Outer diameter pipe
12	1½' Outer diameter pipe	63	1½' Outer diameter pipe
13	1½' Tee (shortened)	64	1½' Elbow
14	1½' Outer diameter pipe	65	1½' Tee
15	1½' Tee	66	1½' Tee (Shortened)
16	1½' Elbow	67	1½' Outer diameter pipe
17	1½' Outer diameter pipe	68	1½' Outer diameter pipe
18	1½' Tee (shortened)	69	1½' Elbow
19	1½' Outer diameter pipe	70	1½' Outer diameter pipe
20	1½' Tee	71	1½' to ½' Reducer
21	1½' Elbow	72.5	1½' Elbow
22	1½' Outer diameter pipe	55	1½' Outer diameter pipe
23	1½' Elbow	56	1½' Elbow (Shortened)
24	1½' Straight Coupler (shortened)	72	1½' Outer diameter pipe
25	1½' Outer diameter pipe	73	½' to ¾' Reducer
26	1½' to ¾' Reducer	74	¾' Outer diameter Pipe with flare end
27	½' Outer diameter Pipe with Flared end	75	¾' Flared Nut
28	½' Flared Nut	76	1½' Outer diameter pipe
29	1½' Outer diameter Sintered Pipe	76.5	28 mm Outer diameter pipe
30	1½' Outer diameter Sintered Pipe	77	28 mm Olive ring
31	1½' Outer diameter Sintered Pipe	78	28 mm Compression ring
32	1½' Outer diameter Sintered Pipe	79	1½' Straight Coupler (shortened)
33	1½' Outer diameter Sintered Pipe	80	1½' Straight Coupler (shortened)
34	1½' Straight Coupler (shortened)	81	1½' Straight Coupler (shortened)
35	1½' Straight Coupler (shortened)	82	1½' Straight Coupler (shortened)
36	1½' Straight Coupler (shortened)	83	1½' Outer diameter Sintered Tube
37	1½' Straight Coupler (shortened)	84	1½' Outer diameter Sintered Tube
38	1½' Straight Coupler (shortened)	85	1½' Outer diameter Sintered Tube
39	1½' Outer diameter Sintered Pipe	86	1½' Outer diameter Sintered Tube
40	1½' Outer diameter Sintered Pipe	87	MDF Wood
41	1½' Outer diameter Sintered Pipe	88	1½' Tee
42	1½' Outer diameter Sintered Pipe	89	1½' Outer diameter pipe
43	1½' Outer diameter Sintered Pipe	90	1½' Outer diameter pipe
44	1½' Outer diameter Sintered Pipe	91	1½' Outer diameter pipe
45	1½' Outer diameter Sintered Pipe	92	1½' Outer diameter pipe
46	1½' Outer diameter Sintered Pipe	93	1½' Outer diameter pipe
47	1½' Outer diameter Sintered Pipe	94	1½' Outer diameter pipe
48	MDF Wood	95	1½' Outer diameter pipe
49	1½' Elbow	96	1½' Outer diameter pipe
50	1½' Elbow	97	1½' Outer diameter pipe
51	1½' Tee	98	1½' Outer diameter pipe

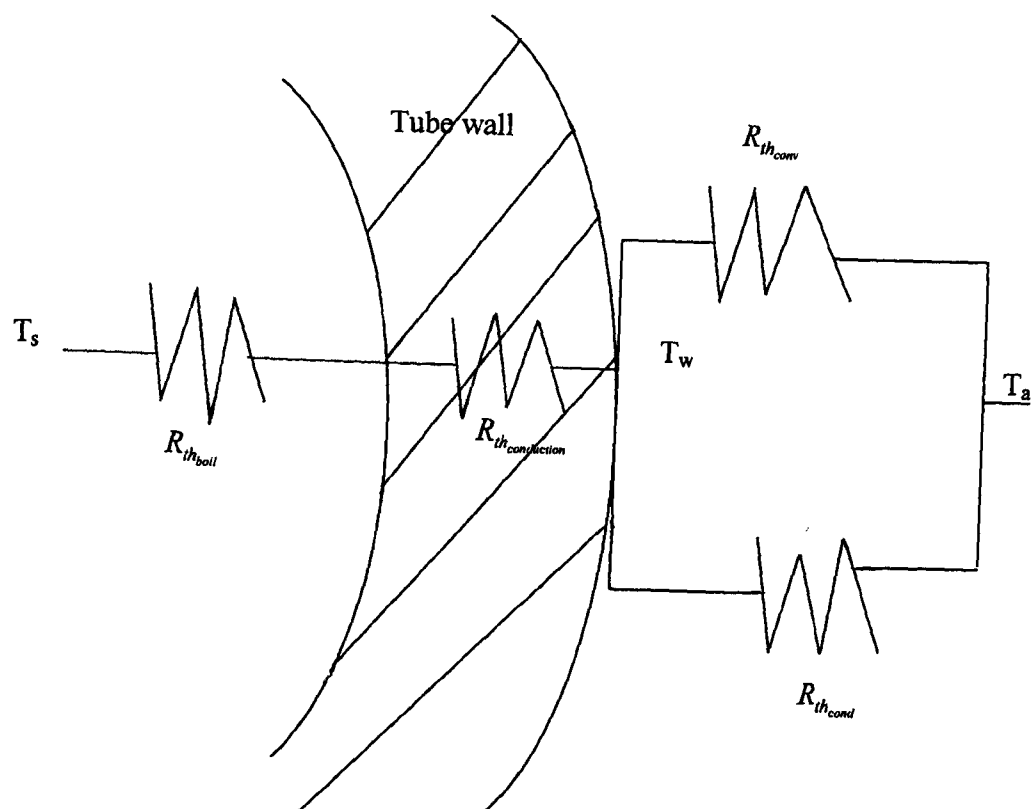


Fig (3.3) Thermal Circuit of an Evaporator Tube

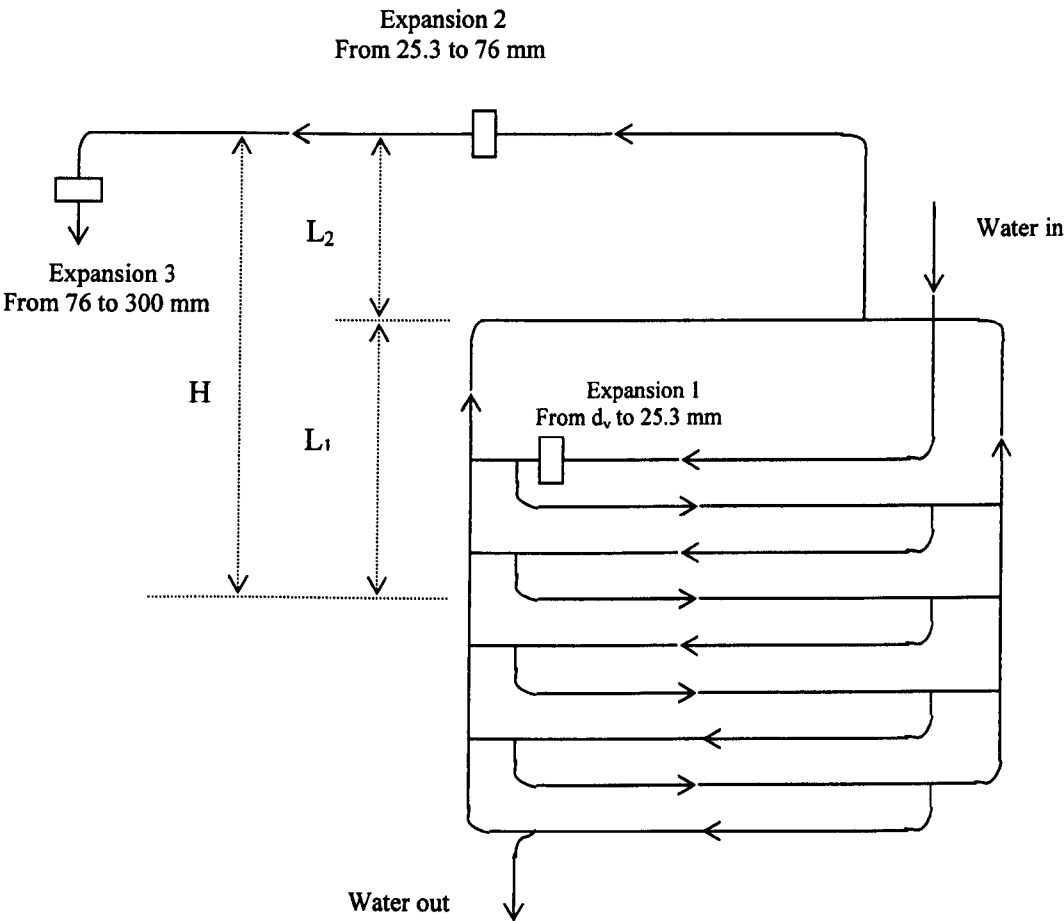
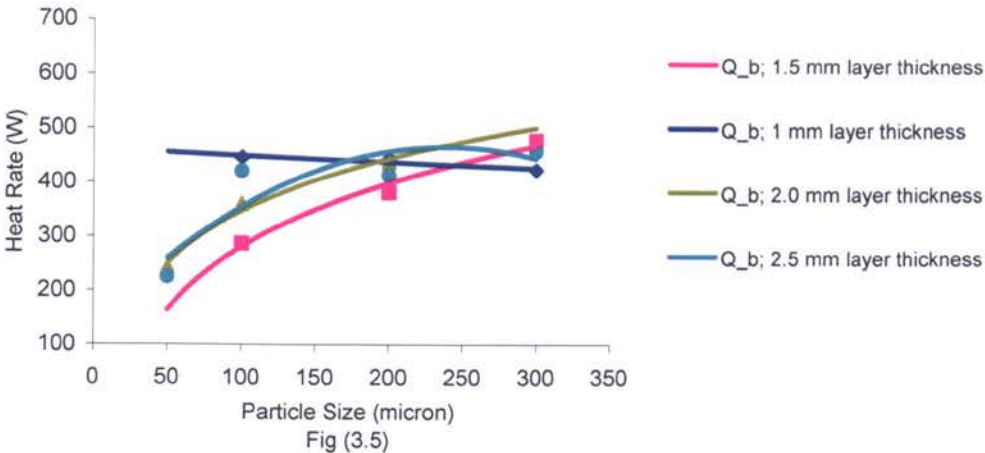
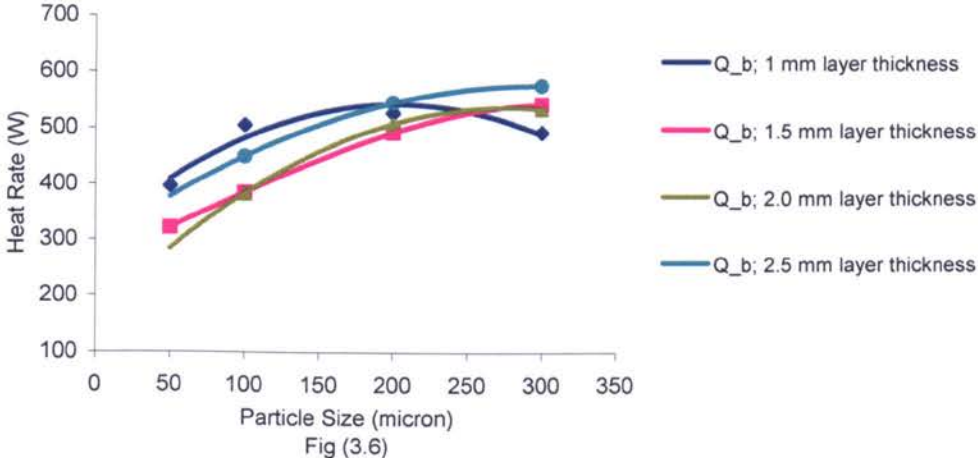


Fig (3.4) Sketch of Capillary-assisted Evaporator

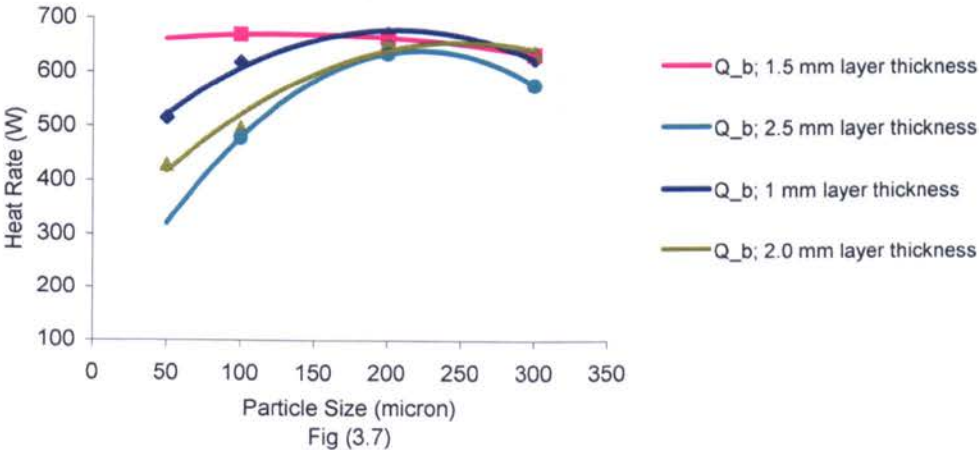
Analytical Boiling Heat Rate Vs Particle Size
at 1.0 m/s and 25 °C air Velocity and Temperature (O'Neil)



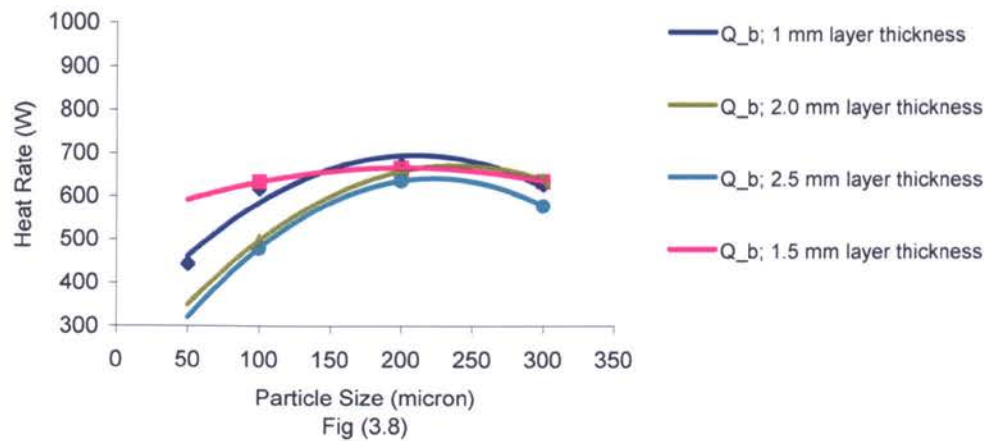
Analytical Boiling Heat Rate Vs Particle Size
at 1.0 m/s and 30 °C air Velocity and Temperature (O'Neil)



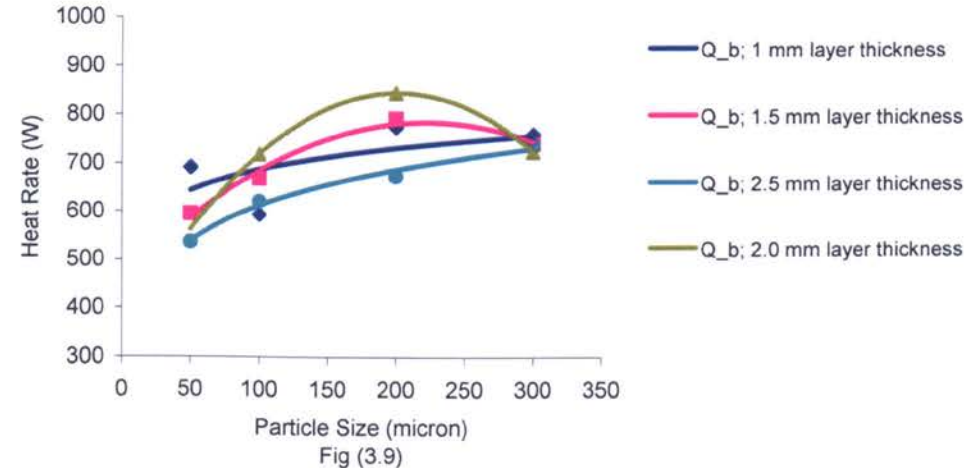
Analytical Boiling Heat Rate Vs Particle Size
at 1.0 m/s and 35 °C air Velocity and Temperature (O'Neil)



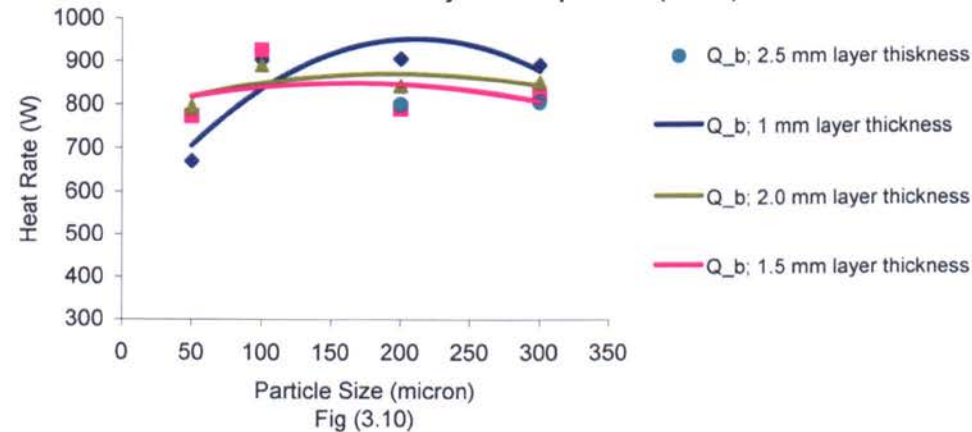
Analytical Boiling Heat Rate Vs Particle Size
at 2.0 m/s and 25 ° C air Velocity and Temperature (O'Neil)

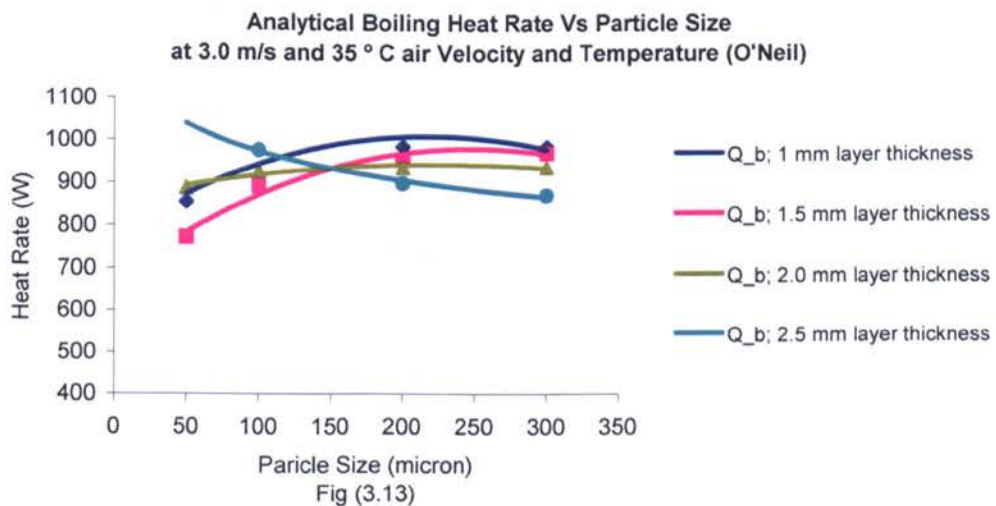
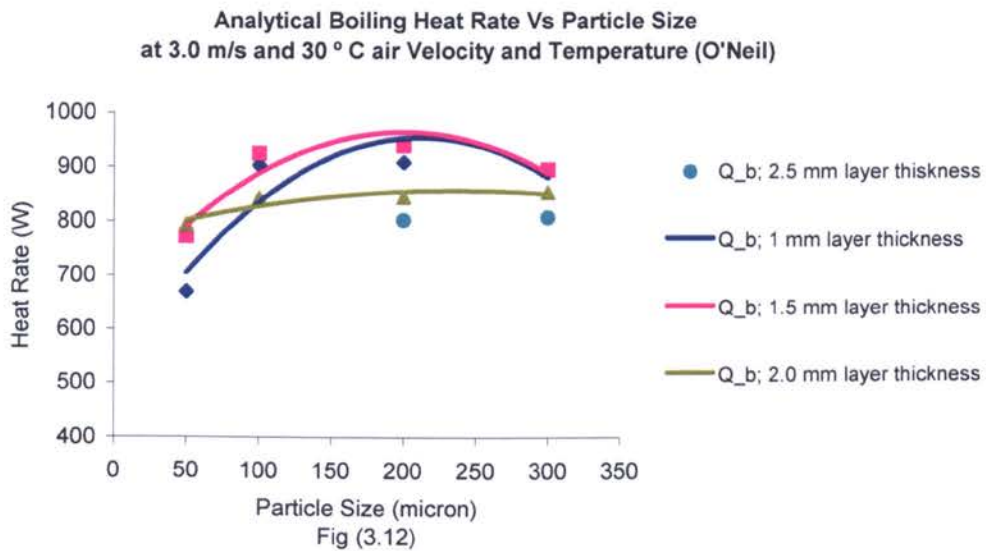
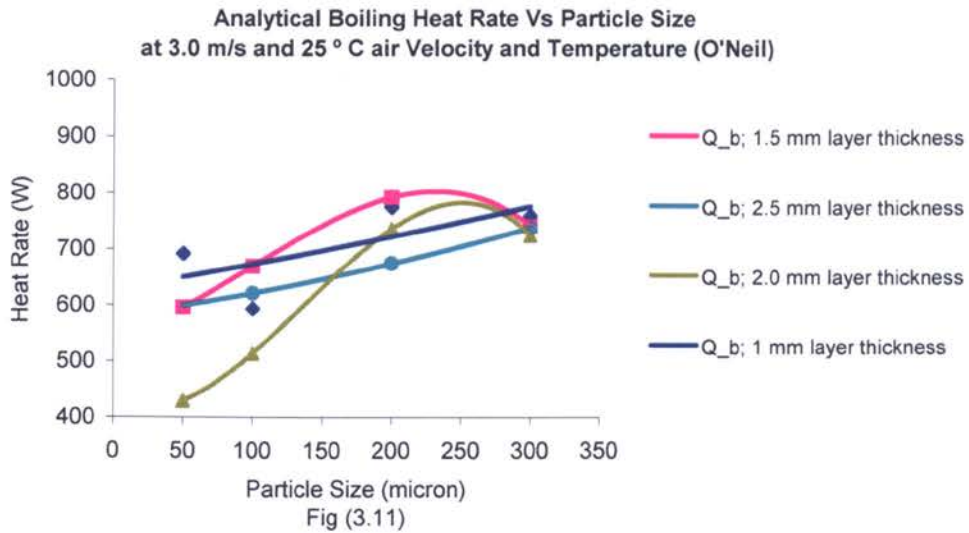


Analytical Boiling Heat Rate Vs Particle Size
at 2.0 m/s and 30 ° C air Velocity and Temperature (O'Neil)

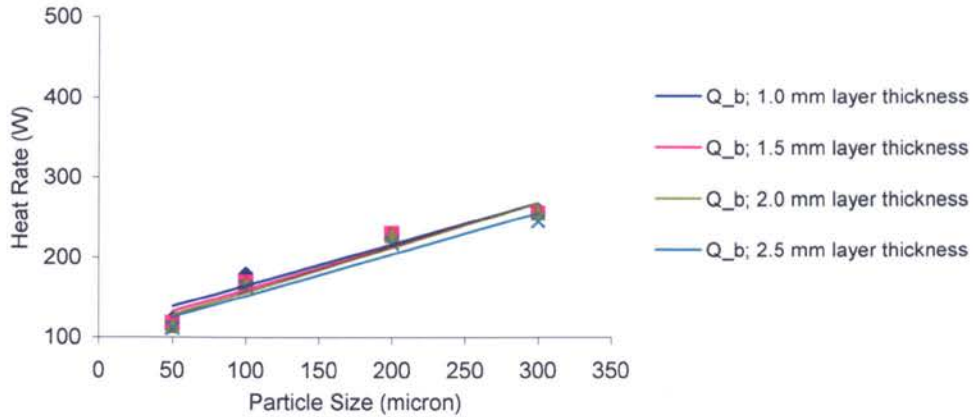


Analytical Boiling Heat Rate Vs Particle Size
at 2.0 m/s and 35 ° C air Velocity and Temperature (O'Neil)

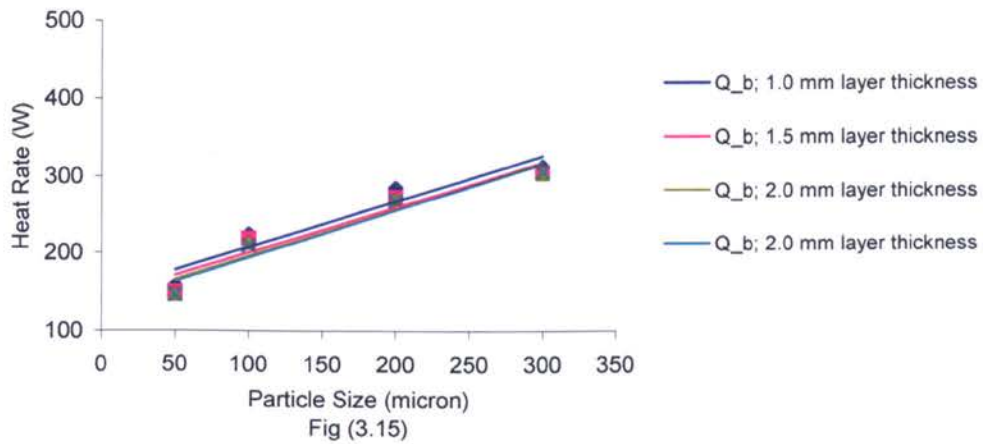




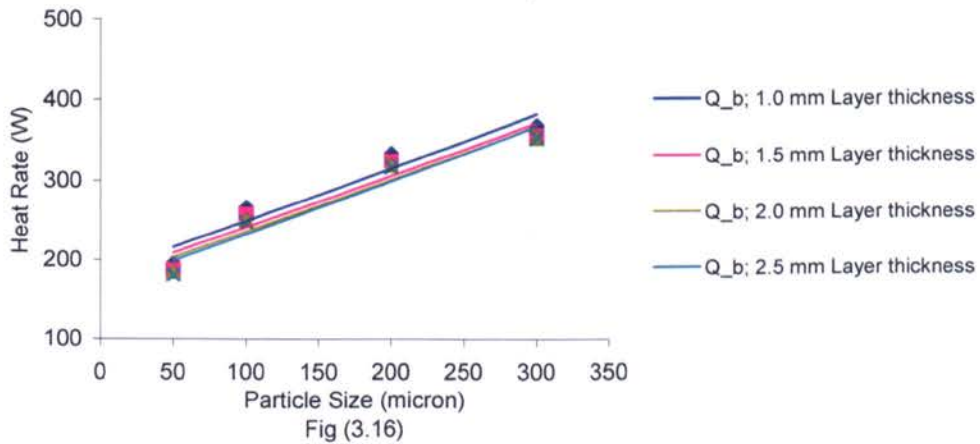
**Analytical Boiling Heat Rate Vs Particle Size
at 1.0 m/s and 25 ° C Air Velocity and Temperature
(Rao & Balkrishnan)**



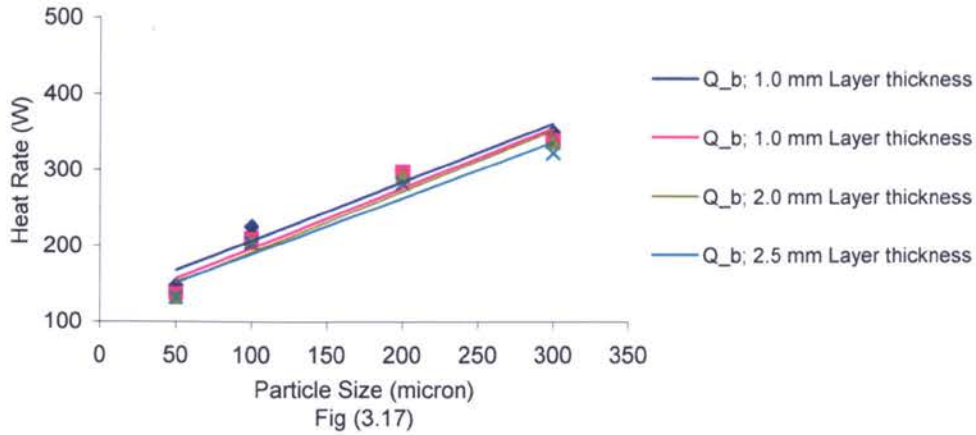
**Analytical Boiling Heat Rate Vs Particle Size
at 1.0 m/s and 30 ° C Air Velocity and Temperature
(Rao & Balkrishnan)**



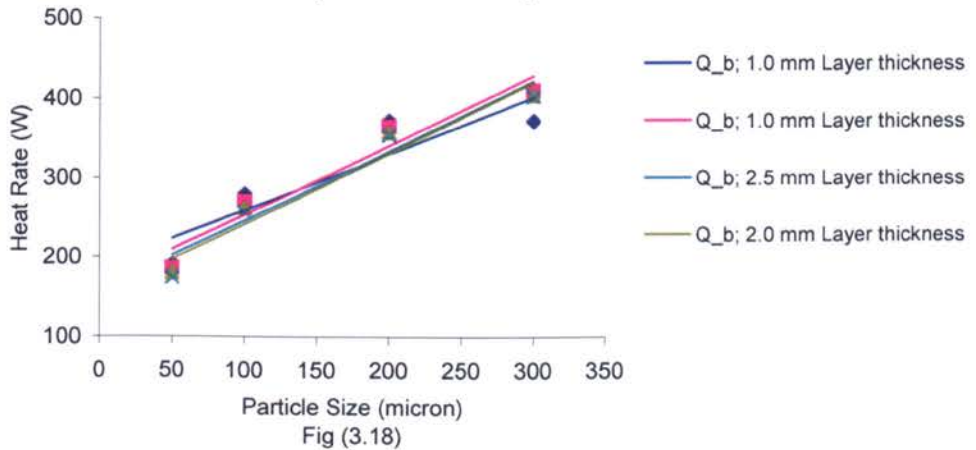
**Analytical Boiling Heat Rate Vs Particle Size
at 1.0 m/s and 35 ° C Air Velocity and Temperature
(Rao & Balkrishnan)**



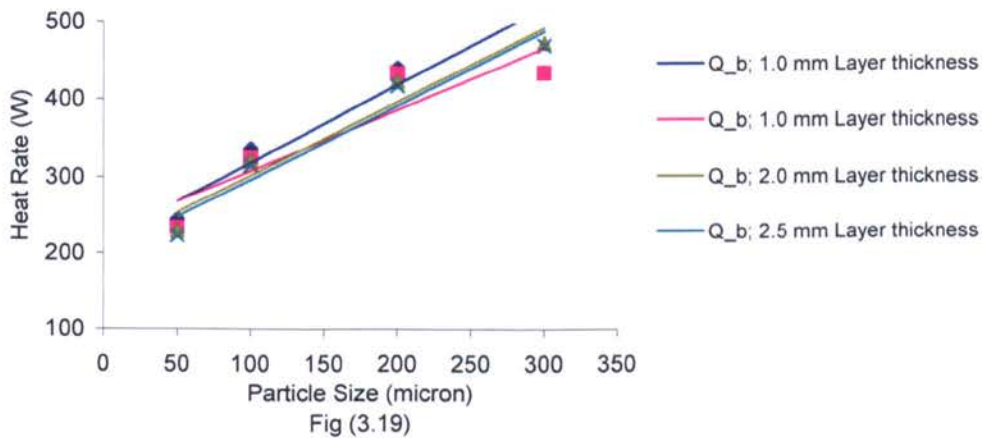
Analytical Boiling Heat Rate Vs Particle Size
at 2.0 m/s and 25 °C Air Velocity and Temperature
(Rao & Balkrishnan)

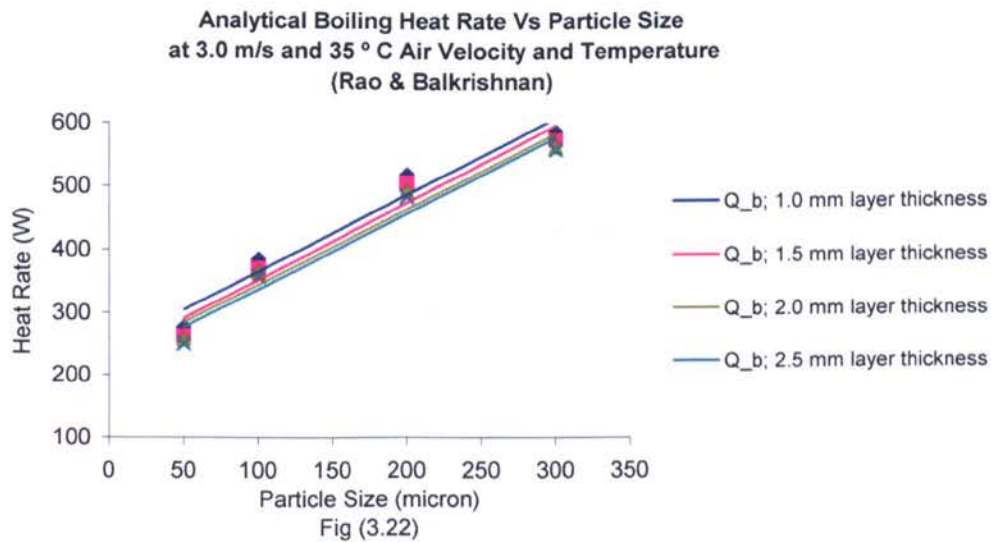
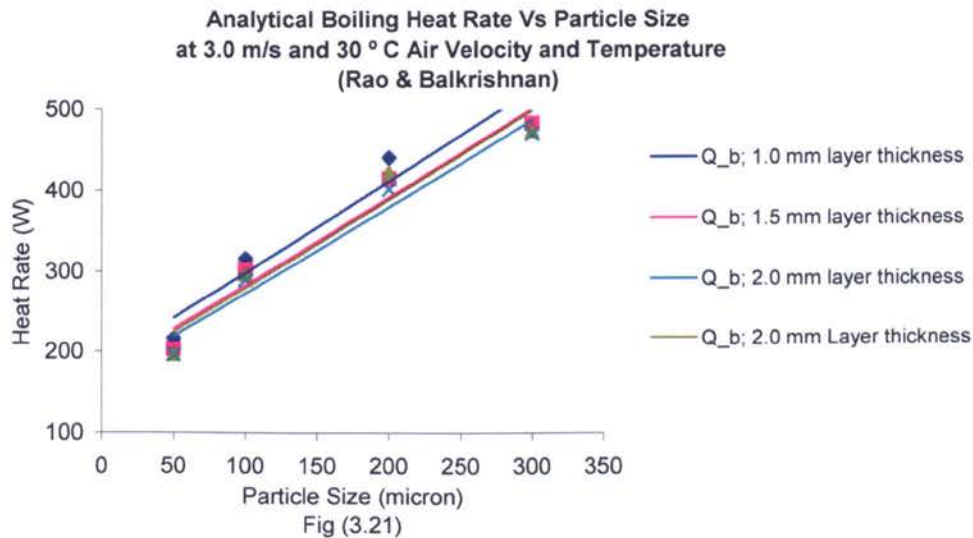
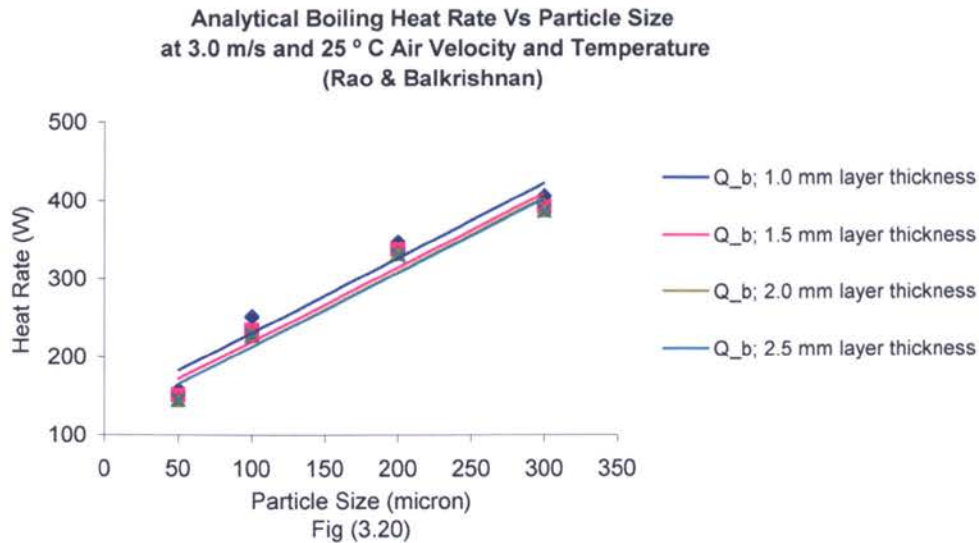


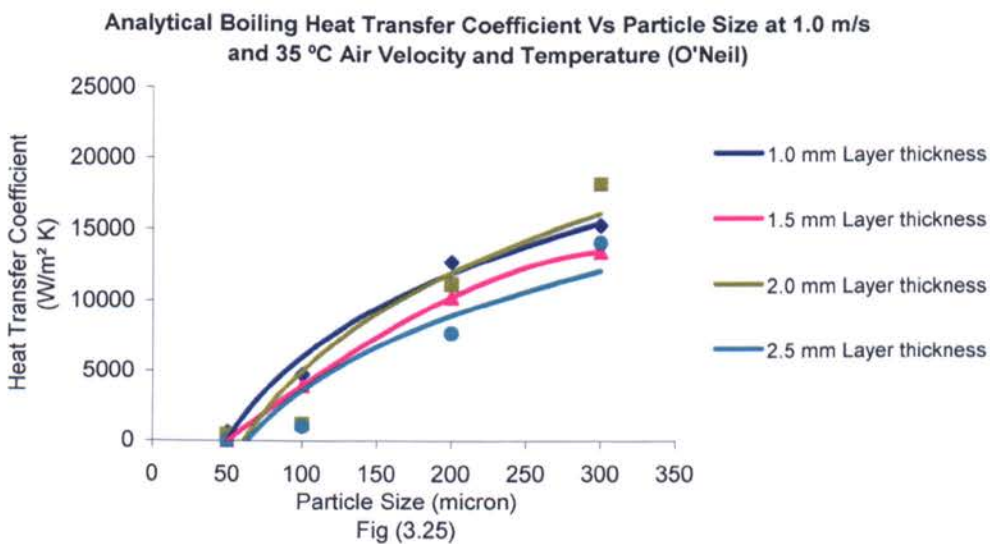
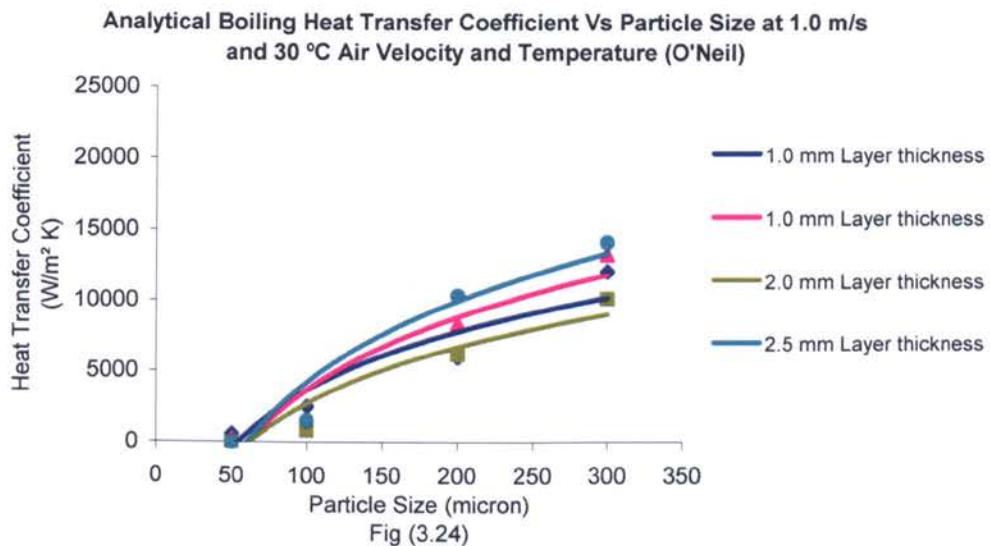
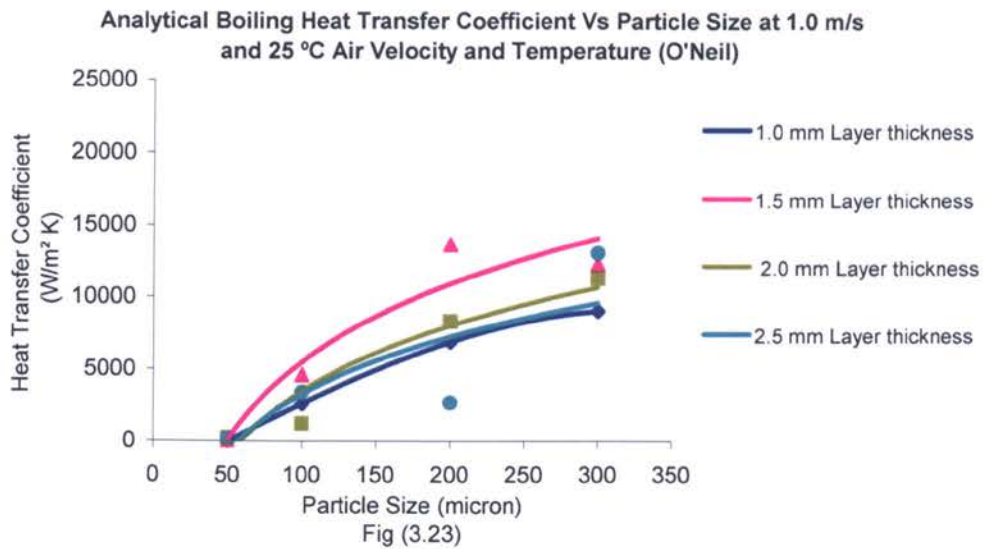
Analytical Boiling Heat Rate Vs Particle Size
at 2.0 m/s and 30 °C Air Velocity and Temperature
(Rao & Balkrishnan)

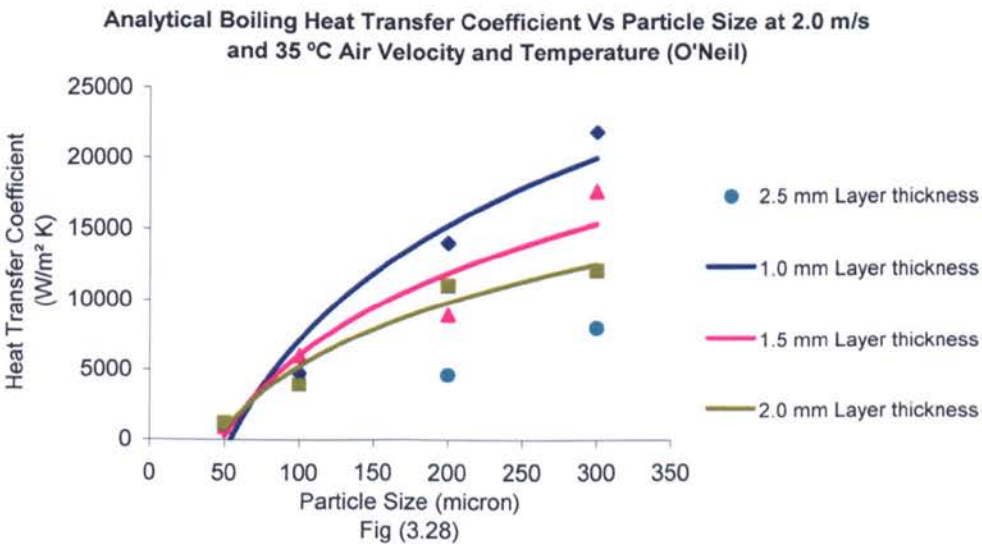
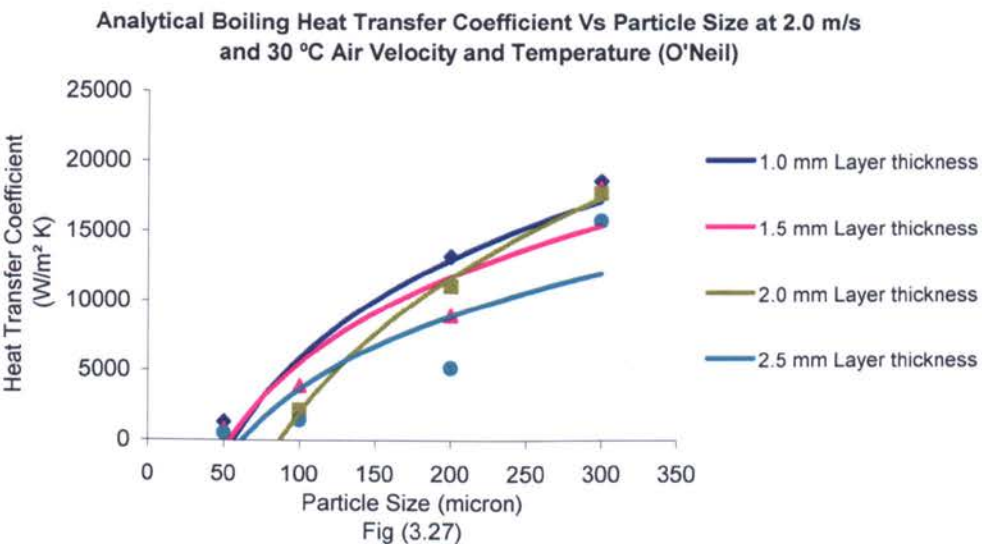
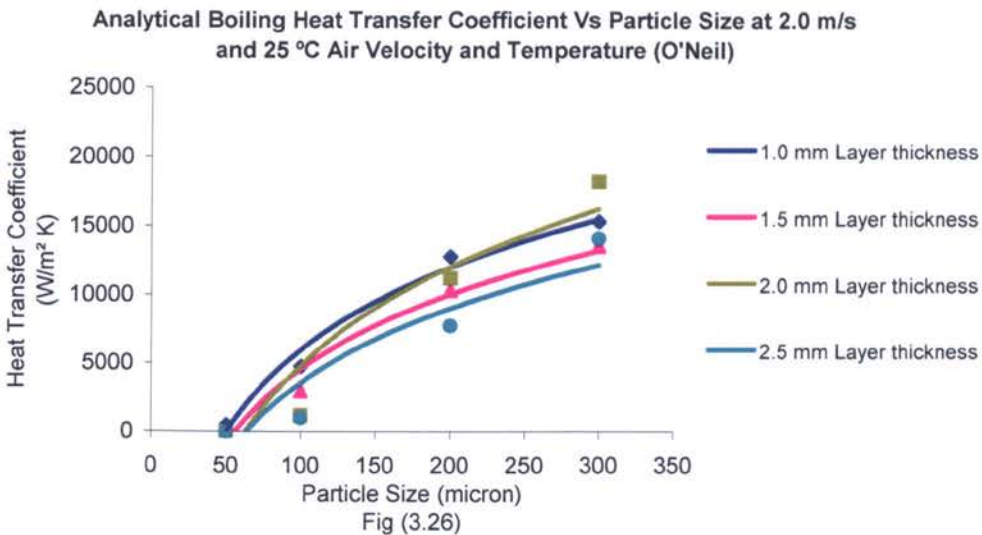


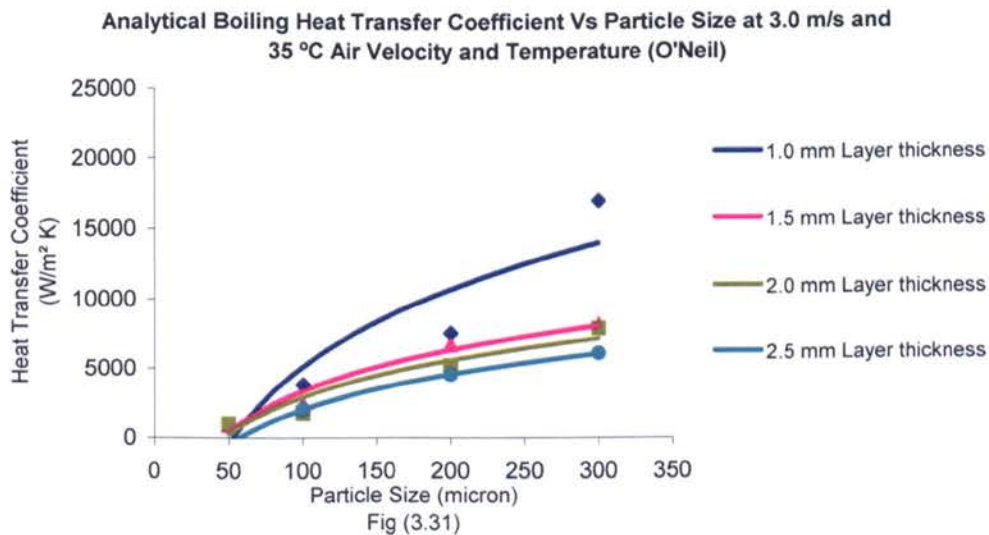
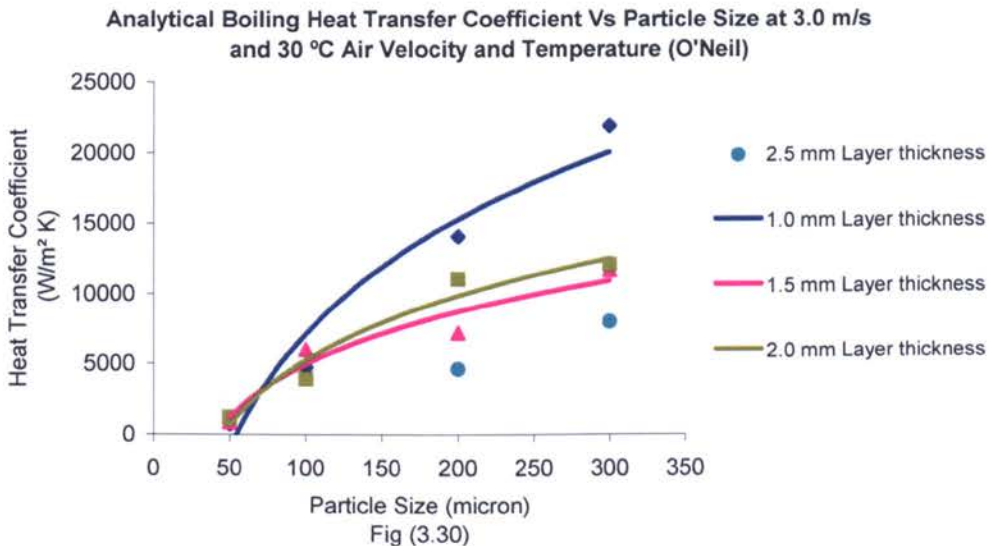
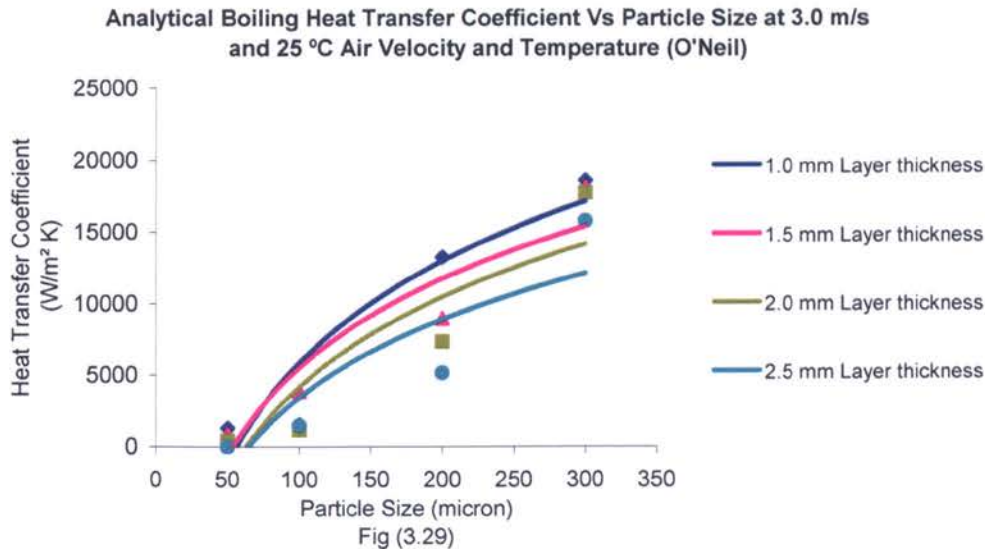
Analytical Boiling Heat Rate Vs Particle Size
at 2.0 m/s and 35 °C Air Velocity and Temperature
(Rao & Balkrishnan)











Analytical Boiling Heat Transfer Coefficient Vs Particle Size at 1.0 m/s & 25 °C Air Velocity and Temperature (Rao & Balkrishnan)

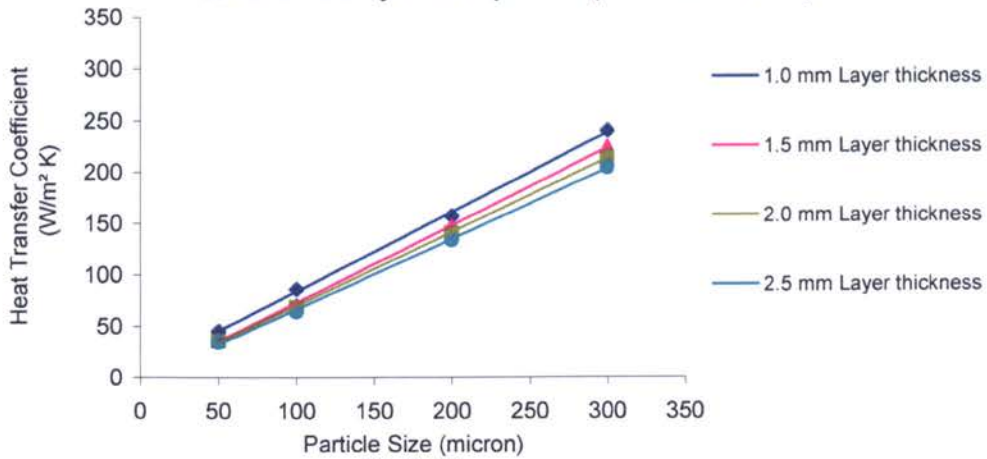


Fig (3.32)

Analytical Boiling Heat Transfer Coefficient Vs Particle Size at 1.0 m/s & 30 °C Air Velocity and Temperature (Rao & Balkrishnan)

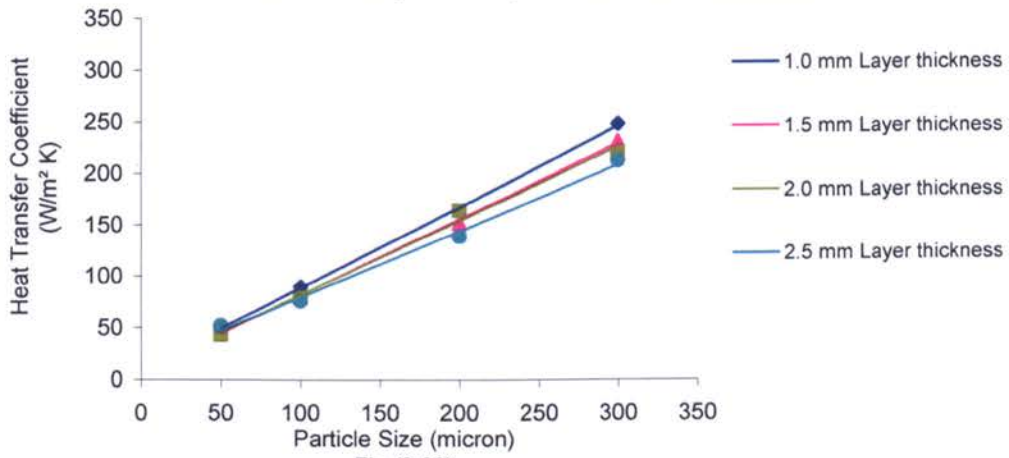


Fig (3.33)

Analytical Boiling Heat Transfer Coefficient Vs Particle Size at 1.0 m/s & 35 °C Air Velocity and Temperature (Rao & Balkrishnan)

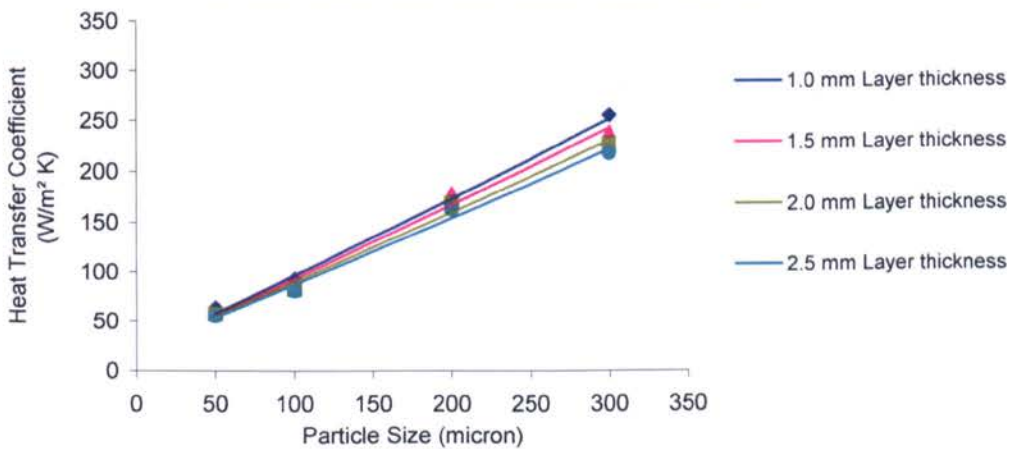
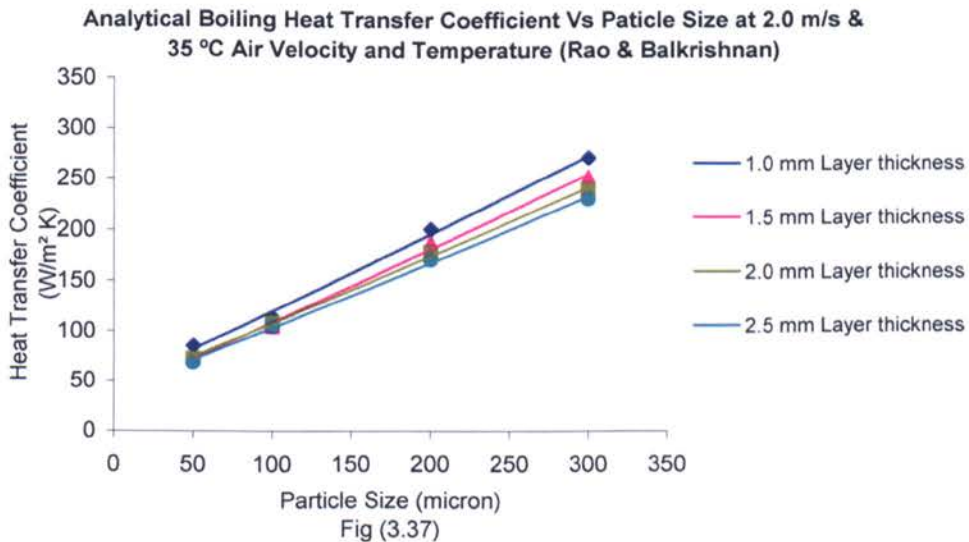
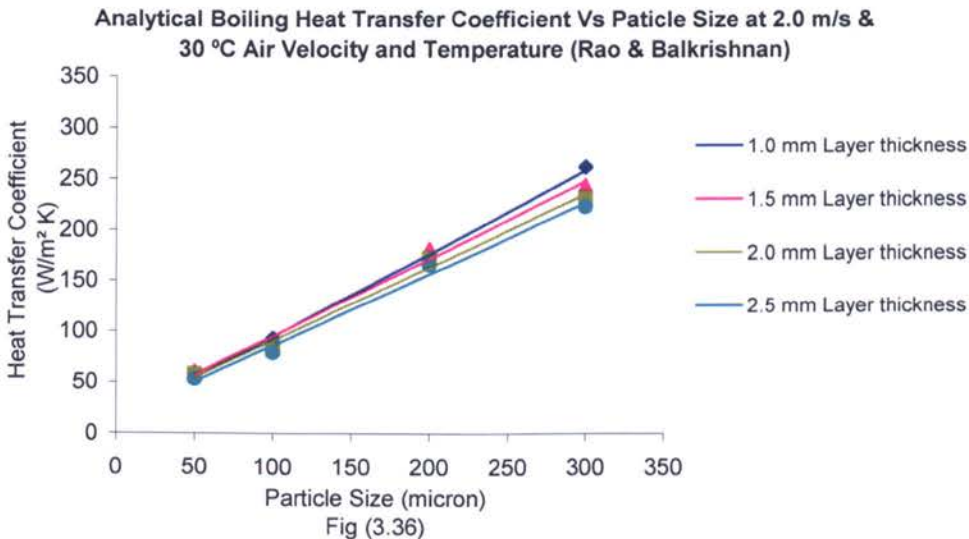
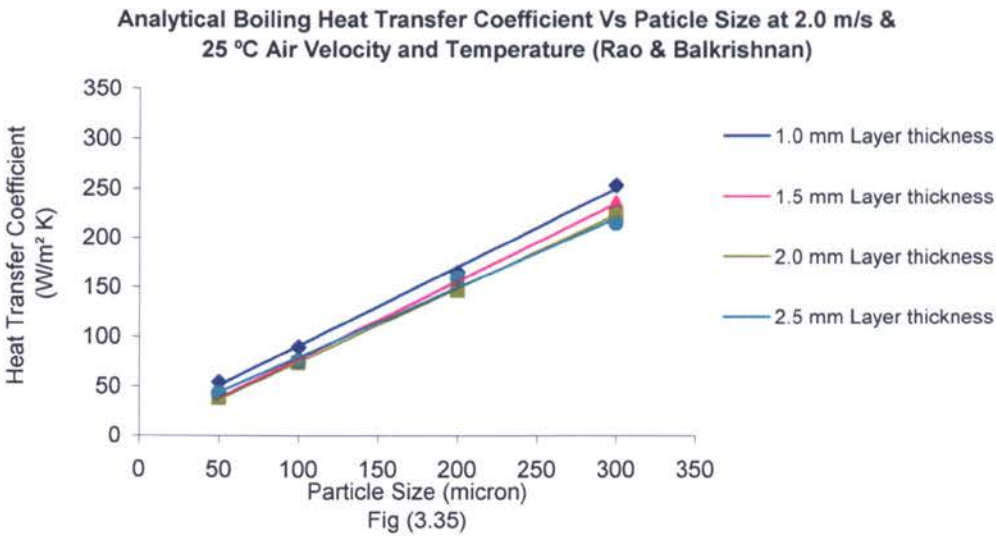
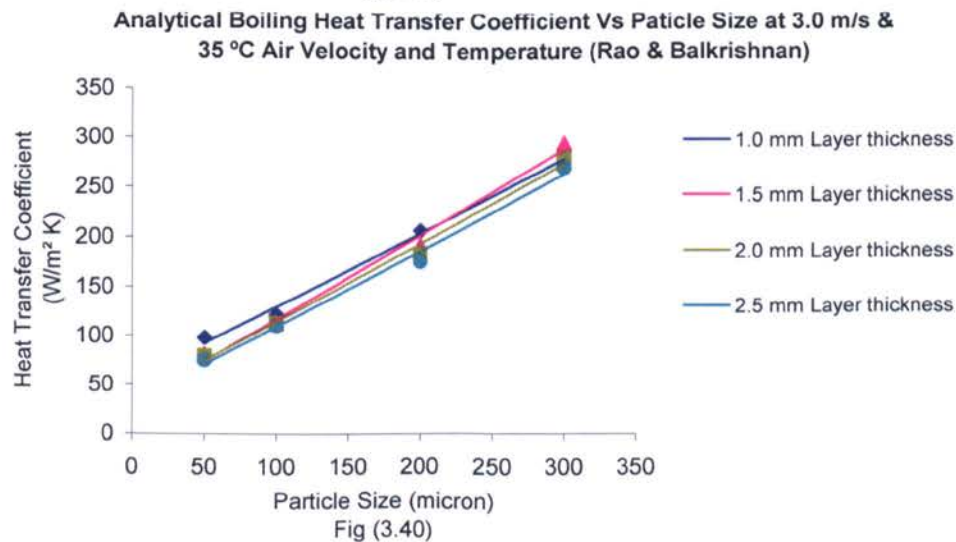
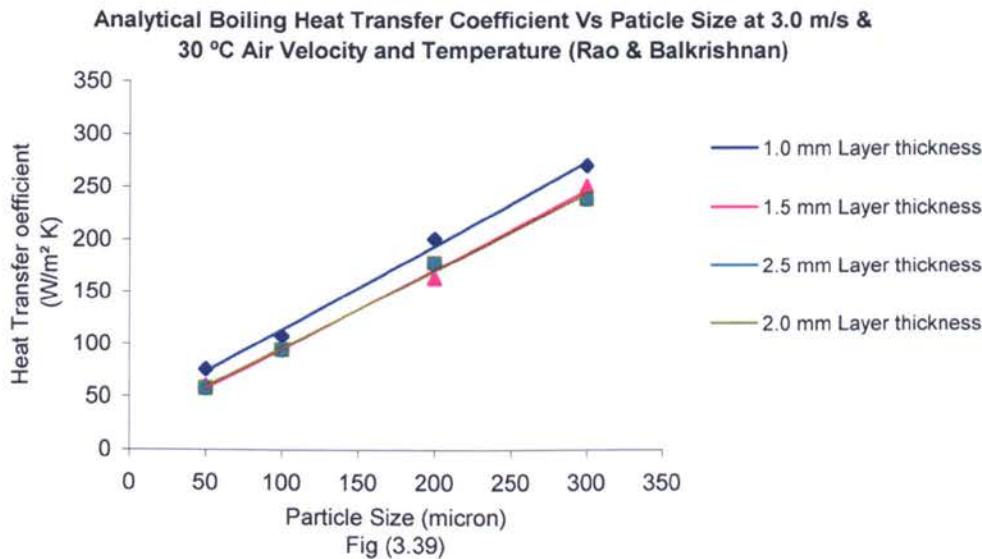
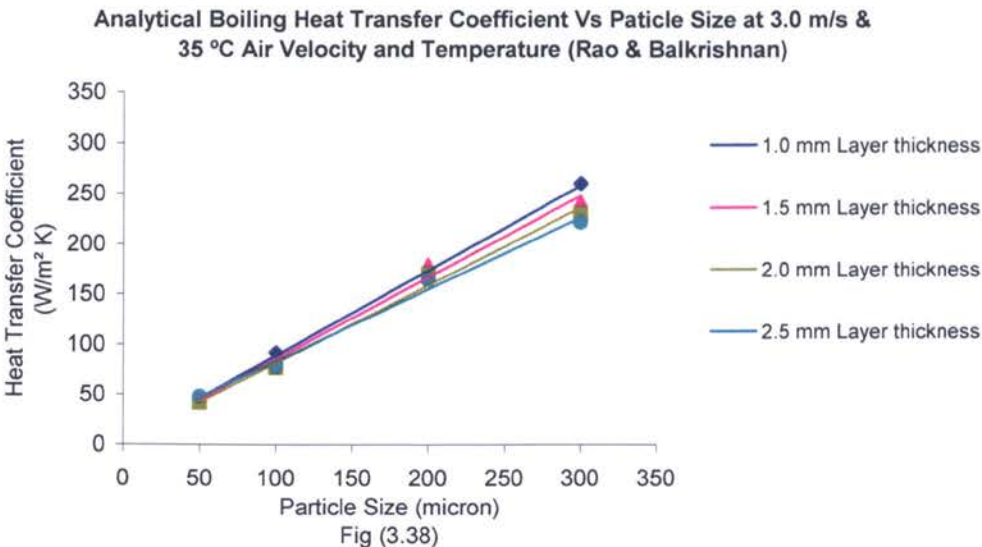


Fig (3.34)





Analytical Boiling Heat Rate Vs Layer Thickness at 1.0 m/s and 25 ° C Air Velocity and Temperature (O'Neil)

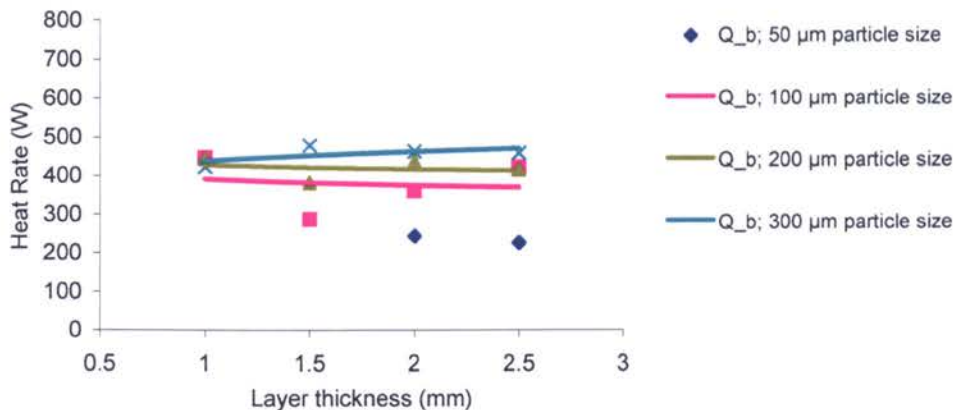


Fig (3.41)

Analytical Boiling Heat Rate Vs Layer Thickness at 1.0 m/s and 30 ° C Air Velocity and Temperature (O'Neil)

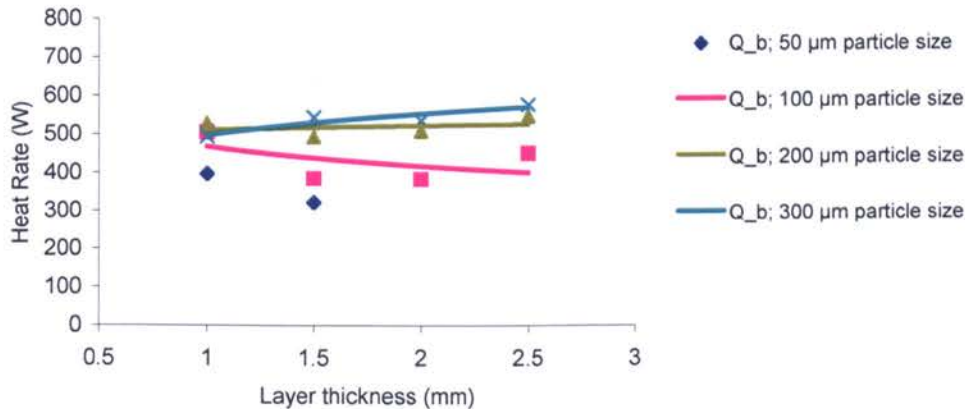


Fig (3.42)

Analytical Boiling Heat Rate Vs Layer Thickness at 1.0 m/s and 35 ° C Air Velocity and Temperature (O'Neil)

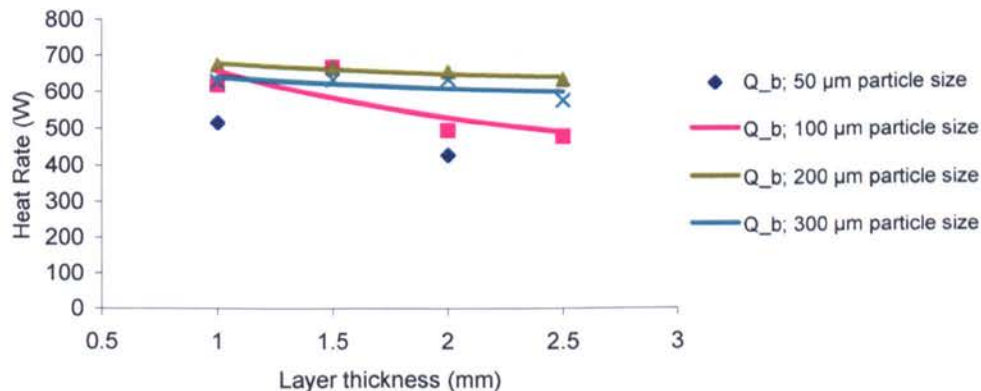


Fig (3.43)

Analytical Boiling Heat Rate Vs Layer Thickness at 2.0 m/s and 25 ° C Air Velocity and Temperature (O'Neil)

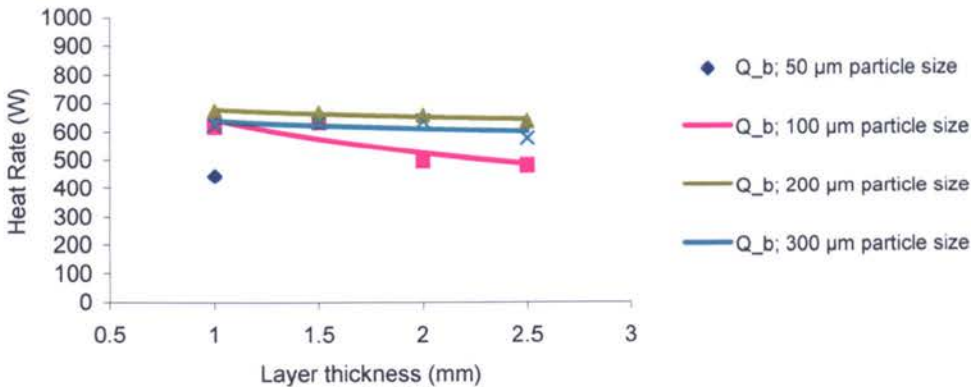


Fig (3.44)

Analytical Boiling Heat Rate Vs Layer Thickness at 2.0 m/s and 30 ° C Air Velocity and Temperature (O'Neil)

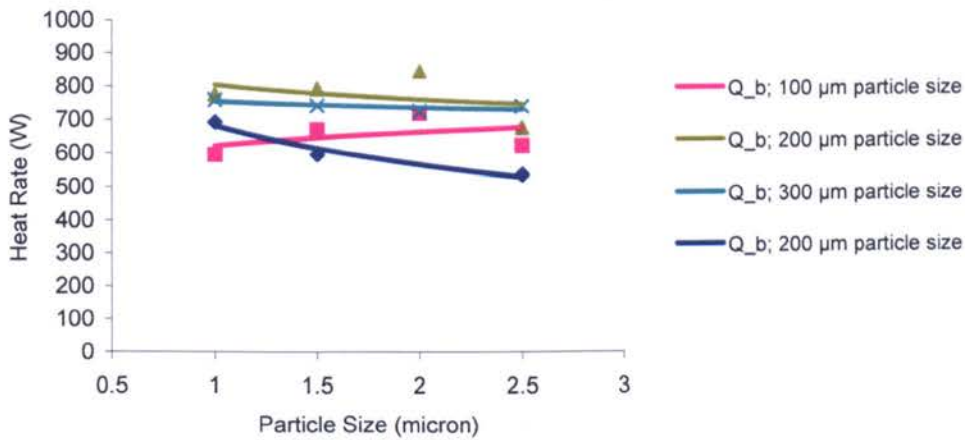


Fig (3.45)

Analytical Boiling Heat Rate Vs Layer Thickness at 2.0 m/s and 35 ° C Air Velocity and Temperature (O'Neil)

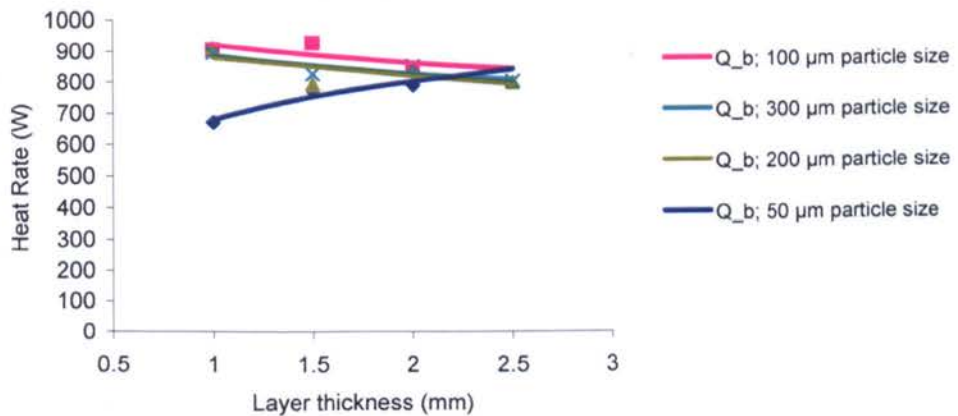
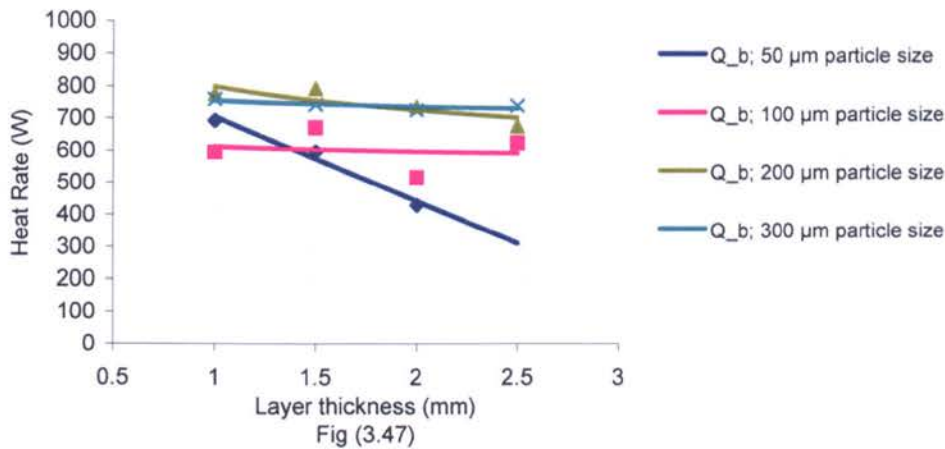
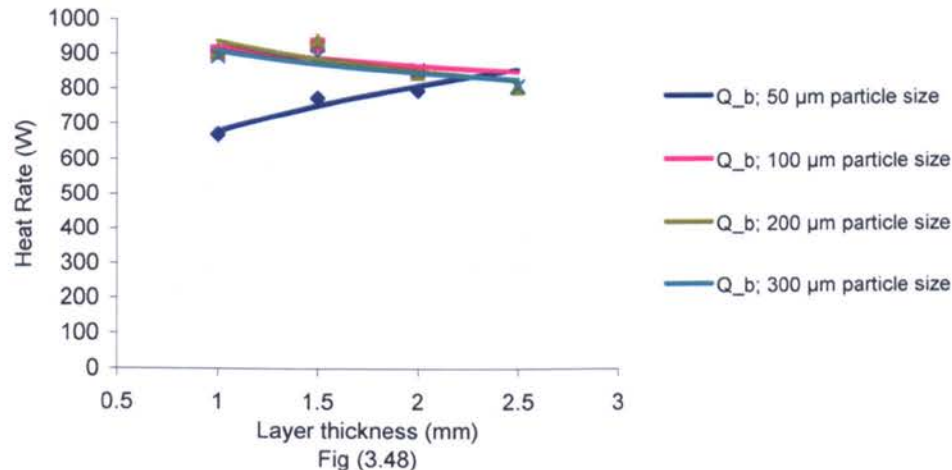


Fig (3.46)

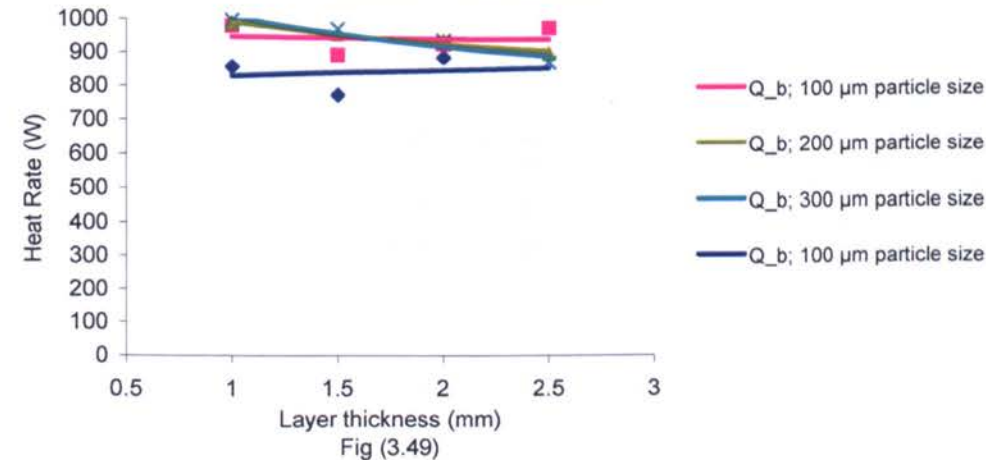
Analytical Boiling Heat Rate Vs Layer Thickness at 3.0 m/s and 25 ° C Air Velocity and Temperature (O'Neil)



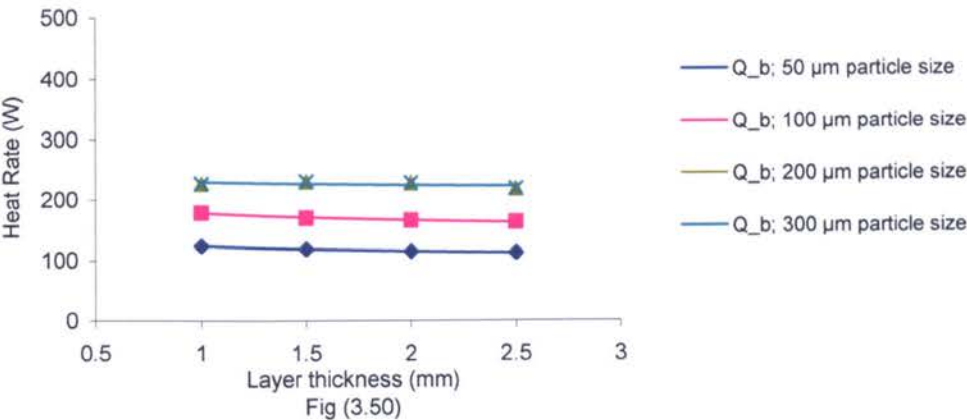
Analytical Boiling Heat Rate Vs Layer Thickness at 3.0 m/s and 30 ° C Air Velocity and Temperature (O'Neil)



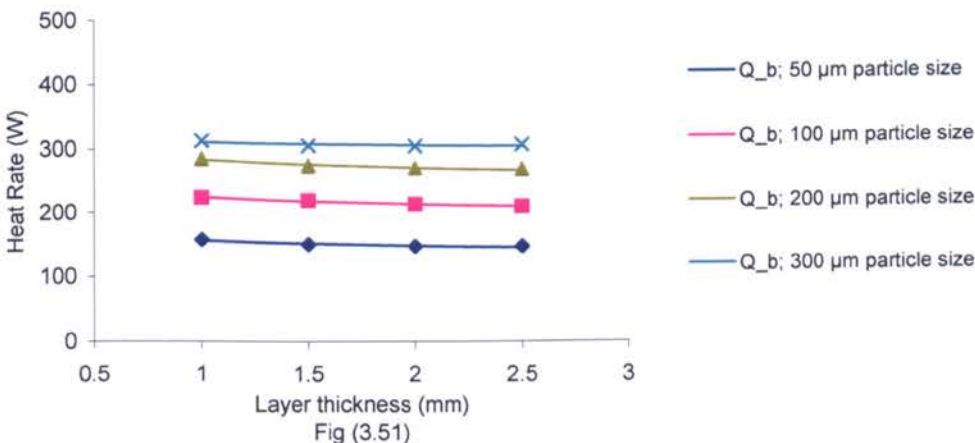
Analytical Boiling Heat Rate Vs Layer Thickness at 3.0 m/s and 35 ° C Air Velocity and Temperature (O'Neil)



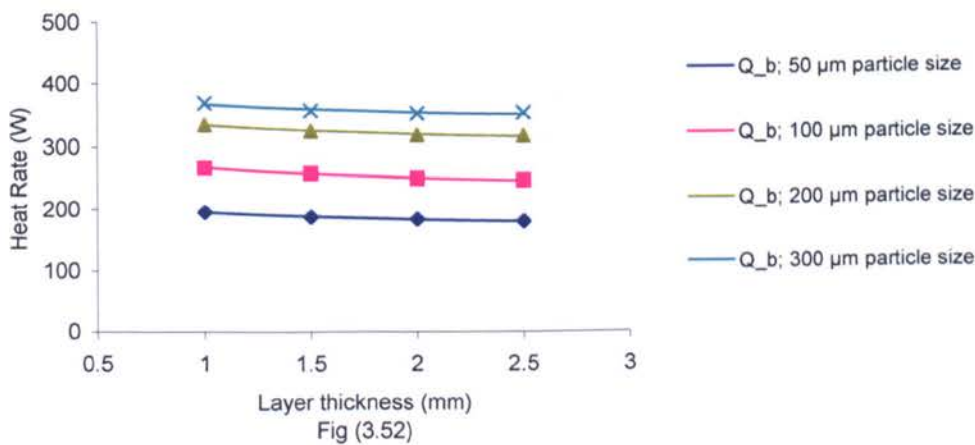
Analytical Boiling Heat Rate Vs Layer Thickness at 1.0 m/s and 25 ° C Air Velocity and Temperature (Rao & Balkrishnan)



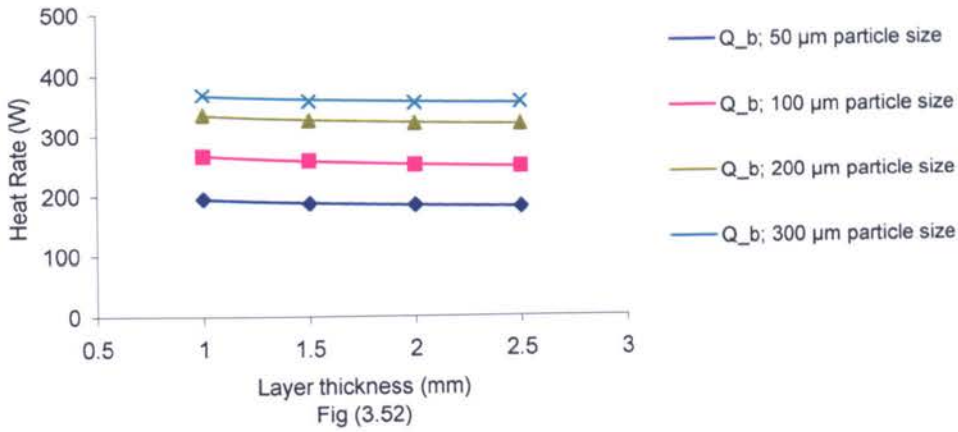
Analytical Boiling Heat Rate Vs Layer Thickness at 1.0 m/s and 30 ° C Air Velocity and Temperature (Rao & Balkrishnan)



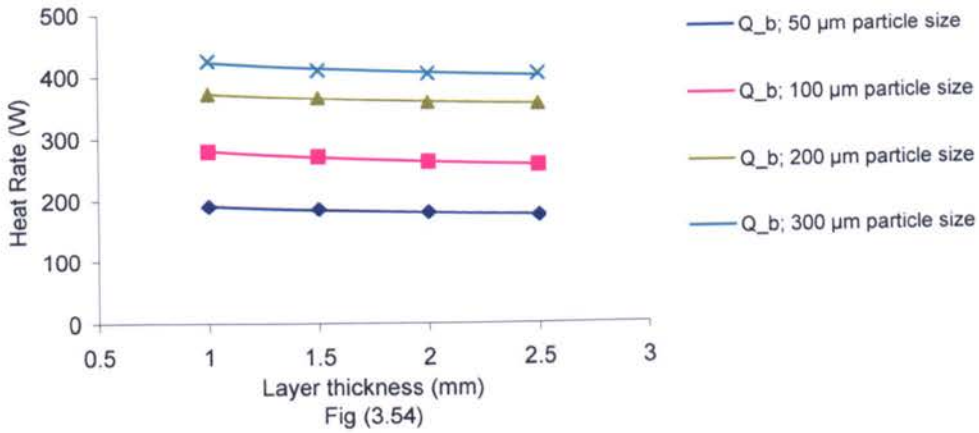
Analytical Boiling Heat Rate Vs Layer Thickness at 1.0 m/s and 35 ° C Air Velocity and Temperature (Rao & Balkrishnan)



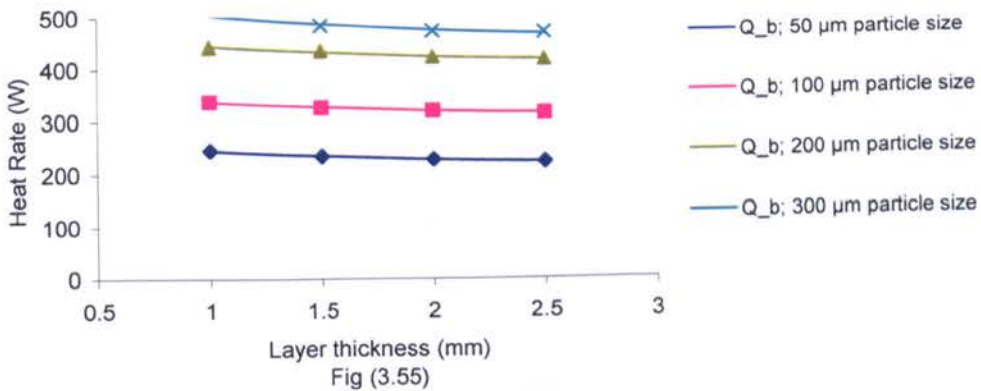
Analytical Boiling Heat Rate Vs Layer Thickness at 1.0 m/s and 35 °C Air Velocity and Temperature (Rao & Balkrishnan)



Analytical Boiling Heat Rate Vs Layer Thickness at 2.0 m/s and 30 °C Air Velocity and Temperature (Rao & Balkrishnan)



Analytical Boiling Heat Rate Vs Layer Thickness at 2.0 m/s and 35 °C Air Velocity and Temperature (Rao & Balkrishnan)



Analytical Boiling Heat Rate Vs Layer Thickness at 3.0 m/s and 25 ° C Air Velocity and Temperature (Rao & Balkrishnan)

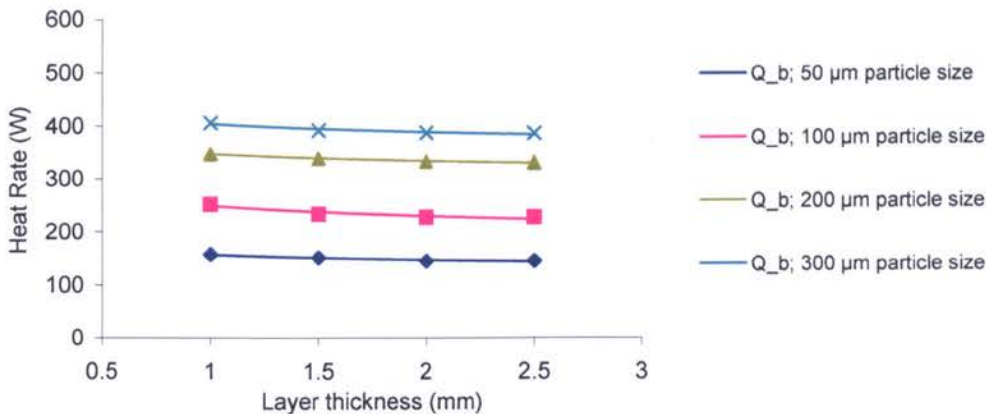


Fig (3.56)

Analytical Boiling Heat Rate Vs Layer Thickness at 3.0 m/s and 30 ° C Air Velocity and Temperature (Rao & Balkrishnan)

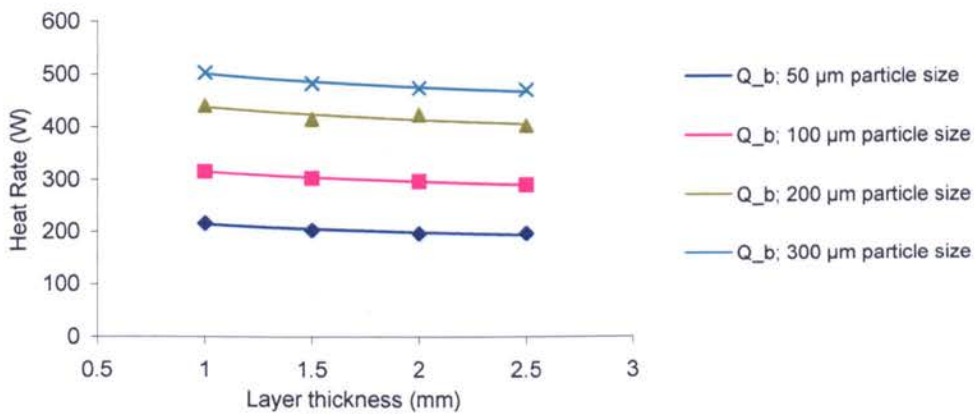


Fig (3.57)

Analytical Boiling Heat Rate Vs Layer Thickness at 3.0 m/s and 35 ° C Air Velocity and Temperature (Rao & Balkrishnan)

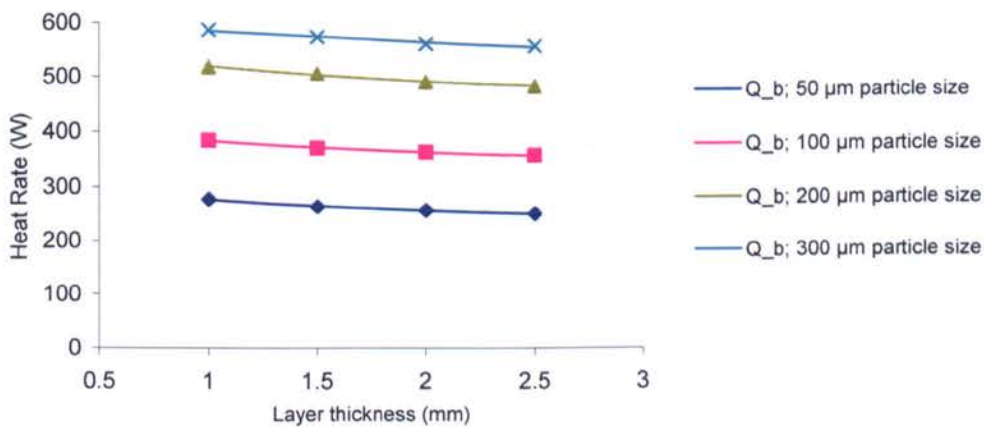
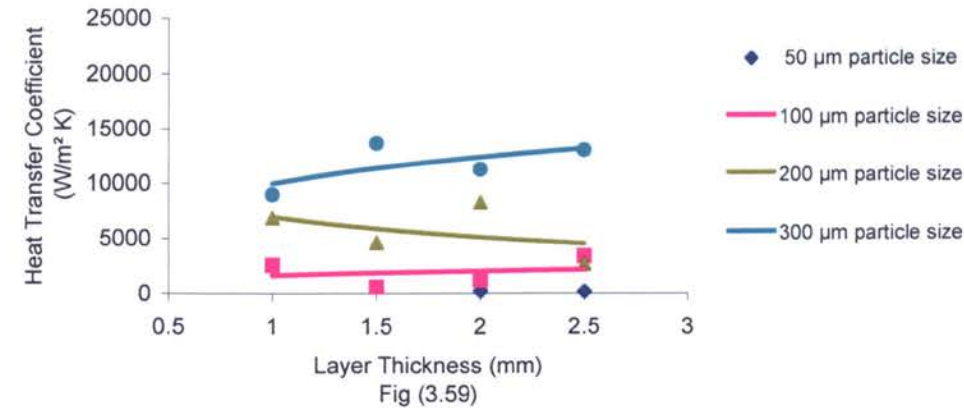
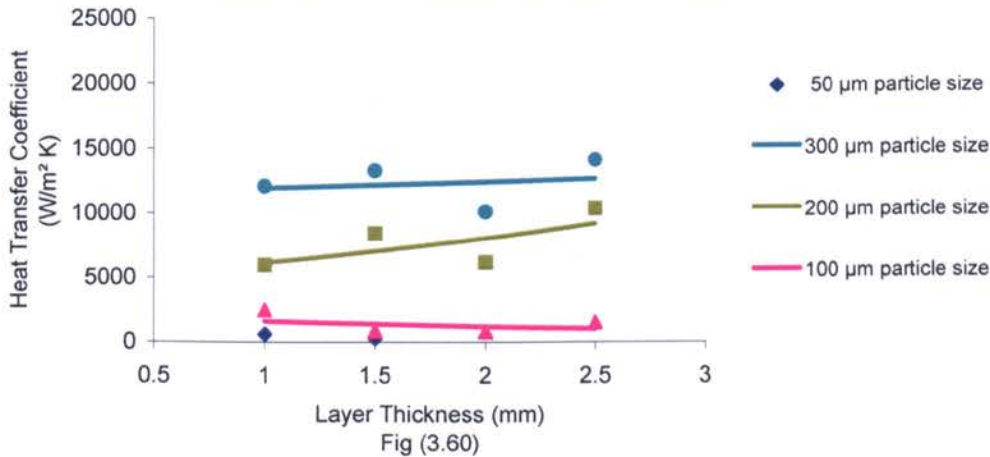


Fig (3.58)

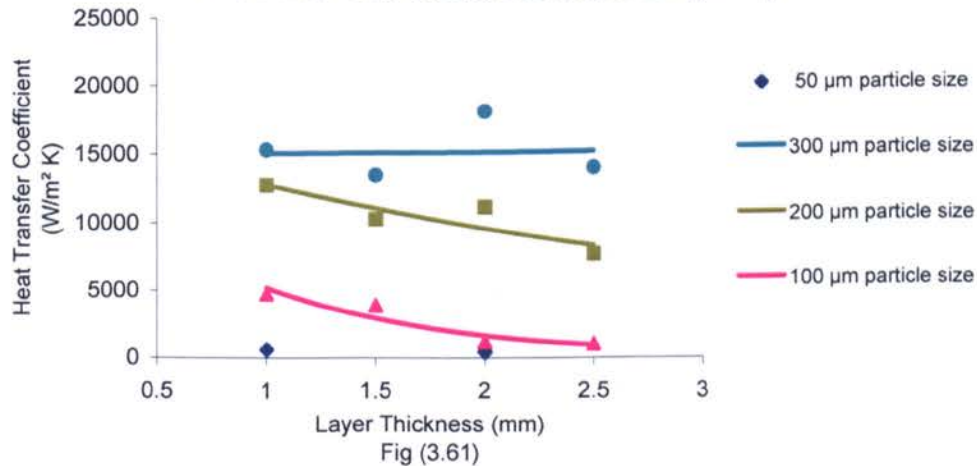
Analytical Boiling Heat Transfer Coefficient Vs Layer Thickness at 1.0 m/s and 25 °C Air Velocity and Temperature (O'Neil)

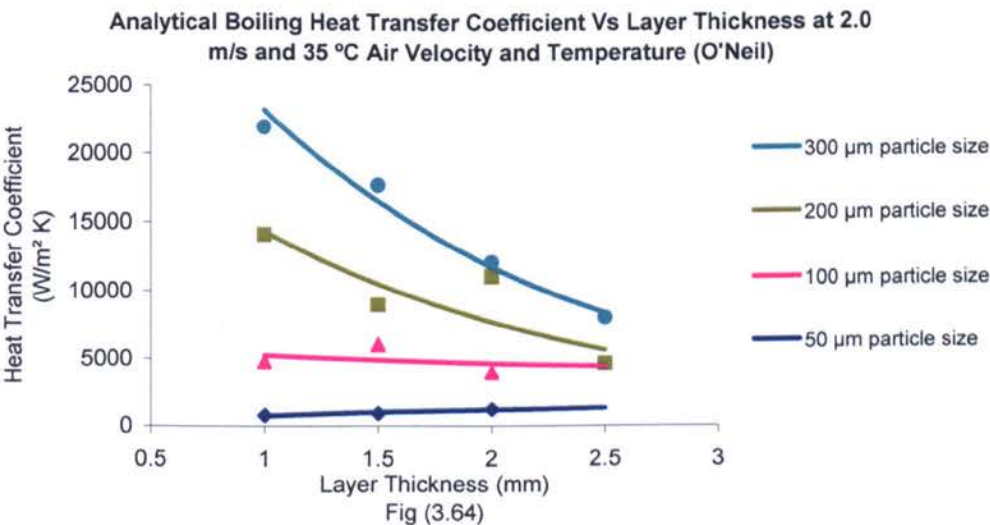
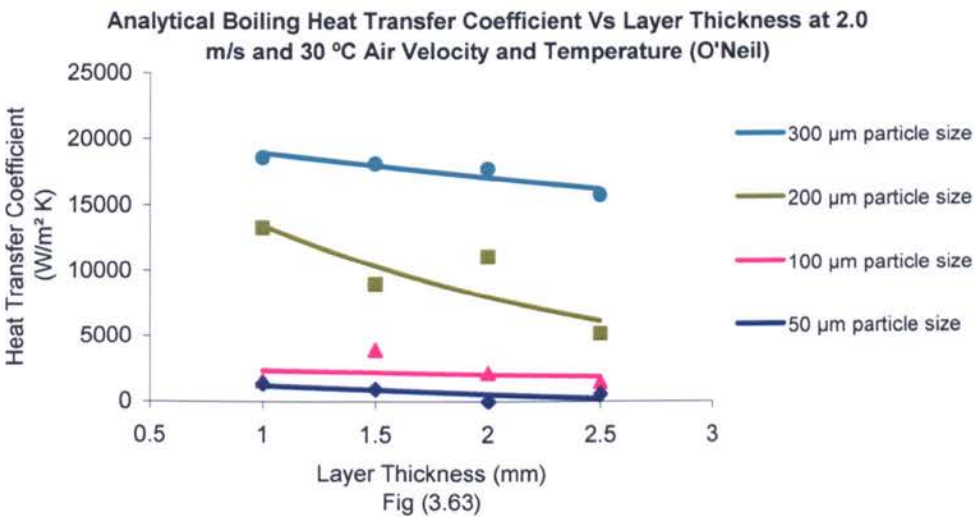
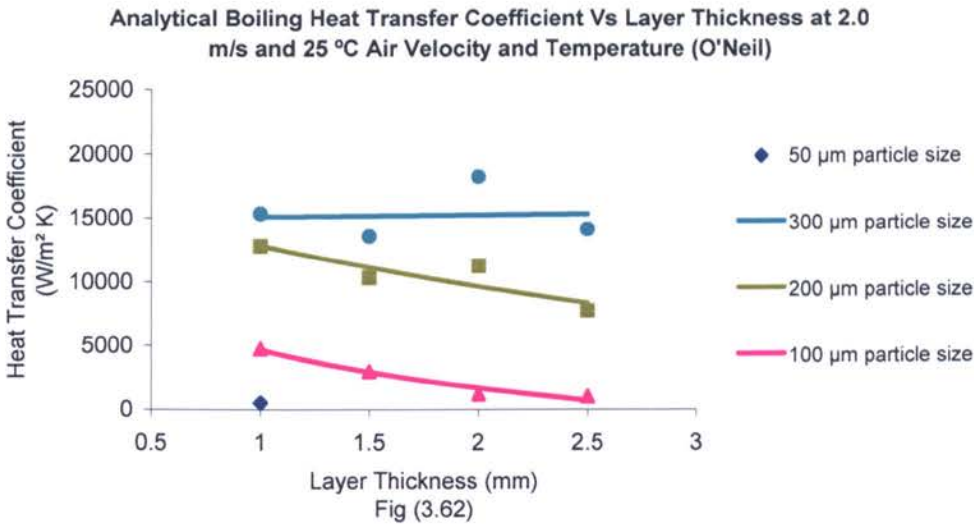


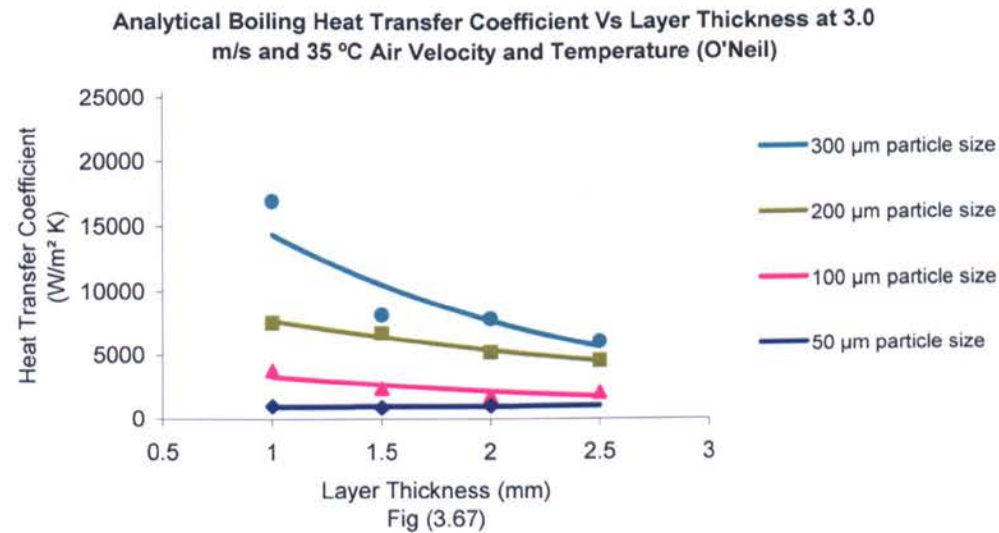
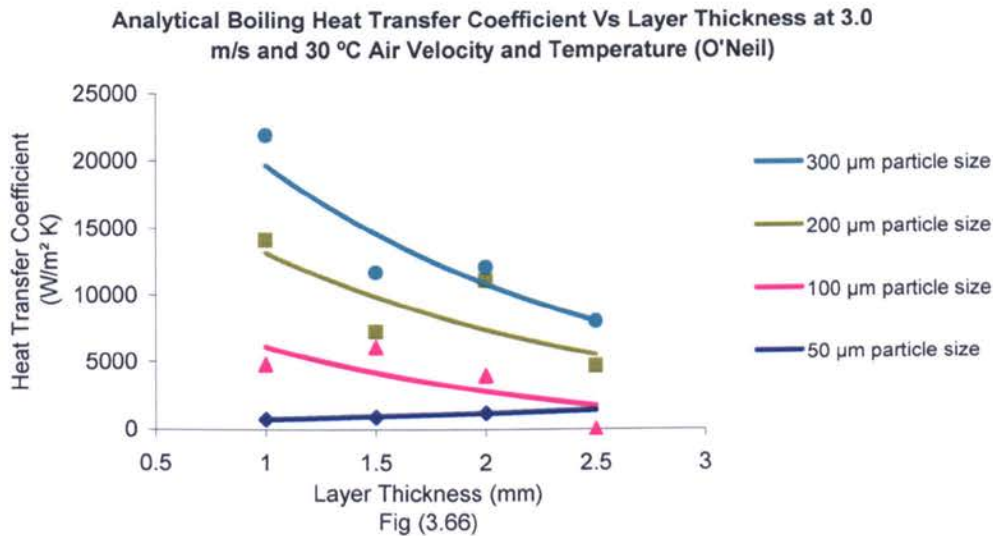
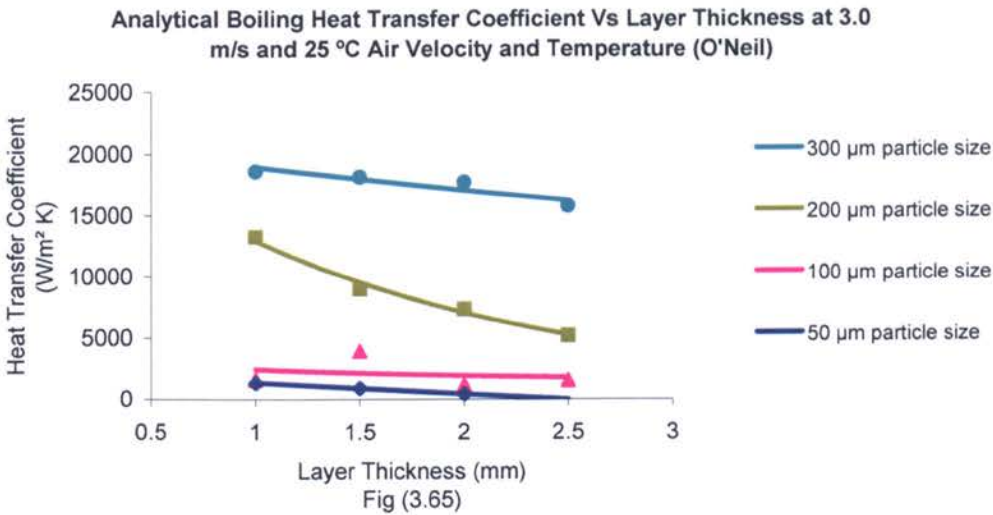
Analytical Boiling Heat Transfer Coefficient Vs Layer Thickness at 1.0 m/s and 30 °C Air Velocity and Temperature (O'Neil)

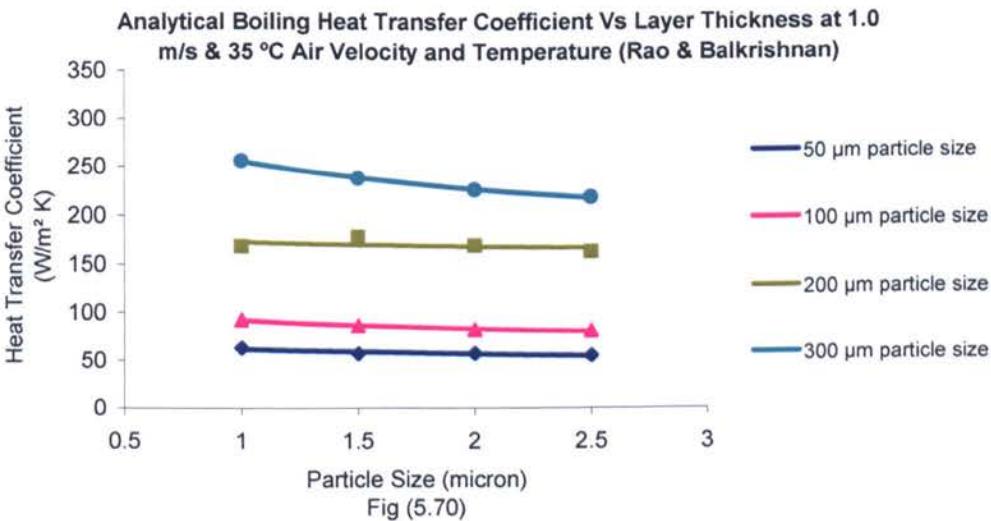
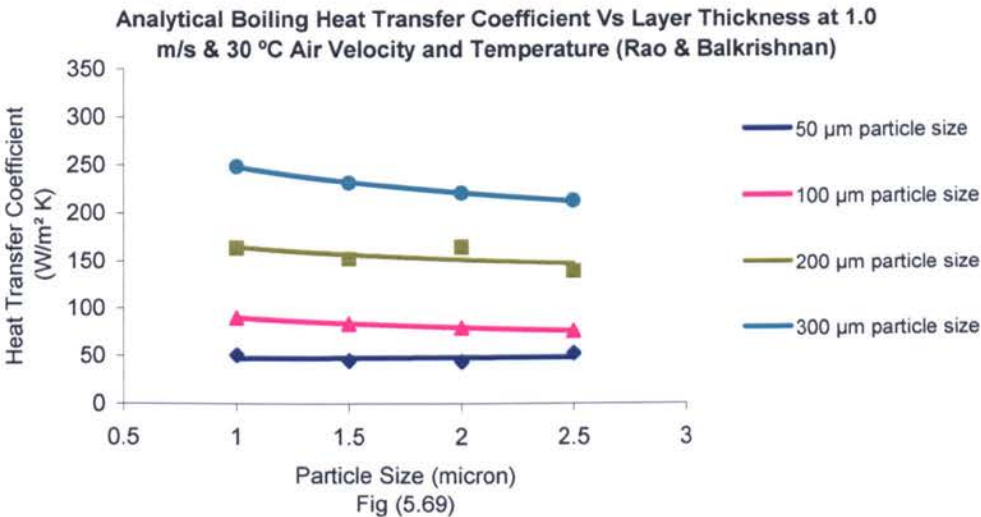
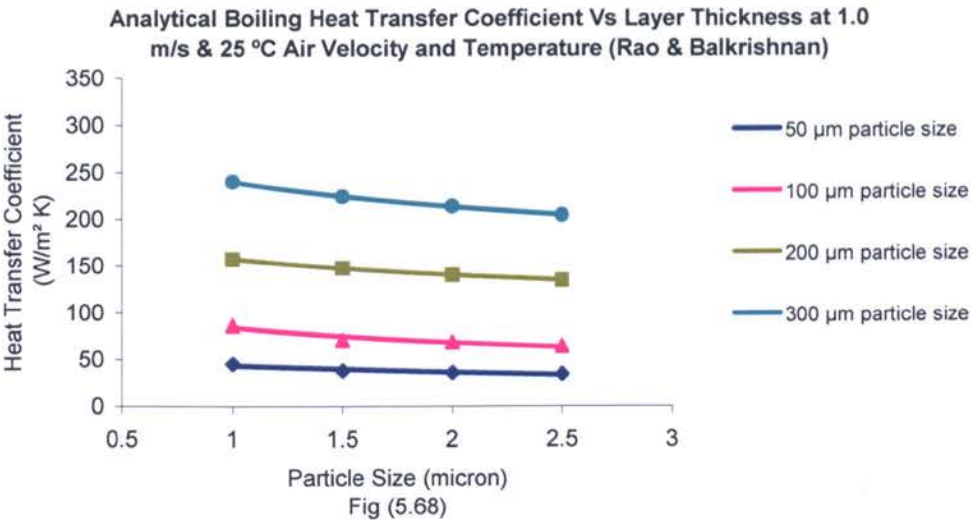


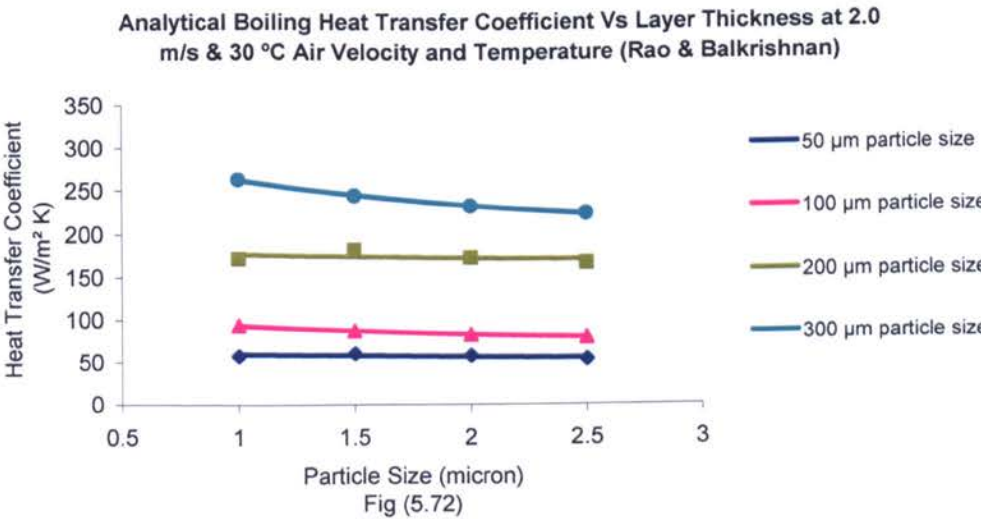
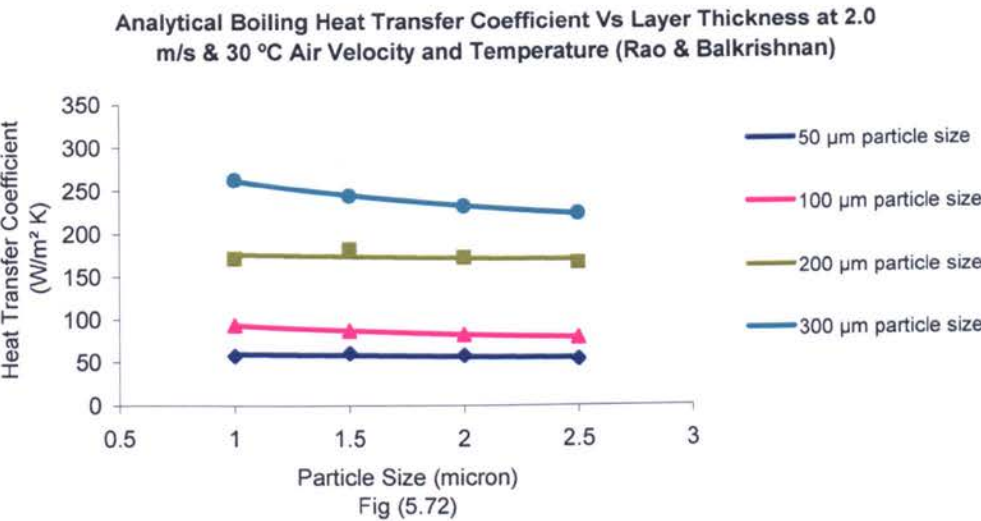
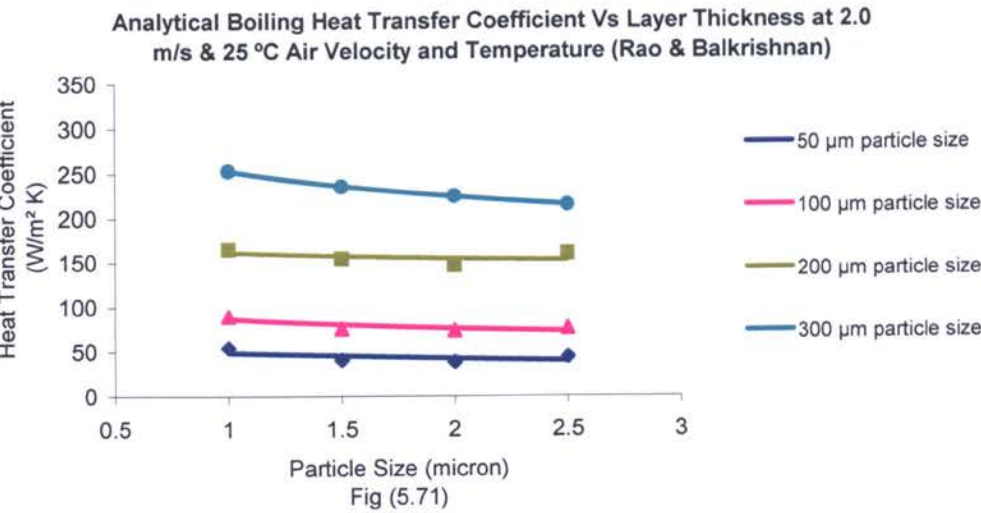
Analytical Boiling Heat Transfer Coefficient Vs Layer Thickness at 1.0 m/s and 35 °C Air Velocity and Temperature (O'Neil)

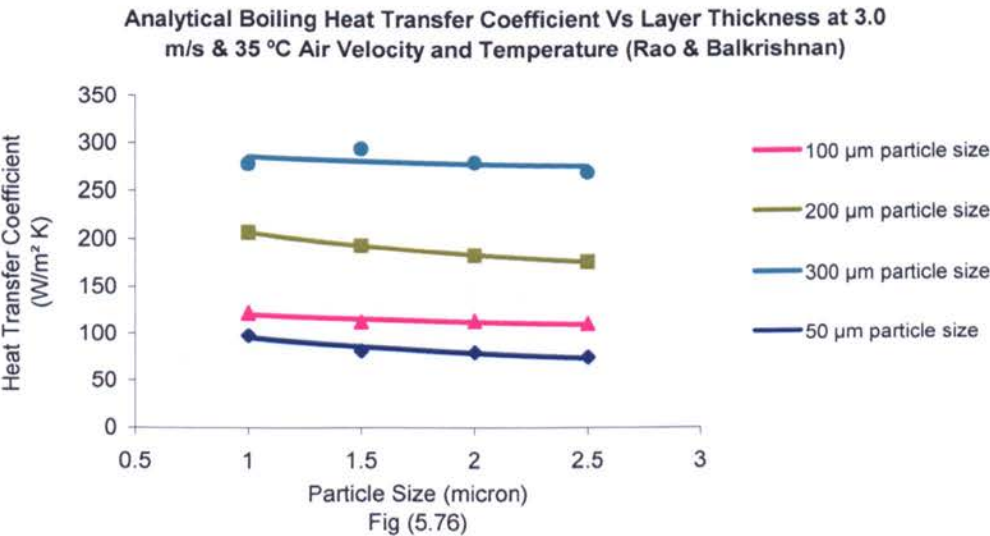
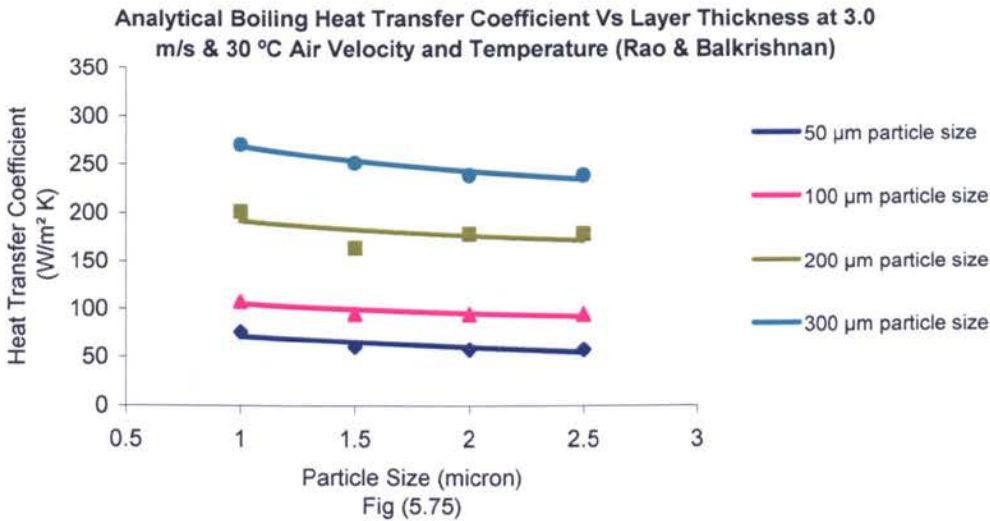
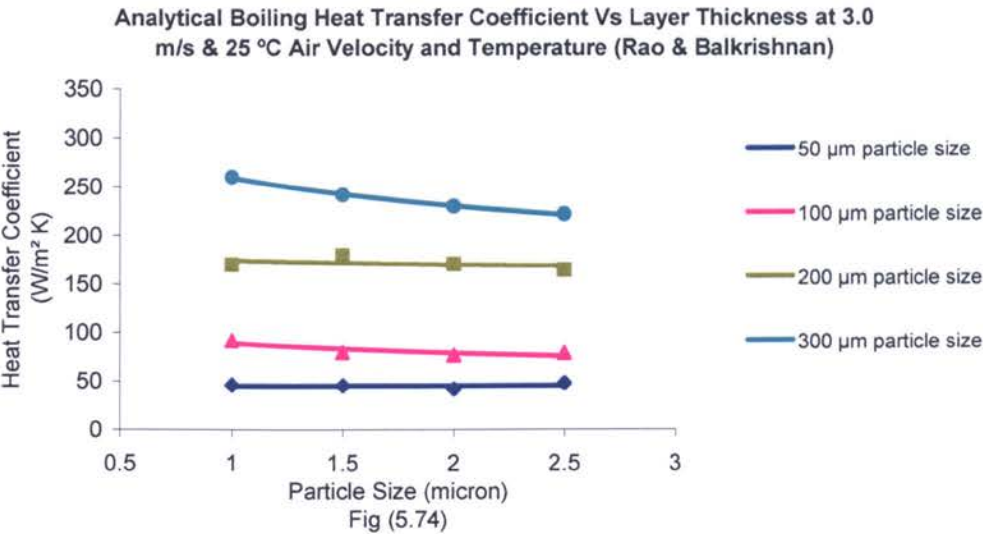


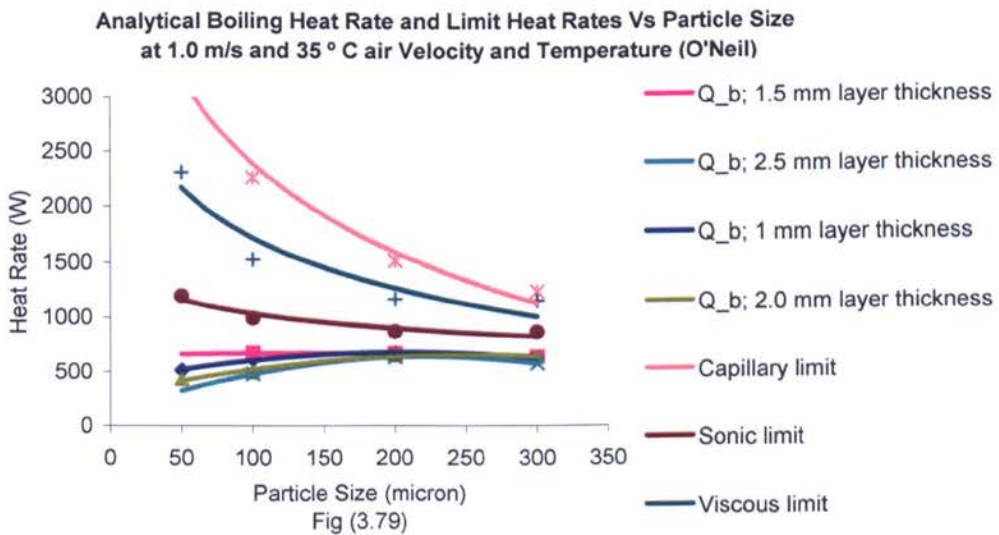
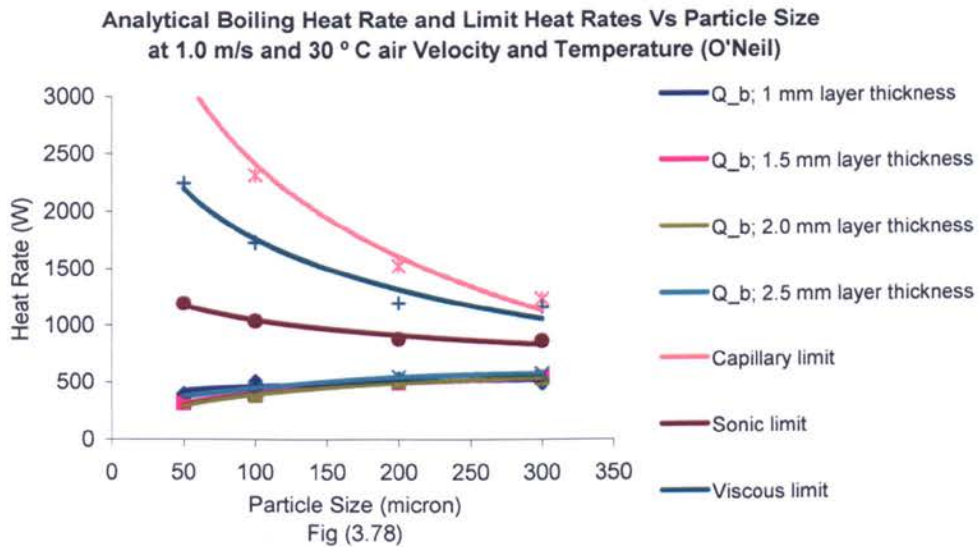
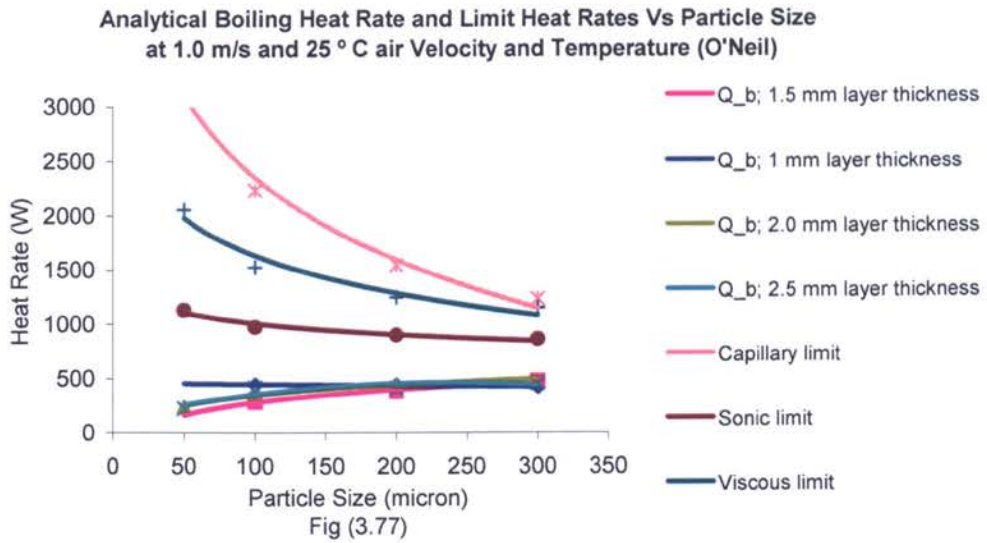












Chapter Four

Experimental Work

4.1 Introduction:

In this research four different particle sizes were tested; 50 μm , 100 μm , 200 μm and 300 μm . For each particle size four different layer thicknesses were tested; 1mm, 1.5 mm, 2 mm and 2.5mm, i.e. 16 different evaporators were tested in total. The porosity¹ was maintained at 48% in all tested evaporators. Each evaporator was tested for 3 different air velocities; 1 m/s, 2 m/s and 3 m/s; and for each air velocity the air temperature at the evaporator inlet was varied 3 times; 25 °C, 30 °C & 35 °C. This means a total of 144 tests were conducted for the whole number of evaporators. Some of these tests were conducted more than once to reach good level of confidence in the results obtained. Boiling heat transfer coefficients and heat fluxes as high as 6890 W/m² K and 7573.84 W/m², respectively were reached and wall superheat temperatures, ΔT_s , as low 0.77 °C was also reached in some tests. In these experiments the effect of varying the particle size and layer thickness on the boiling heat rate and boiling heat transfer coefficient were examined at different operating conditions, i.e. air temperature and velocity.

In this chapter the test rig used for conducting the experiments is described along with the measurements taken and the measuring devices used. Also, the results obtained from these experiments are presented and briefly commented upon, but an in depth discussion of these results is carried out in chapter 5.

4.2 Test-Rig Description:

The test-rig used in this study is shown in Fig (4.1) & (4.2). The following can be mentioned about this rig:

¹ The sintered tube's manufacturer failed to determine the porosity. Mathematical calculations showed that the porosity is almost constant at 48%.

4.2.1 General Function:

The test-rig is a single effect vapour absorption refrigeration system whose main components are absorber, generator, condenser and evaporator. The system is maintained under vacuum (about 8.7 mbar for the low pressure side and 42.4 mbar for the high pressure side). The absorbent solution used in this refrigeration cycle is lithium bromide. This solution is heated in the generator using two electric heaters. Due to heating, pure water vapour is generated and then driven under vapour pressure difference to the condenser. The concentrated solution returns by gravity force to the absorber. In the condenser, water vapour loses its latent heat of condensation to the cooling water flowing through its coil and condenses. This water refrigerant then passes to the evaporator through a throttle valve. In the evaporator, the water boils by absorbing its latent heat of vaporisation from the hot air flowing across it, causing the air temperature to drop. The evaporated refrigerant travels to the absorber where it is absorbed. The absorbent is sprayed onto the absorber cooling coil. The spray and the film formed on the coil help maximise the surface area of heat and mass exchange. The water that doesn't boil in the evaporator flows down to a water tank where it is pumped back to the absorber. The solution is constantly circulated between the absorber and the generator using a diaphragm pump. The pumps also circulate the absorbent through a set of nozzles placed at the top of the absorber. The absorption heat is dissipated to cooling water passing through the absorber's cooling coil. The closed coil also serves as an absorption surface where the absorbent forms a thin falling film.

4.2.2 Test-Rig Components:

The main components of the test-rig are as follows:

4.2.2.1 Absorber:

It is made of a glass cylinder 300 mm diameter and 500 mm high; see Fig (4.3). The top and bottom covers of this absorber are made of stainless steel plates. The absorber

enclosed a vertical copper coil whose inlet and outlet pipes penetrate through the bottom cover plate. Five full-cone nozzles are placed on the top cover plate of the absorber; see Fig (4.4).

4.2.2.2 Generator:

It is made of a glass cylinder 300 mm diameter and 300 mm high; see Fig (4.5). The top and bottom covers of this glass cylinder are made of stainless steel. Two electric heaters, 2.75 kW power each, are fixed to the bottom stainless steel cover and connected to a power variac to control the input heat and temperature of the generator. The generator is placed above the absorber. The solution, which is pumped to the generator from the absorber, is always maintained at a level higher than that of the two electric heaters to ensure that both heaters are immersed inside the solution to avoid burn out. The concentrated heated solution returns to the absorber by gravity. A vapour line, 76 mm diameter connects the generator to the condenser.

4.2.2.3 The Condenser:

It is made of a glass cylinder, 300 mm diameter and 300mm high. The top and bottom covers of this glass cylinder are made of stainless steel. It is placed above the evaporator; see Fig (4.6) and it enclosed a copper coil through which cooling water flows. Water vapour from the generators enters the condenser from the top condenses on the coil and the condensate flows by gravity to the evaporator from the bottom of the condenser.

4.2.2.4 Evaporator:

It is a two-row staggered copper tube bank that has nine tubes; see Fig (4.7). The outer and inner diameters of each tube are 28.6 mm and 25.3 mm and the tube length is 300mm. The inner surfaces of these 9 tubes are covered with a bronze sintered powder layer. The evaporator is placed in an MDF air duct through which hot load air flows. The evaporator is connected to the absorber via a vapour line and is also connected to a water tank below it. Water enters the evaporator from top and passes downwards through the staggered tubes

Chapter 4: Experimental Work

side manifolds. Some of the water boils in the evaporator and the resulting vapour travels to the absorber. The remaining water in the evaporator passes downwards to the excess water collecting tank from where it is pumped back to the absorber.

4.2.2.5 Water Tank:

It is a cylindrical aluminium tank of 127 mm diameter and 280 mm height; see Fig (4.2). A diaphragm pump is continuously running during the test, taking water from this tank and delivering it to the absorber. The tank acts as a buffer for the pump.

4.2.2.6 Diaphragm Pumps:

Two diaphragm pumps are used in this test rig. One is used for circulating the solution to the generator. A branch from the discharge line of this pump reticulates the solution. The other pump is used for transferring the water that accumulates at the evaporator tank to the absorber; see Fig (4.2) & (4.3).

4.2.2.7 Load Air System:

Air is used to provide thermal loading to the evaporator. The air is heated in a heat exchanger using hot water from a hot water tank; see Fig (4.2). The temperature of water, and consequently the temperature of air, is controlled by adjusting the power input to the immersion heaters of the tank. Finer control is achieved by adjusting the water flow to the air heater. The velocity of air is controlled by three fans connected to a step motor. Finer control is further obtained by adjusting the opening of a damper at inlet to the fans. The air flows in the wind tunnel enclosing the evaporator as shown in Fig (4.2).

4.2.2.8 Vacuum Pumps:

Two vacuum pumps are used alternately to completely evacuate the system from air and other non-condensable gases prior to testing.

4.2.2.9 Cooling Water:

Cooling water taken from the laboratory tap was used to cool the absorber and condenser in parallel. Valves were used to control the flow and temperature of the vessels.

4.2.3 Evaporators Manufacturing and Production:

A company specialised in sintered metal products manufactured the modified tubes that were used in the evaporators of this study. The tubes' inner surfaces were covered with sintered layer made of bronze powder. Sixteen sets of sintered tubes, differing in particle size and layer thickness were produced. Four particle sizes were used; 50, 100, 200 & 300 μm . For each particle size, four evaporator tube sets, which differed in layer thickness, were produced. The tubes were supplied at 155 mm in length, of which 150 mm pipe length was covered with sintered layer; see Fig (4.8). Each evaporator tube was made by joining two supplied tubes. Manufacturing restrictions on the sintering process meant that the evaporator tubes could not be produced in one piece. Each evaporator was made of nine tubes, i.e. eighteen supplied tubes. Part of the evaporator manufacturing procedure is shown in Figs (4.9).

4.3 Test Measurements and Measuring Devices:

In this experimental work many measurements have been taken to assess the thermal performance of sintered tube evaporators and to monitor the performance of the test-rig.

These measurements were:

- Air velocity measurements.
- Temperature measurements.
- Pressure measurement.
- Flow measurements.
- Humidity measurements.

Fig (4.1) shows the locations of these measurements. A data logger was used to record the measurements.

4.3.1 Air Velocity Measurements:

Air velocity was controlled by a combination of adjusting the fans and the damper. Two pitot tubes were used to measure air velocity inside the wind tunnel at the upstream of the

evaporator. Measurements were taken along horizontal and vertical lines from the mid points of vertical plane. Five measurements were taken along each line and the arithmetical average of the ten readings was used as the average velocity of air at inlet to the evaporator. Fig (4.10) & (4.11) shows the locations of air velocity measurements and the velocity grid on the vertical plane.

4.3.2 Temperature Measurements:

Many temperature measurements were taken in these experiments. Some of the measurements were primary, used in calculating the thermal performance of the evaporator. Other measurements were secondary in that they were used to monitor and control the operation of the test-rig. Fig (4.12) shows samples of the thermocouples used in these experiments.

4.3.2.1 Primary Temperature Measurements:

These included measuring air temperature at inlet (upstream) and outlet (downstream) of the evaporator. A grid of temperature measurements were taken on each side of the evaporator (inlet & outlet). For each grid, nine measurements, equally distanced in three rows and three columns, were taken using thermocouples type K. The arithmetic average of every nine measurements was taken as the average temperature of air on each side of the evaporator (inlet & outlet). Fig (4.13) shows the grid of temperature measurements at inlet and outlet of the evaporator.

Other temperature measurements included measuring refrigerant temperature at inlet to the evaporator; see Fig (4.1) & (4.7). The water temperature after the throttle valve was measured using type K thermocouple. Also, eight surface temperature measurements were taken from different positions on the evaporator tubes' surfaces; see Fig (4.14). The arithmetic average of these eight measurements was used in calculating the evaporator tubes' surface temperature.

4.3.2.2 Secondary Temperature measurements:

Secondary temperature measurements were taken to monitor the performance of the test-rig for operational purposes, were:

- Solution temperature around the cycle.
- Cooling water inlet and outlet temperatures.
- Refrigerant and vapour temperatures around the refrigerants cycle.

These measurements were taken using type K tube surface temperature thermocouples and temperature probes. Thermal insulator was wrapped around the measuring tip of the thermocouples; see Fig (4.1) for the location of these measurements.

4.3.3 Pressure Measurement:

Vapour pressure at evaporator and condenser pressure were recorded using pressure transducers connected to the data logger. Also, two dial vacuum gauges were used to indicate high and low pressures for purposes of leak diagnosis. Fig (4.1), (4.6) & (4.7) shows the location of these measurements.

4.3.4 Flow Measurement:

Refrigerant's flow rate at inlet and outlet of the evaporator were measured using two sensitive flow meters. The meters were capable of indicating the instantaneous and the cumulative flow rates. The refrigerant's evaporation rate was taken to be the difference between the flow rates of liquid in and out of the evaporator. Fig (4.1) shows the location of these flow meters.

4.3.5 Data Logging:

A data logger having 44 temperature channels and 4 pressure channels was used. This data logger was run using special software. The recorded data was downloaded on a spreadsheet where calculation of various parameters was performed; see Fig (4.13b).

4.3.6 Test Execution Stages:

Each test was conducted in two stages, stability stage and measurements stage.

4.3.6.1 Stability Maintaining Stage:

This stage started by maintaining the required vacuum into the system, which was done by running the vacuum pump for 15 – 20 minutes to eliminate any air/non-condensable gases present in the system. Then, the air velocity and temperature (at evaporator inlet) were adjusted to the desired values. This was done by running the air fans, electric heaters on the water tank and circulating hot water between the air heater and the water tank. Then, the solution pump was started to circulate the solution between the absorber and the generator. The immersion electric heaters of the generator were then switched on. The system performance was closely monitored on the computer screen and locally on the test-rig itself, where necessary correcting adjustments to the solution flow, cooling water flow and refrigerant's flow to the evaporator were made. The refrigerant pump was started when reasonable level of excess water accumulated on the excess water tank. Performance of the test-rig was closely monitored until stability indicated by reaching steady state conditions was achieved. This was achieved by steady temperatures, flow rates, pressures and velocities around the system.

4.3.6.2 Measurement Taking Stage:

Once stability was established, the data logger was started and measurements were taken at four seconds intervals. The test would typically run for 25 – 30 minutes. The data was down loaded to excel sheet where it was averaged and used to calculate the performance as explained below.

4.4 Problems and Trouble Shootings:

Various problems have been encountered in running the test-rig in this research. These are:

4.4.1 Air Ingress:

The fact that the system should be maintained under vacuum has created substantial difficulty in maintaining the system well-sealed to prevent air-ingress into and in detecting the locations of such air-ingress when it occurred. An inert gas (nitrogen) was used to

Chapter 4: Experimental Work

pressurise the system and then foam was sprayed on suspected joints to detect the location of air-ingress. The inert gas was used instead of air to avoid possible chemical reaction with oxygen that could affect the solution absorbability.

4.4.2 Entrainment to The Condenser:

On rare occasions, when the condenser pressure had become too much lower than the generator pressure, solution droplets during boiling of the solution might transfer to the condenser side and contaminate the condensate. When this happened it would lead to precipitating some lithium bromide salt on the evaporator tubes which would block the pores of the sintered layer and result in hindering water boiling inside the evaporator tubes. The condenser and evaporator were thoroughly washed by distilled water whenever such contamination took place.

4.4.3 Flow Meters Sensitivity:

The flow meters used in this research are low-flow turbine flow meters. When the turbine rotates due to the flow of the liquid, its blades intersect a beam of infra-red rays and that generates frequency pulses proportional to the flow that has passed through the flow meter. The entrained solution as explained in section 4.4.2 contaminates the condensate in the condenser. When contaminated water had passed through the flow meter some particles of the lithium bromide solution would precipitate on the electronic parts of the flow meter and degrade the ability of the flow meter to accurately measure the flow rate of the condensate. For this reason, periodic checks to the accuracy of the flow meter were constantly carried out and the flow meters were sent back to the manufacturer several times to be recalibrated and sometimes replaced with new ones.

4.4.4 Adequacy of Absorbent Concentration in the Absorber:

The solution concentration in the absorber used to change after several tests are carried out and become relatively dilute. To ensure that subsequent tests were carried out with adequate solution concentration in the absorber (i.e. 45– 50 %), the concentrated solution

Chapter 4: Experimental Work

in the generator at the end of each test was mixed thoroughly with the dilute solution in the absorber. A drain line was added to the test rig to drain all the solution from the generator into the absorber to enable mixing the two solutions together; see Fig (4.5)

4.4.5 Crystallisation:

Sometimes, the solution used to crystallise inside the solution lines, especially the horizontal ones. This usually happened when the temperature of the solution dropped below the crystallisation temperature at the corresponding concentration, e.g. due to drop in atmospheric temperature. To resolve this problem line trace-heating electric wires were used to heat up the solution lines prior to start-up. Mixing the concentrated solution in the generator with the dilute one in the absorber at the end of each test, as explained in section 4.4.4, ensured that the solution in the generator had become dilute enough to avoid crystallisation over night in the generator. However, sometimes the solution in the absorber and solution pump's chambers used to crystallise. In this case, the absorber cooling coil was connected to the hot water tank and used as a heater to melt the concentrated solution in the absorber cylinder. The solution diaphragm pump was disconnected and washed thoroughly with hot water to melt the crystallised solution. In addition to that, when the solution returning from the generator to the absorber had become so concentrated, it crystallises on the return line at the downstream of the heat exchanger. This problem was resolved by removing the heat exchanger from the cycle as removing it has no effect on the evaporator's thermal performance.

4.4.6 Degradation of Absorbent:

Lithium bromide reacts chemically with copper to produce copper bromide which in turn may react with oxygen at high temperature to produce copper oxide that degrades the solution ability to absorb water vapour. Although the test rig was under vacuum, it was almost inevitable to have some oxygen getting into the system when a joint/seal had broken down. Thus, the solution had to be replaced few times during the course of

Chapter 4: Experimental Work

experimental phase of this research. However, when there was a need to break the vacuum into the system for any reason, e.g. to pressurise the system to look for air ingress positions, an inert gas like nitrogen was used, instead of atmospheric air, to pressurise the system.

4.4.7 Blockage of Nozzles:

Sometimes, the nozzles get blocked by the crystals of the solution when crystallisation took place. In this case the nozzles were either heated using hot air from a hand held air blower until the crystals causing the blockage were melted or the whole system was shut down and the blocked nozzle was disconnected and cleaned mechanically. Nozzle blockage has rarely been caused by dirt; however, when that happened the cleaning was done mechanically.

4.4.8 Frequent Breakdown of Joints on the Solution Lines:

The joints in the solution lines used to breakdown more often than any other joints on the test-rig. This was mainly due to the joints' solder being attacked by corrosion. The problem was further aggravated on the discharge line of the solution pump, including the nozzles' connecting pipe work, as this line was subjected to high vibration forces due to the pulsating discharge flow of the diaphragm pump. This problem was resolved by replacing the soldered joints on both suction and discharge lines of the solution pump by good quality compression fittings which showed better resistance to corrosion and to the forces resulting from vibration.

4.5 Calculation:

The parameters calculated from the experimental data were the boiling heat rate, Q_b , the boiling heat transfer coefficient, h_b . Section 4.5.1 below gives more details as to how these parameters were calculated:

4.5.1 Boiling Heat Rate Q_b :

The boiling heat rate, Q_b , was calculated from:

$$Q_b = \dot{m}_v h_{fg} \dots\dots\dots(4.1)$$

The mass flow rate of the vapour that evaporated from the sintered layer evaporator during each test, \dot{m}_v , was obtained from the difference between the total flow that passed through the two flow meters positioned before and after the evaporator. The measured total vapour flow was divided by the recorded time for the duration of the test.

The latent heat of vaporisation, h_{fg} , was taken at the temperature of water entering the evaporator; see; Fig (4.7). This implicitly assumes that the refrigerant water entering the evaporator was saturated. This might not be entirely accurate. Theoretically speaking refrigerant water enters the evaporator as slightly wet steam. However, the error resulting from assuming saturation condition of the refrigerant entering the evaporator was small because the experimental condition was such that the difference between the condensate temperature at exit from the condenser and the refrigerant water temperature at inlet to the evaporator was in the order of 10-15 °C. Such relatively small difference combined with the fact that the liquid saturation line is fairly steep, Fig (4.15) means that the error resulting from the assumption of saturation is very small. In fact the error resulting from using equation (4.1) was calculated to be of the order of 2%.

4.5.2 Boiling Heat Transfer Coefficient:

The boiling heat transfer coefficient was calculated from:

$$h_b = q / \Delta T_s \dots\dots\dots(4.2)$$

Where

$$q = Q_b / A \dots\dots\dots(4.3)$$

$$\Delta T_s = T_w - T_s \dots\dots\dots(4.4)$$

The tube wall temperature, T_w , is the wall temperature measured on the exterior of the tubes. In theory, the wall temperature should be measured on the inner side surface of the

Chapter 4: Experimental Work

tube wall. However, and due to the small thermal resistance of the tube wall, the temperature drop across the wall is negligible. The resulting error in h_b is, consequently, small and the simplification of the temperature arrangement is justified.

$$R_{th} = L/kA.....(4.5)$$

In fact, the error, as calculated below, is less than 3%.

Substituting in equation (4.5) $k = 401 \text{ W/m K}$ for copper, $L = 1.65 \text{ mm}$ & $d_i = 25.3 \text{ mm}$, shows that $R_{th} = 1.92 \times 10^{-5} \text{ }^\circ \text{C/W}$. Given that the average boiling heat flux, q , in these experiments was about 4500 W/m^2 and the average wall super heat, ΔT_s , was $3 \text{ }^\circ \text{C}$, this leads to an average temperature drop of $0.086 \text{ }^\circ \text{C}$ across the tube's wall ($q \times R_{th}$) which in turn leads to an error of 2.9% in calculating the boiling heat transfer coefficient.

4.6 Results:

In this section the experimental results are presented graphically with respect to particle size and layer thickness. Tabulated experimental data is presented in appendix E. Detailed analysis of the experimental results is given in chapter 5.

4.6.1 Effect of Varying Particle size:

Fig (4.16) to Fig (4.24), show the effect of variation of particle size on boiling heat rate. The general trend of the Figures is one where the heat rate rises gently to a peak. A few curves showed some variation on this theme, but the general picture emerging shows that there are conditions in terms of layer thickness and particle size, where the performance is optimal.

Figs (4.25) to (4.33) show the variation of the experimentally obtained boiling heat transfer coefficient with particle size. The trend was more or less similar to that of the boiling heat rate. The heat transfer coefficient increased with particle size to a maximum and then dropped. The highest maximum value of the boiling heat transfer coefficient was consistently achieved by the evaporator with 2.0 mm layer thickness and $200 \text{ }\mu\text{m}$ particle sizes.

4.6.2 Effect of Varying Layer Thickness:

The effect of varying layer thickness on boiling heat rate and boiling heat transfer coefficient seems to be relatively slight as shown in Fig (4.34) to Fig (4.51). The layer thickness appears to have varying effects on boiling performance of the tested evaporators. This is indicated by the fact that some of the curves decrease monotonically with increasing layer thickness while the others increase monotonically. Although most of the points are reasonably close enough to their trend lines as appears on Fig (4.43) to (4.51), some of the points of the evaporator 200 μm and 2 mm layer thickness seemingly lie far away. The analytical results for the variation of heat transfer coefficient with layer thickness show a similar behaviour for this point but with less intensity; see Fig (3.59) and (3.63) to (3.66).

4.7 Summary of Chapter 4:

In this chapter the test-rig used for conducting the experiments was described and the procedure of the executing the experiments was explained. The practical problems encountered and remedial actions taken have also been explained. Furthermore, the method followed for calculating the boiling heat rate was explained along with the possible sources of errors expected in this calculation. The results were presented graphically and briefly described; however, thorough discussion of these results is made in chapter 5.

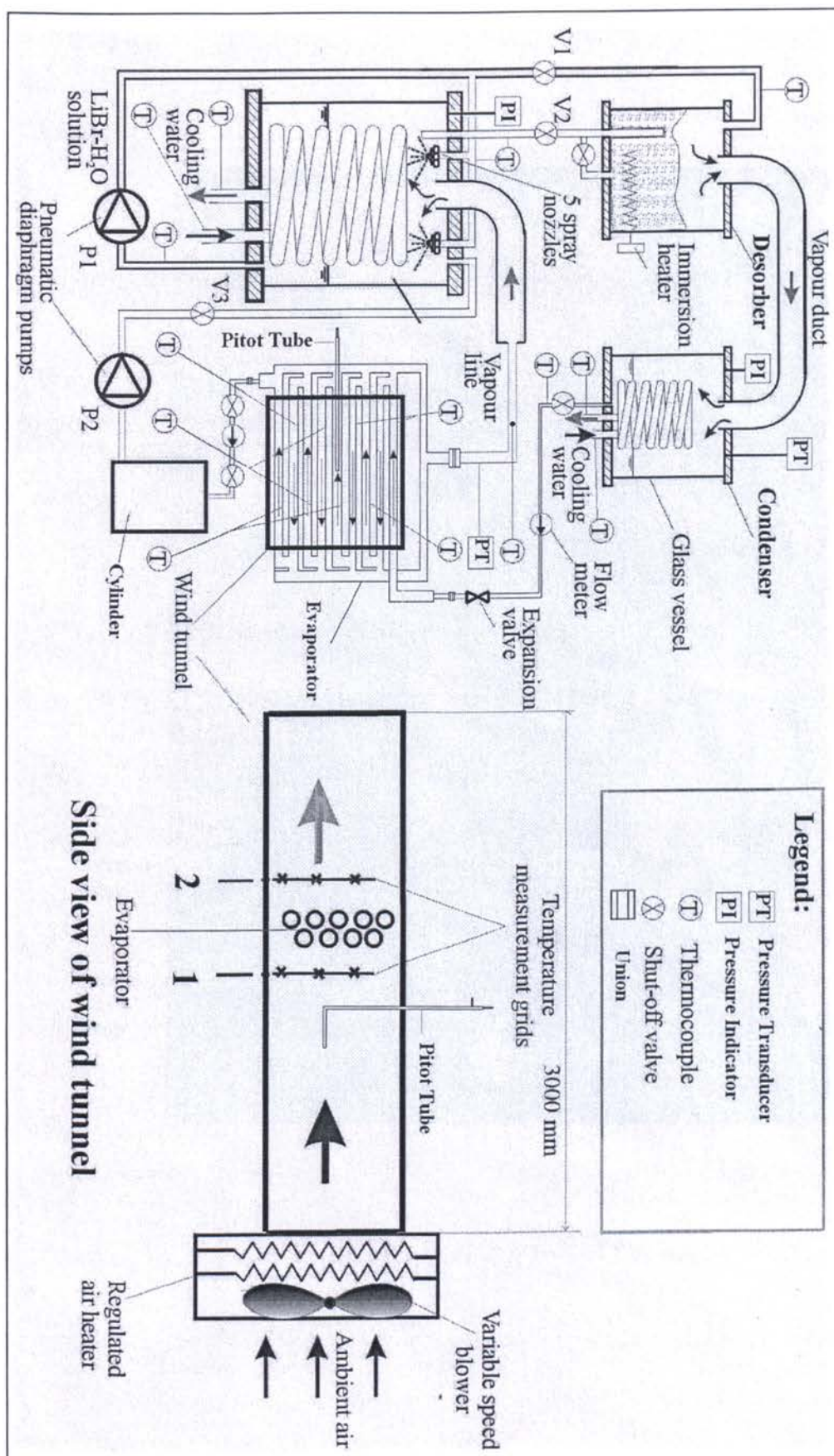


Fig (4.1) Schematic Representation of Test-rig

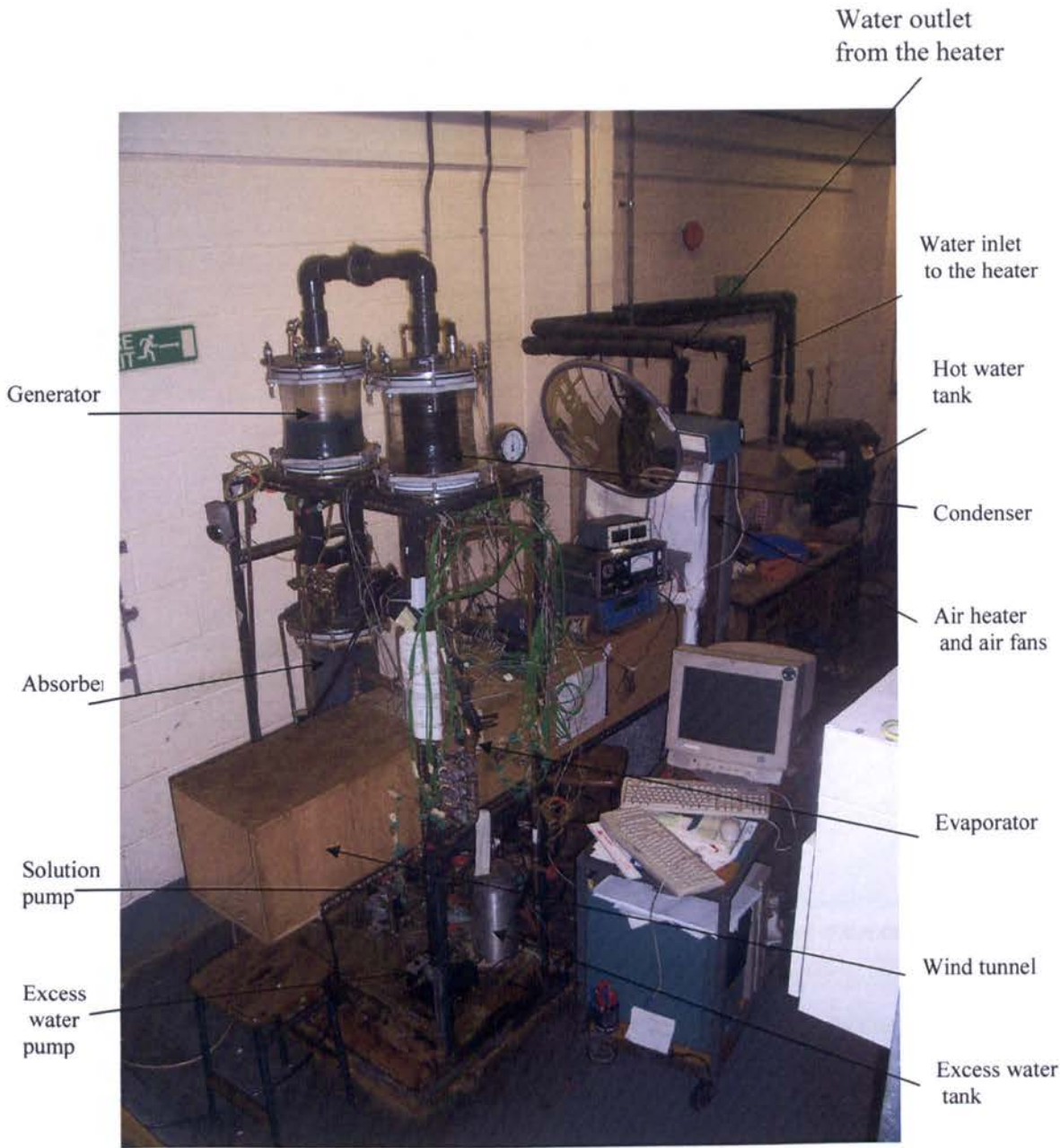


Fig (4.2) Overview of the Test-rig

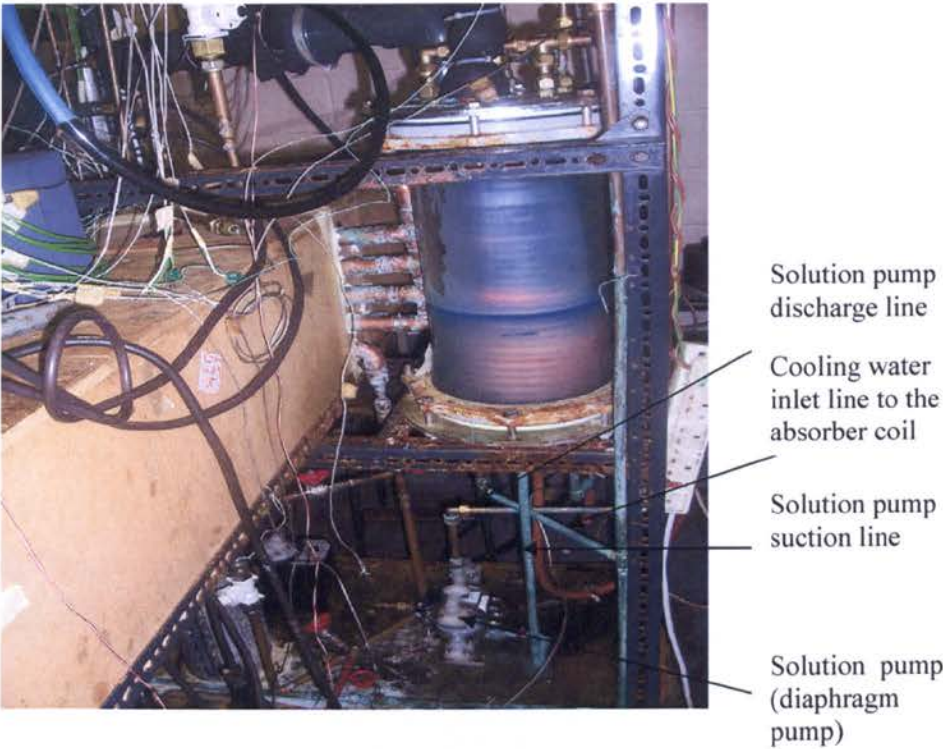


Fig (4.3) Absorber

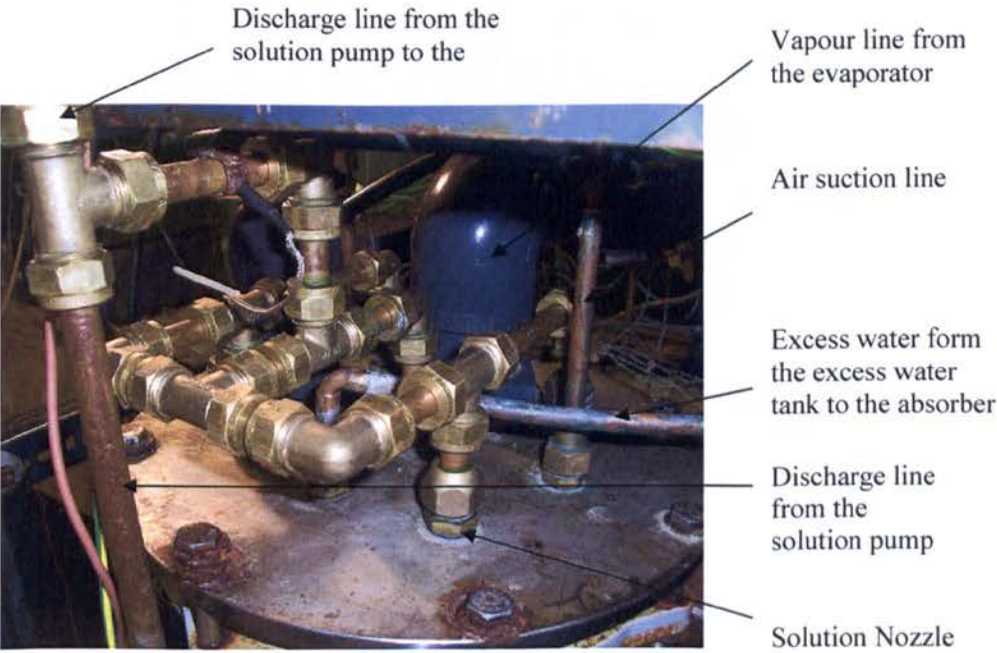


Fig (4.4) Nozzles



Fig (4.5) Generator

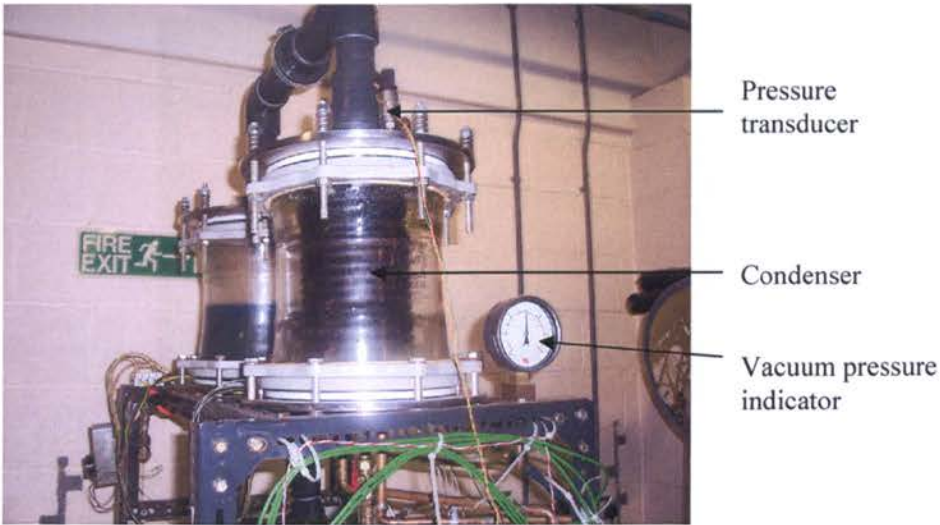
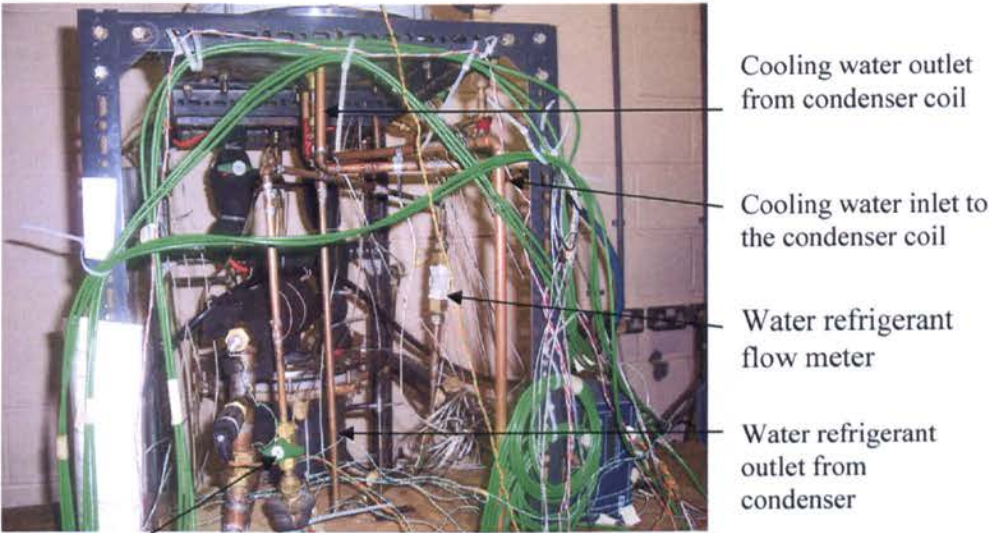


Fig (4.6 a) Condenser



Water refrigerant
throttle valve

Fig (4.6 b) Condenser

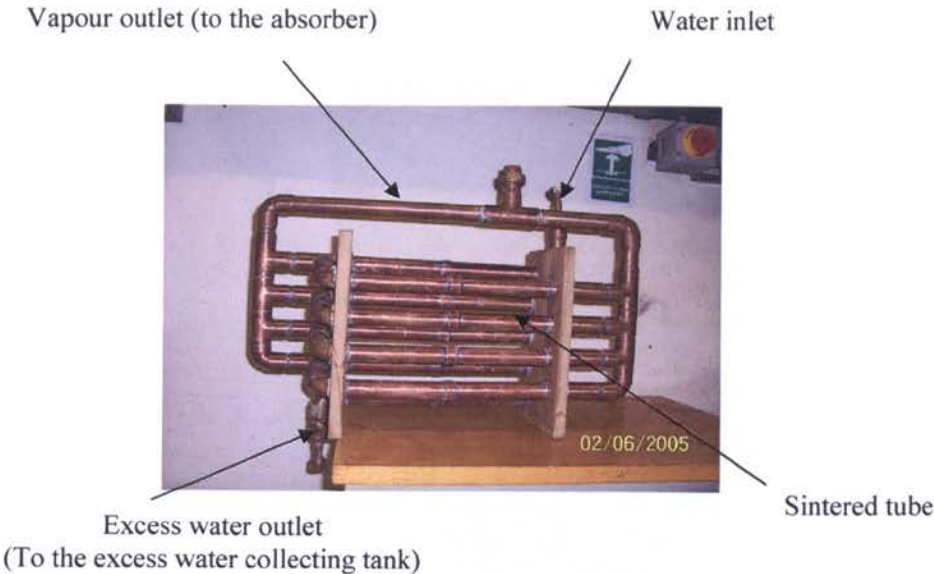


Fig (4.7a) Sintered tubes Evaporator



Fig (4.7b) Sintered Tubes Evaporator

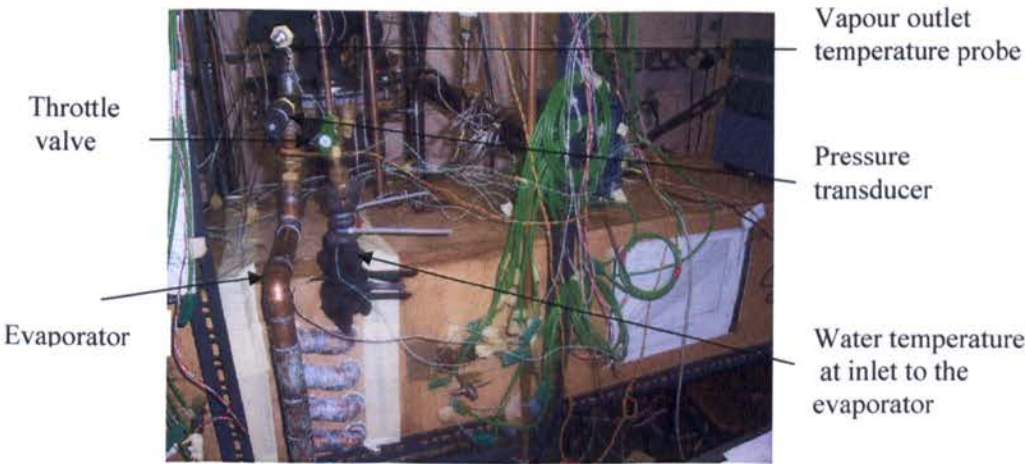
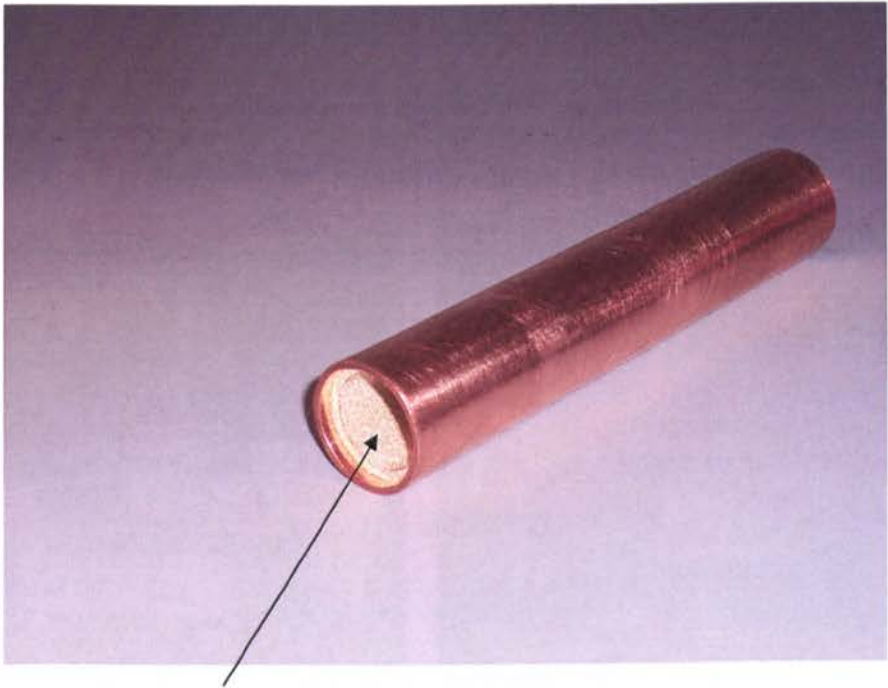


Fig (4.7c) Sintered Tubes Evaporator



Fig (4.7d) Sintered Tube Evaporators



Bronze sintered layer

Fig (4.8) 155 mm long Sintered Tube

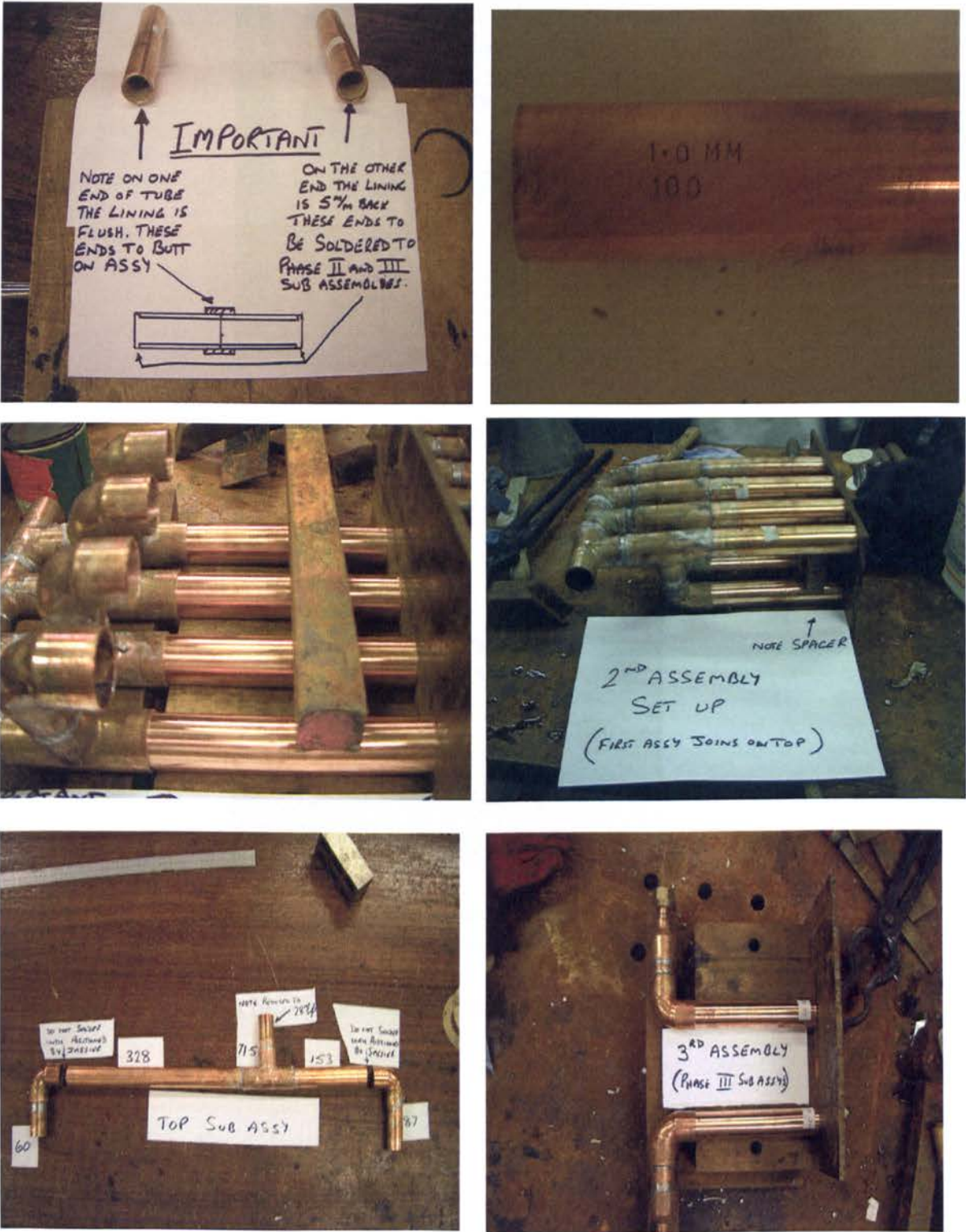
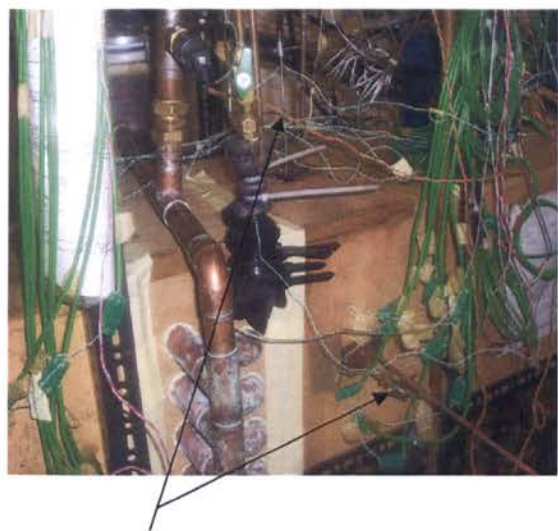


Figure (4.9) Evaporator Production Work



(a) Two pitot tubes for measuring air velocity



(b) The two pitot tubes are connected to this manometer for measuring air velocity

Fig (4.10) Pitot tubes for measuring air velocity

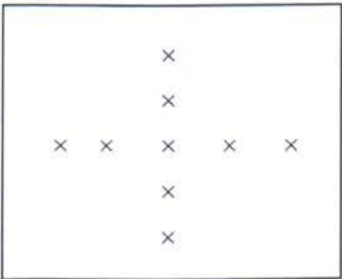


Fig (4.11) Air velocity measurement grid



(a) Pipe Surface Temperature Thermocouple



(b) Insulated Probe Temperature Thermocouple for Measuring Vapour Temperature



(c) Insulated Probe Temperature Thermocouple for Measuring Air Temperature

Figure (4.12) Temperature Thermocouple

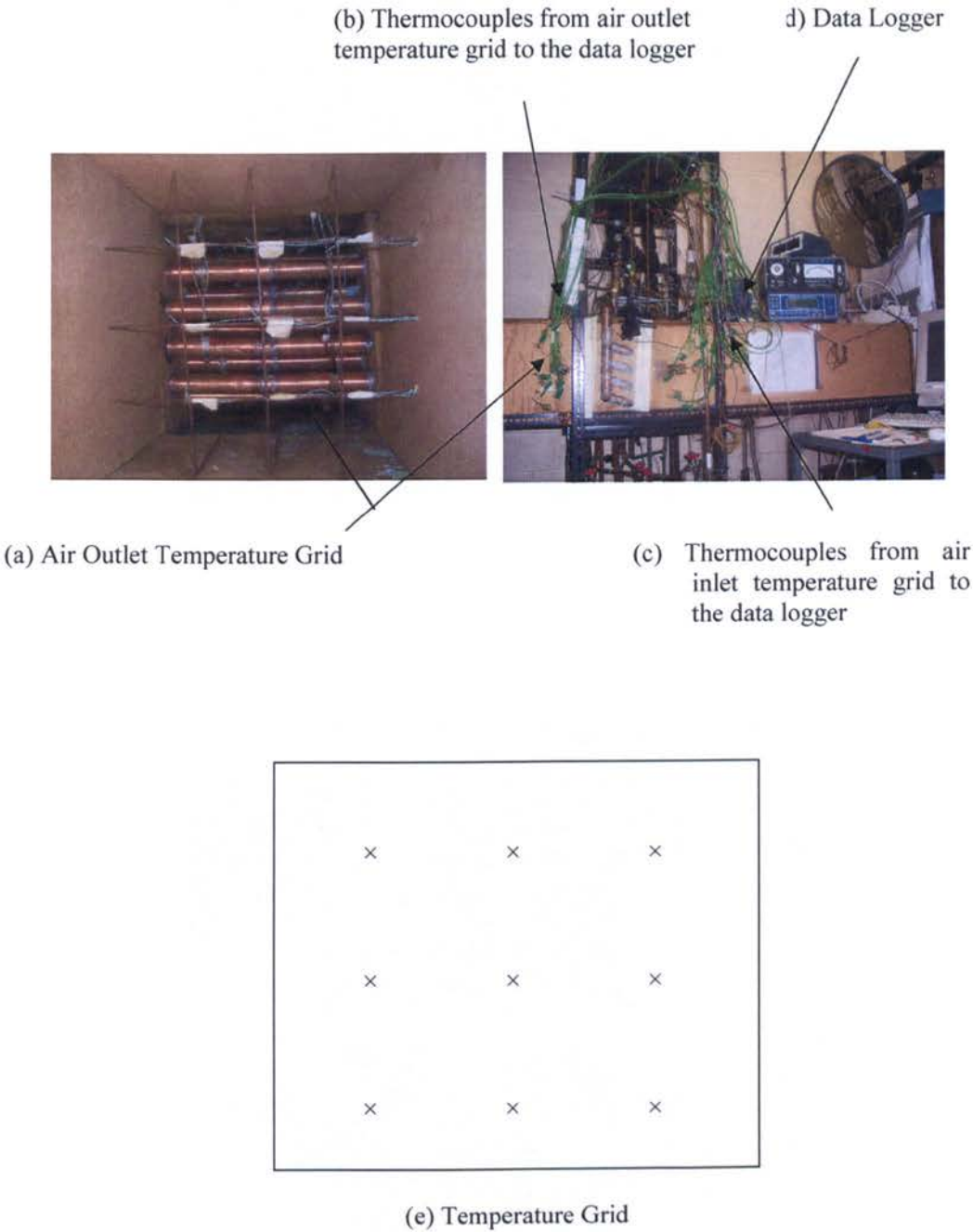


Fig (4.13) Air inlet and Outlet Temperature Measurements



Fig (4.14a) Measurement of the Evaporator Tube’s Surface Temperature



Fig (4.14b) Measurement of the Evaporator Tube’s Surface Temperature

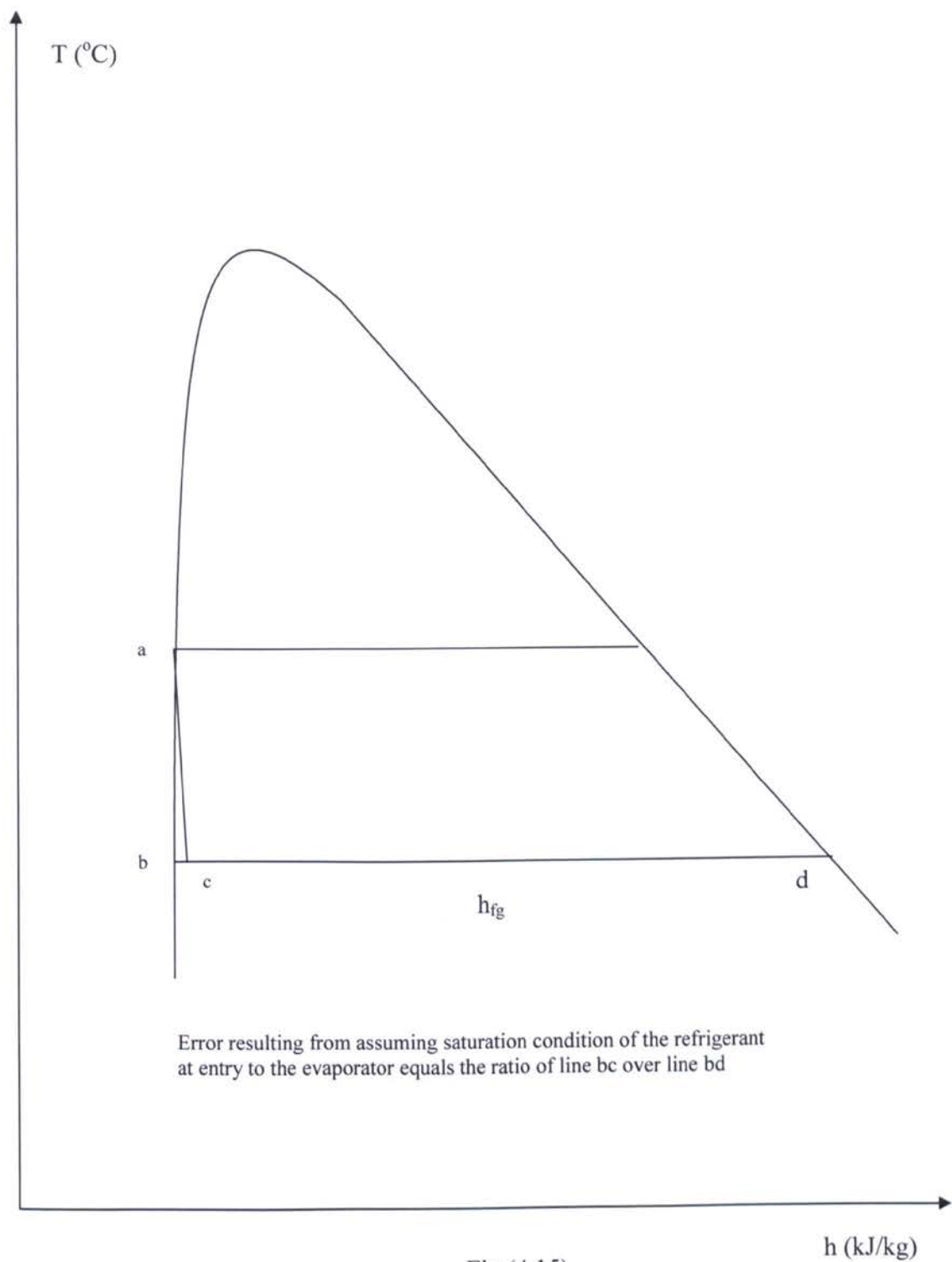
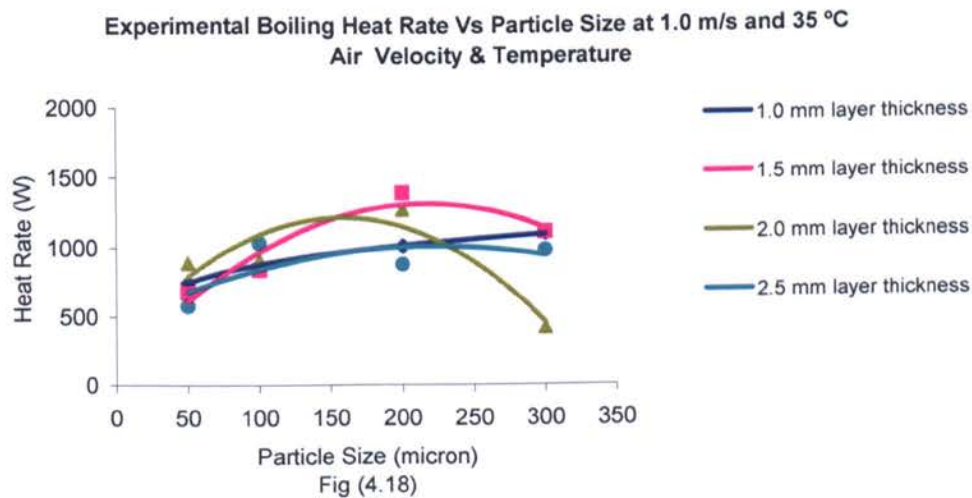
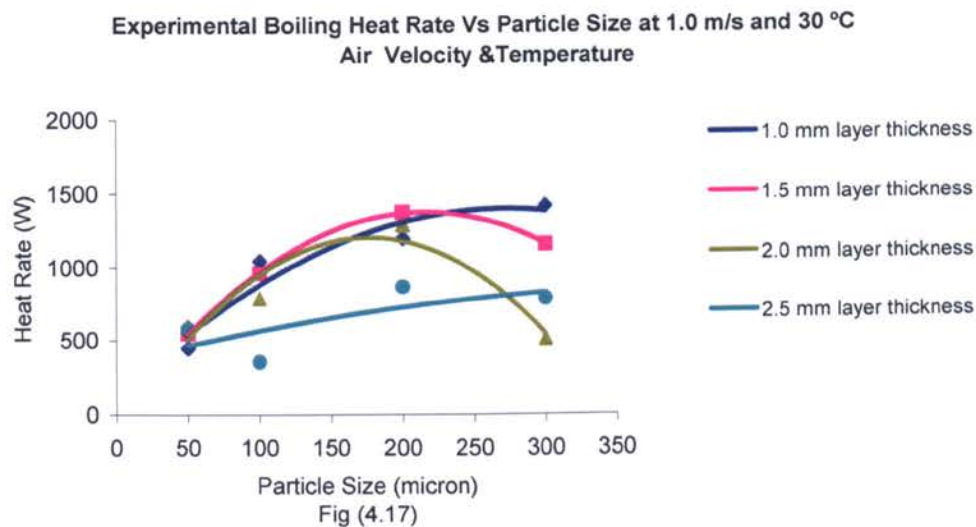
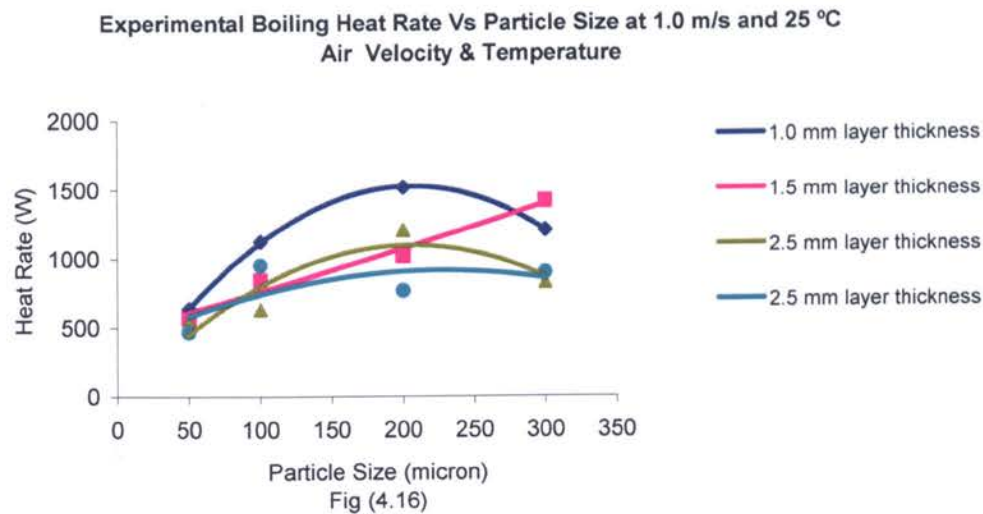
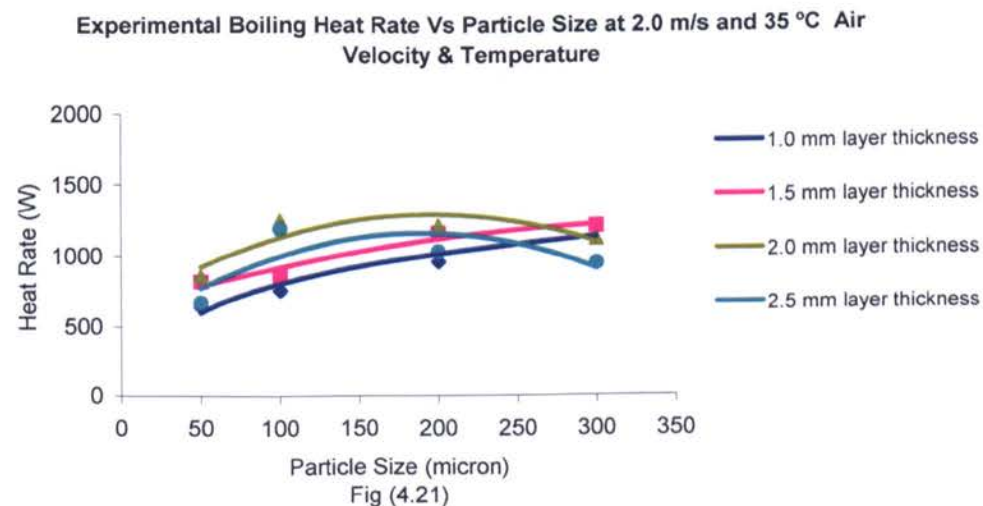
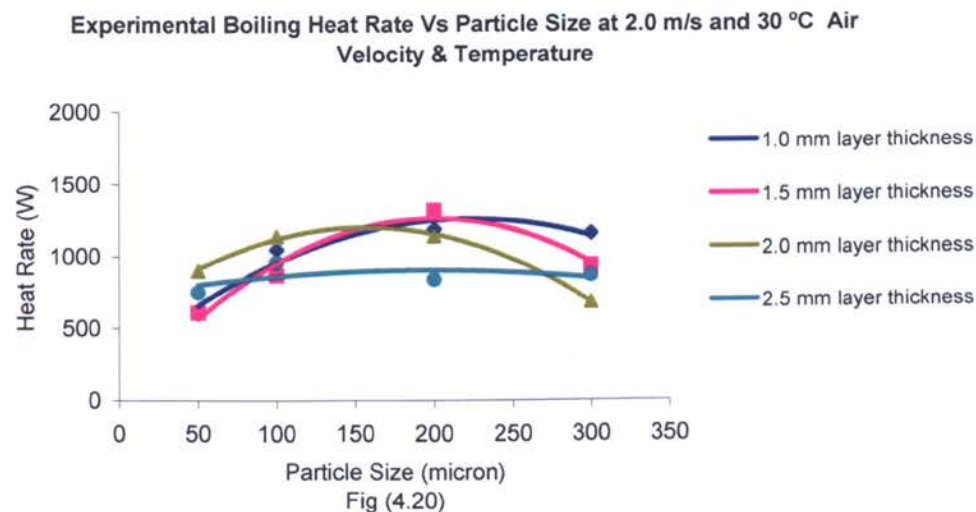
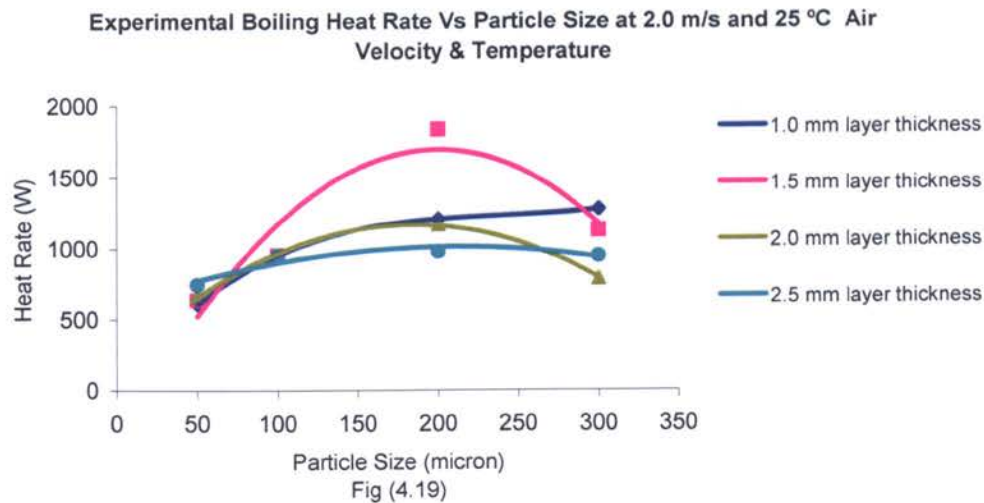
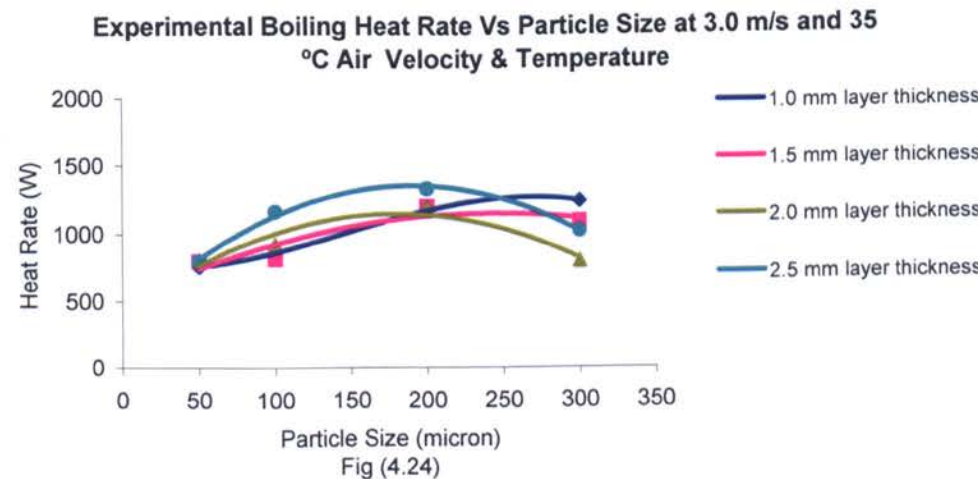
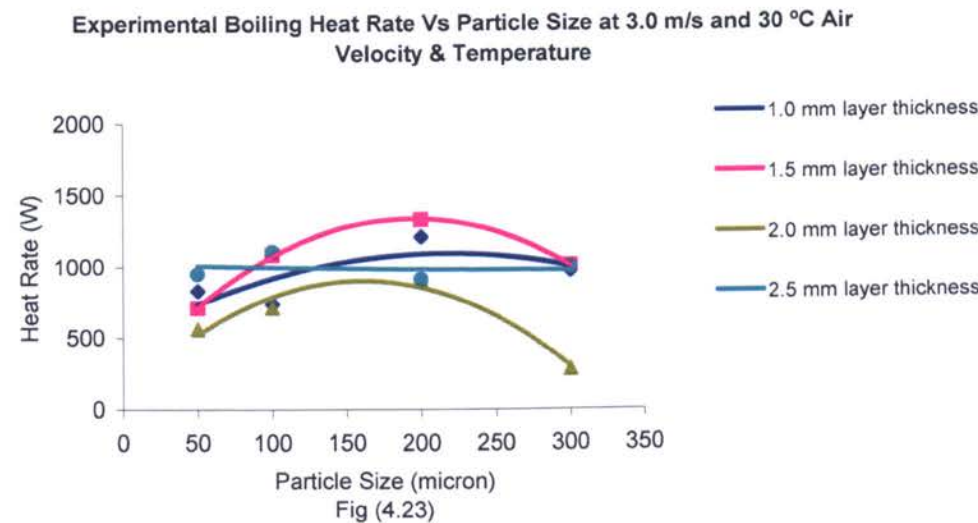
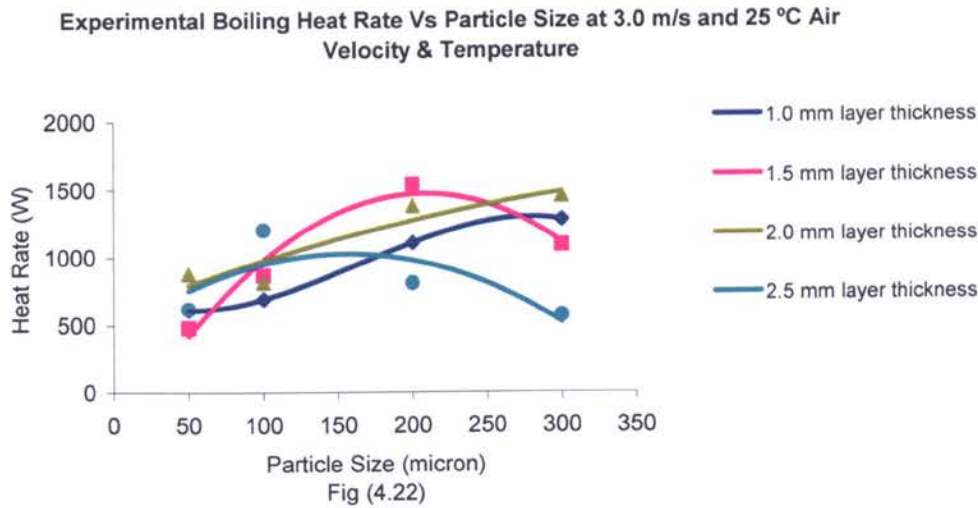


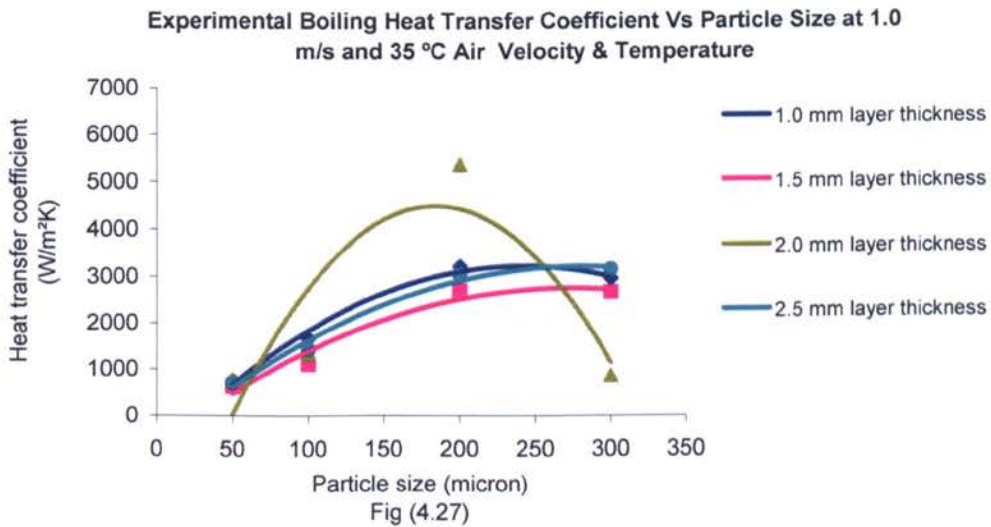
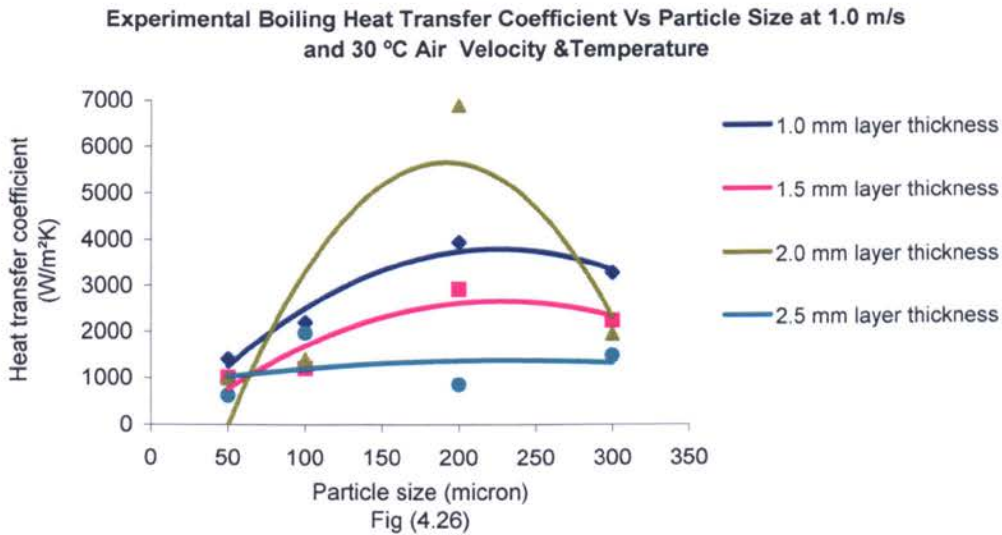
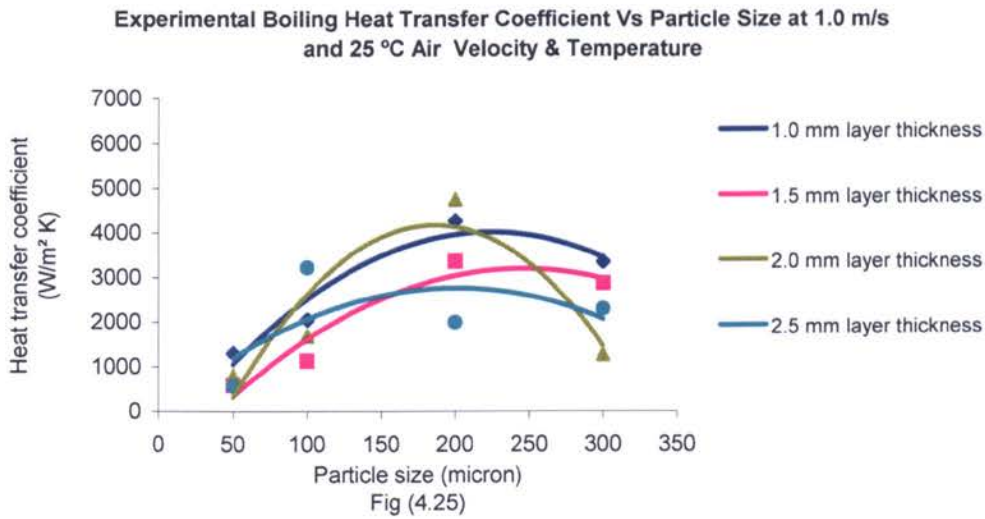
Fig (4.15)

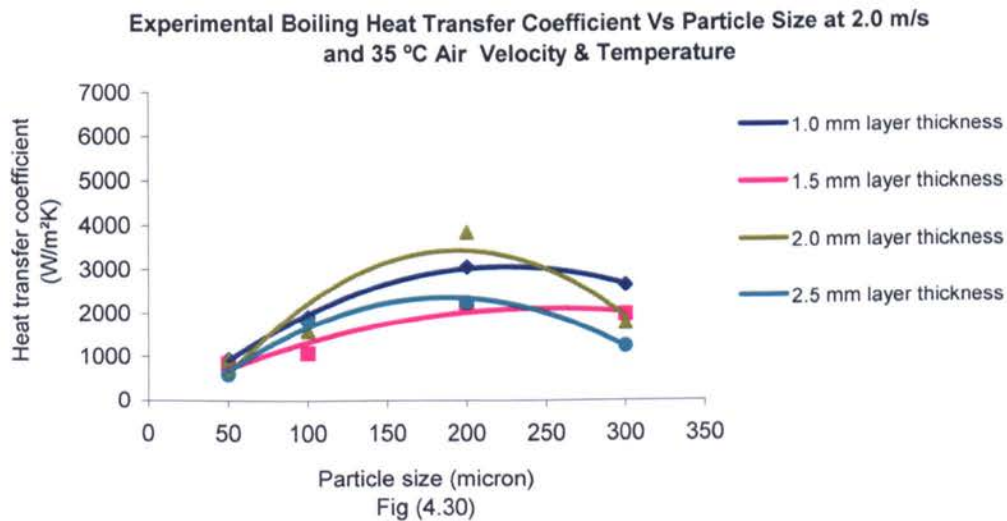
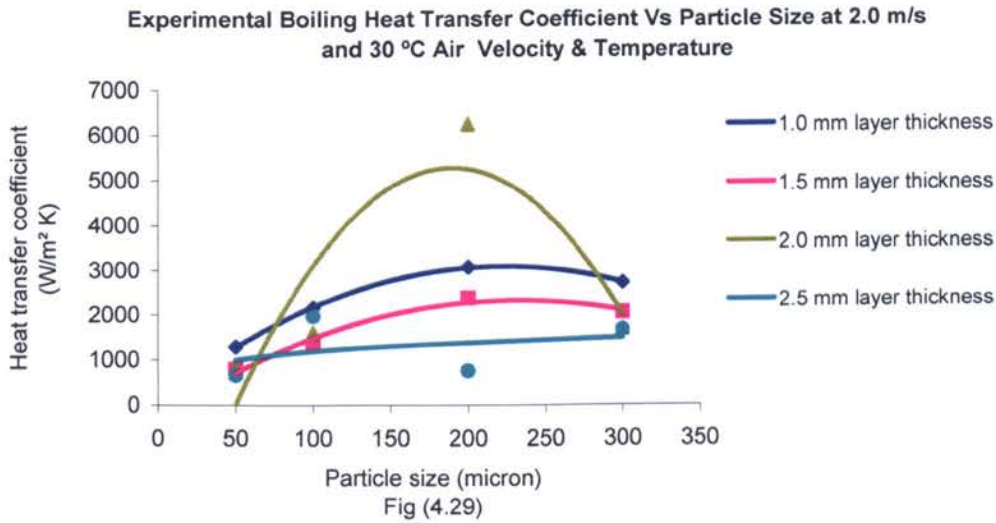
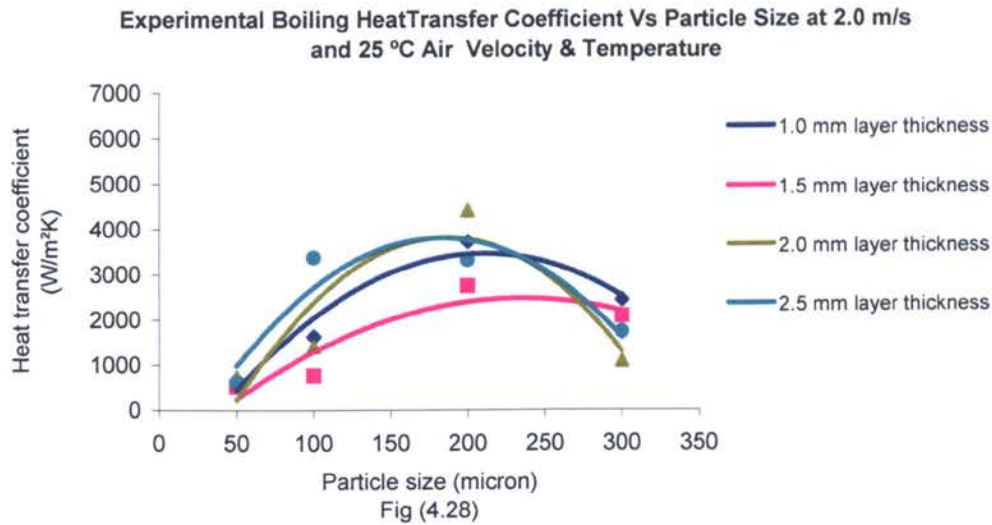
Error in Calculating h_{fg}

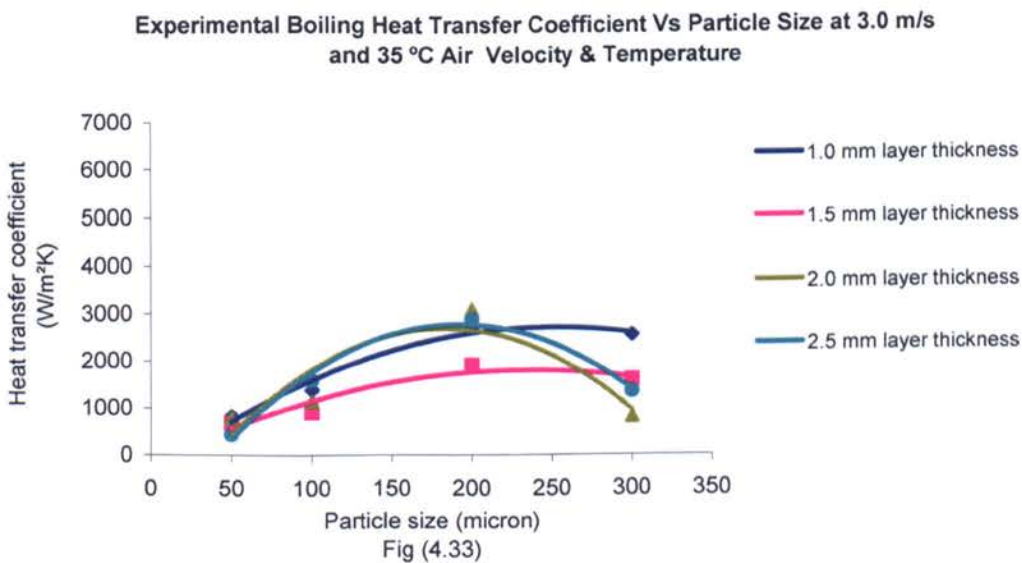
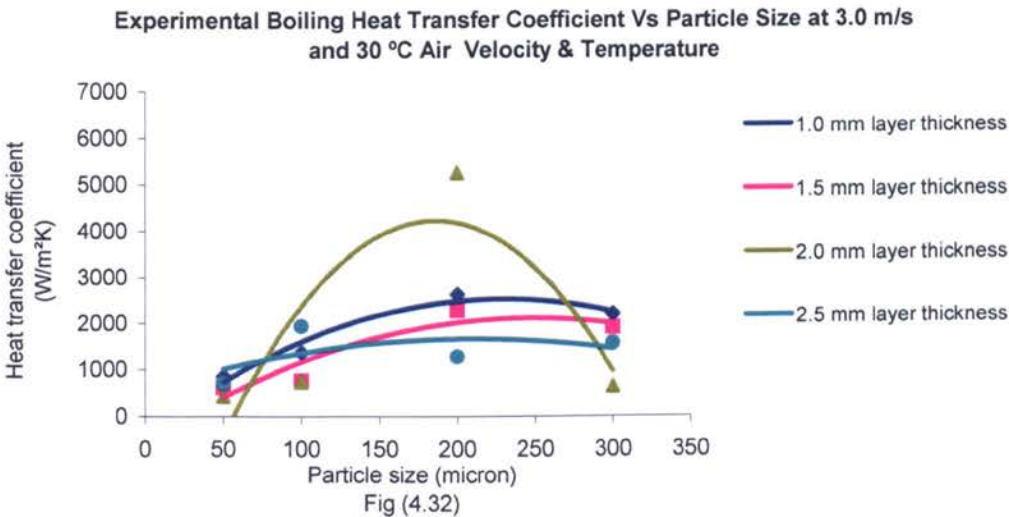
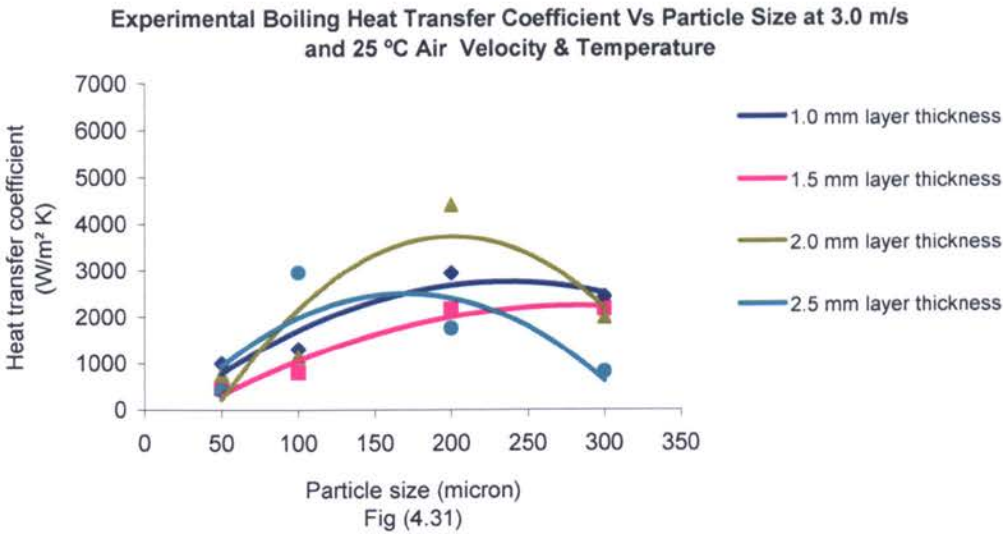




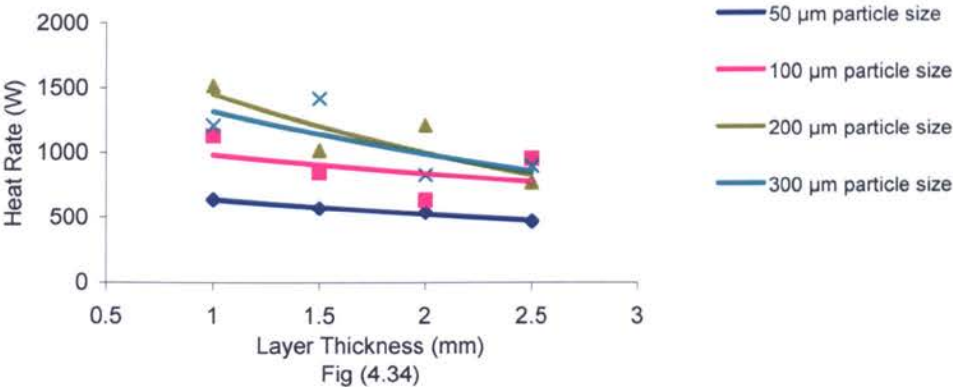




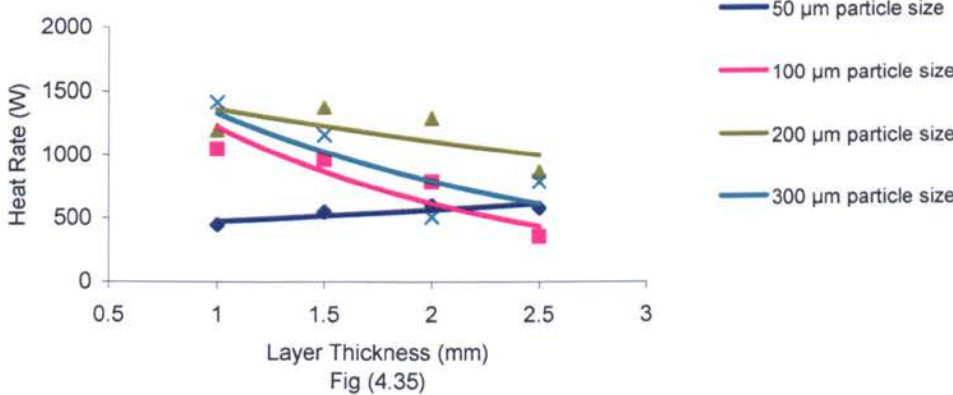




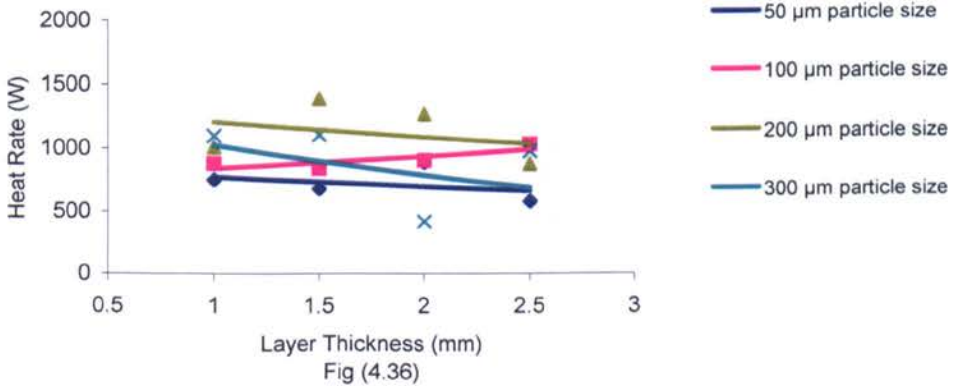
Experimental Boiling Heat Rate Vs Layer Thickness at 1.0 m/s and 25 °C Air Velocity & Temperature

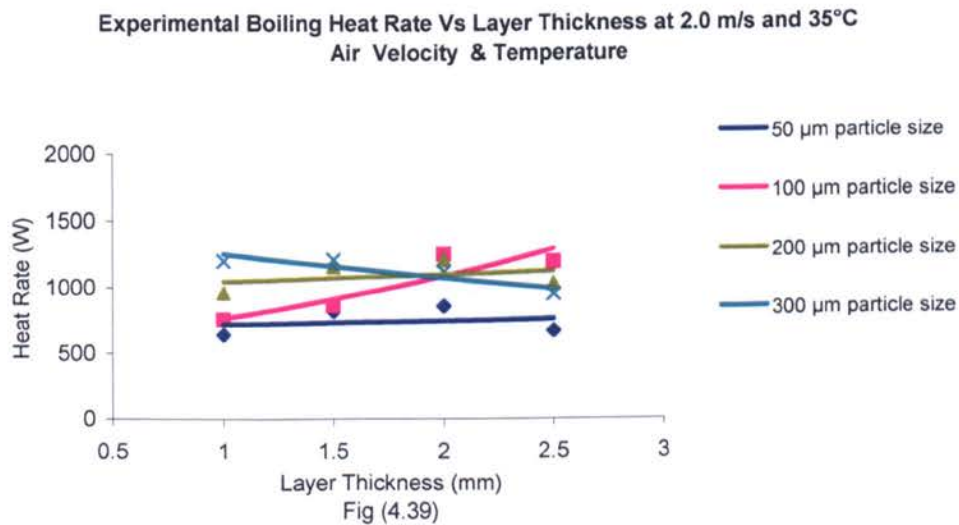
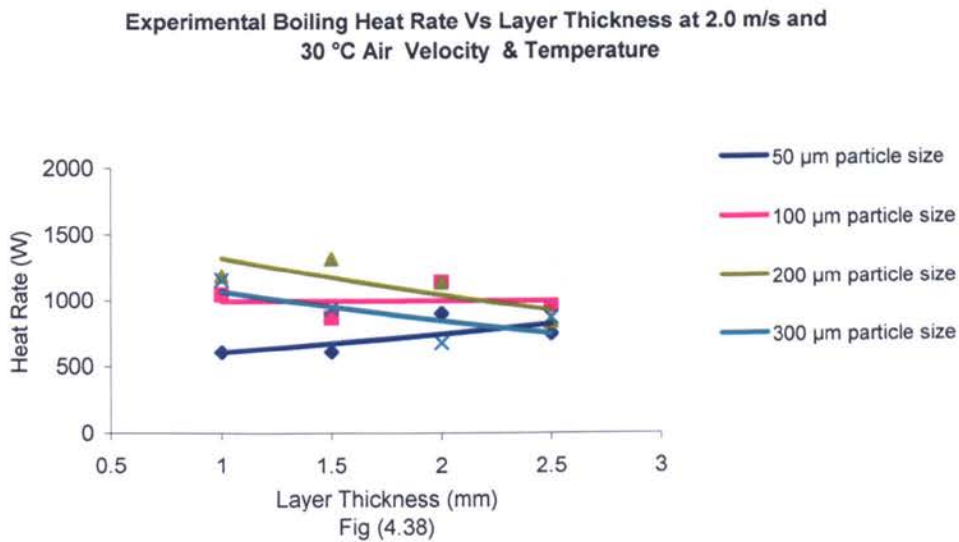
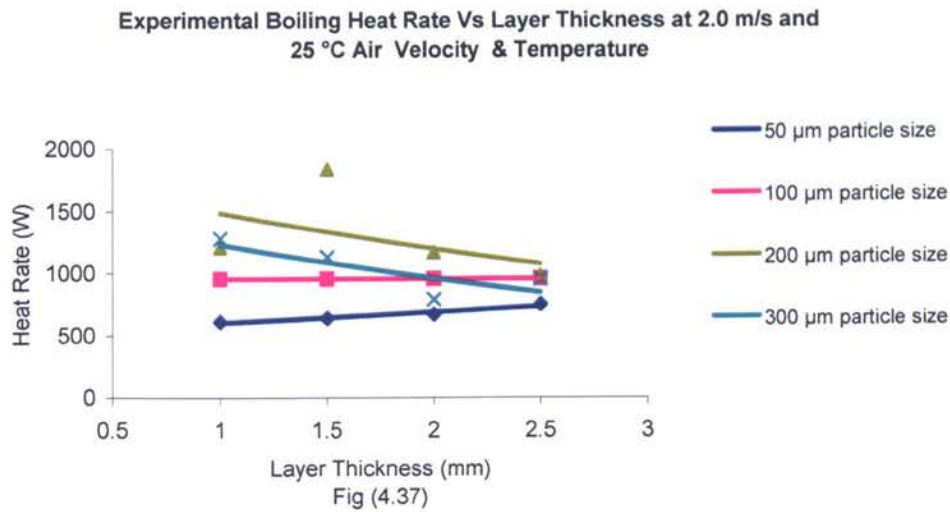


Experimental Boiling Heat Rate Vs Layer Thickness at 1.0 m/s and 30 °C Air Velocity & Temperature



Experimental Boiling Heat Rate Vs Layer Thickness at 1.0 m/s and 35 °C Air Velocity & Temperature





Experimental Boiling Heat Rate Vs Layer Thickness at 3.0 m/s and 25 °C Air Velocity & Temperature

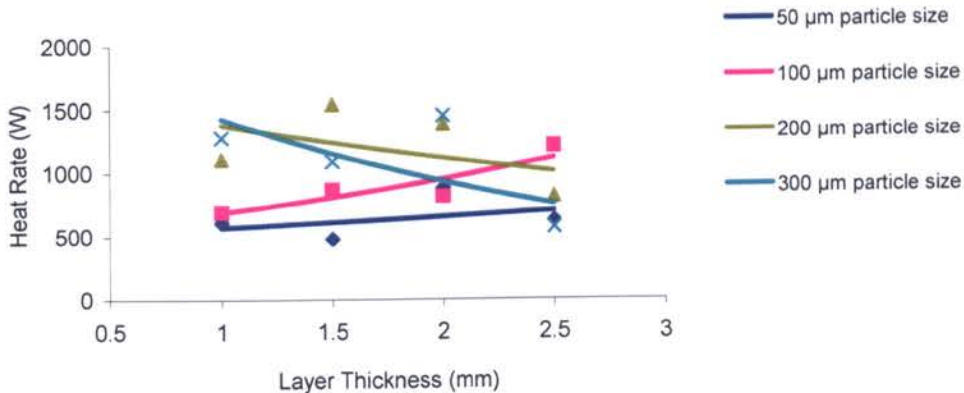


Fig (4.40)

Experimental Boiling Heat Rate Vs Layer Thickness at 3.0 m/s and 30 °C Air Velocity & Temperature

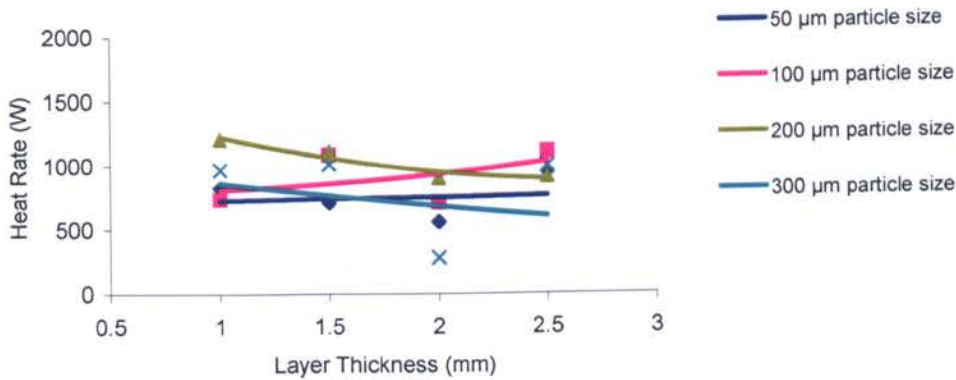


Fig (4.41)

Experimental Boiling Heat Rate Vs Layer Thickness at 3.0 m/s and 30 °C Air Velocity & Temperature

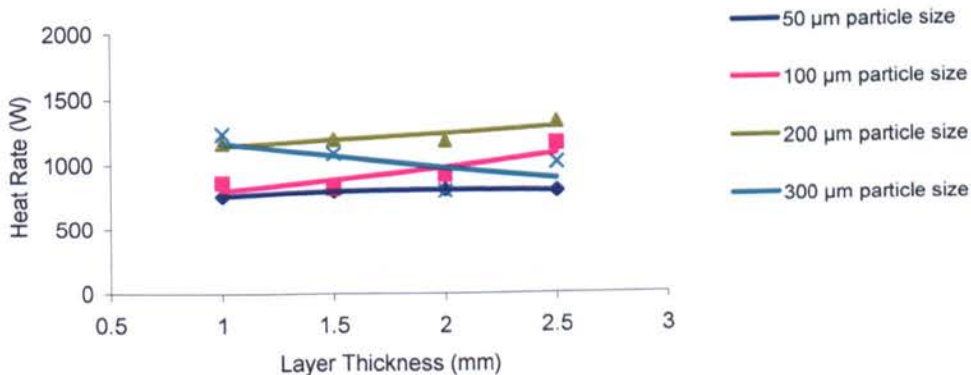
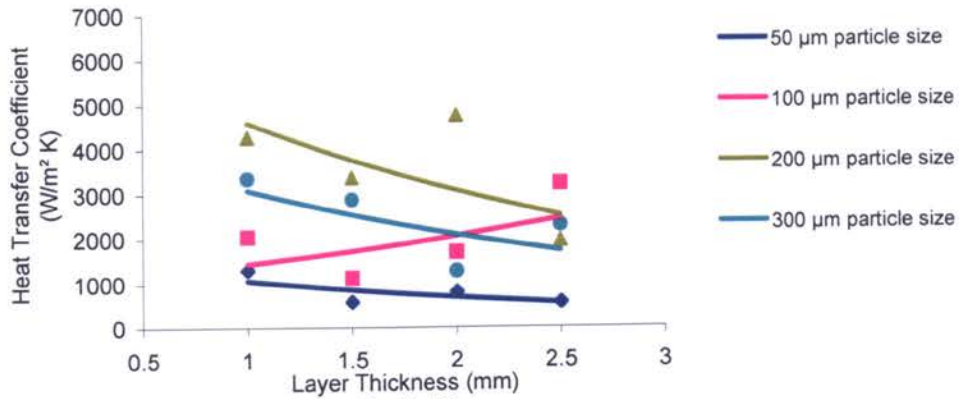
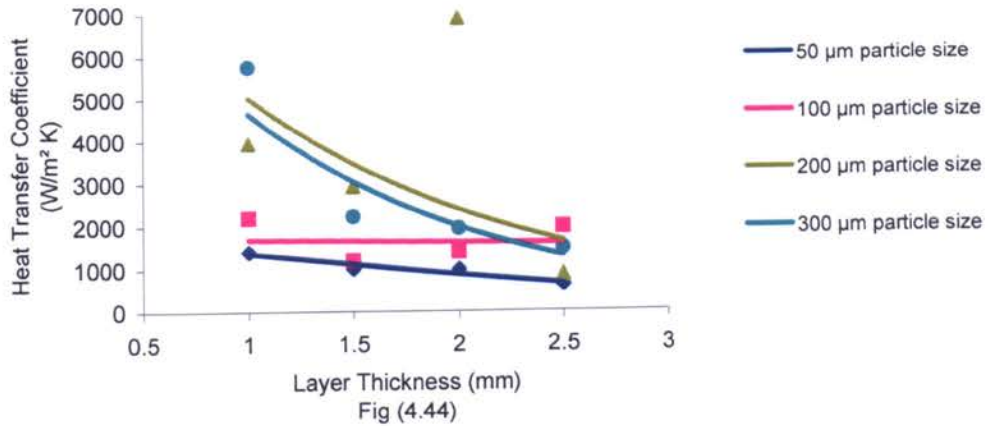


Fig (4.42)

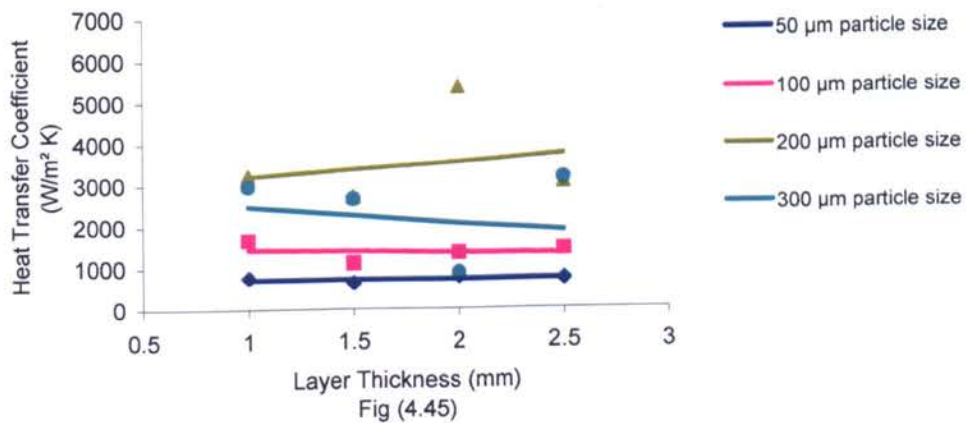
Experimental Boiling Heat Transfer Coefficient Vs Layer Thickness at 1.0 m/s and 25 °C Air Velocity & Temperature

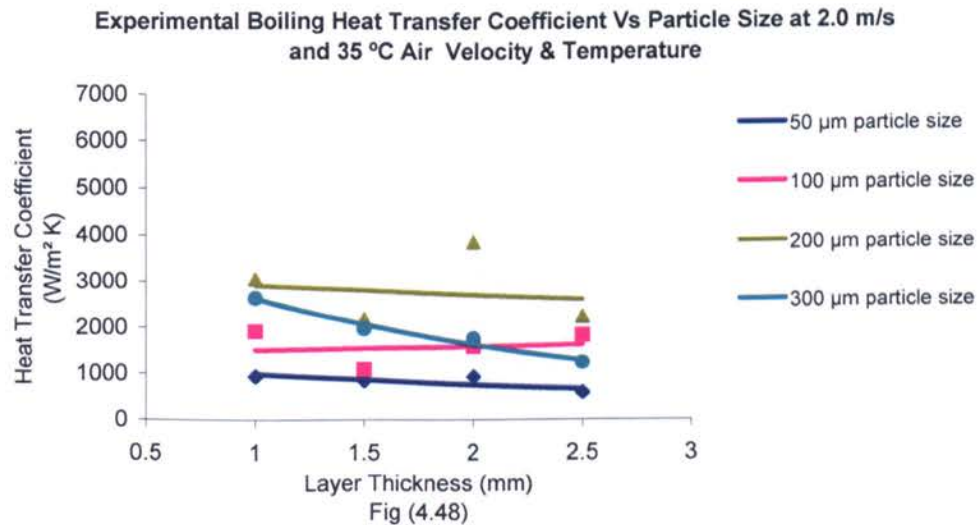
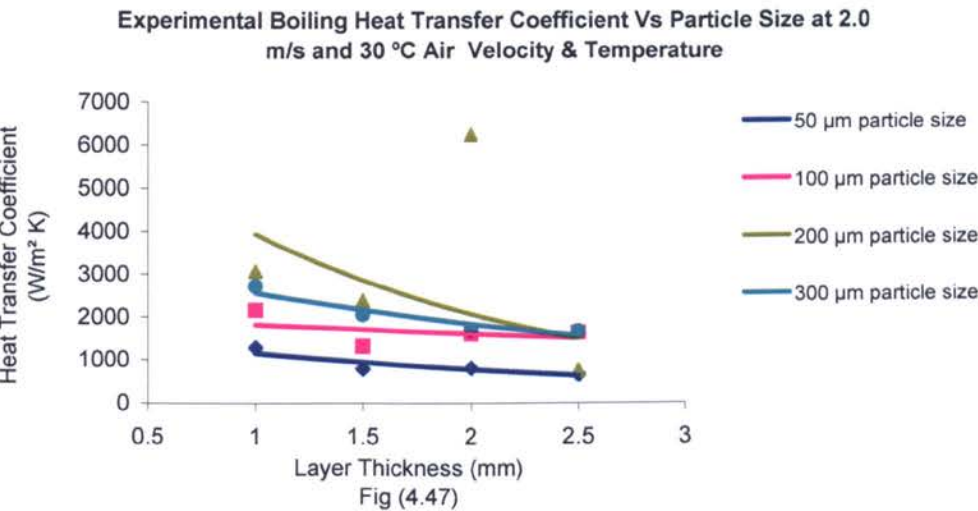
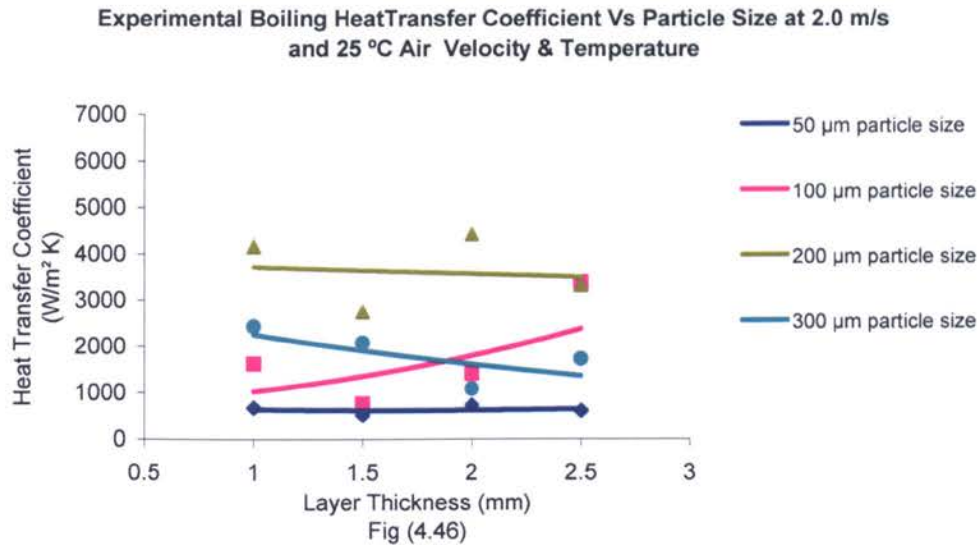


Experimental Boiling Heat Transfer Coefficient Vs Layer Thickness at 1.0 m/s and 30 °C Air Velocity & Temperature

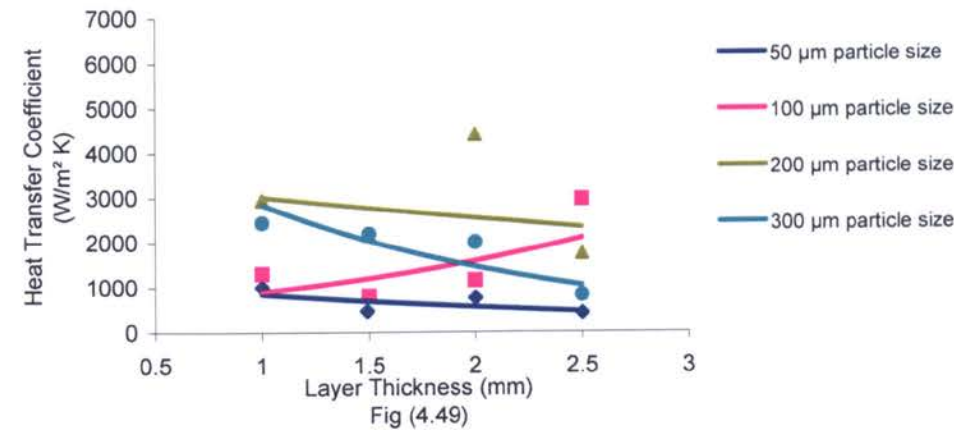


Experimental Boiling Heat Transfer Coefficient Vs Layer Thickness at 1.0 m/s and 35 °C Air Velocity & Temperature

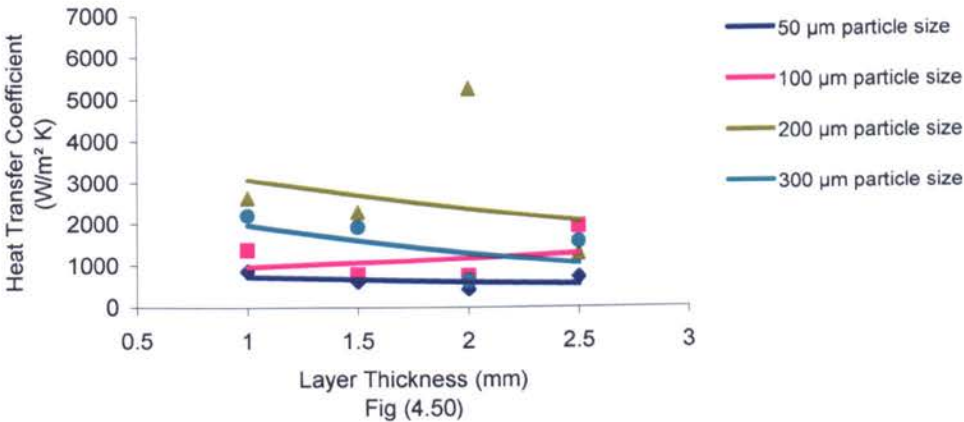




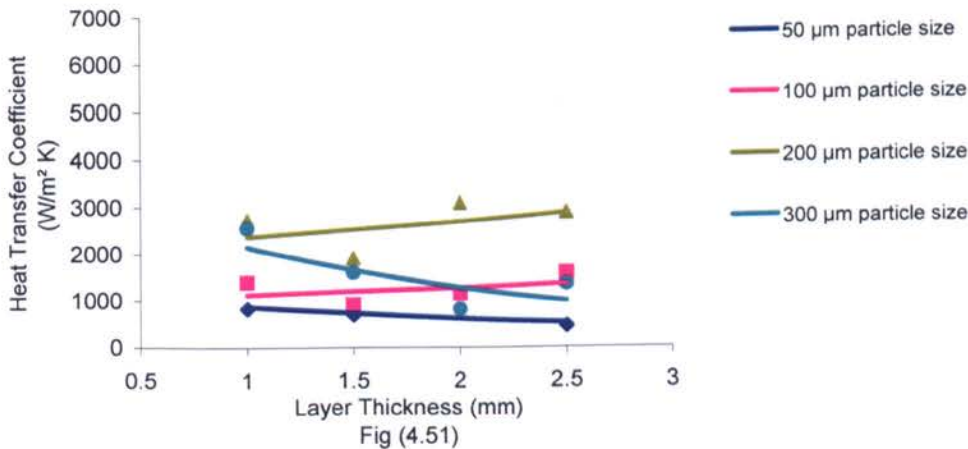
Experimental Boiling Heat Transfer Coefficient Vs Layer Thickness at 3.0 m/s and 25 °C Air Velocity & Temperature



Experimental Boiling Heat Transfer Coefficient Vs Layer Thickness at 3.0 m/s and 30 °C Air Velocity & Temperature



Experimental Boiling Heat Transfer Coefficient Vs Layer Thickness at 3.0 m/s and 35 °C Air Velocity & Temperature



Discussion

5.1 Introduction:

In this chapter, the analytical and experimental results presented and described in chapter three and four are discussed after being re-presented, this time, in a way that facilitates comparison between the two results for the same test conditions, i.e. for the same air inlet temperature and velocity.

The factors that affect the boiling performance of the tested evaporators are listed below:

1. The size of the particles of which the sintered layer is made.
2. The thickness of the sintered layer.
3. Conditions of air at inlet to the evaporator, i.e. air inlet temperature, velocity and humidity.
4. The thermo physical properties of the sintered layer, i.e. porosity, permeability and thermal conductivity.

In effect each factor, bar the last one, is discussed below¹.

5.2 Effect of Particle Size:

The variation of boiling heat rate with particle size is shown in Fig (5.1) to Fig (5.18) for both analytical and experimental results. Boiling heat rates obtained analytically using O'Neil's [35] boiling formula are shown in Fig (5.1) to Fig (5.9) and those obtained using Rao & Balkrishnan [32] formula are shown in Fig (5.10) to Fig (5.18). In this section the effect of particle size on boiling heat rate and on boiling heat transfer coefficient is discussed and the differences between analytical and experimental trends are highlighted and explained.

¹ The evaporators are not designed to test their thermo physical properties as the porosity and thermal conductivity of all the sintered tubes are almost constant.

5.2.1 Experimental Boiling Heat Rates Compared to O'Neil's Analytical Results:

It is evident from Fig (5.1) to Fig (5.9) that the experimental results agree in trend with O'Neil's analytical results in that they increased gradually to a maximum before decreasing. However, the experimental heat rates are noticeably higher than the analytical ones (in average analytical values are about 74% of the experimental ones) and their curves, in general, are steeper on their down-the-hill portion. To better understand the effect of particle size on boiling in a porous structure, four points need to be looked at. These are:

1. Easiness of liquid supply to the nucleation sites.
2. Vapour removal capability of the porous layer.
3. Meniscus shape inside the pores.
4. Excessive capillary pressure.

Each of the above points is discussed briefly below:

1- Easiness of liquid supply to the nucleation sites:

It is known that capillary pressure generated within the porous structure, which is the main pumping force that drives the liquid to nucleation sites, is inversely proportional to the effective capillary radius. In other words, the smaller the particle size (i.e. smaller pore size and smaller effective capillary radius), the larger the capillary pressure. However, the small pore sizes will induce greater resistance to liquid flow hence excessive liquid pressure drop. The analytical work in chapter three explained that to ensure continuity of boiling in the evaporator tubes, capillary pressure should be equal to or greater than the sum of all liquid and vapour pressure drops. The maximum boiling heat rate sustained by the evaporator tubes before boiling cessation occurs due to capillary failure has been defined

Chapter 5: Discussion

as capillary limit heat rate or simply capillary limit². It seems that for small particle sizes large portion of the expectedly high capillary pressure generated is wasted as liquid pressure drop to overcome the high resistance to liquid flow in such small pores. Consequently water flow to small pores is expected to be lower than that for large pores. This suggests that it is possible to have lower boiling heat rates for the small particle sizes than that for large ones due to restricted water flow to the nucleation sites. However, water flow to nucleation sites could be counter productive if it exceeds an optimum value as will be explained later in the following sections.

2- Easiness of Vapour Removal:

Boiling in a porous structure requires rapid removal of vapour to allow continuation of nucleation. In contrast, insufficient vapour removal could result in suppressing the nucleation sites which could eventually lead to their stoppage. This suggests that for larger particle sizes, i.e. larger pores where the possibility of removing the generated vapour is great, boiling is enhanced.

3- Meniscus Shape inside the Channel Pores:

For boiling in porous structures, the formation of a thin film of boiling liquid as part of the liquid menisci that form inside the pores plays an important role in enhancing the boiling; see Fig (1.6). Holm and Goplen [68] found that more than 80% of the total heat dissipation occurred in a very small region of the meniscus thin transition region. Höhmann and Stephan [59] showed that a strong temperature drop, caused by local cooling due to evaporation, occurred in a micro region of the meniscus. Hanlon and Ma [43] confirmed that the thin film region has an essential role in boiling in porous structures. Since for larger pores, the length of the thin liquid film responsible for the bulk of boiling is longer, boiling is expected to be enhanced. The experimental and analytical findings of this

² Fig (5.20) shows a plot for the variation of the capillary limit of the evaporators tested in this research with particle size evaluated at 5 °C temperatures for water inside the evaporator tube. Other limit heat rates are also shown in this figure.

research seem to explain why the performance is enhanced with particle size up to a maximum.

4- Excessive Capillary Pressure:

The capillary pressure is the main driving force for boiling in porous structures and its amount should be greater than or equal to the total vapour and liquid pressure drops to avoid boiling cessation due to reaching the capillary limit. However, excessively high capillary pressure than that needed to overcome the total pressure drops in the tested capillary evaporators could cause the liquid layer in the porous structure to be subjected to a pressure higher than the saturation pressure at the prevailing temperature. This might contribute to hindering liquid boiling at low temperatures. In other words, excessively high capillary pressure might suppress boiling in the tested evaporators in a way possibly similar to the effect of hydrostatic head on boiling in a flooded evaporator. However, it should be stated here that the resistance to liquid flow in the small pores is large, relative to that that in wide pores; hence a greater portion of the high capillary pressure will be wasted in overcoming this resistance. Fig (5.19) shows the variation of the capillary pressure with particle size. It is apparent that the capillary pressure for small particle size evaporators is much higher than that of the large particle ones. This could be a possible cause for the low values of boiling heat rate for the small particle size evaporators.

5.2.1.1 Reasons for Decrease in Boiling Performance after Reaching a Maximum:

Having reached a maximum, associated with optimum particle size, the heat rates starts to either drop, or remain constant as shown by the figures. This can be explained by the following:

a- Reaching the Sonic Limit:

As more vapour is generated with increased particle size due to increased water flow, increased vapour removal capability, longer evaporating thin films and approaching

Chapter 5: Discussion

optimum levels of capillary pressure as explained earlier, the velocity of vapour inside the evaporator tubes increases. The large specific volume of vapour, at the low temperature level prevailing inside the evaporator tubes ($1 - 5\text{ }^{\circ}\text{C}$), results in large vapour velocity which reaches its maximum at the vapour outlet pipe where all the vapour generated inside the individual evaporator tubes accumulates; see Fig (4.2a). This suggests that the increase in vapour velocity could possibly be so high. When vapour velocity reaches that of sound (sonic velocity) the flow becomes choked. This would lead to increased vapour pressure which, in turn, may cause suppression of boiling inside the evaporator. The boiling heat rate at which such a situation occurs is known as the sonic limit. The predicted results using the iterative computational scheme developed in this research showed that the sonic limit decreases with increase in particle size; see Fig (5.20). This explains why the boiling heat rate curves in Fig (5.1) to Fig (5.9) reverse their trends of monotonous increase after reaching a maximum with increasing particle size. It has to be stated here that the increase in the temperature of vapour due to viscous friction in the vapour path would defer the sonic limit but does not stop it from happening.

b- Reaching the Viscous Limit:

The sintered evaporator fitted to a lithium bromide absorption system could be similar to a heat pipe working at very low temperatures. The increased vapour generation rate with increase in particle size as explained earlier could possibly lead to increased viscous forces within the vapour region. When these viscous forces become larger than the pressure gradient between the evaporator and absorber, then vapour flow to the absorber may stagnate or becomes very low. The occurrence of this condition is known as viscous limitation in heat pipes and it is quite possible that it has occurred in the capillary evaporators tested in this research. The analytical calculation carried out in this research showed that the viscous limit decreases with the increase of the particle size; see Fig (5.20). Thus, it is reasonable to assume that this limit might have interrupted the increase of

Chapter 5: Discussion

the boiling heat rate with increasing particle size and forced it to decrease after reaching a maximum as it appears in Fig (5.1) to Fig (5.9).

c- Reaching the Capillary Limit:

The analytical calculations showed that the capillary limit decreases with increasing particle size. This is logical as the capillary pressure, which is the main deriving force for pumping the liquid in capillary structures, is inversely proportional with the effective pore radius, i.e. inversely proportional with the particle size. Thus, as the particle size increases, the capillary limit is expected to restrict the increase in boiling heat rate. A factor that could accelerate the occurrence of the capillary limit is the high vapour velocities in the evaporator and adiabatic section. The high vapour velocities would result in high friction losses which increase vapour pressure drop and vapour temperature as well. Ultimately, this might prevent the boiling heat rate exceeding a certain limit when the sum of vapour and liquid pressure drops exceeds the total capillary pressure generated by the porous wick. The occurrence of such condition is known in heat pipe theory as capillary limit. The fact that the capillary limit, which was calculated as explained in section (3.9.3), is found to decrease as the particle size increases, is possibly an essential factor in forcing the monotonously increasing boiling heat rate to reverse its direction.

5.2.1.2 Discrepancies between O'Neil's Analytical Results and the Experimental

Ones:

Although analytical results using O'Neil's formula agree well with the experimental ones in trend, some differences are evident. The analytical boiling heat rates are less, in value, than the experimental ones and their curves are less steep in their down-the-hill portion. Also, it is noticeable that the peak value for most of the experimentally obtained boiling heat rates occurs approximately at the 200 μm particle size whereas most of the analytically obtained results reach their peaks approximately at the 100 μm particle size. In

Chapter 5: Discussion

explanation to these differences it has to be stated here that the error percentages of the equations used in the iterative computational scheme have been taken into account. This might have resulted in widening the gap between predicted and experimental values of boiling heat rates. To interpret the high rate of decrease in experimental boiling heat rates after reaching their peak referral is made to the notion of Zhang & Zhang [38] who explained that ejection of vapour from within the wick pores produces a suction force that sucks the liquid and supply it to the vapour nucleation sites. The wider pores for larger particle sizes would result in increased vapour generation rate as explained earlier due to easiness of liquid supply, higher vapour removal capability and long evaporative thin liquid film. Bearing in mind the notion of Zhang & Zhang [38], it might be right to assume that increase in vapour generation rate might cause increased suction force that draws extra liquid flow to the nucleation sites. The excess water supply to the nucleation sites would act counter productively to boiling as indicated earlier in this section by increasing the level of liquid inside the nucleation sites i.e. increasing the hydrostatic head and consequently the saturation temperature. Hence, the nucleation sites would be functioning under conditions that could be described as suboptimum conditions in terms of water flow rate and saturation temperature. Thus, the capability of the nucleation sites to transform all the water fed to them into vapour would be impaired³. Eventually, this would cause deterioration in the boiling performance of the large particle size evaporators. The iterative computational programme doesn't account for flooding some nucleation sites with additional supplement of water. This might explain the discrepancy between the experimental and analytical trends of boiling heat rates. Furthermore, the discrepancy could be furthered by inaccuracies of the formula used (O'Neil), which are not specified by

³ The occurrence of impaired functioning of the nucleation sites due to excessive water flow will be referred to in the rest of this thesis as flooding of nucleation sites.

its authors. It is also possible that systematic and random errors, though small, may have contributed to the discrepancy.

5.2.2 Experimental Boiling Heat Rates Compared to Rao and Balkrishnan's

Analytical Results:

The boiling heat rates obtained using Rao & Balkrishnan's [32] boiling formula are shown in Fig (5.10) to Fig (5.18) together with the experimental ones. It is evident that Rao & Balkrishnan's results increase monotonically with the increase in particle size for the range of particle size tested. It is not known whether they will increase to a maximum and then decrease again for larger particle sizes or not. However, this trend appears to confirm the explanation given in section (5.2.1) that high liquid pressure drops, difficulty of vapour removal, short thin evaporating films and excessive capillary pressures seem to be major constraints of boiling in the small particle size evaporators. The results of Rao & Balkrishnan [32] boiling formula seem to comply well with the rule stated earlier that the boiling heat rate should be lower than the smallest heat transfer limit. In spite of that, they fail to demonstrate the fact that at a certain point sonic, viscous or capillary limit would interrupt the monotonous increase of boiling heat rate with increasing particle size and force the boiling heat rate to decrease. However, it might not be possible to confirm whether this would not happen if particle size range larger than the one investigated in this research (50 to 300 μm) is inspected. It is apparent from the figures that these boiling heat rates are very low compared to the experimental ones shown in the same Figures (in average analytical values are about 30% of the experimental ones). This low value is probably an indication of lack of accuracy and reliability of Rao and Balkrishnan [32] boiling formula in evaluating boiling heat rates. The formula adopts Darcy's law which evaluates the liquid mass flow rate through the porous wick by evaluating the resistance to liquid flow between two points along a porous structure; see equation (5.1), below, and Fig (5.22):

$$-\frac{dP}{dx} = \frac{\mu}{K} V_D \dots\dots\dots(5.1)$$

Kaviany [4] explained that Darcy's model, which has been extensively examined, is not closely followed for liquid flows at high velocities and for gas flows at very low and very high velocities. Rao and Balkrichanan [32] did not verify, in deriving their model for boiling in porous structures, that the velocity of the vapour leaving the porous wick lies within a safe range to that which justifies using Darcy's law. Thus, the accuracy of their model is seemingly questionable. More over, the fact that during boiling the porous wick is occupied with a mixture of vapour and liquid flowing in different directions and that the intensity of each nucleation site is different from one another makes it quite impossible to attain uniform vapour velocity as Fig (5.21) suggests. For all the above reasons, it is believed that Balkrishnan's formula is not reliable. Its inclusion in this study is done for the purpose of completion.

5.2.3 Experimental Boiling Heat Transfer Coefficient Compared to O'Neil's Analytical Results:

The variation of boiling heat transfer coefficients obtained analytically using O'Neil's [35] boiling formula versus particle size is shown in Fig (5.22) to Fig (5.30). The experimental heat transfer coefficient curves seem to either pass through a peak or increase at a diminishing rate. The latter trend indicates that these heat transfer coefficients approach a peak value or plateau outside the range of particle size tested. The trend of the experimental heat transfer coefficient is followed largely by the analytical curves for particle sizes 50, 100 and 200 μm , i.e. up to the peak of the experimental curves. Beyond that point the analytical curves continue to rise but at a lower rate. This is thought to be due to the fact that the analytical model underestimates the wall superheat temperatures. The average experimental wall superheats are found to be in the range of 1 – 5 $^{\circ}\text{C}$ whereas the analytical one is in the range of 0.2 – 2 $^{\circ}\text{C}$. In explanation to this discrepancy, the

Chapter 5: Discussion

following arguments are presented as possible causes for the higher experimental wall superheats:

- 1- The relatively high liquid flow to the nucleation sites linked with larger particle sizes as explained in section (5.2.1) might have played a role in this discrepancy. For large particle sizes liquid is not just supplied to the nucleation sites by capillary effect but additional liquid is fed to them by the suction force resulting from vapour ejection. This relatively high liquid flow leads to flooding some of the nucleation sites with water and eventually causes retarded rate of heat exchange between the tube wall and the liquid inside the tube due to decreased boiling. That would be reflected in an increased wall temperature hence increased wall superheats.
- 2- Once the wick is flooded with water as explained above, the vapour removal capacity will relatively be degraded. That might lead to the formation of thin vapour film separating the bulk of the wick from the tube wall, which in turn, would decrease exchange of heat between the tube wall and the liquid inside the tube. Also, that would be reflected in an increased wall temperature hence increased wall superheats.
- 3- The formation a thick film of vapour that prevents the liquid from reaching the heated surface is a possible scenario for the increased wall superheats of the experimental results. However, this scenario might be ruled out to some extent because of the following:
 - a) In most of the tests the evaporator inlet temperature was either stable or had a slight tendency to decrease with passage of time. Had a thick film of vapour formed, then liquid supply to the heating surface would have likely been prevented and that would have lead to rapid tube wall temperature rise.
 - b) Theoretically the formation of a thick vapour layer preventing the liquid from reaching the heating surface is known as the boiling limit (refer to section 1.5.14.2 for the explanation of the boiling limit). The analysis adopts Peterson's

[5] nucleation site radius of 2.54×10^{-6} m for evaluating the boiling limit for the tested evaporators. This is thought to result in an overestimation of the boiling limit. The implication of a high boiling limit is that the excessive vapour formation dries out the nucleation sites and increases the superheat temperature. It has to be stated here that the points stated in the explanation given in points 1, 2 & 3 above have not been accounted for in the analytical model. This could possibly be the reason behind the low wall superheats obtained analytically.

5.2.4 Experimental Boiling Heat Transfer Coefficient Compared to Rao & Balkrishnan's Analytical Results:

The boiling heat transfer coefficient obtained analytically using Rao and Balkrishnan's [32] boiling formula versus particle size is shown in Fig (5.31) to Fig (5.39). It is apparent from these figures that the analytical boiling heat transfer coefficient is small compared to the experimental one. This might be due to using Clapeyron equation in deriving the analytical model for boiling in porous structures by Rao and Balkrishnan [32] in addition to the thought shortcoming of using Darcy's law explained in section (5.2.2). The Clapeyron equation is given by [95]:

$$\frac{dP}{dT} = \frac{\lambda_{12}}{T(v_2 - v_1)} \dots\dots\dots (5.2)$$

Under saturation conditions, $T = T_{sat}$, $P = P_{sat}$, thus, dP in equation (5.2) represents the change in saturation pressure due to change of state from 1 to 2 i.e. from liquid to vapour in the case of water boiling. This concept becomes clearer if the latent heat in equation (5.2) is expressed in terms of entropy change i.e. $\lambda = T\Delta S$. Thus, equation (5.2) becomes:

$$\frac{dP}{dT} = \frac{s_2 - s_1}{v_2 - v_1} \dots\dots\dots (5.3)$$

Equations (5.2) & (5.3) show that the change in pressure, dP , of Clapeyron equation is related to change of state (due to boiling). In deriving their model for boiling in porous

Chapter 5: Discussion

media, Rao and Balkrishnan [32] substituted for dP in equation (5.2) by the value of vapour pressure drop across the porous layer which they obtained from equation (5.1). It seems inaccurate to substitute for dP in equation (5.2) by the value of dP obtained from equation (5.1). In other words, whilst the change in pressure in Clapeyron equation is due to phase change from liquid to vapour, Rao and Balkrishnan [32] dealt with it as a pressure drop due to vapour flow across the porous layer. This may explain the low values for the analytical boiling heat transfer coefficient along with low boiling heat rates when using the boiling formula developed by Rao and Balkrishnan [32].

5.3 Effect of Layer Thickness:

The effect of varying layer thickness on boiling heat rates and heat transfer coefficients is shown in Fig (5.40) to (5.57). In this section, this effect is discussed and the differences between analytical and experimental trends are highlighted.

5.3.1 Experimental Boiling Heat Rate Compared to O'Neil's Analytical Results:

It is apparent from Fig (5.40) to Fig (5.48) that the dependency of boiling heat rate (both experimental and analytical) on layer thickness is not strong. The analytical results are in line with experimental ones; however, the experimental results are relatively higher than the analytical ones. The 200 μm particle size curve seems to outperform other particle sizes for all layer thicknesses. The varying effects of the layer thickness on the boiling performance curves (which rise up in some cases and fall down in others) are probably the result of contradicting factors. The following factors form a possible cause of decrease in boiling heat rate with increased porous layer thickness:

1. The thermal resistance of the porous layer increases with increasing layer thickness; hence the boiling heat rate decreases in this direction.
2. An increase in the porous layer thickness means a decrease in the vapour core diameter which in turn leads to a decrease in the viscous limit due to increased viscous forces within the vapour region. This, again, leads to decreased heat rates.

Chapter 5: Discussion

3. A decrease in the vapour core diameter also leads to a decrease in the sonic limit due to increased vapour velocity leading to decreased thermal performance.

On the other hand, a number of factors lead to boiling augmentation with increasing porous layer thickness; these are:

1. A thicker porous layer allows the nucleation sites to increase in number.
2. A thicker porous layer thickness allows better coalescence of vapour jets which leads to increased water flow, i.e. better liquid feeding to the nucleation sites, through the increased suction force created by the large-size vapour jets.

The fact that the curves shown in Fig (5.40) to Fig (5.48) show varying effects of the layer thickness on boiling performance could be an indication that the general trend with larger ranges of layer thickness is one of a wavy nature. This suggests the existence of more than one optimum condition of performance which presents the designer with more flexibility in choosing the system parameters.

5.3.2 Experimental Boiling Heat Rate Compared to Rao & Balkrishnan's Analytical

Results:

The variation of the experimental boiling heat rates and the analytical ones obtained using Rao & Balkrishnan [32] boiling formula with layer thickness is shown in Fig (5.49) to Fig (5.57). The analytical values are much lower than the experimental ones and show that the variation of the boiling heat rate with layer thickness is insignificant. This finding is in line with the results obtained using O'Neil's boiling formula. The justifications given in section (5.2.2) and (5.2.4) for the possible shortcomings of Rao and Balkrishnan [32] boiling formula are thought to be behind the low values of boiling heat rates obtained using their model.

5.3.3 Experimental Boiling Heat Transfer Coefficient Compared to O'Neils's

Analytical Results:

The variation of experimental and analytical boiling heat transfer coefficients with layer thickness is shown in Fig (5.58) to (5.66). The relatively weak influence of the layer thickness, compared to that of particle size, on the boiling performance is again reflected on these figures. The analytical values of boiling heat transfer coefficient are somewhat higher than the experimental ones. In the analytical results the larger particle sizes are seen to outperform the smaller ones. This is also true for the experimental results except that the 200 μm is consistently achieving the best results of which some of the points of the evaporator of 2 mm layer thickness lie unexplainably far from the trend line.

The low values of the analytical wall superheats, especially for larger particle sizes as explained in section (5.2.3), is thought to be behind the fact that the analytical results are better than the experimental ones. Furthermore, the fact that the interfacial temperature, T_i , has been neglected in evaluating the analytical boiling heat transfer coefficient might have had a role in attaining low analytical wall superheat values. In addition, the explanation given in section (5.2.3) for obtaining high values of experimental wall superheat could be behind the discrepancy between the analytical and experimental boiling heat transfer coefficients. The combination of the contradicting factors explained in section (5.3.1) that could lead to a decrease/increase in boiling heat rate, depending on which factor dominates the boiling process, could be behind the rising and falling curves of Fig (5.58) to (5.66).

5.3.4 Experimental Boiling Heat Transfer Coefficient Compared to Rao & Balkrishnan's Analytical Results:

The variation of the experimental and analytical boiling heat transfer coefficients with layer thickness is shown in Fig (5.67) to (5.75). The figures show that the layer thickness has little or no effect on the boiling heat transfer coefficient. The very low values of the analytical boiling heat transfer coefficients are a remarkable feature. The effect of

Chapter 5: Discussion

neglecting the interfacial temperature on estimating the analytical boiling heat transfer could have contributed to the low heat transfer coefficient of Rao and Balkrishnan. In addition to the inherent inaccuracies of this boiling formula, which were explained in section (5.2.2) and (5.2.4) are another contributory to the low values of the analytical boiling heat transfer coefficients.

5.4 Effect of Air Inlet Conditions:

The conditions of air at inlet to the evaporator; namely air inlet temperature, velocity and humidity, have varying effect on the boiling performance of the evaporators tested in this research. In this section the effect of these parameters is discussed:

5.4.1 Effect of Air Inlet Temperature and Velocity:

Fig (5.76) to Fig (5.81) show the effect of air inlet velocity and temperature on the experimentally obtained boiling heat transfer coefficients. It could be concluded from these figures that the boiling performance was largely independent or perhaps slightly dependant on air temperature and velocity. This finding agrees well with the results obtained analytically as shown in Fig (5.82) to Fig (5.93). The dependency on velocity seems to be slightly stronger than on temperature. In explanation to this trend, it is first noted that the air conditions affect the boiling through increasing the forced convection and condensation heat transfer components on the outside of the evaporator tubes as indicated by equations (3.25) to (3.28) and equation (3.30). In this case, however, the velocity increases three folds- from 1 to 3 m/s, whereas the air temperature increase is relatively moderate; 25 to 35 °C. Therefore, the magnitude of velocity change compared with that of the air can explain the slightly stronger dependency on velocity.

5.4.2 Effect of Air Inlet Relative Humidity:

The relative humidity of air at inlet to the evaporators is expected to have considerable effect on the performance of the tested evaporators. The evaporator tube's surface temperatures were typically in the range of 0.6 -10 °C, i.e. well below the dew point of the

load air. This resulted in condensation on the tube’s surface. The latent heat of condensation represented an important part of the total heat transferred by the evaporators. In fact, the results revealed that the amount of heat transferred by condensation of air moisture on the evaporator tubes’ surface was greater than that transferred by convection from load air. This could be seen in Fig (5.94) to (5.102)⁴. Thus, considerable part of the cooling capacity of the evaporator; affected through boiling the water inside the evaporator tubes, is wasted in condensing some of the air moisture instead of sensibly cooling the air. This analytical finding is inline with the experimental measurements taken for the air outlet temperature which showed that the drop in air temperature is relatively small. It must be stated that in the iterative computational scheme developed in this research the condensation heat rate, Q_{cond} , is given by:

$$Q_{cond} = h_{cond} A_T (T_a - T_w) \dots\dots\dots(3.32)$$

The above expression ignores the interfacial temperature⁵, T_i . It might be argued that, using the tube wall temperature, T_w , instead of the interfacial temperature, T_i , had led to higher values of the condensation heat rate Q_{cond} since T_w is invariably smaller than T_i . However, this bias is probably balanced by neglecting T_i when calculating the convective heat rate, Q_{conv} , which was calculated using equation (3.29):

$$Q_{conv} = h_{conv} A_T (T_a - T_w) \dots\dots\dots(3.29)$$

Furthermore, the interfacial temperature, T_i , is very close to the tube wall temperature, T_w , as the condensate film on the evaporator tubes was visually observed to be thin. However, had the interfacial temperature T_i , been taken into account, it would have considerably complicated the iteration process and jeopardised the conversion of the computational scheme.

⁴ These figures only show representative layer thickness, air velocity & temperature to avoid explosion of curves in this thesis.
⁵ The interfacial temperature is the temperature on interface between the condensate film and the air stream. The condensate film is the liquid layer that forms on the tubes’ surface due to condensation of air moisture.

Chapter 5: Discussion

In an attempt to study the effect of air moisture content on the performance of the capillary-assisted evaporators, a model incorporating air inlet relative humidity was built. In this model the boiling, convective and condensation heat rates were calculated using the equations given in chapter three⁶. The solutions obtained from this model were patchy resulting from singular points, at which unreasonably high boiling heat rates values were noted. This might be attributable to the incompatibilities in application conditions and accuracies between the different formulae used in this model, which were mostly empirical.

⁶ The flow chart of this computational scheme is shown in appendix D.

Experimental & Analytical (O'Neil) Boiling Heat Rates Vs Particle Size
at 1.0 m/s & 25 °C Air Velocity and Temperature

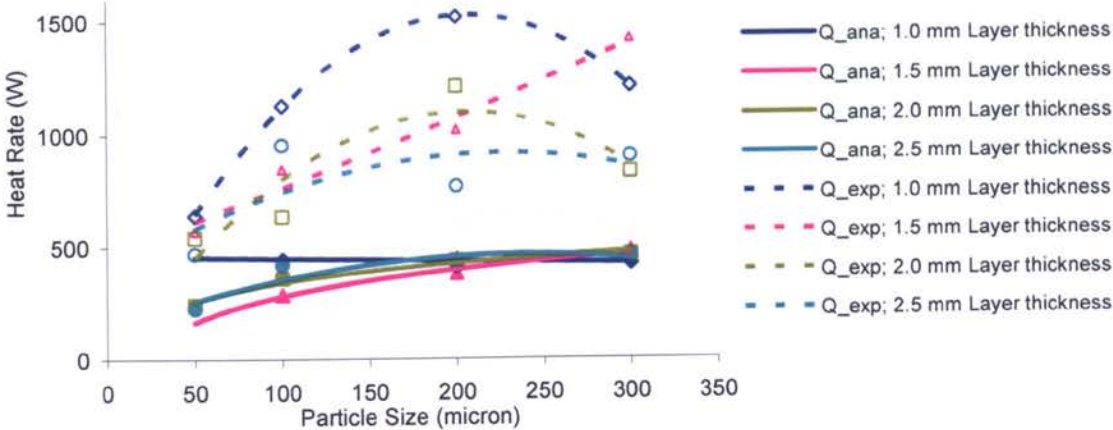


Fig (5.1)

Experimental & Analytical (O'Neil) Boiling Heat Rates Vs Particle Size
at 1.0 m/s & 30 °C Air Velocity and Temperature

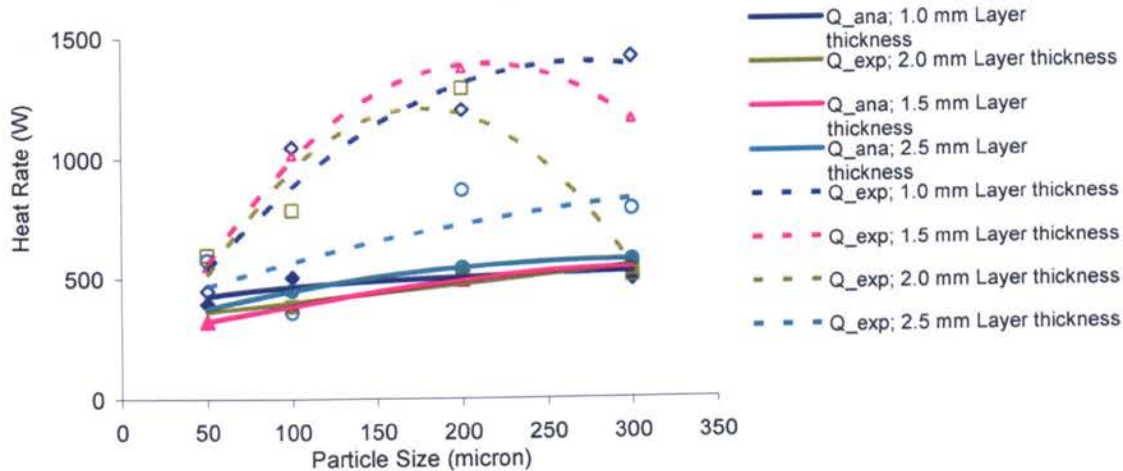


Fig (5.2)

Experimental & Analytical (O'Neil) Boiling Heat Rates Vs Particle Size
at 1.0 m/s & 35 °C Air Velocity and Temperature

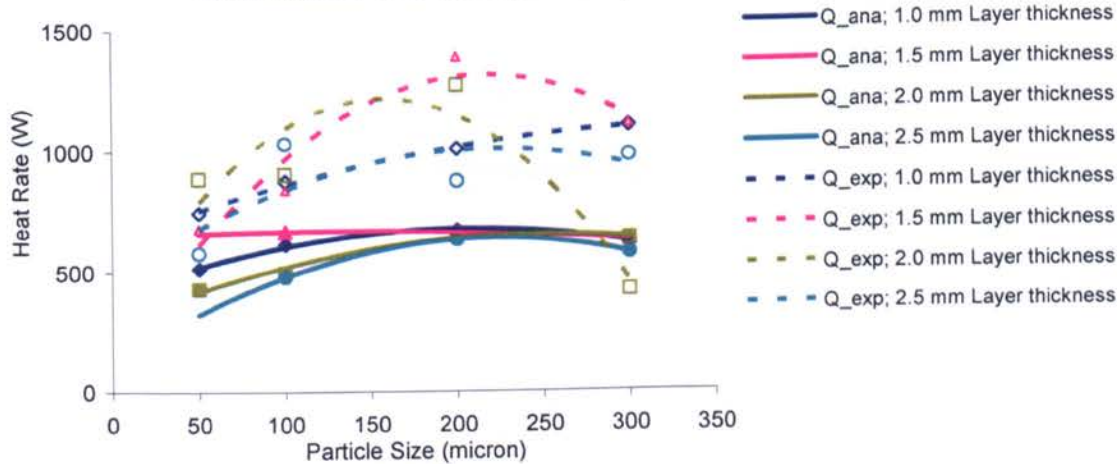
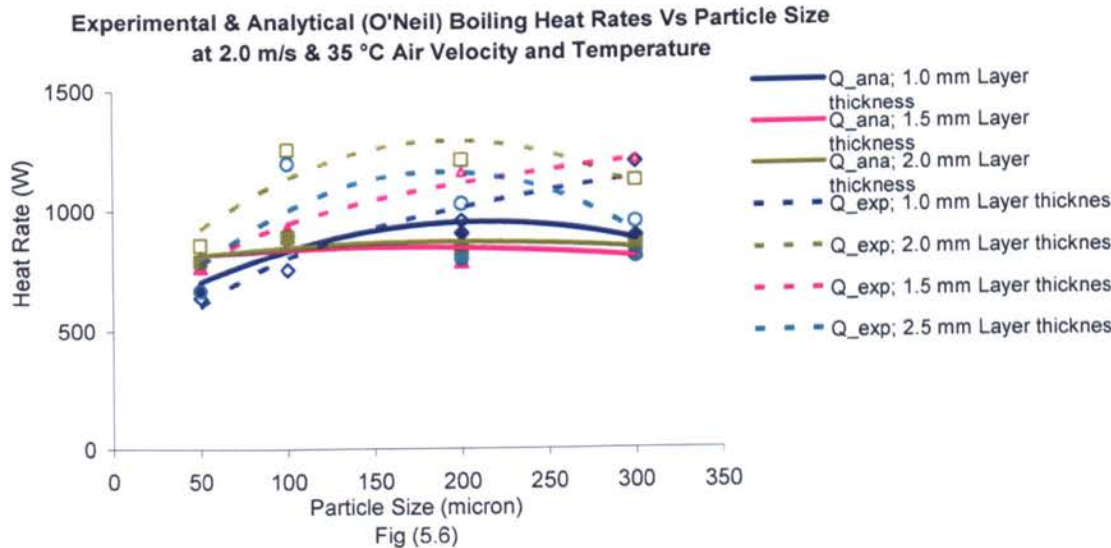
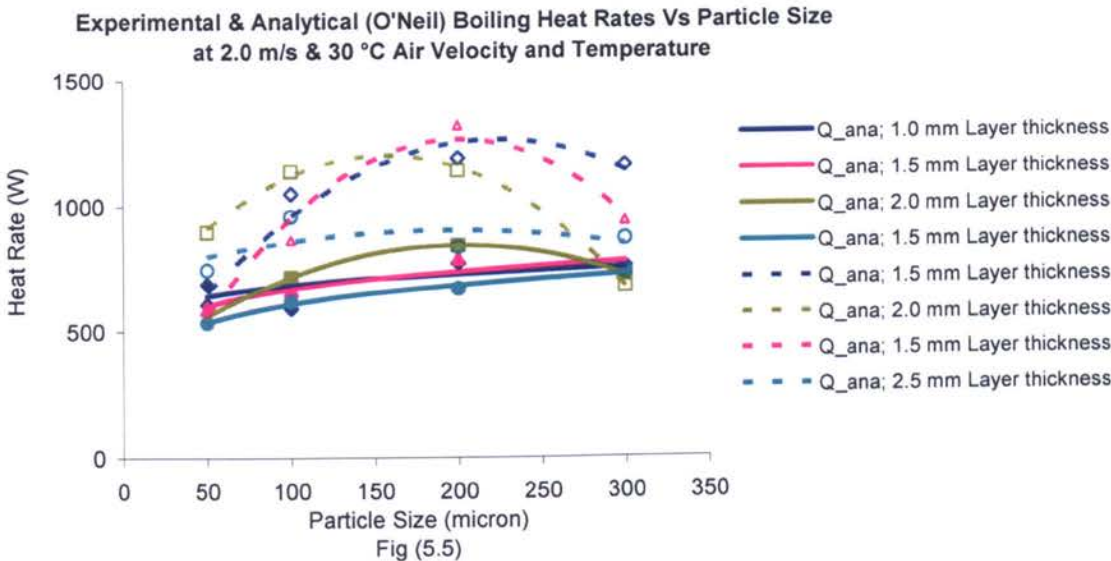
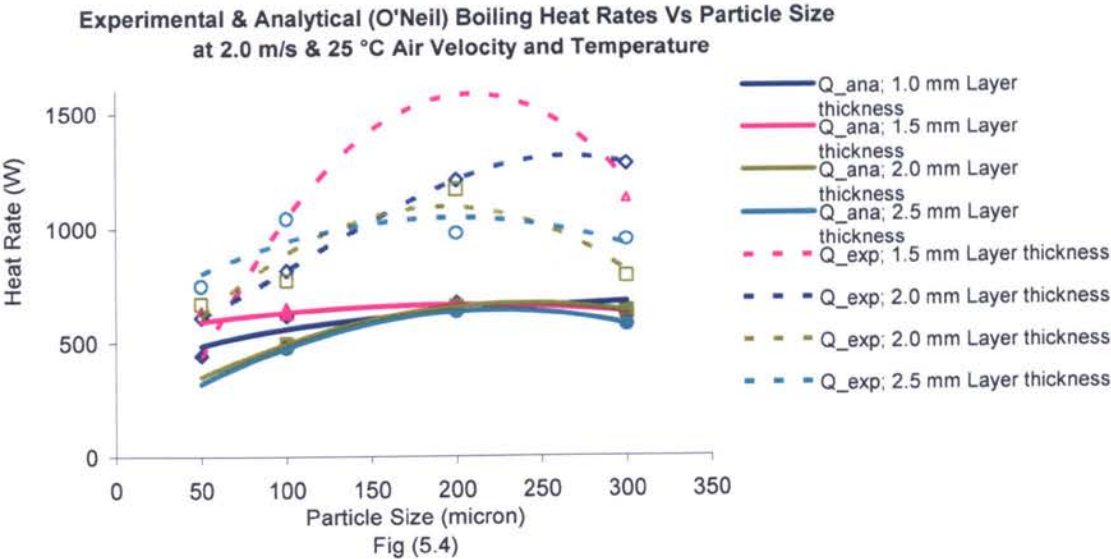


Fig (5.3)



Experimental & Analytical (O'Neil) Boiling Heat Rates Vs Particle Size
at 3.0 m/s & 25 °C Air Velocity and Temperature

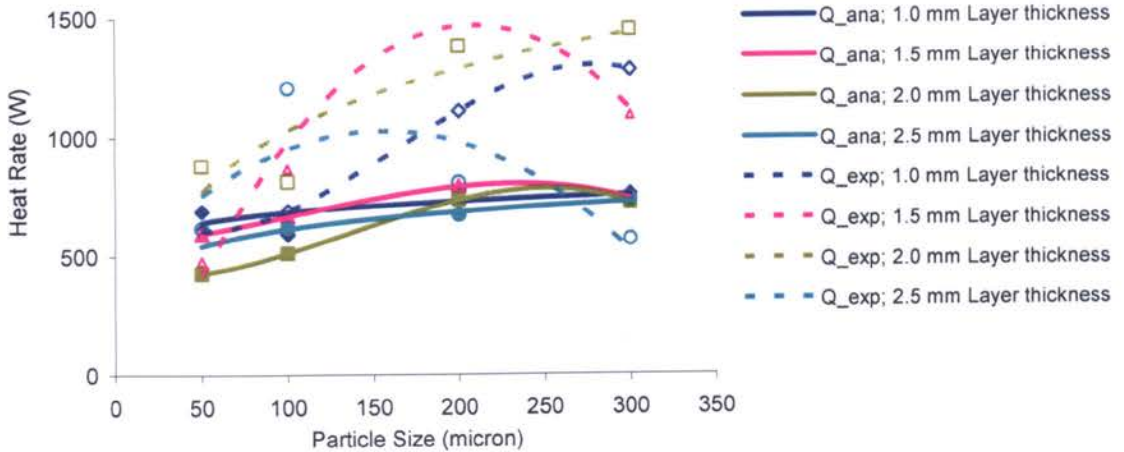


Fig (5.7)

Experimental & Analytical (O'Neil) Boiling Heat Rates Vs Particle Size
at 3.0 m/s & 30 °C Air Velocity and Temperature

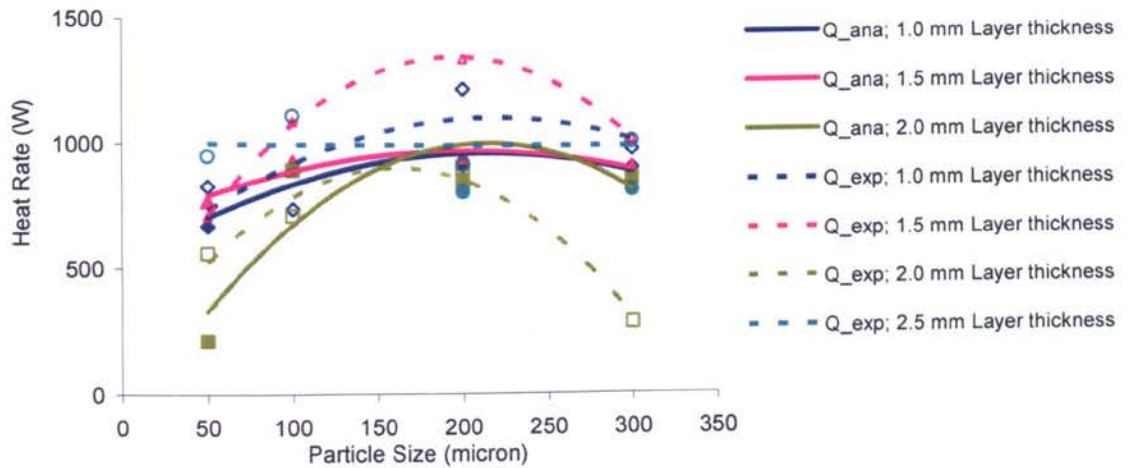


Fig (5.8)

Experimental & Analytical (O'Neil) Boiling Heat Rates Vs Particle Size
at 3.0 m/s & 35 °C Air Velocity and Temperature

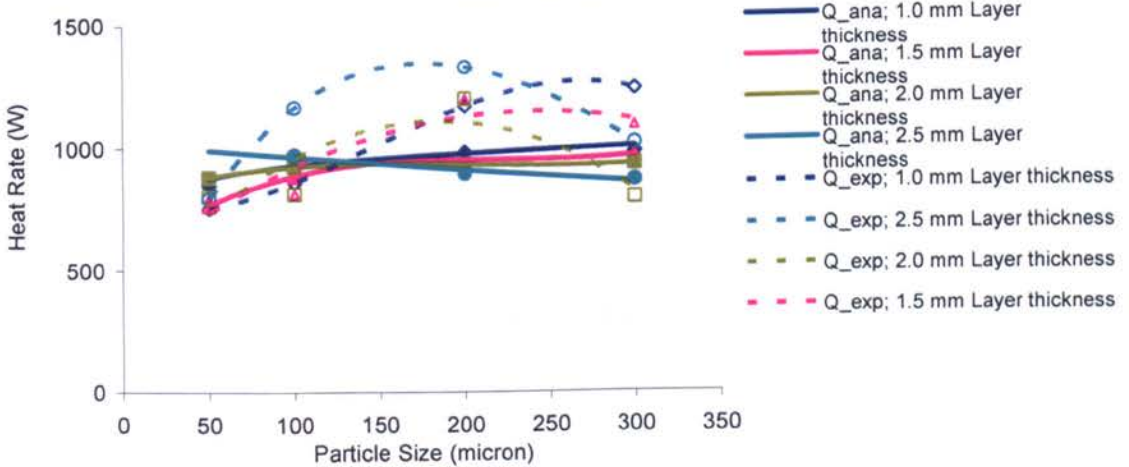
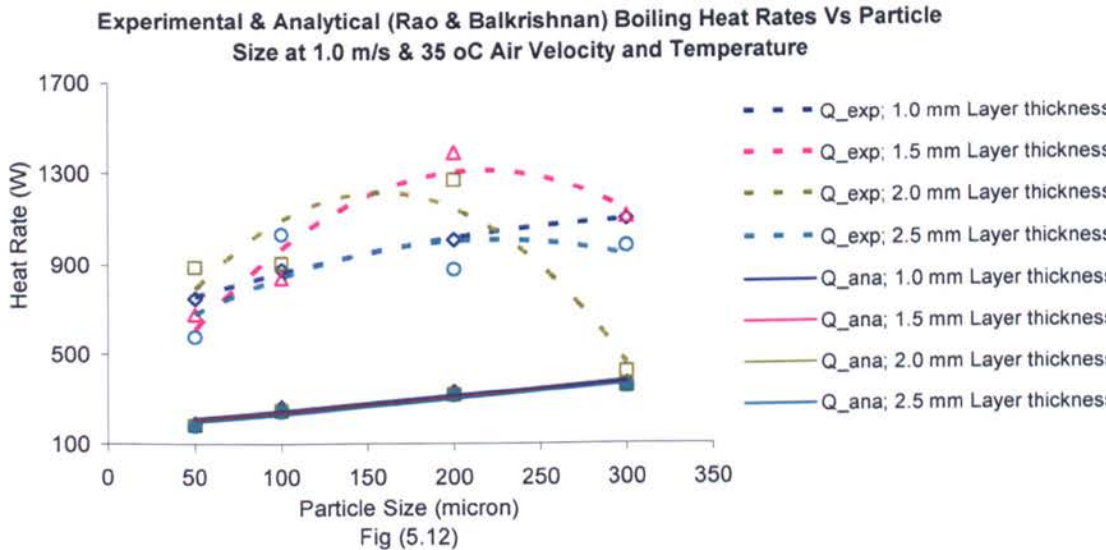
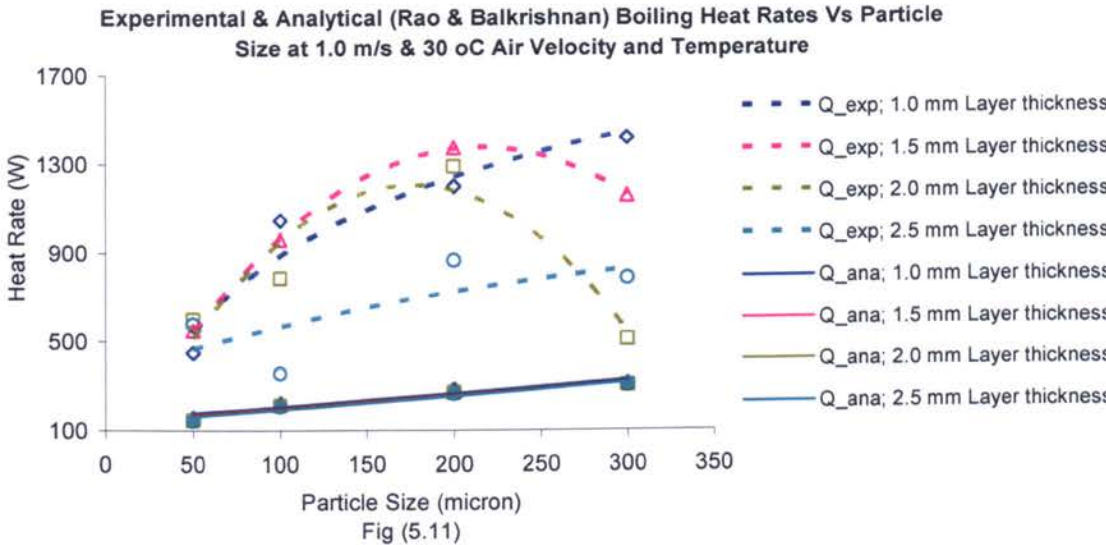
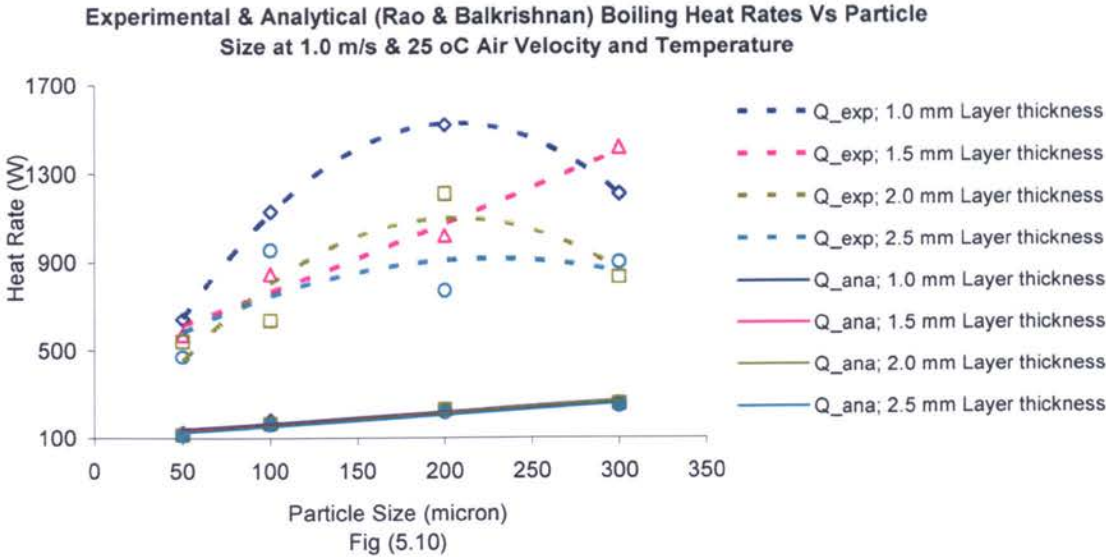
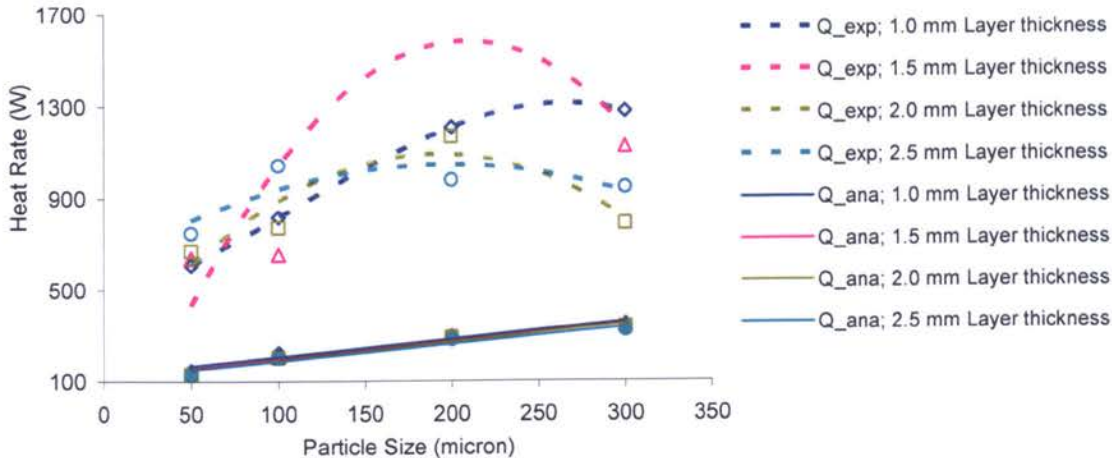


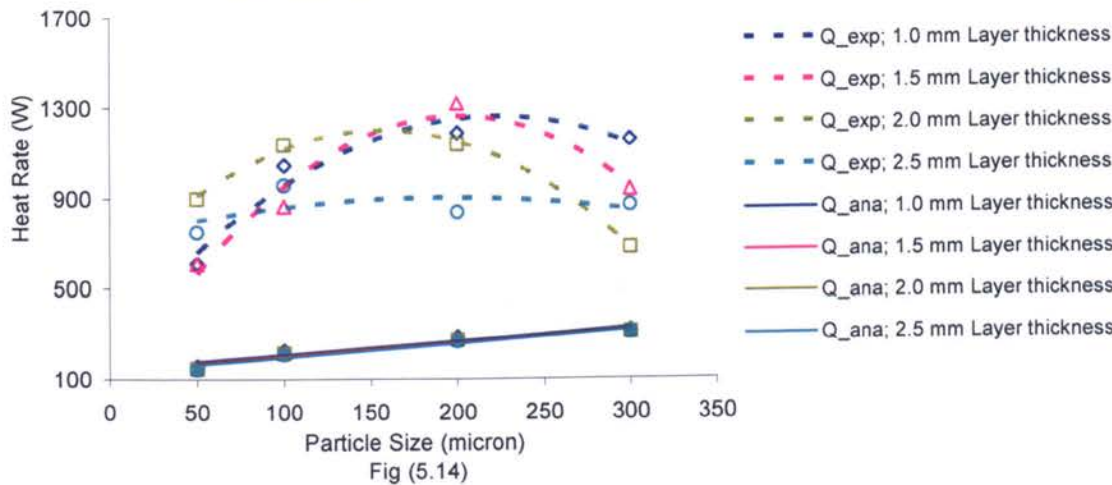
Fig (5.9)



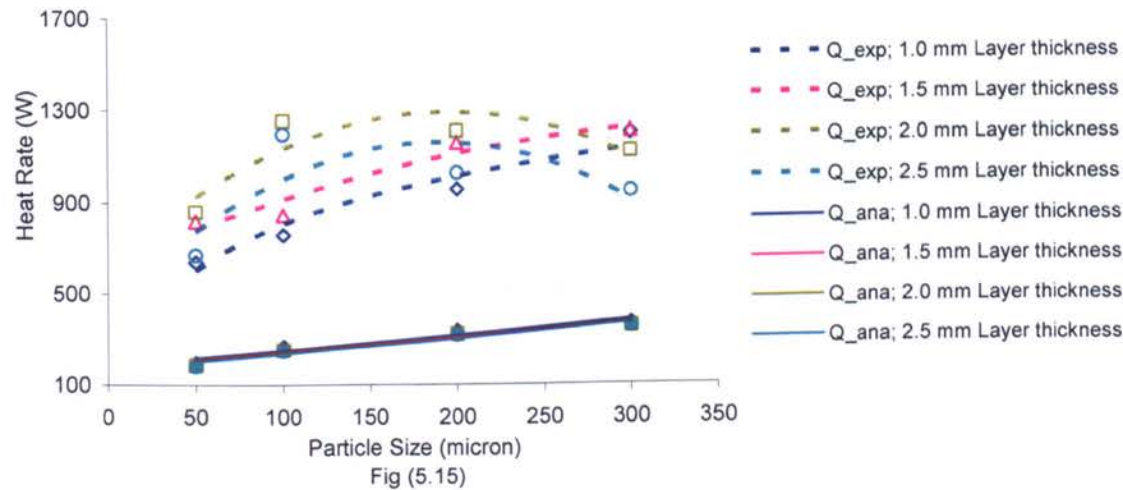
Experimental & Analytical (Rao & Balkrishnan) Boiling Heat Rates Vs Particle Size at 2.0 m/s & 25 oC Air Velocity and Temperature



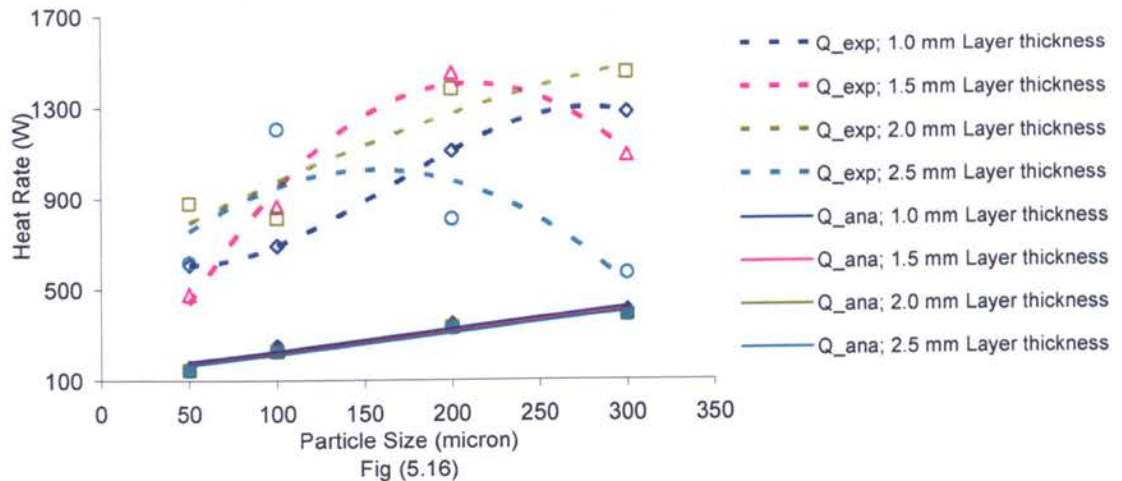
Experimental & Analytical (Rao & Balkrishnan) Boiling Heat Rates Vs Particle Size at 2.0 m/s & 30 oC Air Velocity and Temperature



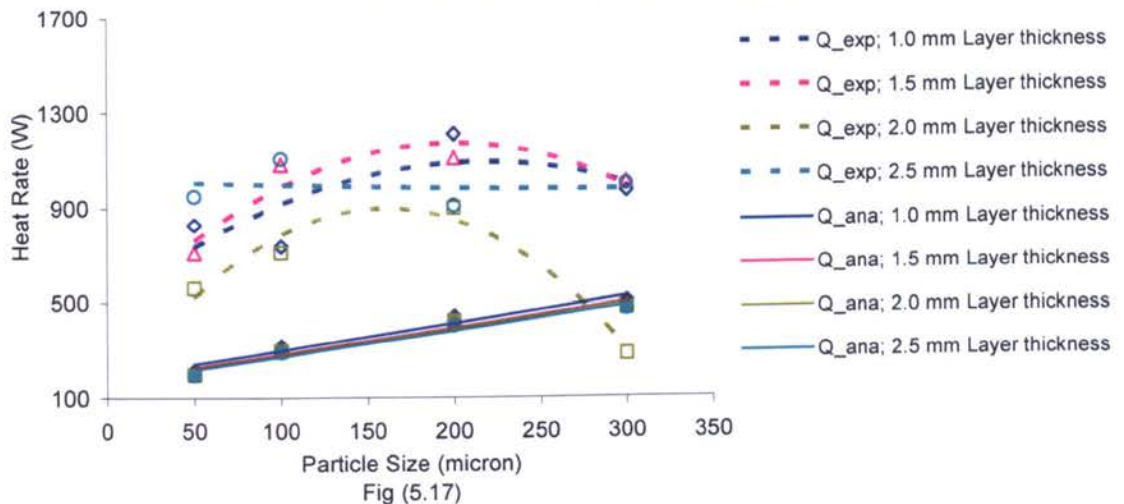
Experimental & Analytical (Rao & Balkrishnan) Boiling Heat Rates Vs Particle Size at 2.0 m/s & 35 oC Air Velocity and Temperature



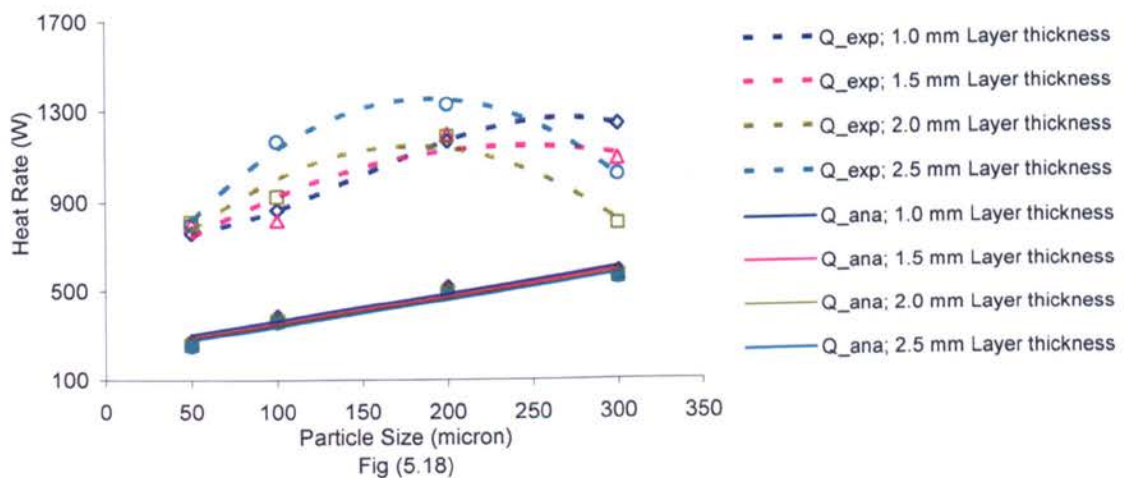
Experimental & Analytical (Rao & Balkrishnan) Boiling Heat Rates Vs Particle Size at 3.0 m/s & 25 oC Air Velocity and Temperature

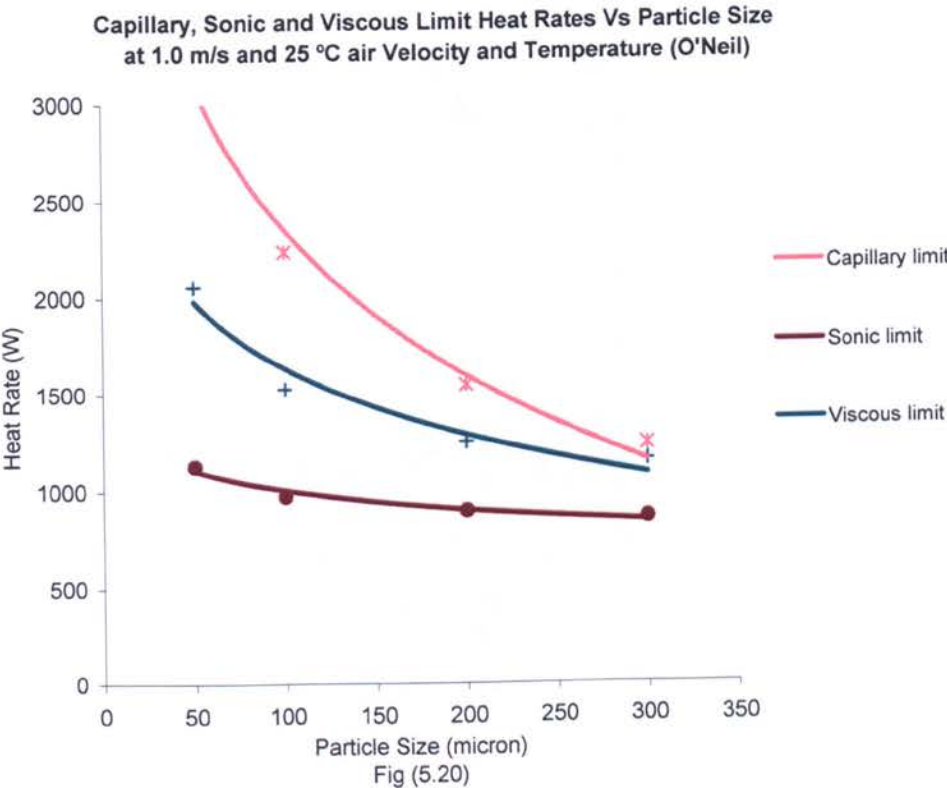
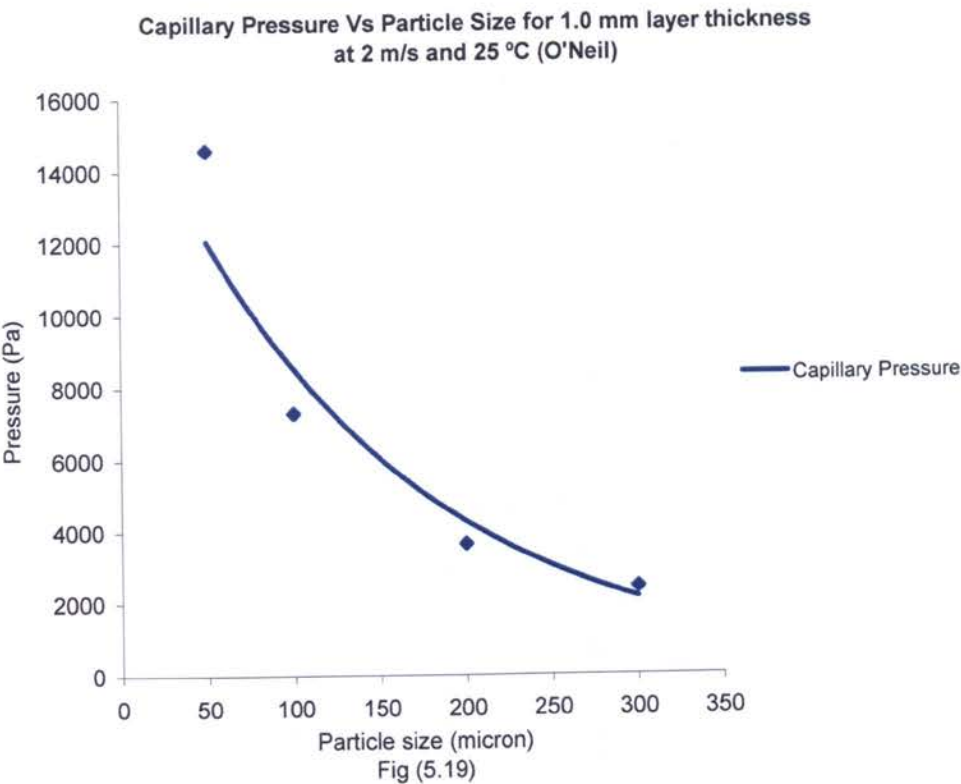


Experimental & Analytical (Rao & Balkrishnan) Boiling Heat Rates Vs Particle Size at 3.0 m/s & 30 oC Air Velocity and Temperature



Experimental & Analytical (Rao & Balkrishnan) Boiling Heat Rates Vs Particle Size at 3.0 m/s & 35 oC Air Velocity and Temperature





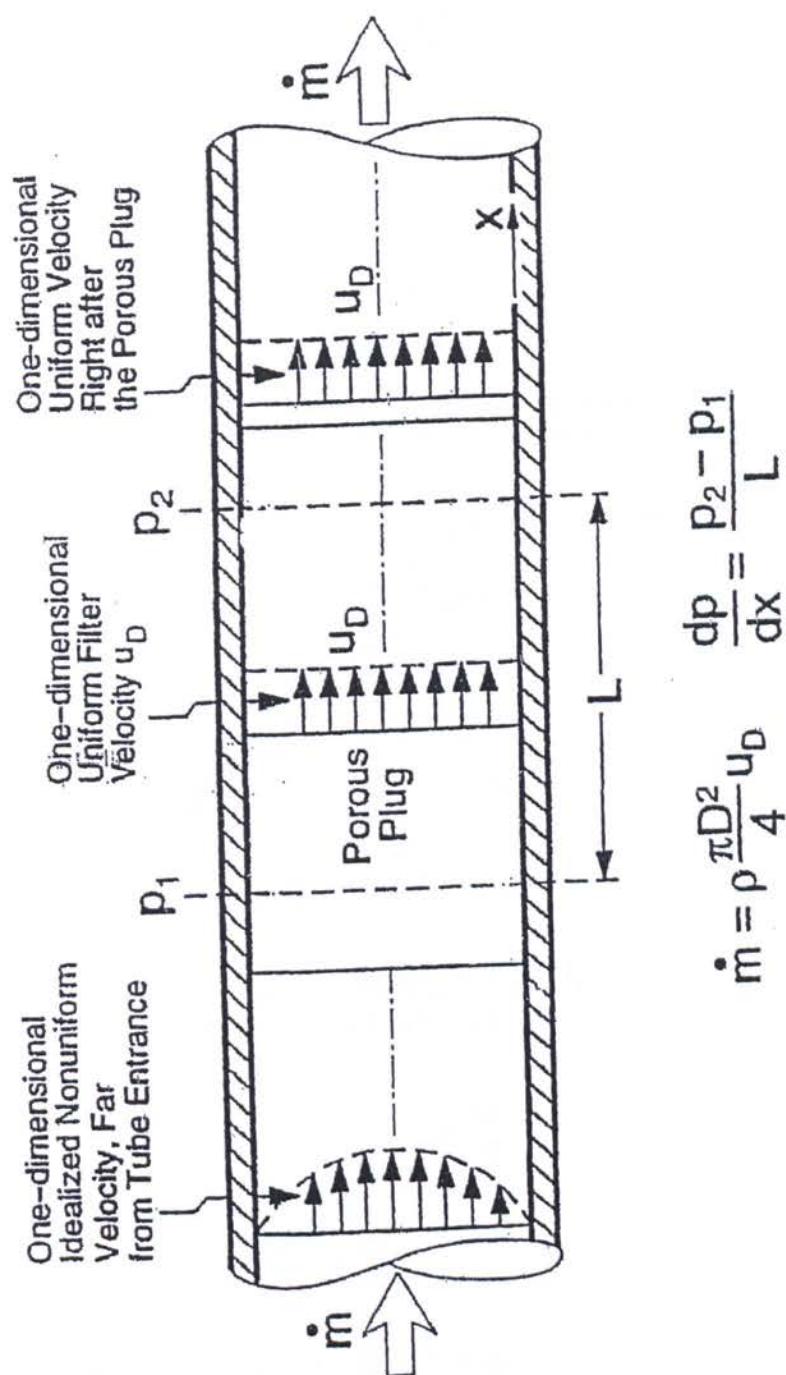
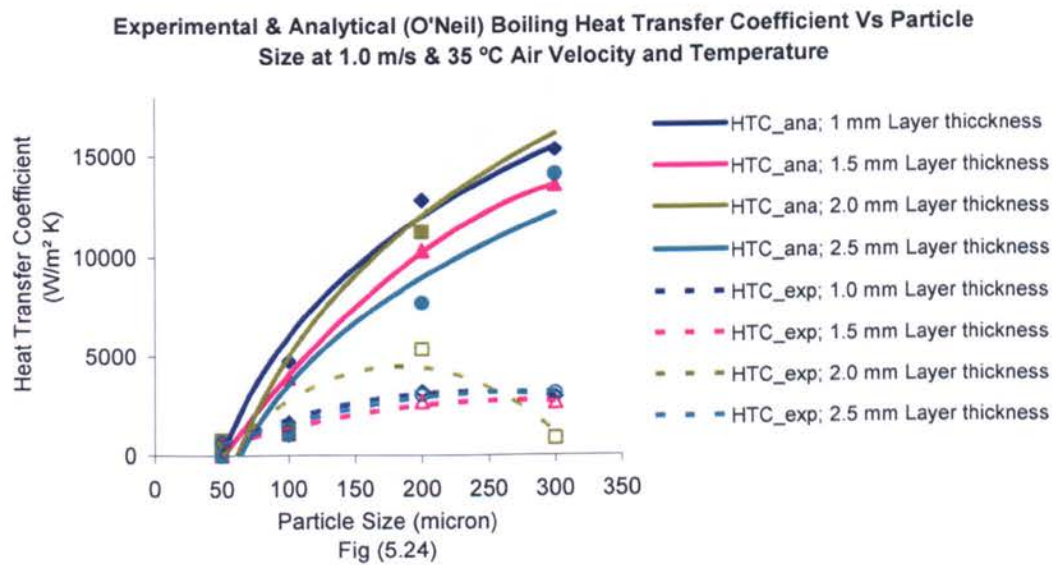
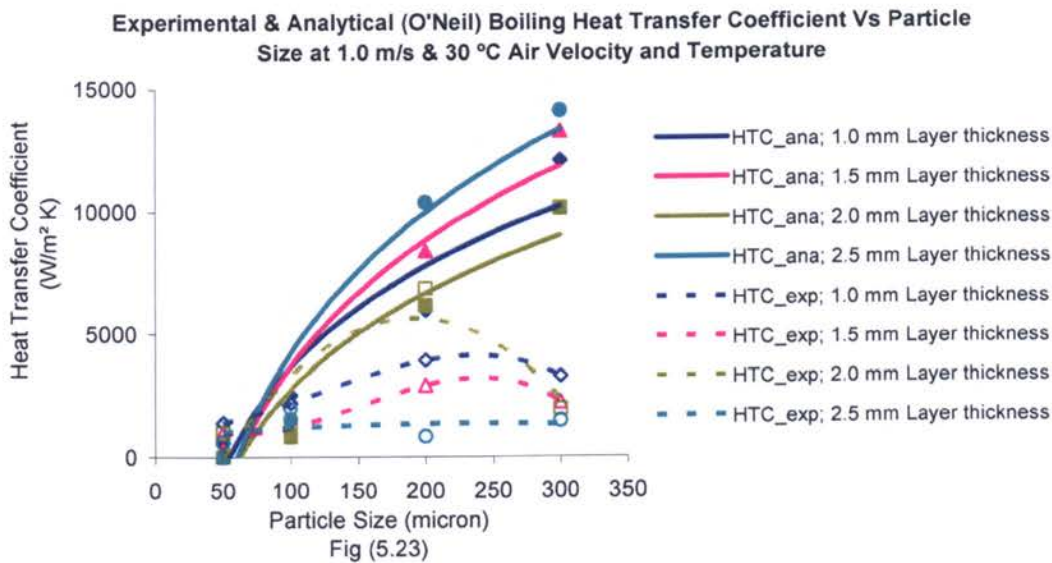
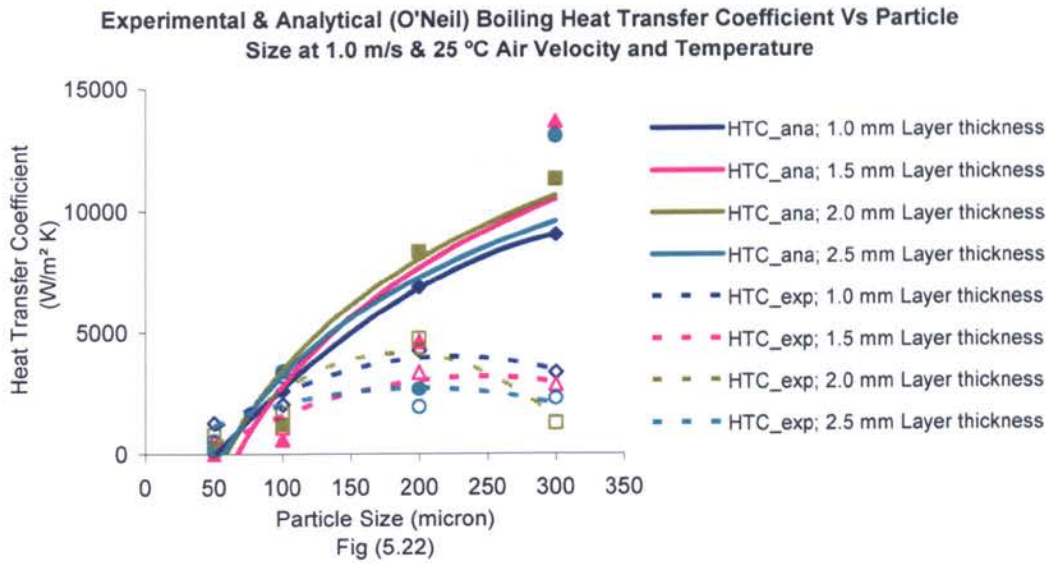
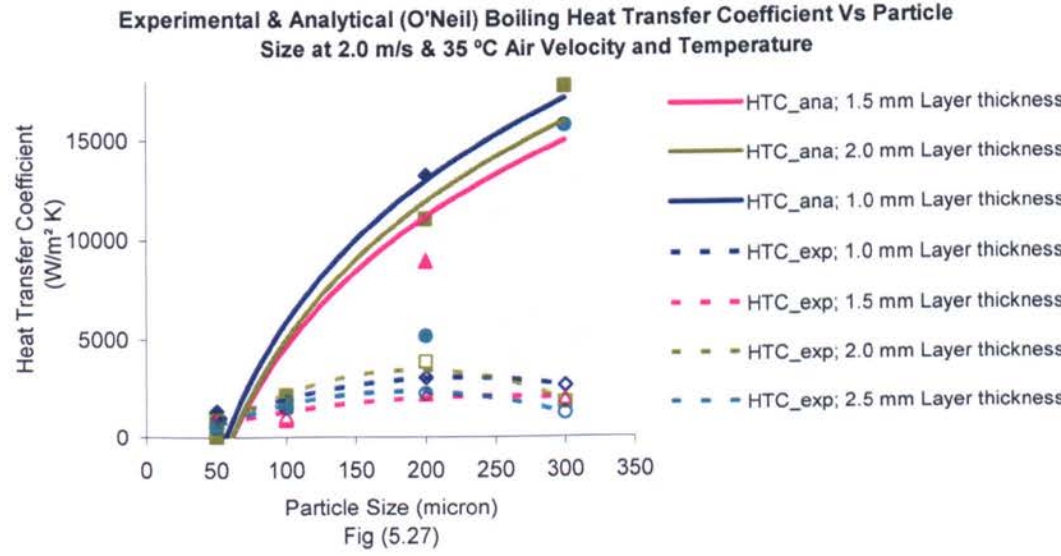
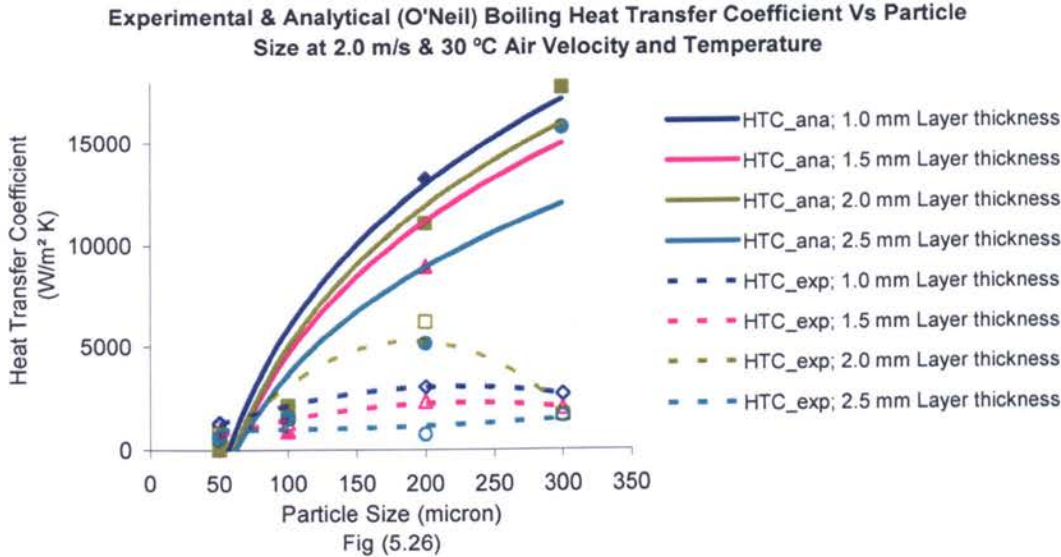
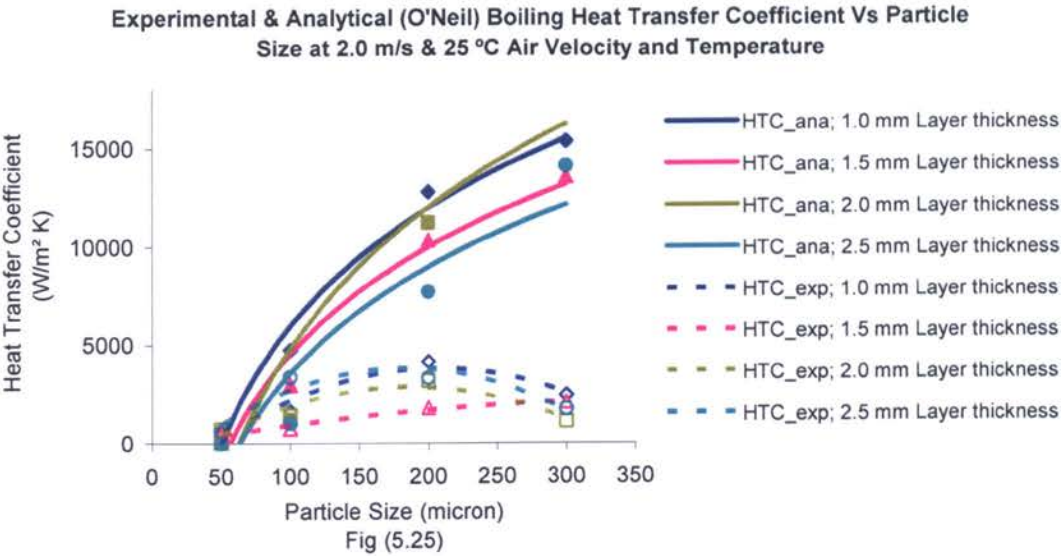
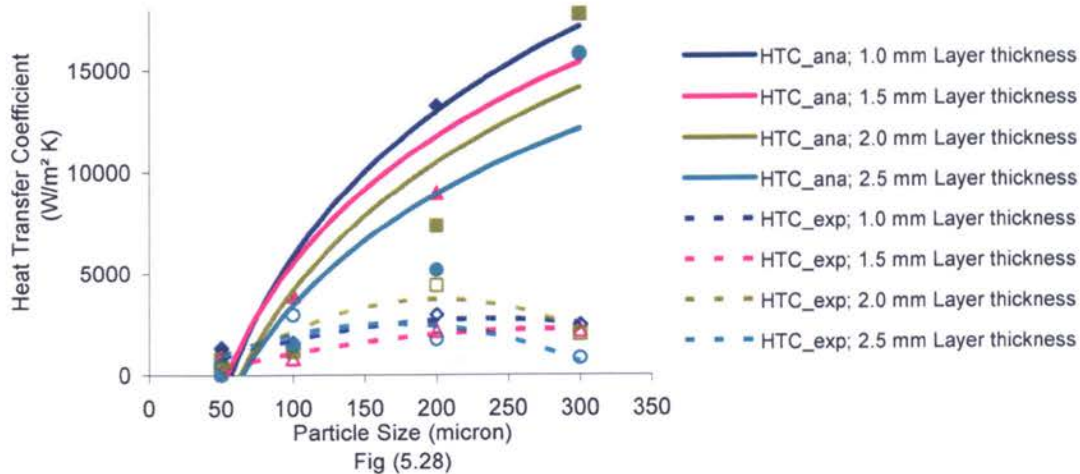


Fig (5.21) Determination of Darcy Velocity

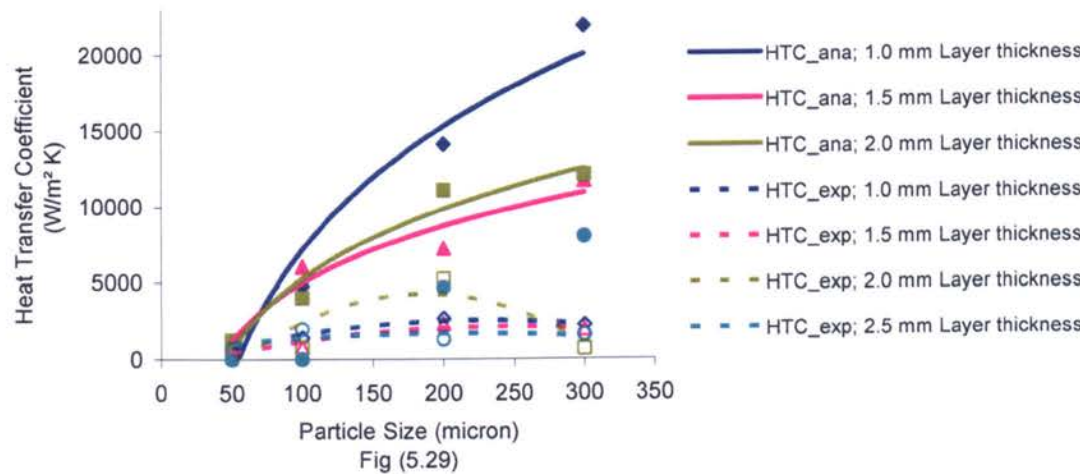




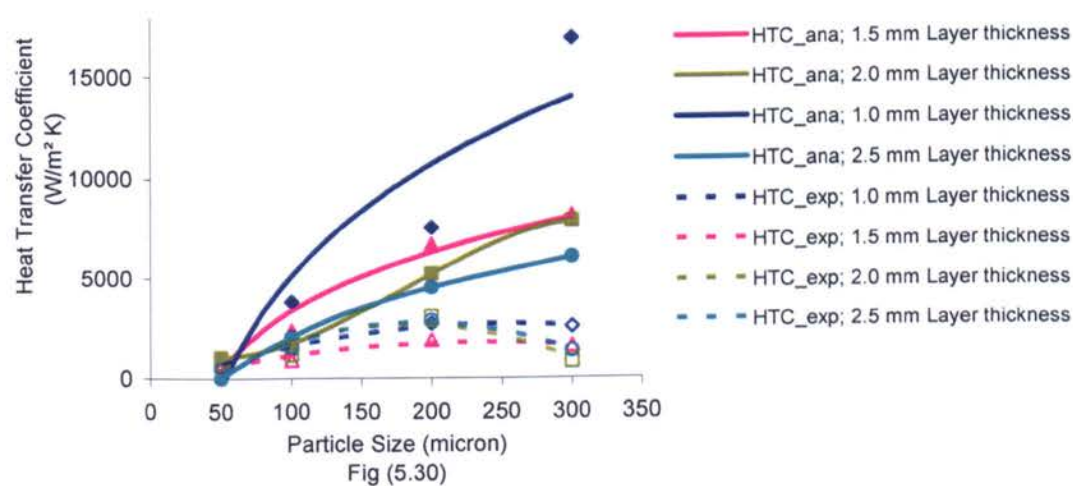
Experimental & Analytical (O'Neil) Boiling Heat Transfer Coefficient Vs Particle Size at 3.0 m/s & 25 °C Air Velocity and Temperature



Experimental & Analytical (O'Neil) Boiling Heat Transfer Coefficient Vs Particle Size at 3.0 m/s & 30 °C Air Velocity and Temperature



Experimental & Analytical (O'Neil) Boiling Heat Transfer Coefficient Vs Particle Size at 3.0 m/s & 35 °C Air Velocity and Temperature



**Experimental & Analytical (Rao & Balkrishnan) Boiling Heat Transfer Coefficient
Vs Particle Size at 1.0 m/s & 25 °C Air Velocity and Temperature**

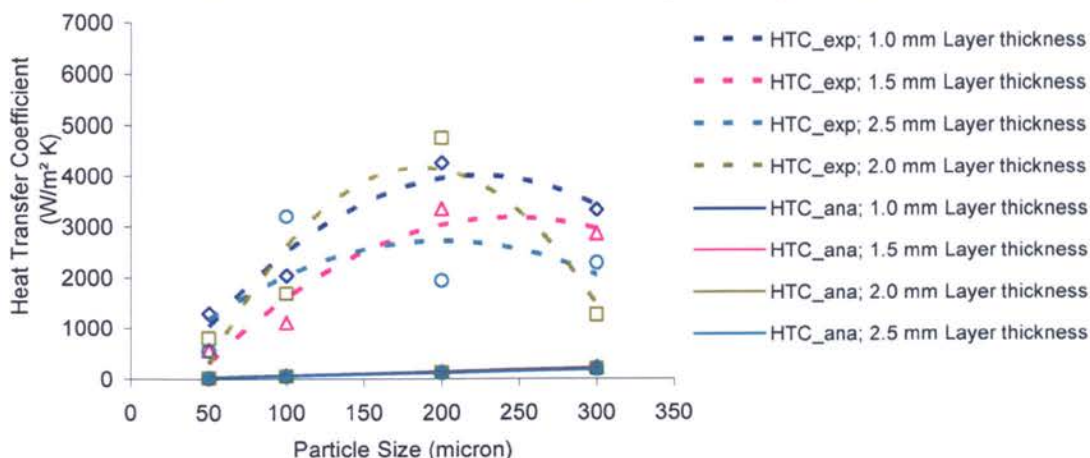


Fig (5.31)

**Experimental & Analytical (Rao & Balkrishnan) Boiling Heat Transfer Coefficient
Vs Particle Size at 1.0 m/s & 30 °C Air Velocity and Temperature**

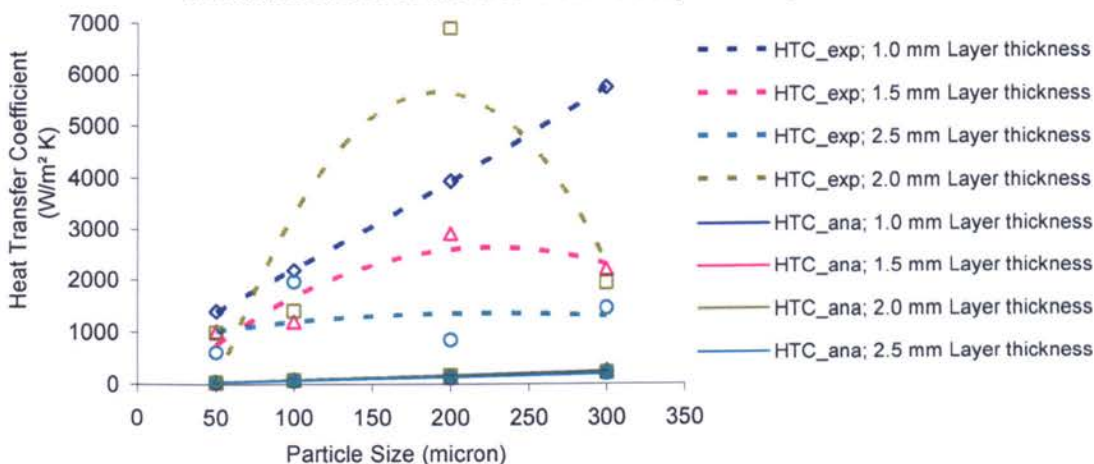


Fig (5.32)

**Experimental & Analytical (Rao & Balkrishnan) Boiling Heat Transfer Coefficient
Vs Particle Size at 1.0 m/s & 35 °C Air Velocity and Temperature**

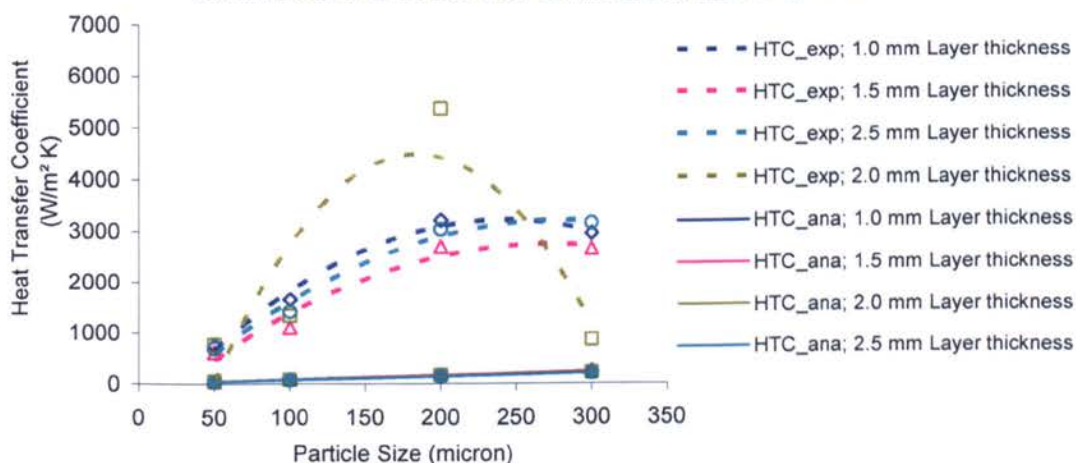
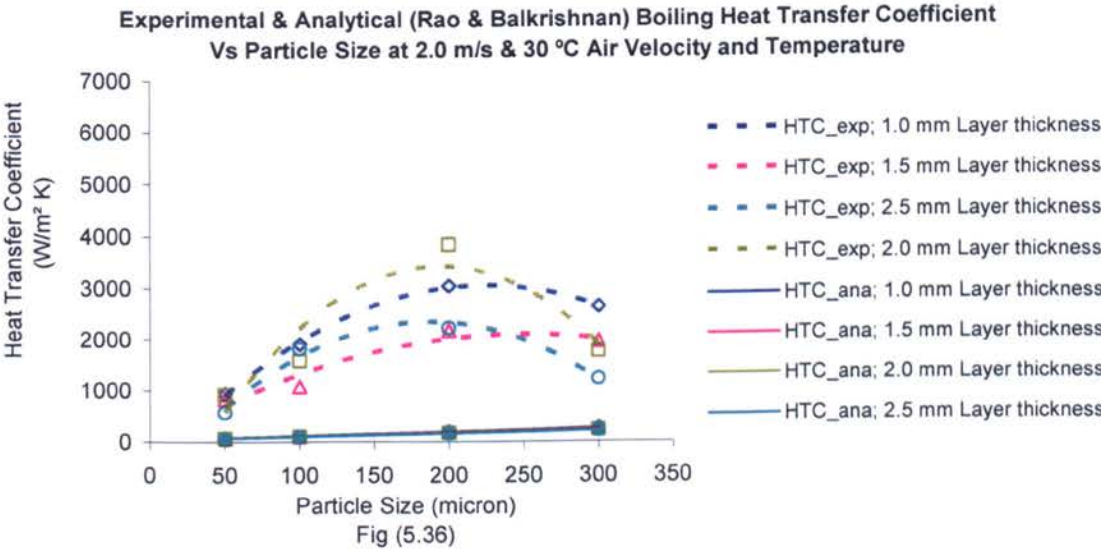
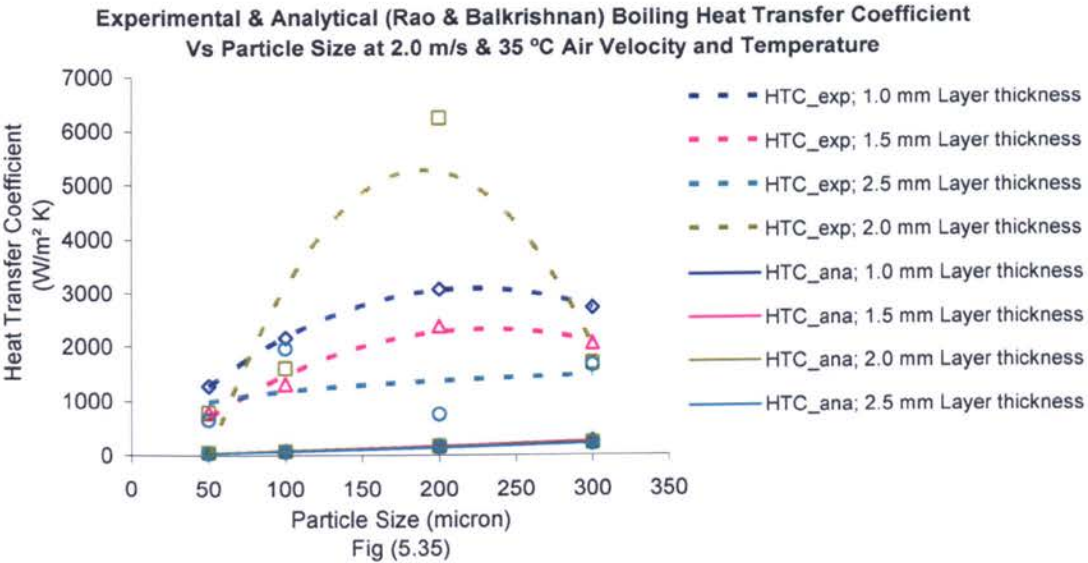
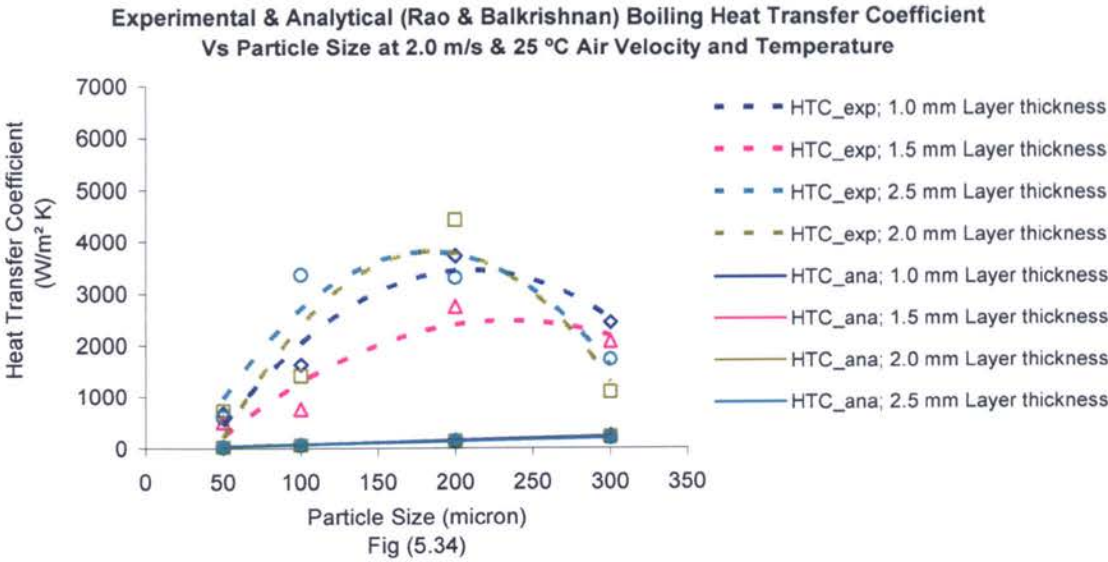
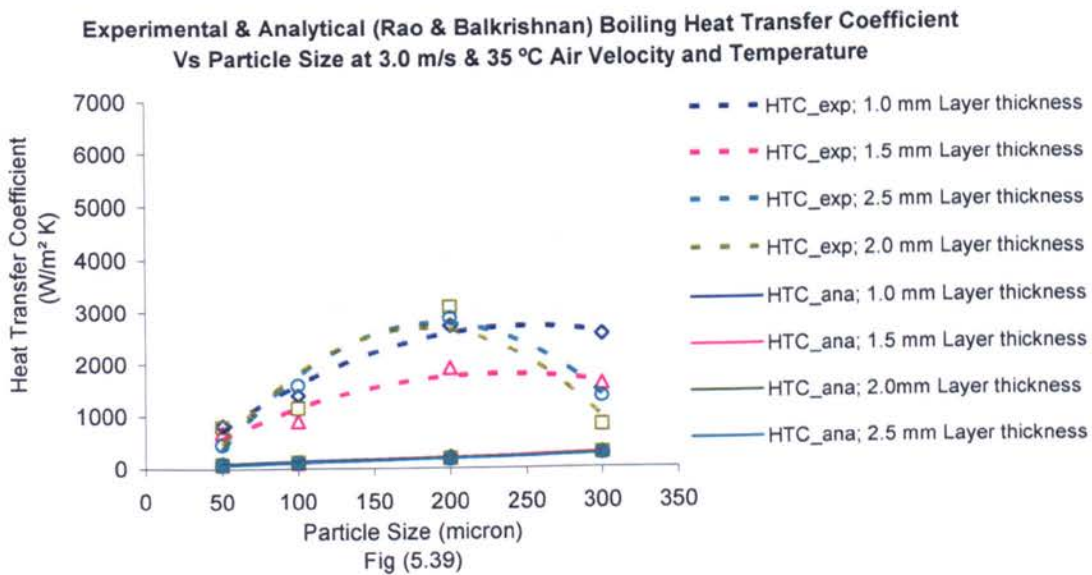
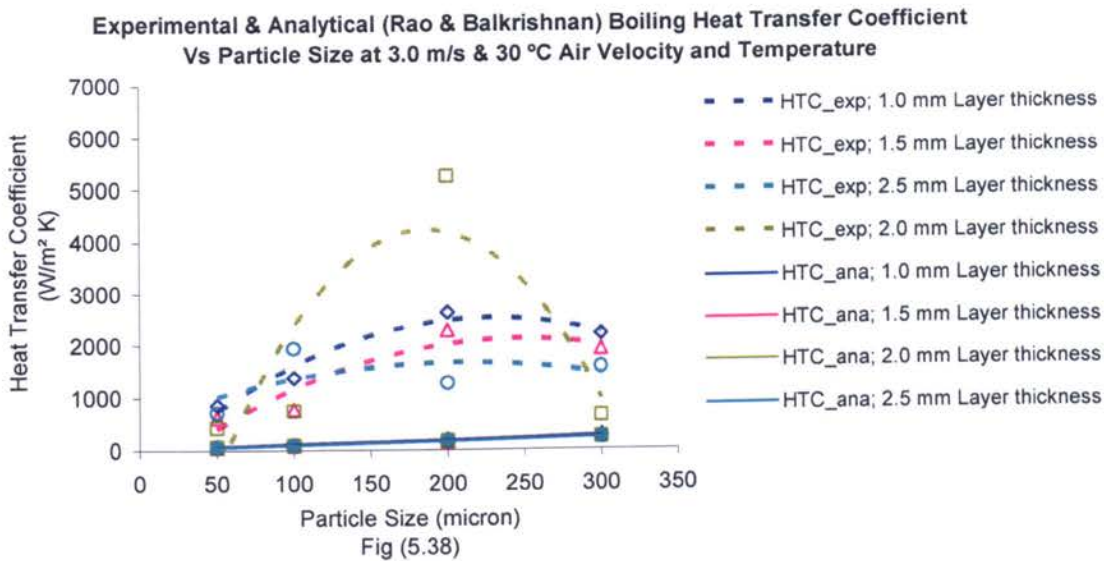
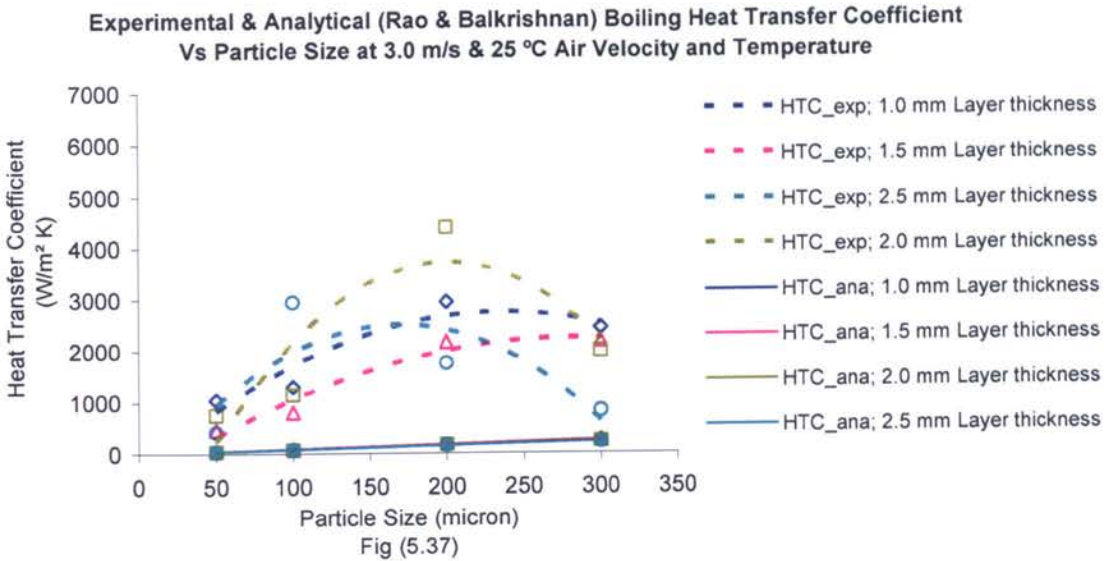
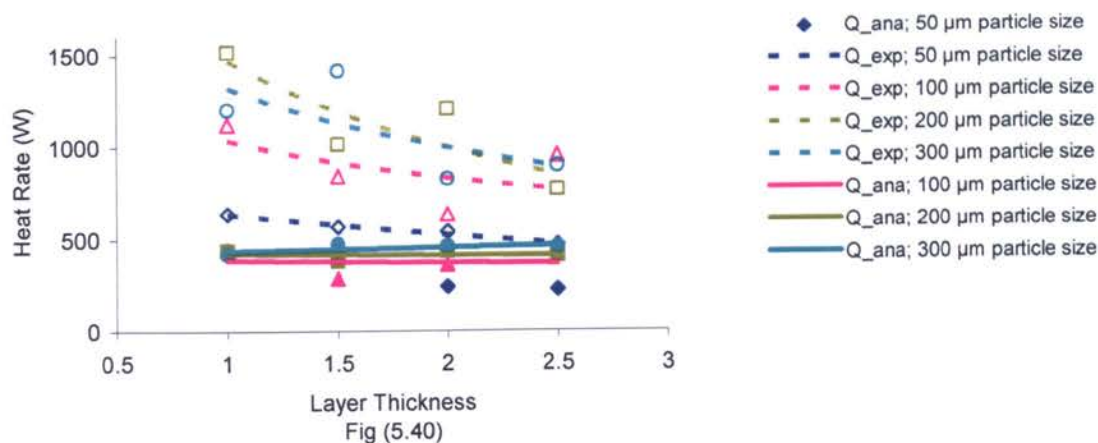


Fig (5.33)

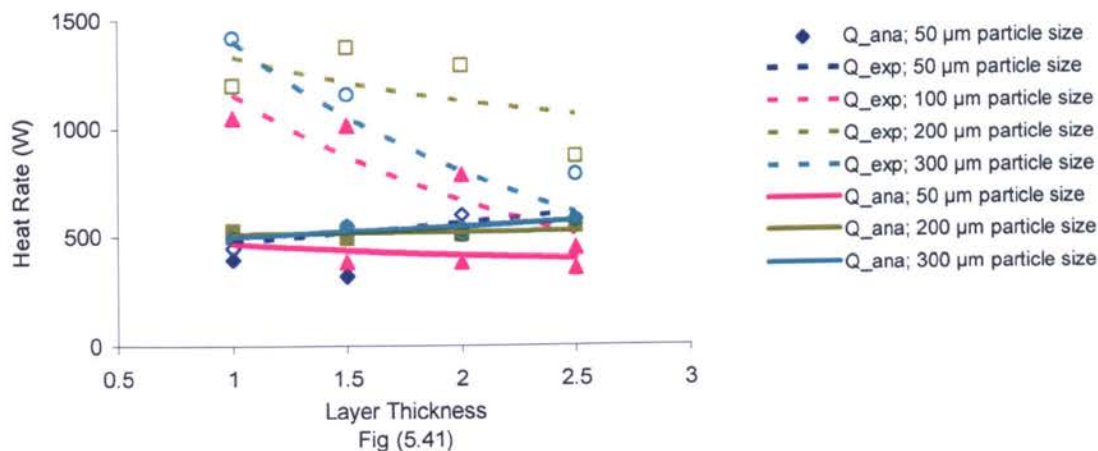




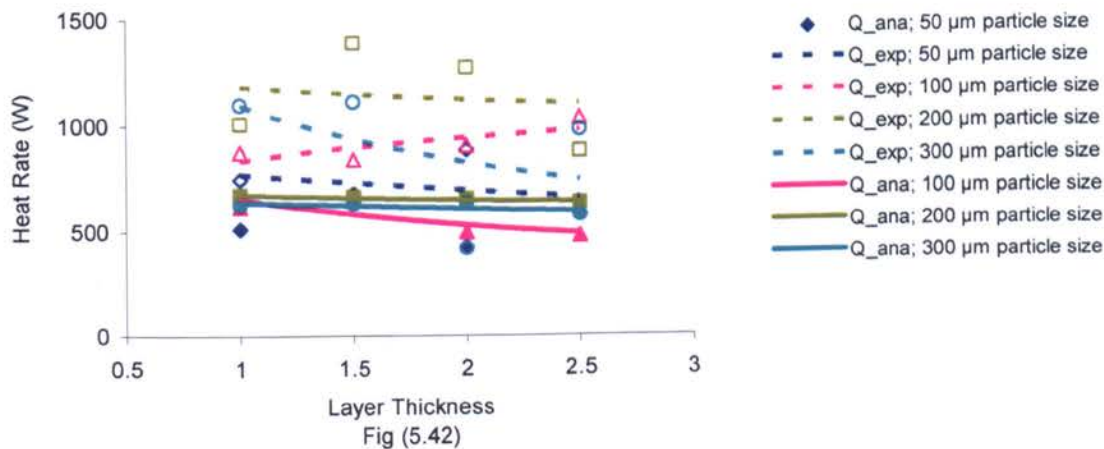
Experimental & Analytical (O'Neil) Boiling Heat Rates Vs Layer Thickness
at 1.0 m/s & 25 °C Air Velocity and Temperature



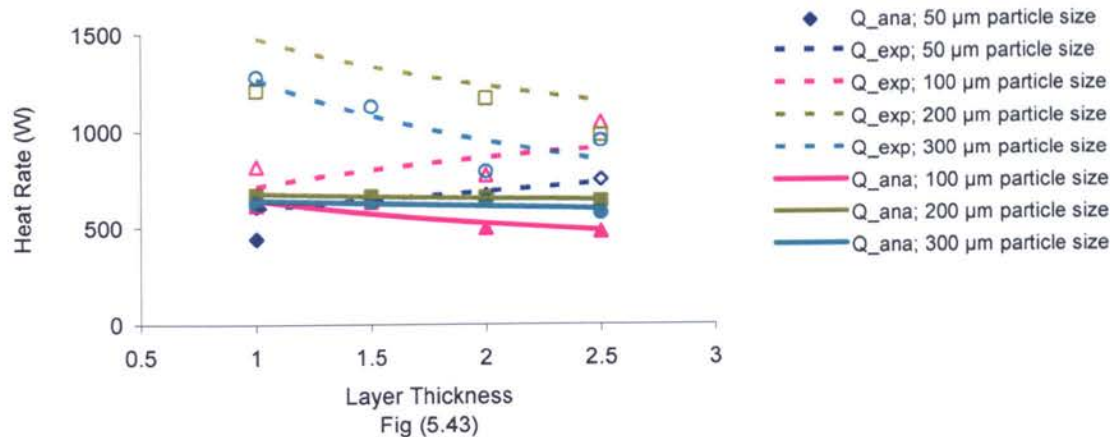
Experimental & Analytical (O'Neil) Boiling Heat Rates Vs Layer Thickness
at 1.0 m/s & 30 °C Air Velocity and Temperature



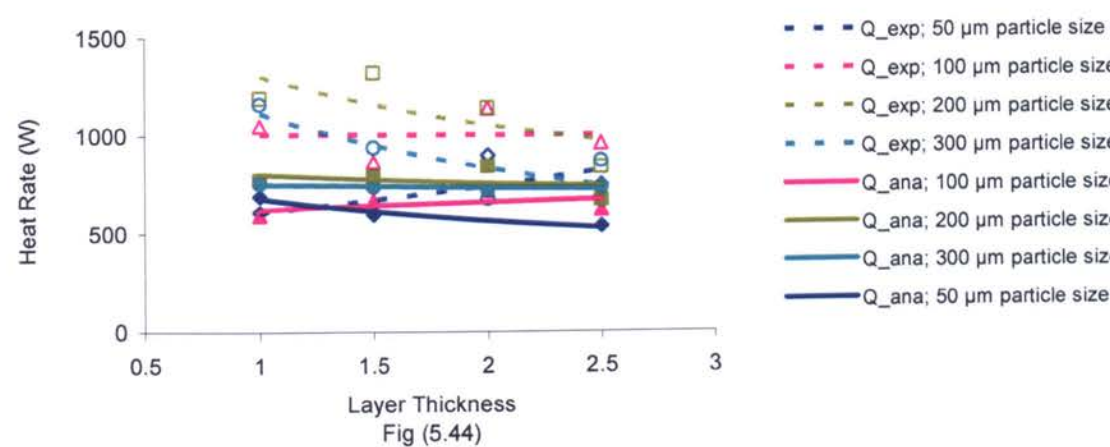
Experimental & Analytical (O'Neil) Boiling Heat Rates Vs Layer Thickness
at 1.0 m/s & 35 °C Air Velocity and Temperature



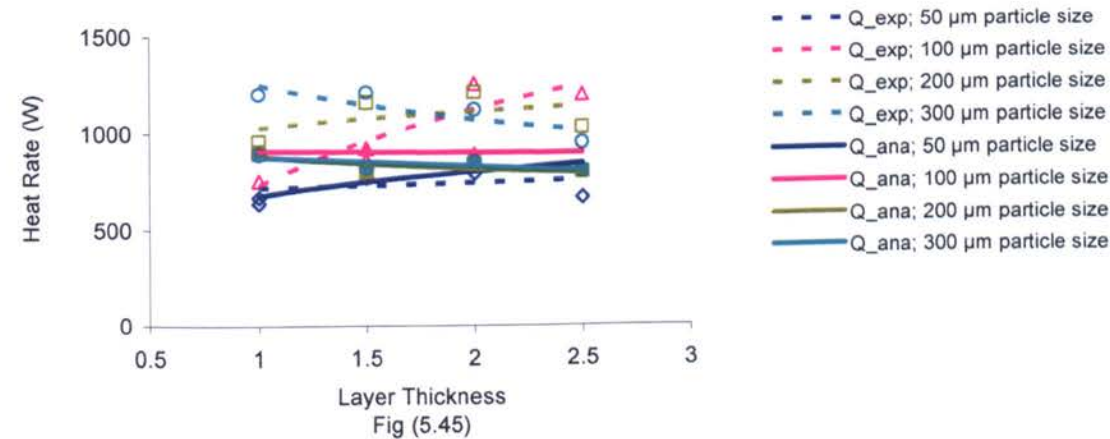
Experimental & Analytical (O'Neil) Boiling Heat Rates Vs Layer Thickness
at 2.0 m/s & 25 °C Air Velocity and Temperature

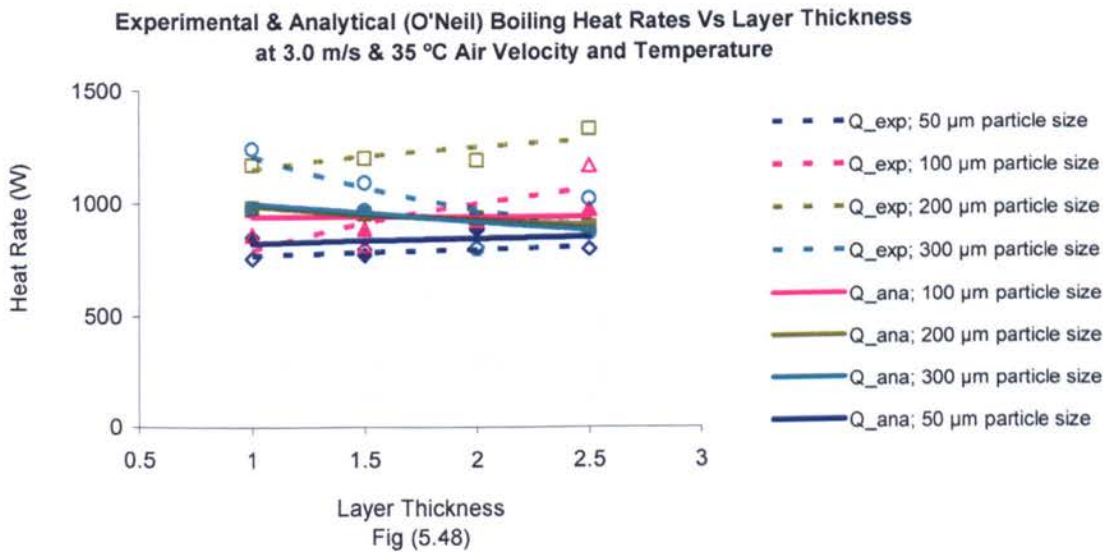
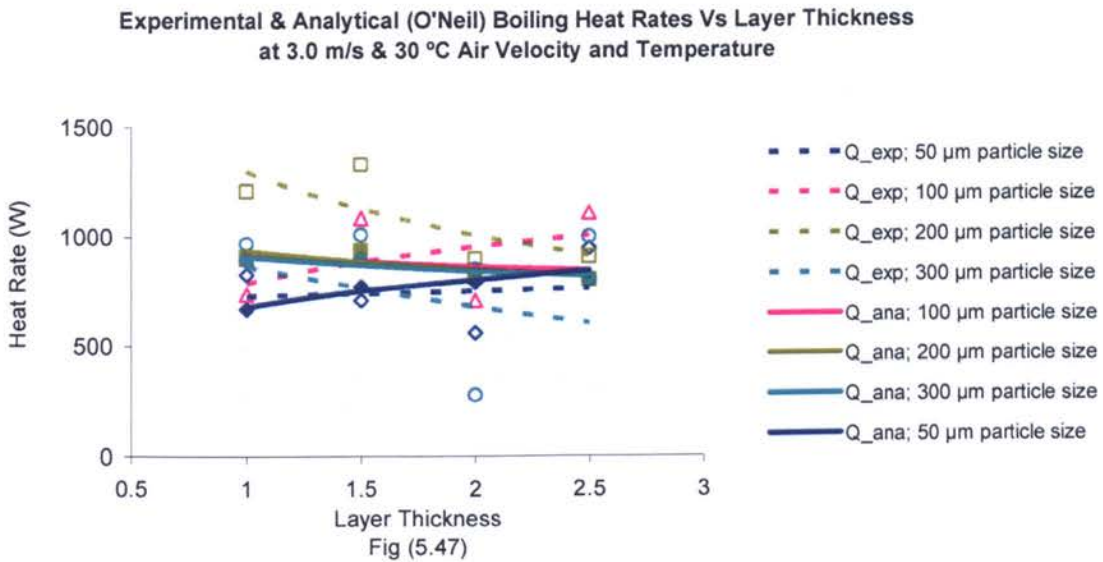
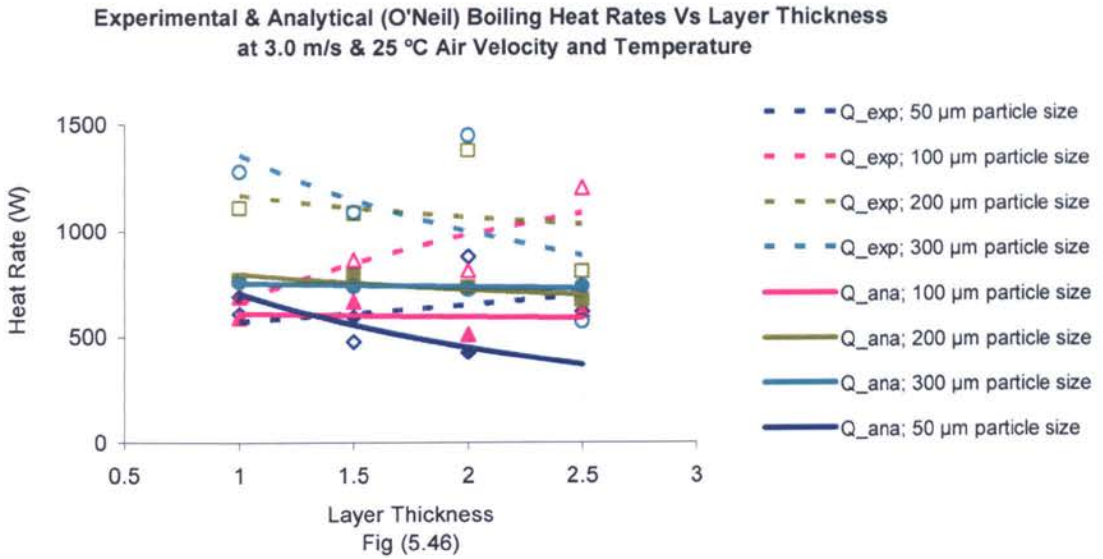


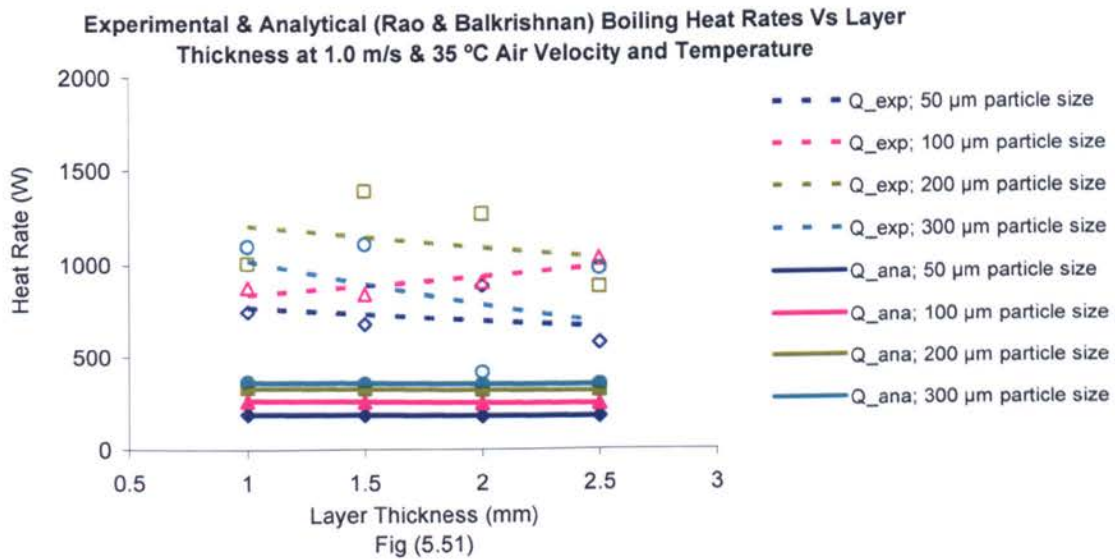
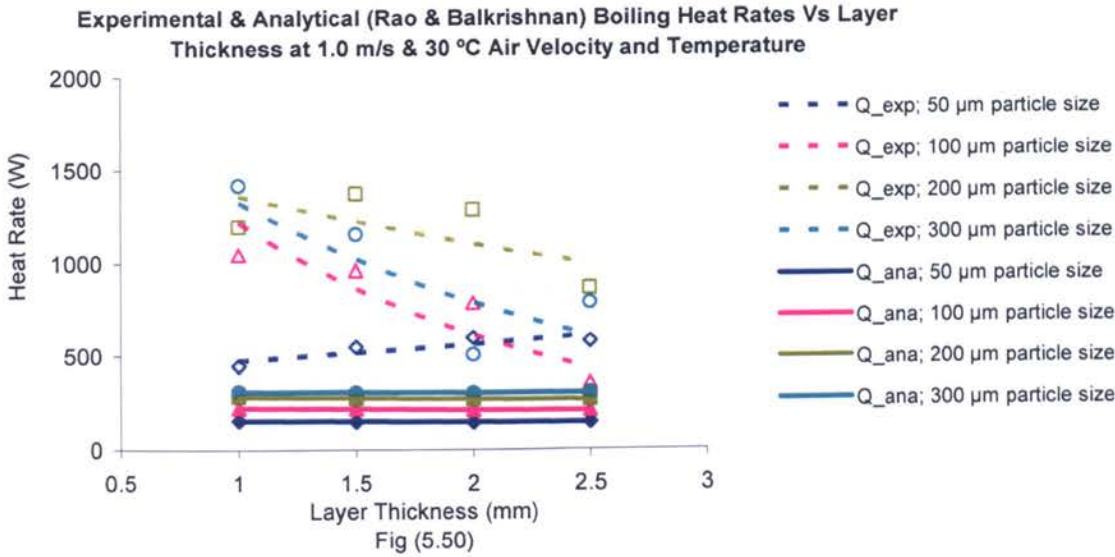
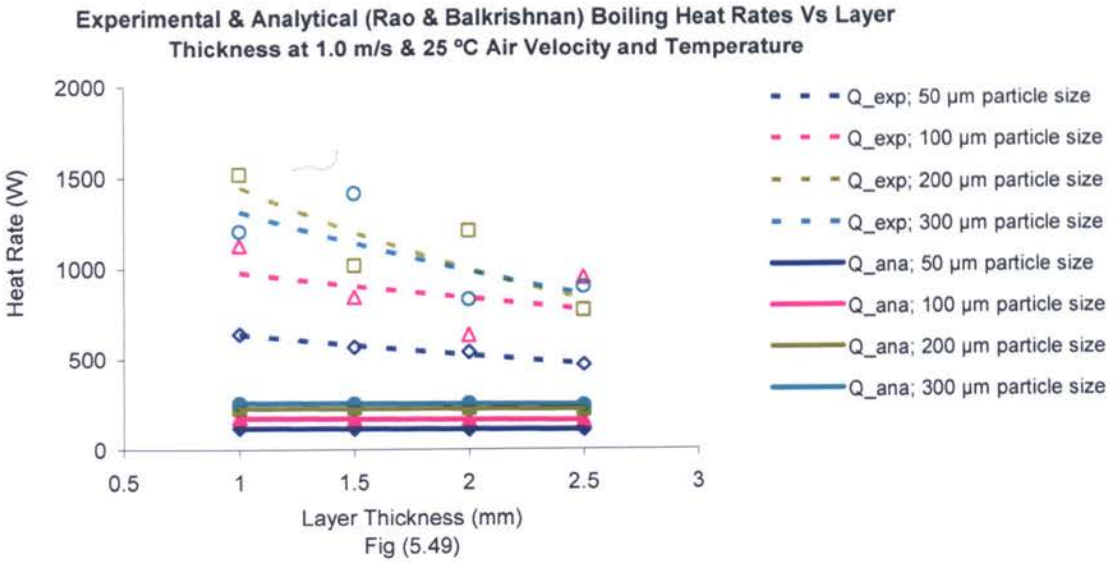
Experimental & Analytical (O'Neil) Boiling Heat Rates Vs Layer Thickness
at 2.0 m/s & 30 °C Air Velocity and Temperature

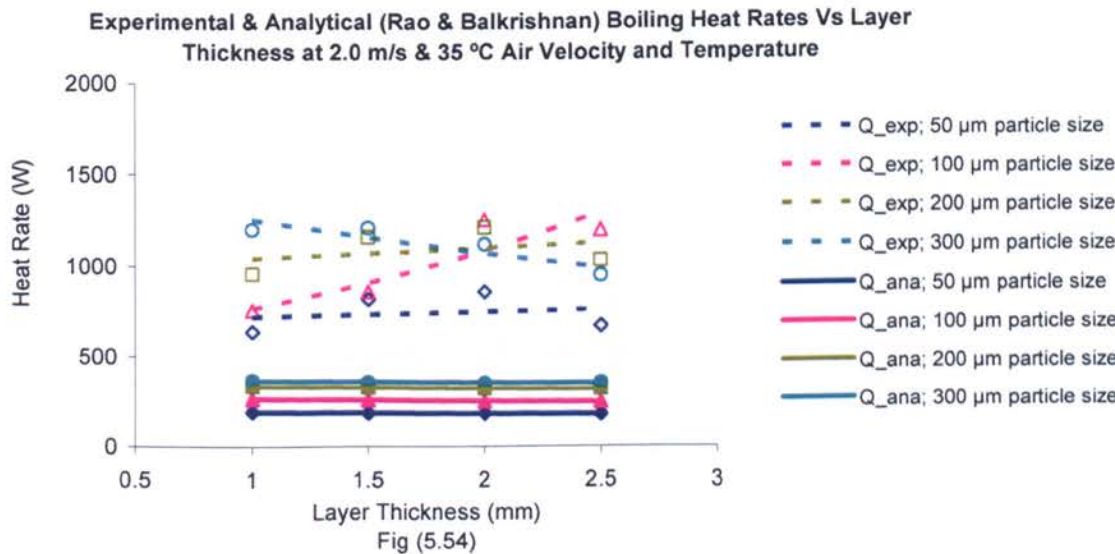
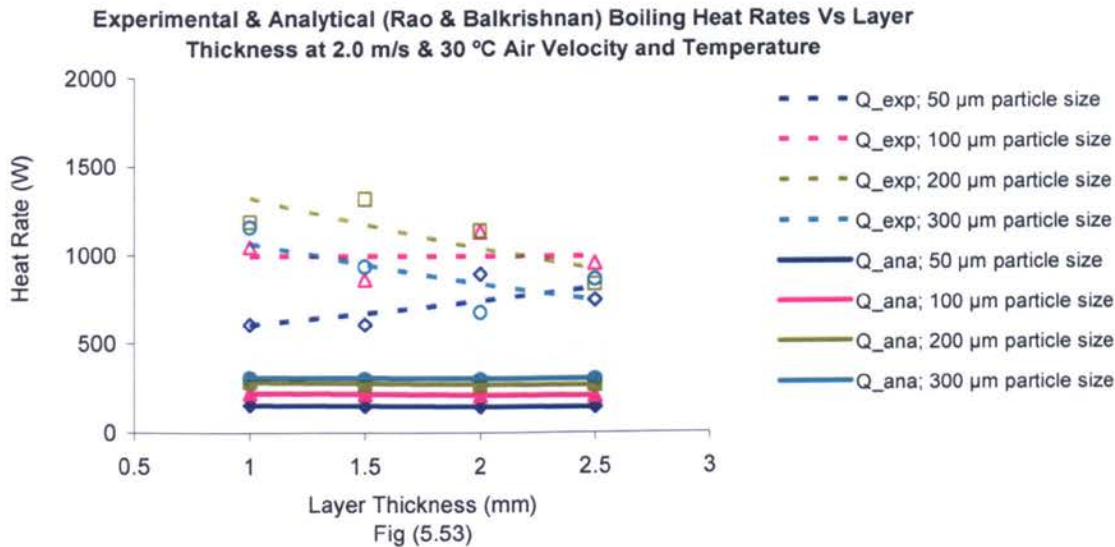
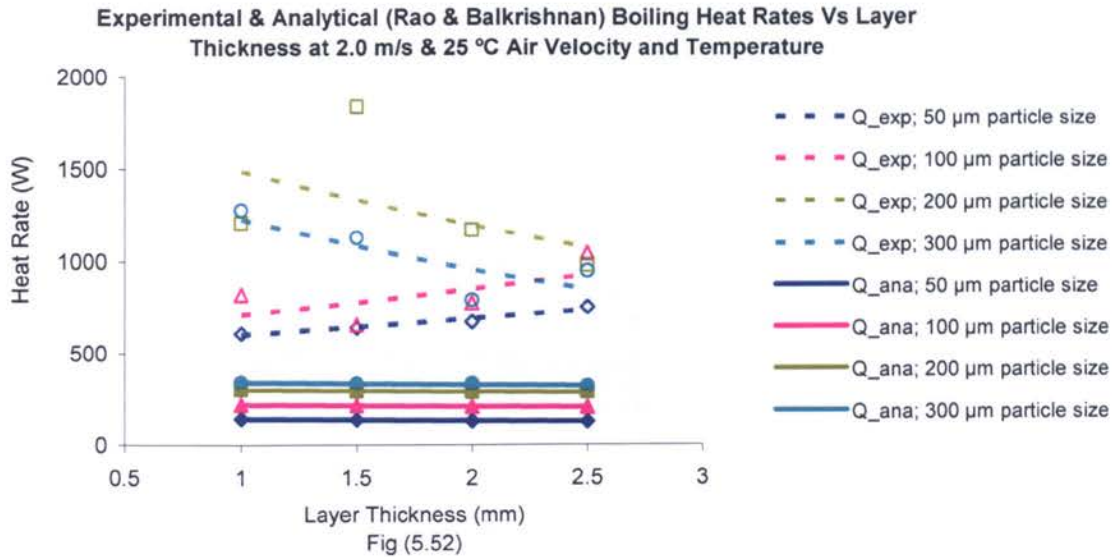


Experimental & Analytical (O'Neil) Boiling Heat Rates Vs Layer Thickness
at 2.0 m/s & 35 °C Air Velocity and Temperature

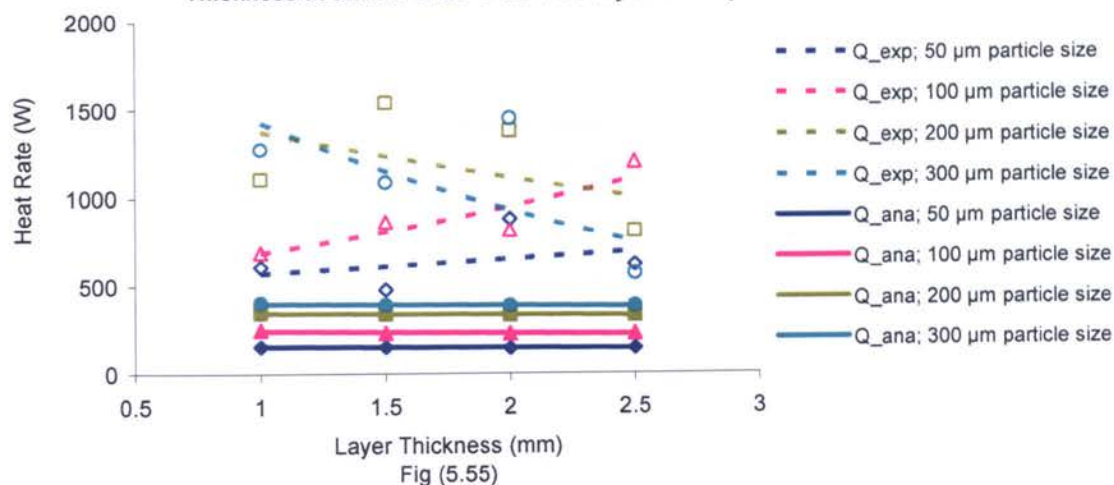




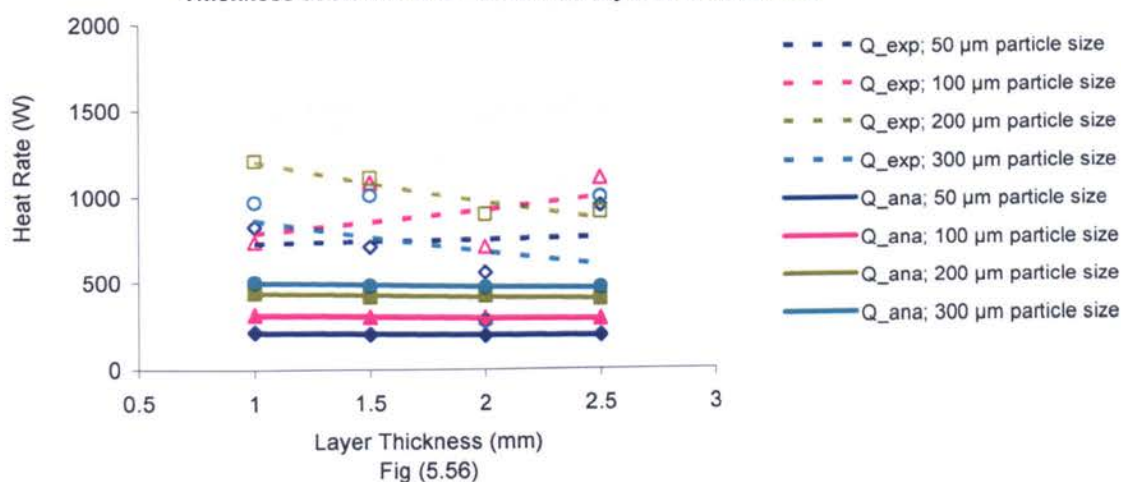




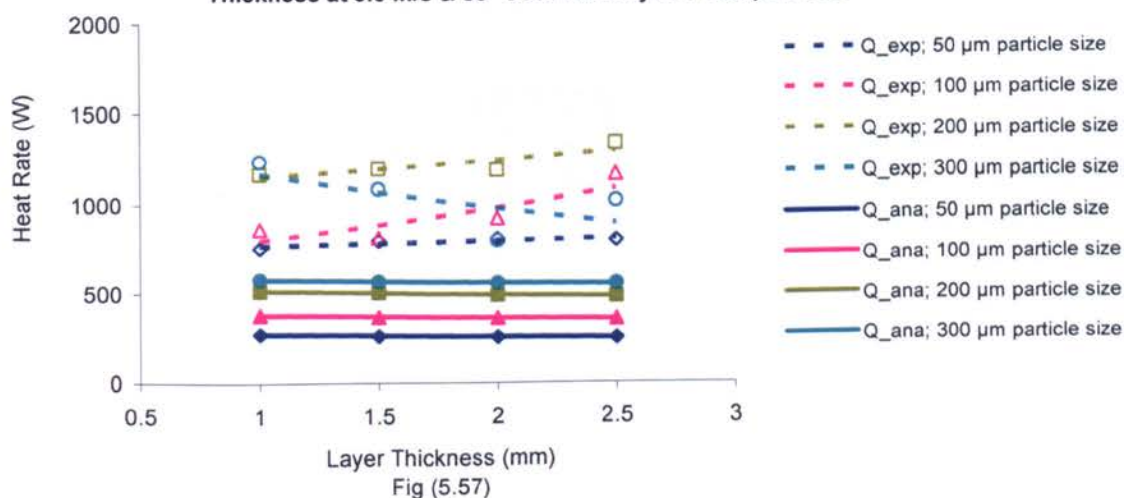
Experimental & Analytical (Rao & Balkrishnan) Boiling Heat Rates Vs Layer Thickness at 3.0 m/s & 25 °C Air Velocity and Temperature



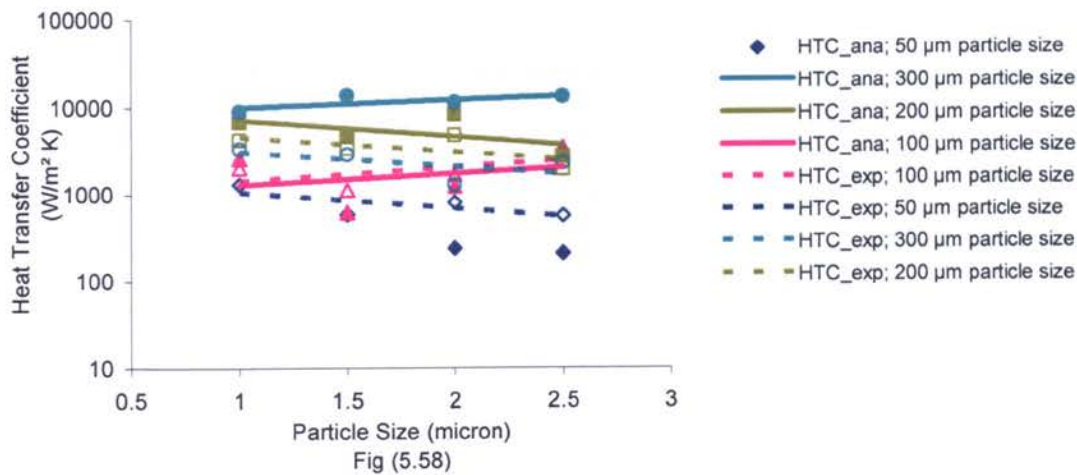
Experimental & Analytical (Rao & Balkrishnan) Boiling Heat Rates Vs Layer Thickness at 3.0 m/s & 30 °C Air Velocity and Temperature



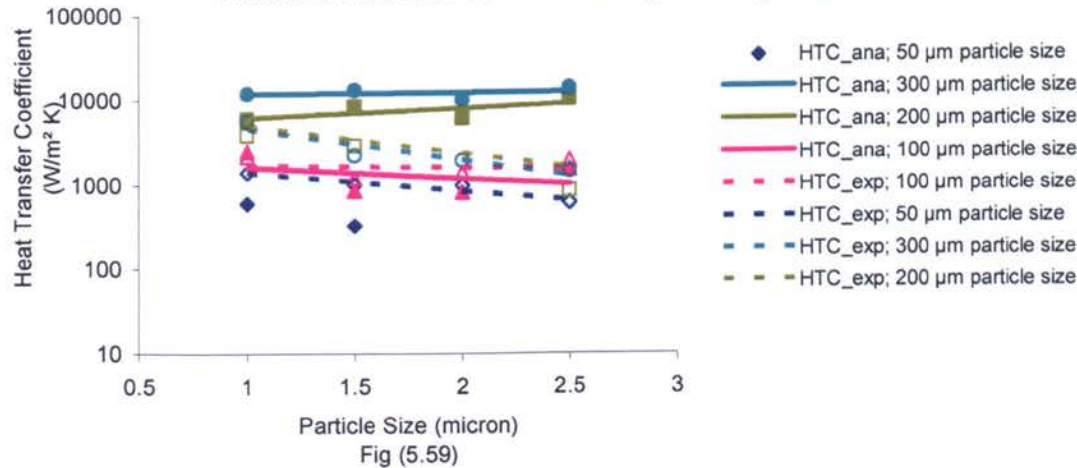
Experimental & Analytical (Rao & Balkrishnan) Boiling Heat Rates Vs Layer Thickness at 3.0 m/s & 35 °C Air Velocity and Temperature



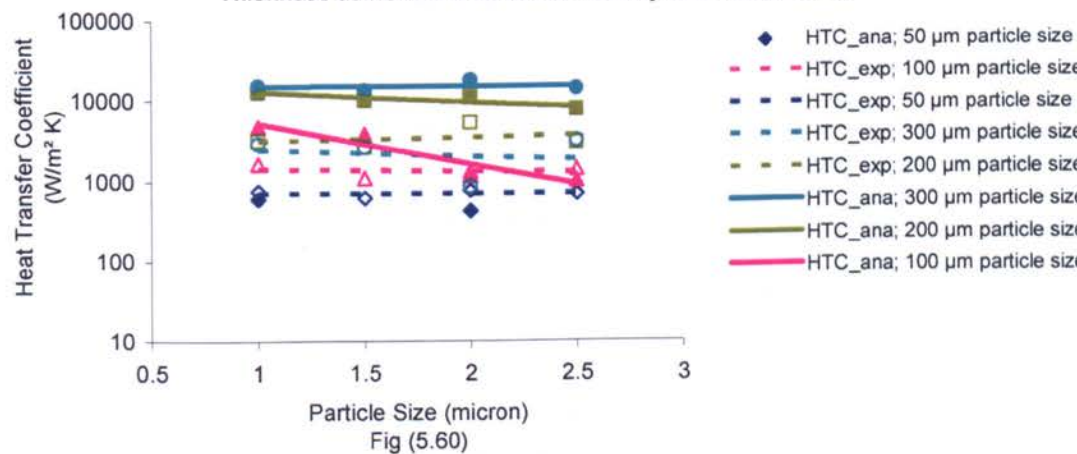
Experimental & Analytical (O'Neil) Boiling Heat Transfer Coefficients Vs Layer Thickness at 1.0 m/s & 25 °C Air Velocity and Temperature

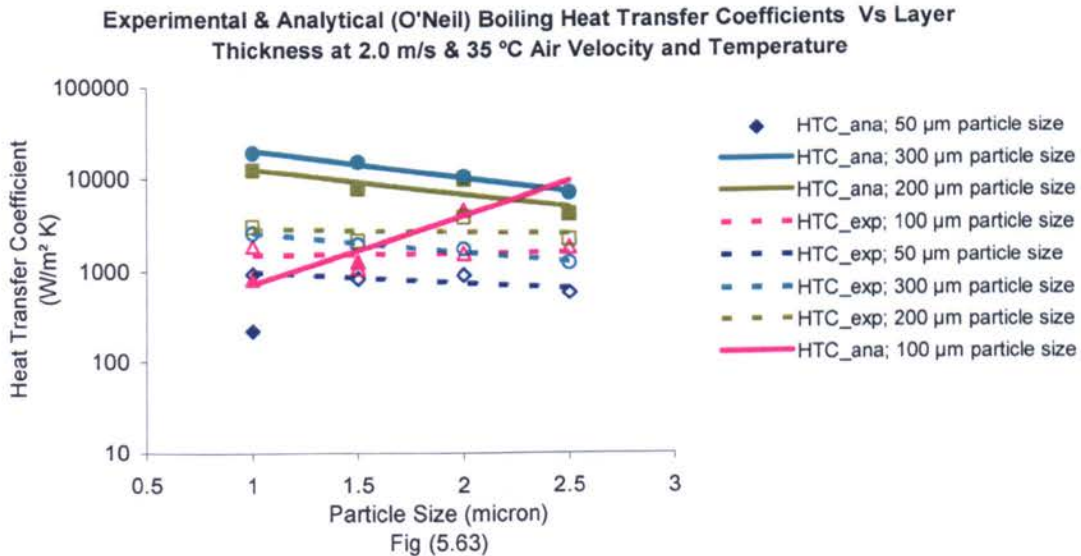
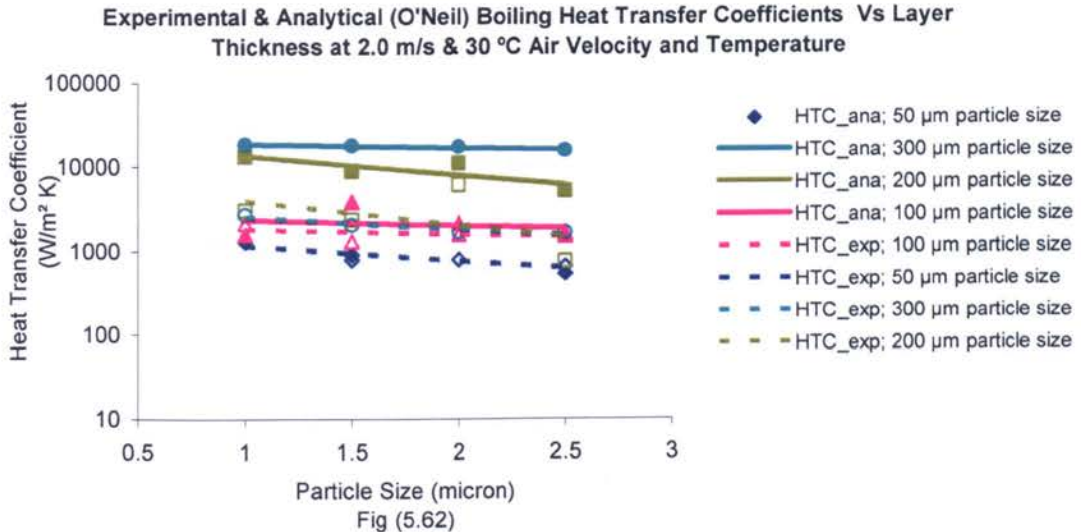
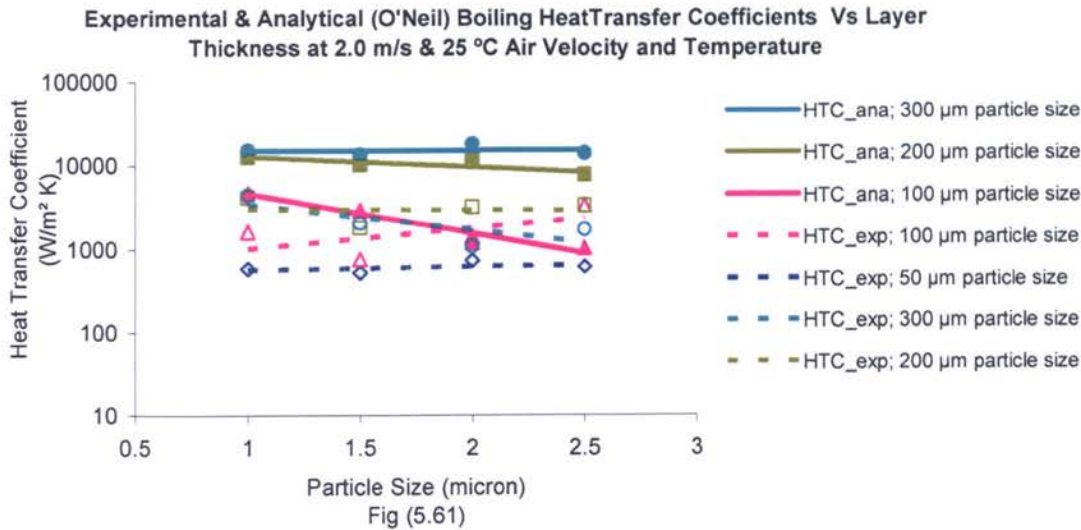


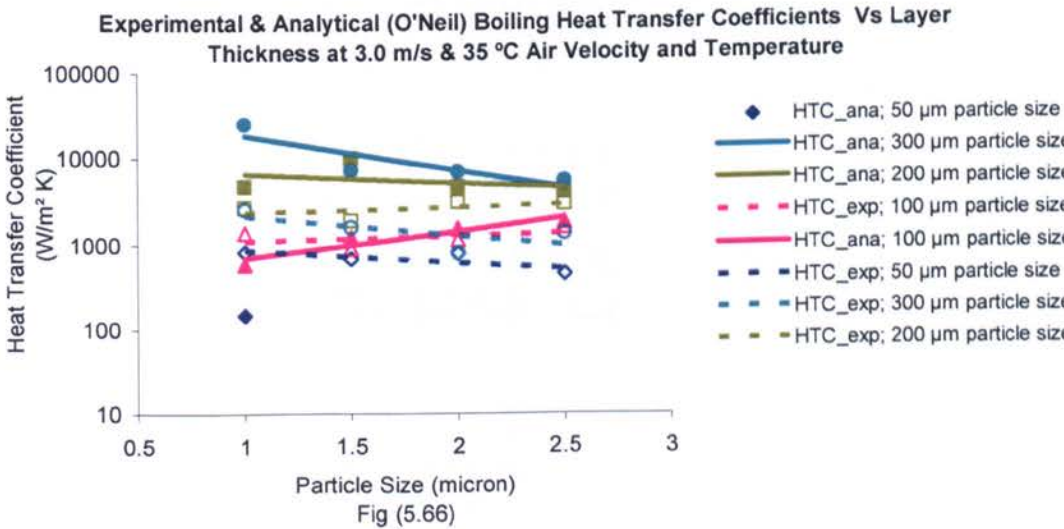
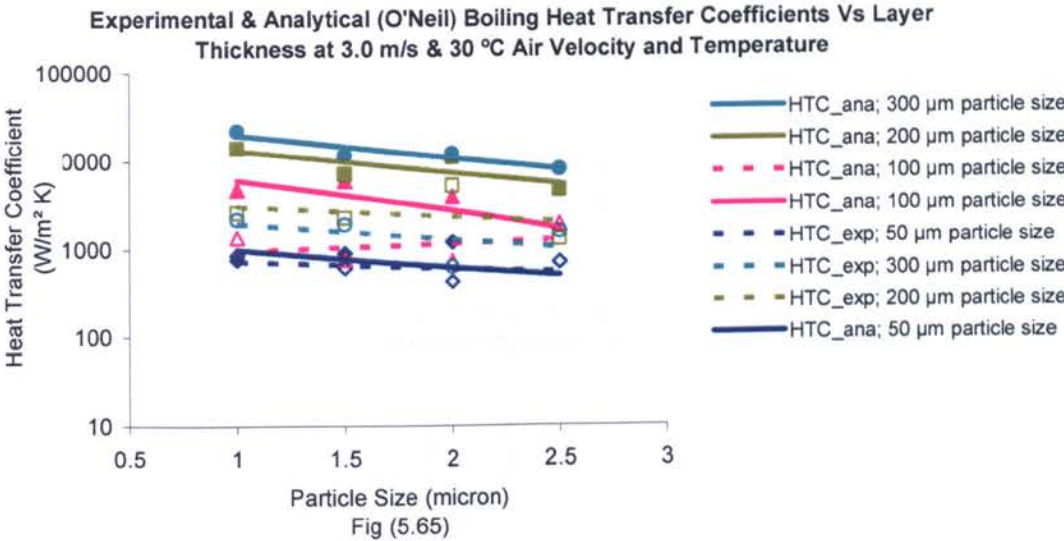
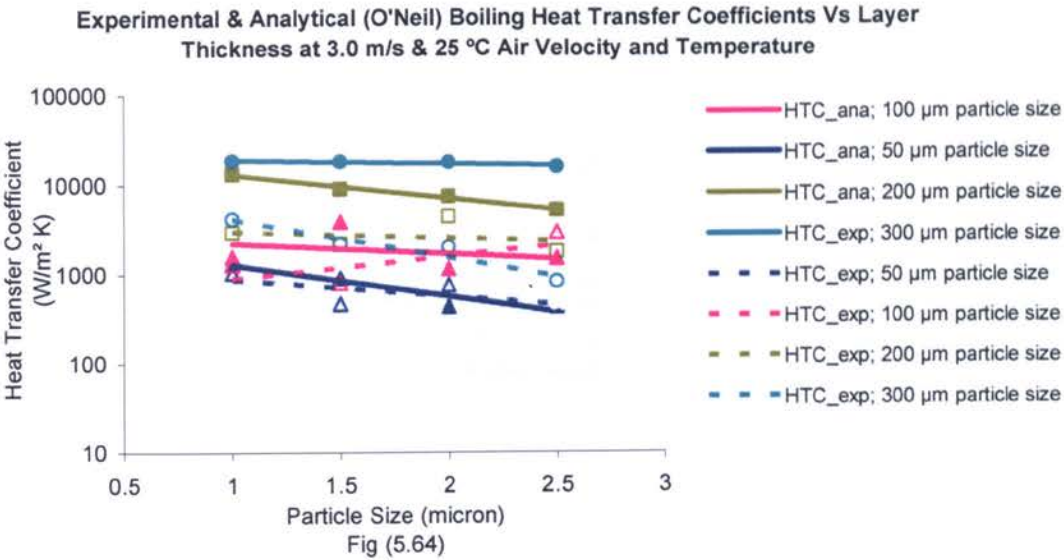
Experimental & Analytical (O'Neil) Boiling Heat Transfer Coefficients Vs Layer Thickness at 1.0 m/s & 30 °C Air Velocity and Temperature

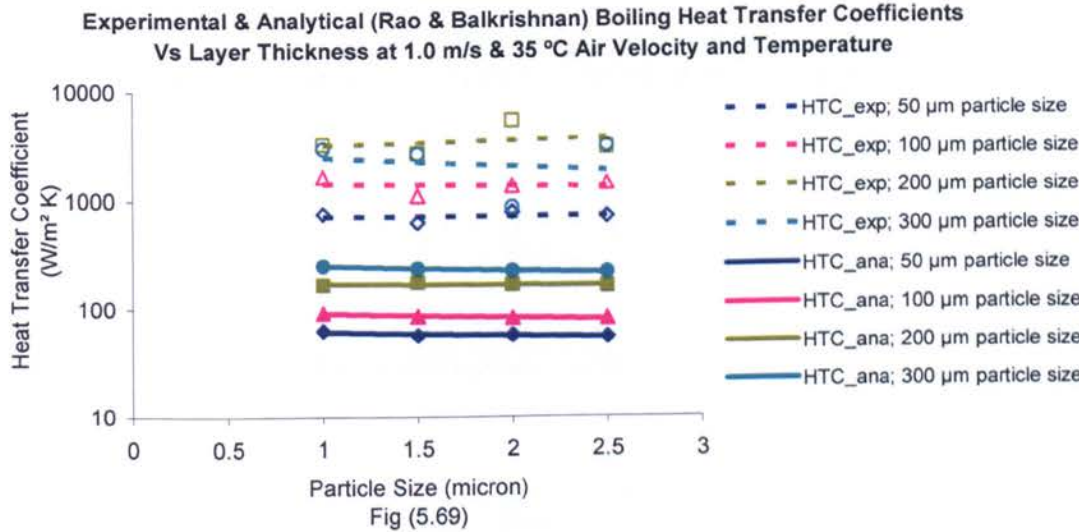
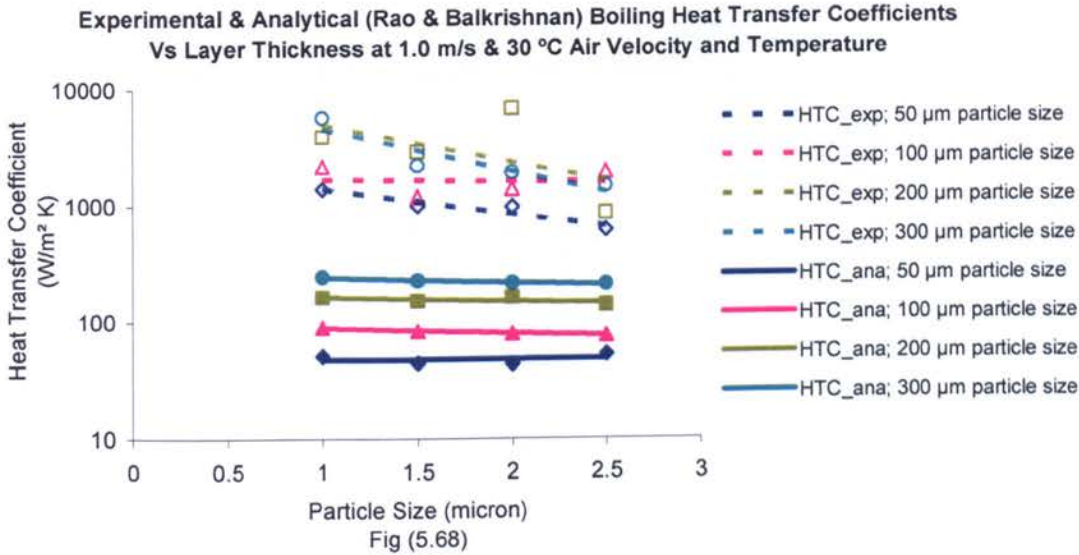
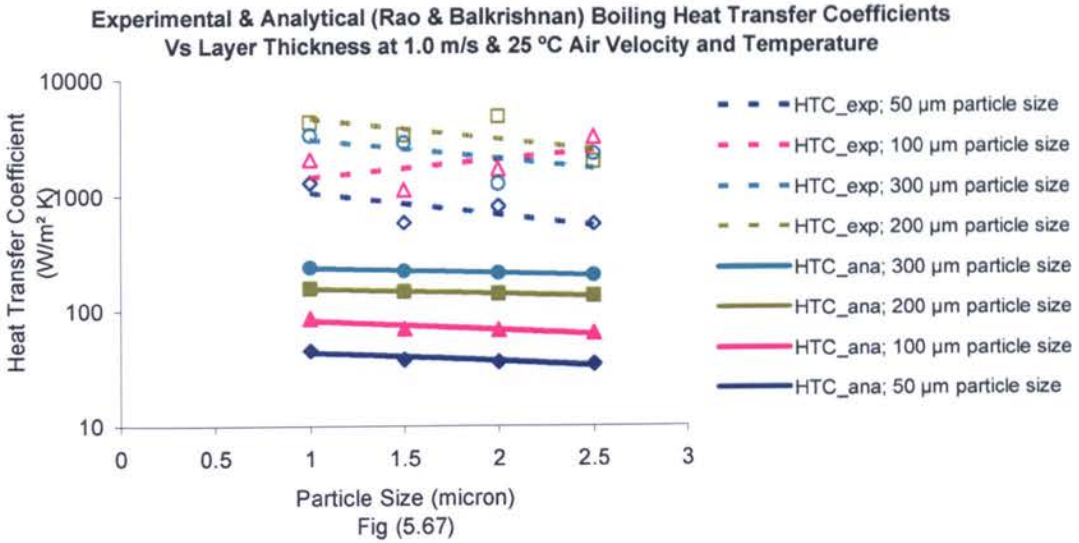


Experimental & Analytical (O'Neil) Boiling Heat Transfer Coefficients Vs Layer Thickness at 1.0 m/s & 35 °C Air Velocity and Temperature

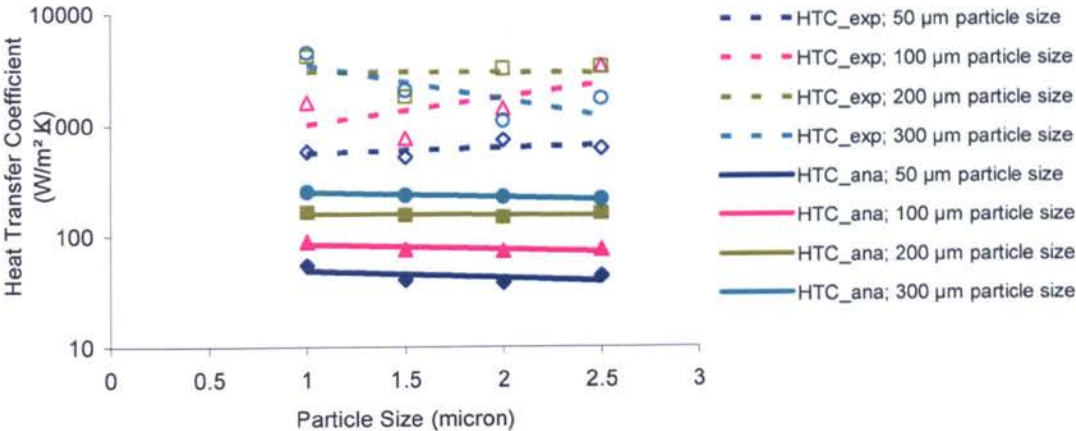




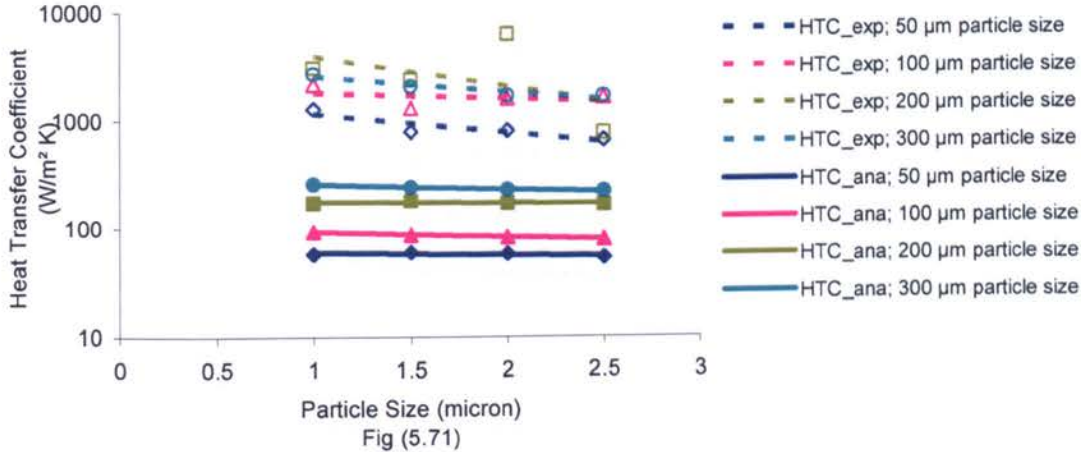




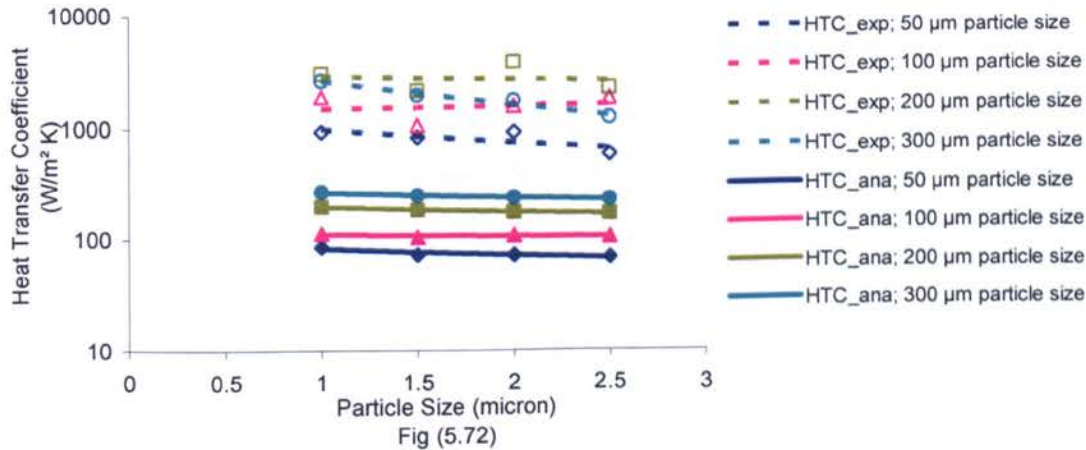
Experimental & Analytical (Rao & Balkrishnan) Boiling Heat Transfer Coefficients
Vs Layer Thickness at 2.0 m/s & 25 °C Air Velocity and Temperature



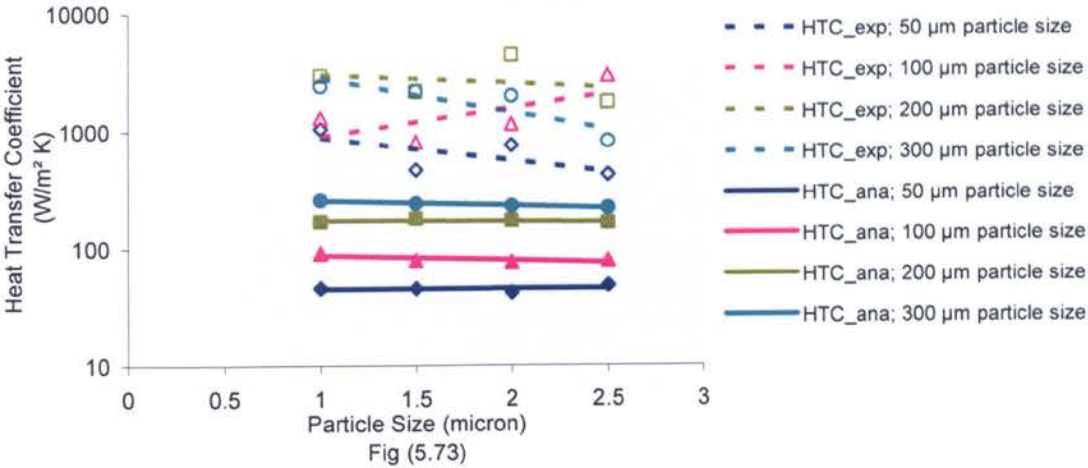
Experimental & Analytical (Rao & Balkrishnan) Boiling Heat Transfer Coefficients
Vs Layer Thickness at 2.0 m/s & 30 °C Air Velocity and Temperature



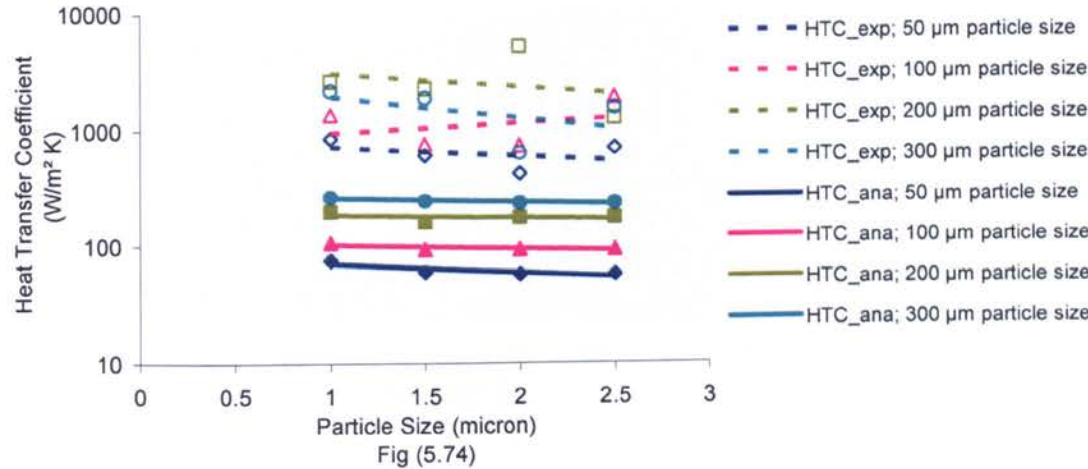
Experimental & Analytical (Rao & Balkrishnan) Boiling Heat Transfer Coefficients
Vs Layer Thickness at 2.0 m/s & 35 °C Air Velocity and Temperature



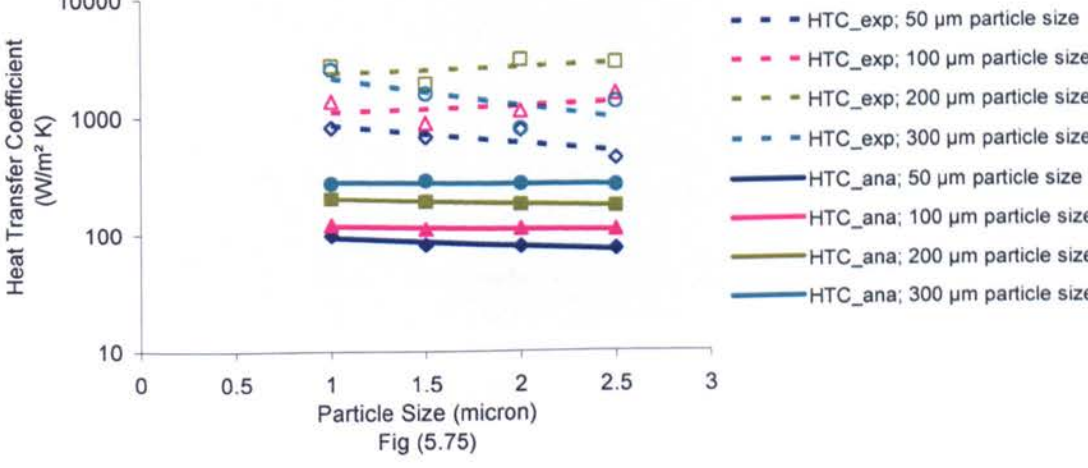
Experimental & Analytical (Rao & Balkrishnan) Boiling Heat Transfer
Coefficients Vs Layer Thickness at 3.0 m/s & 25 °C Air Velocity and Temperature

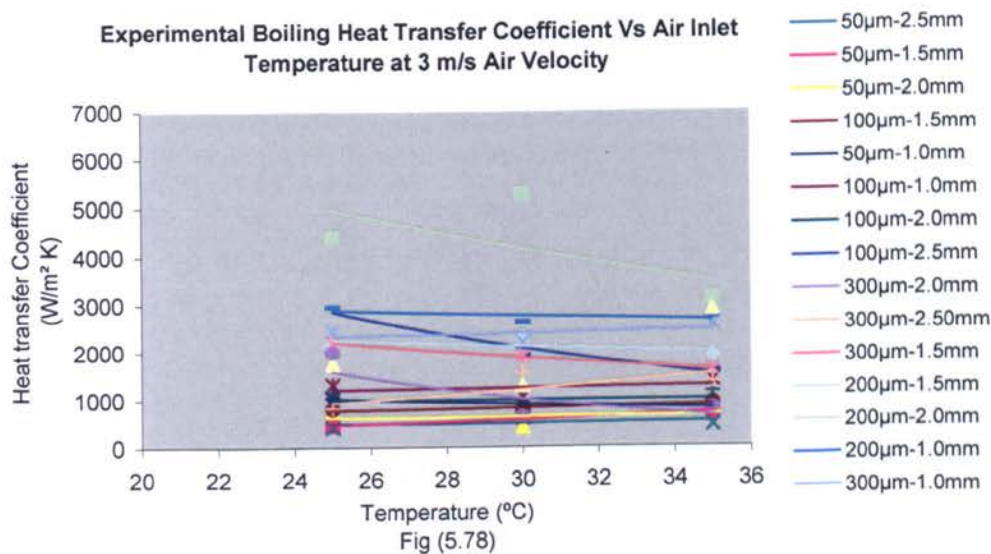
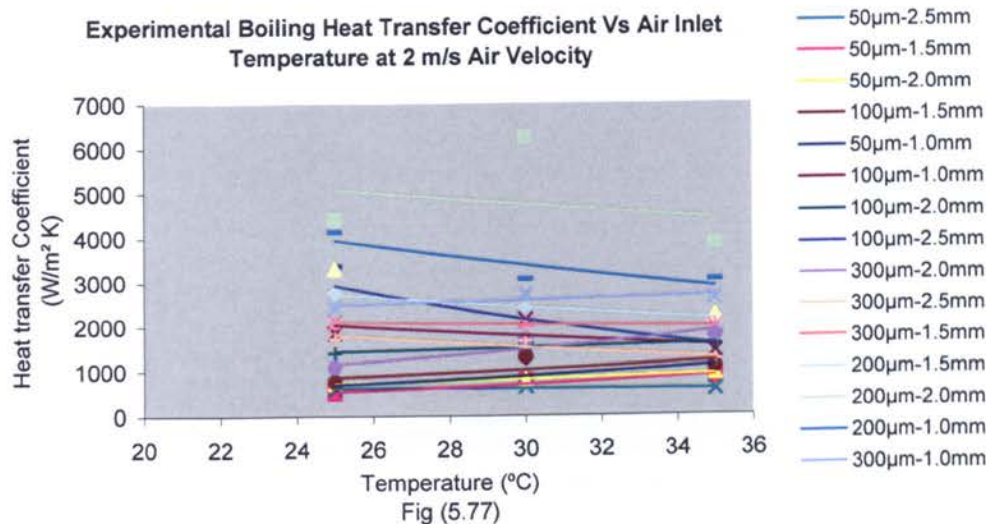
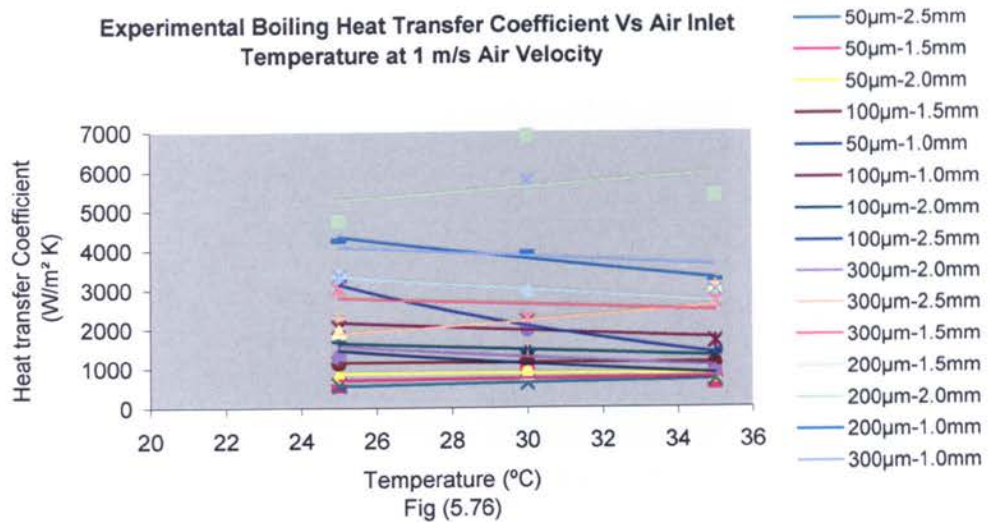


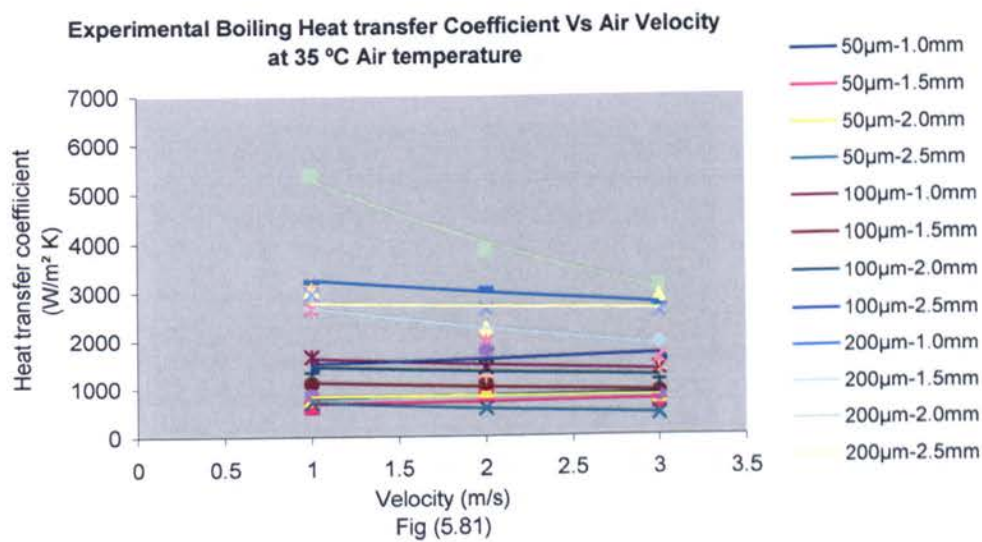
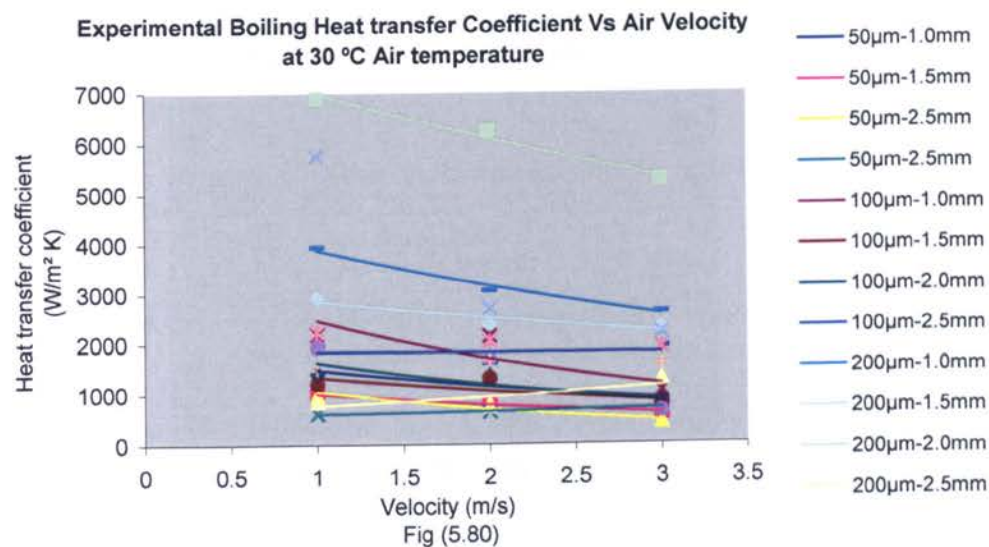
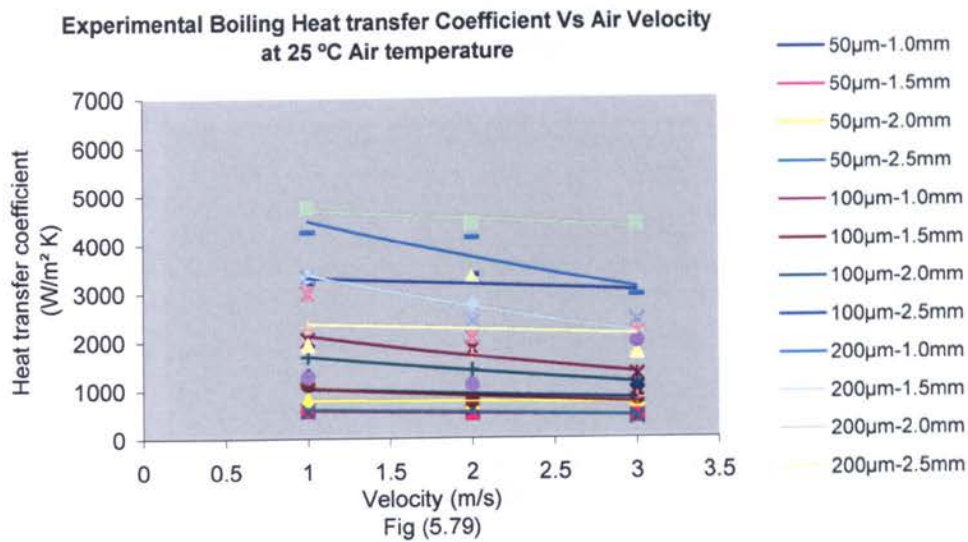
Experimental & Analytical (Rao & Balkrishnan) Boiling Heat Transfer
Coefficients Vs Layer Thickness at 3.0 m/s & 30 °C Air Velocity and Temperature

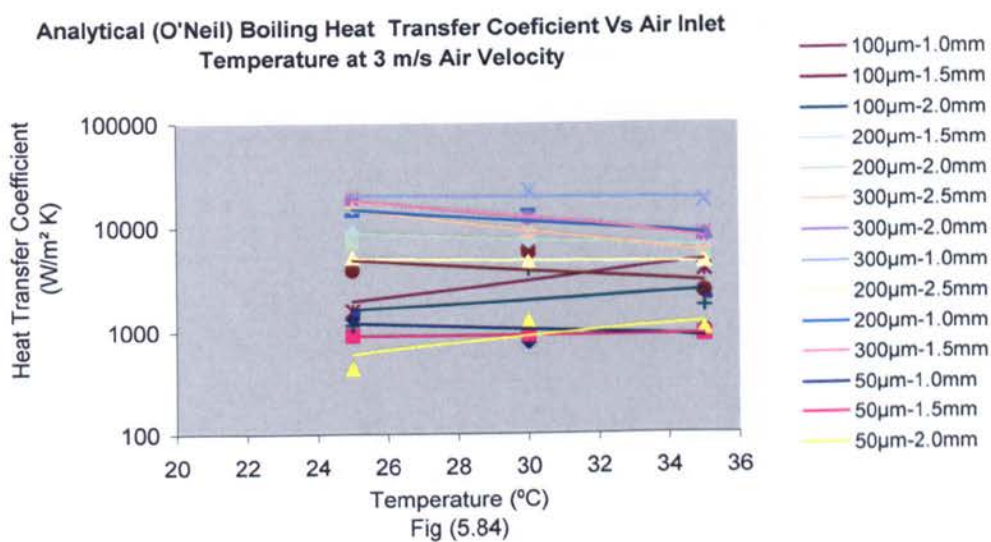
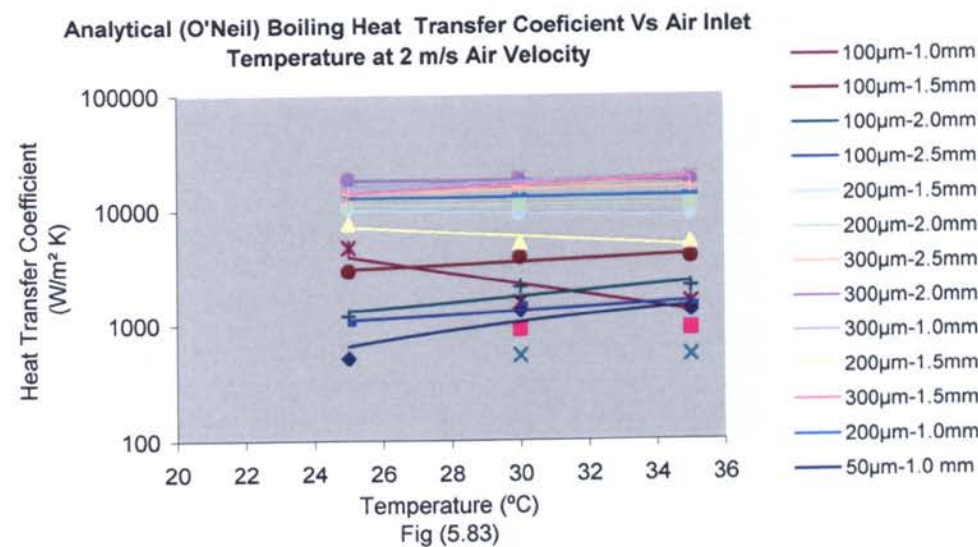
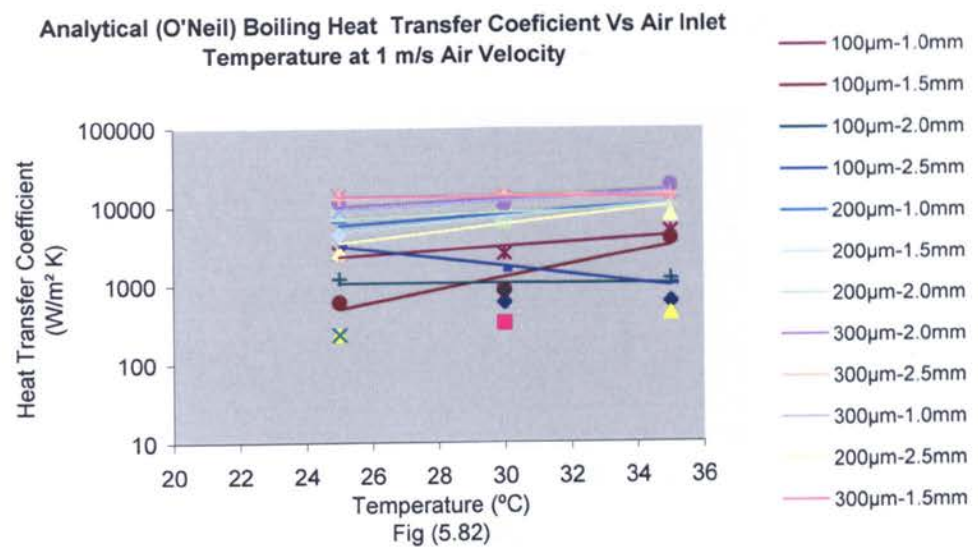


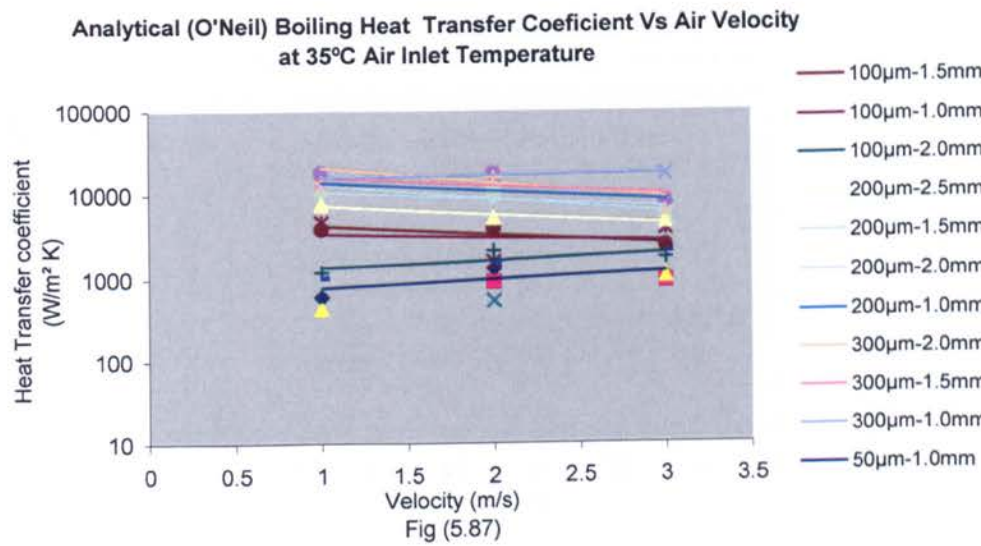
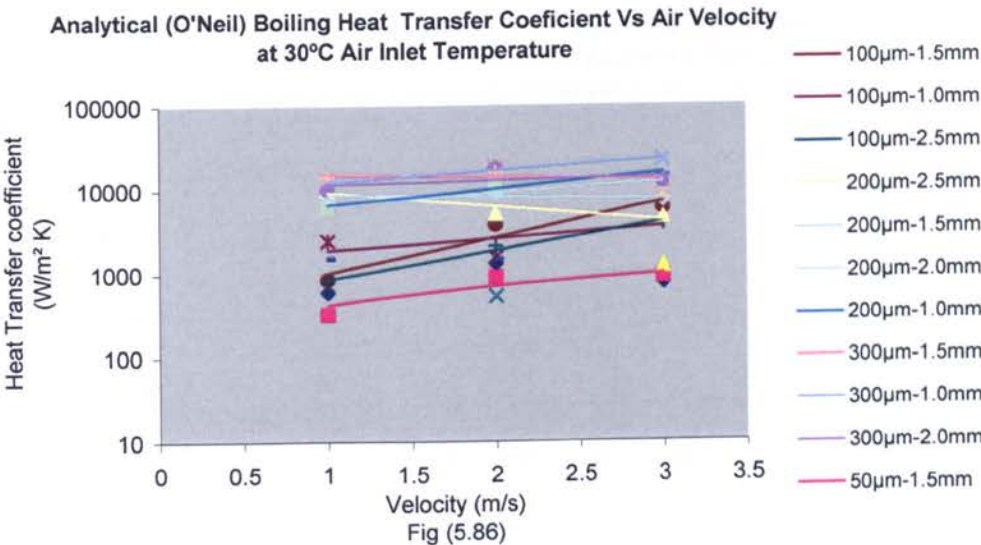
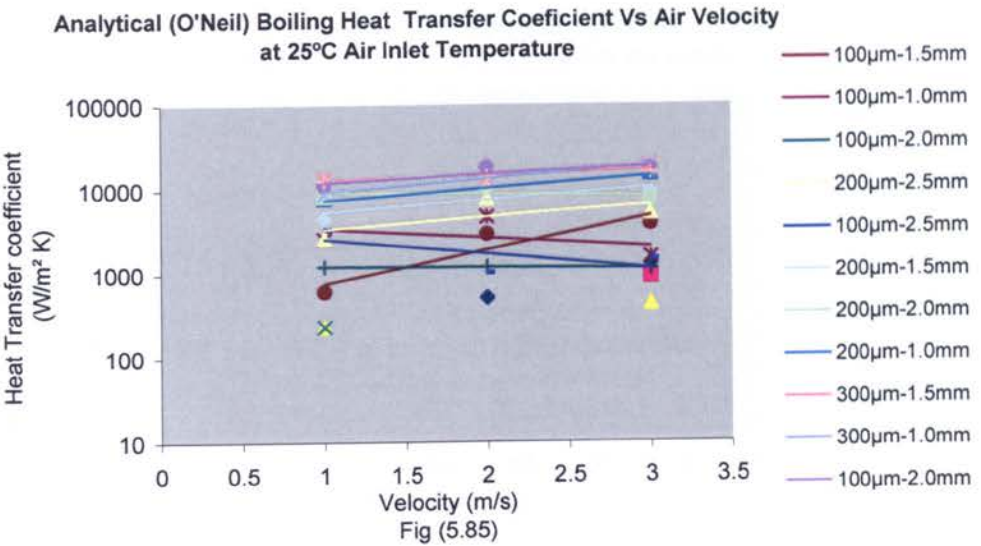
Experimental & Analytical (Rao & Balkrishnan) Boiling Heat Transfer
Coefficients Vs Layer Thickness at 3.0 m/s & 35 °C Air Velocity and Temperature

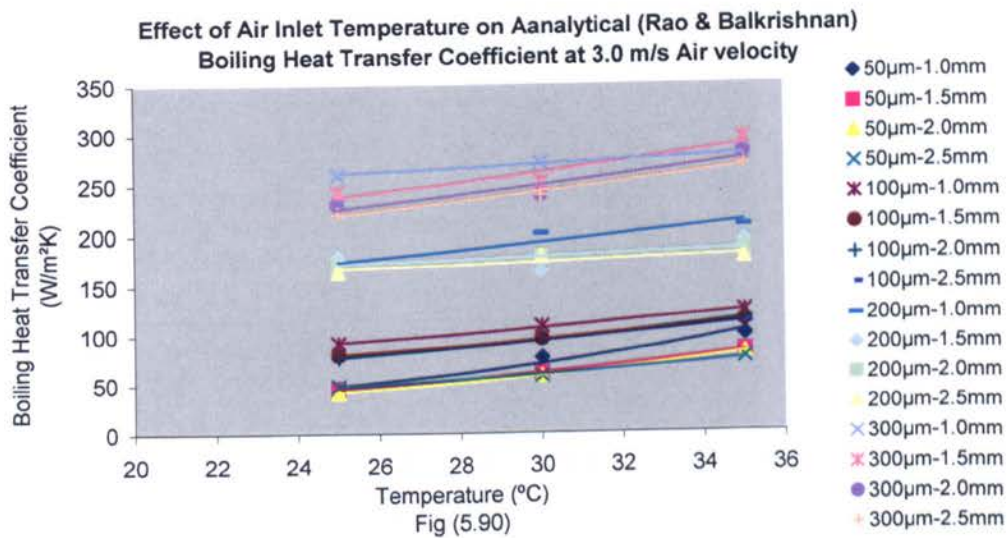
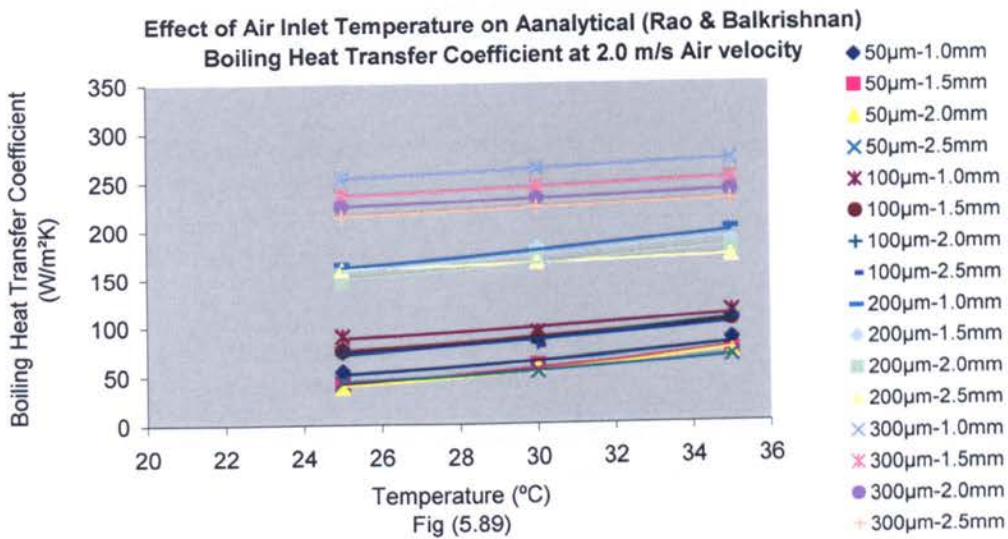
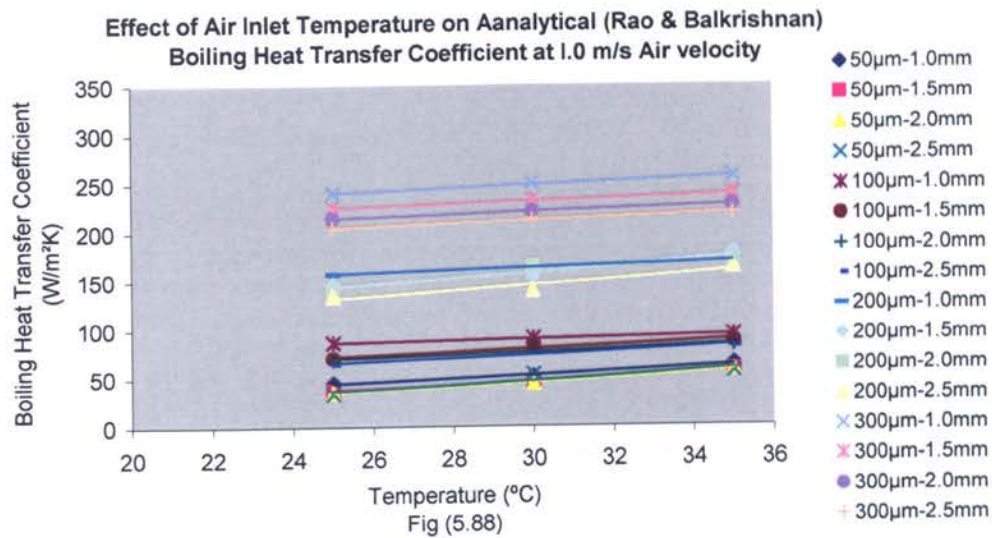


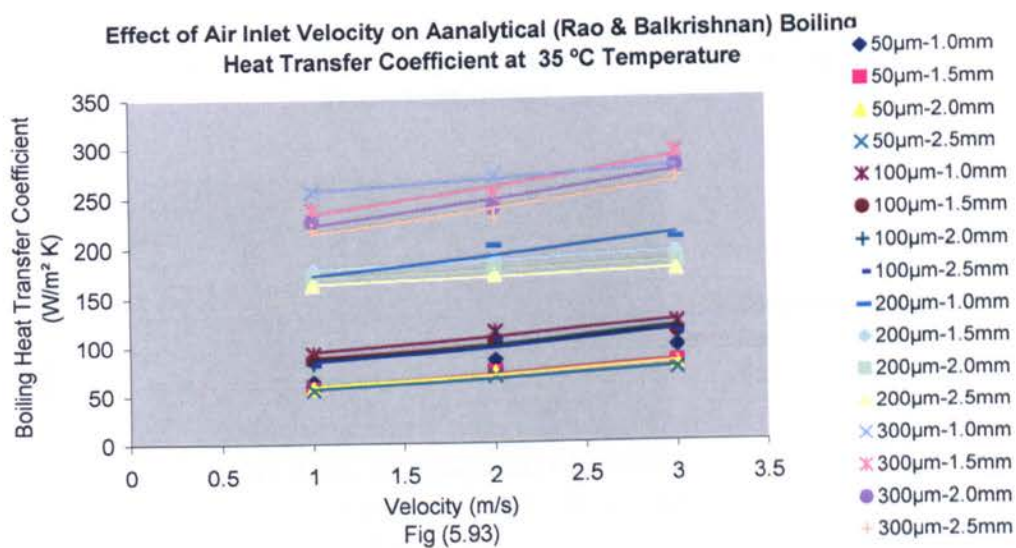
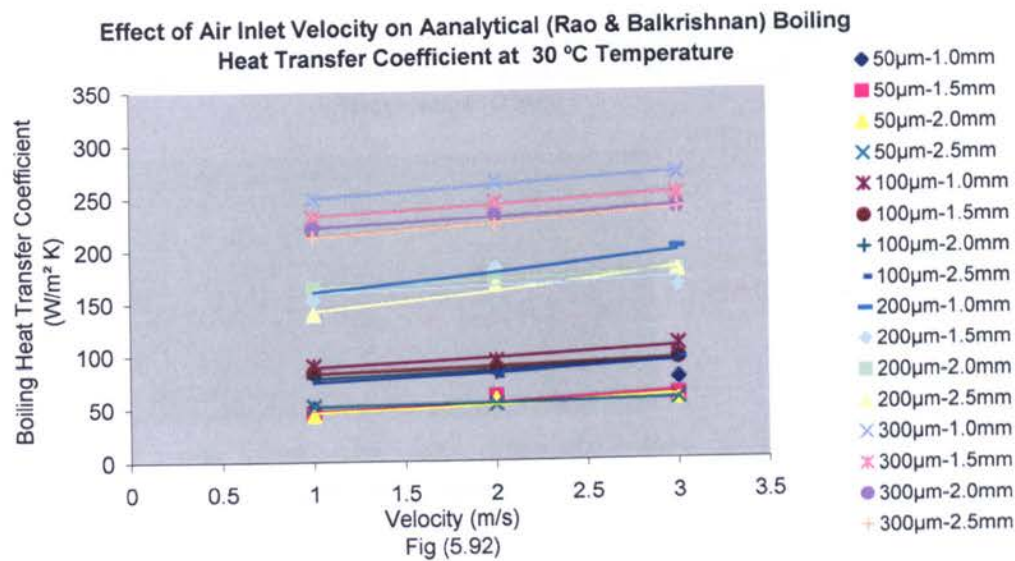
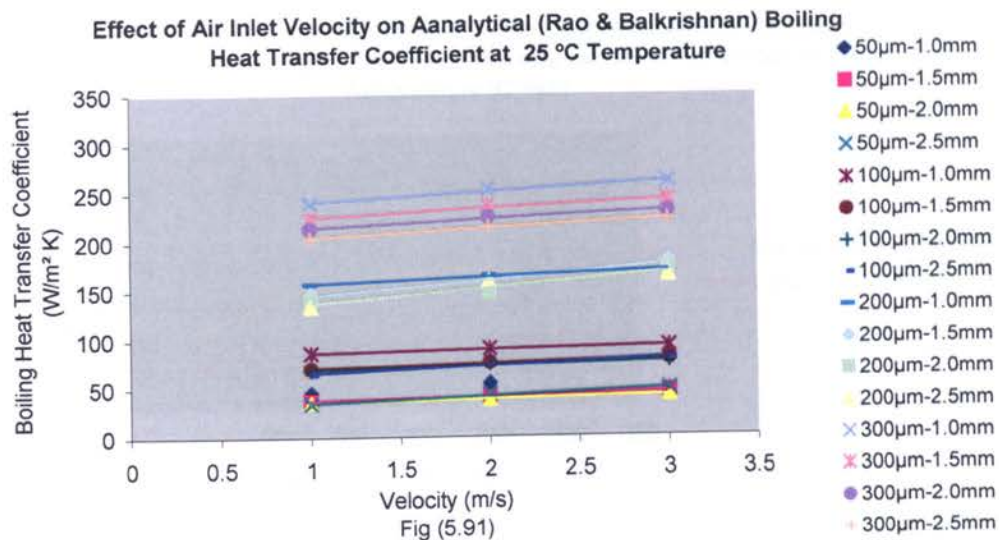




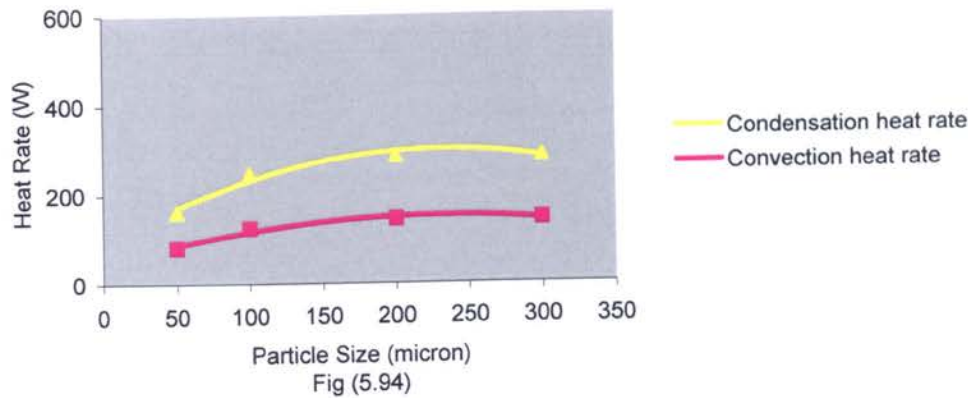




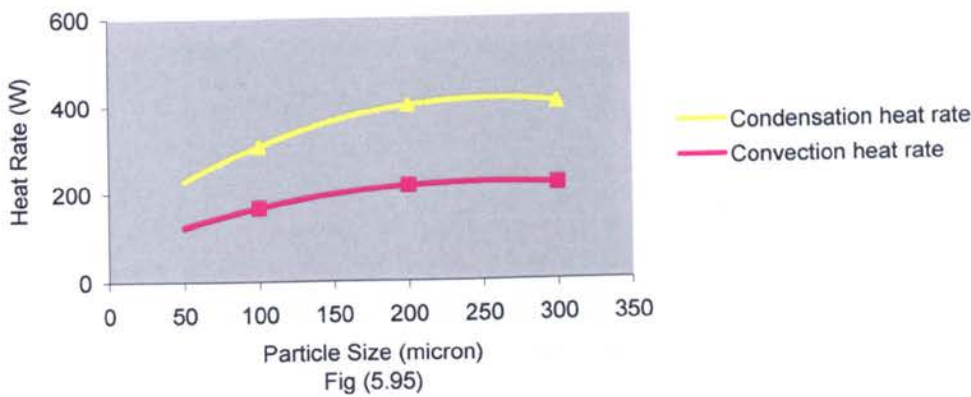




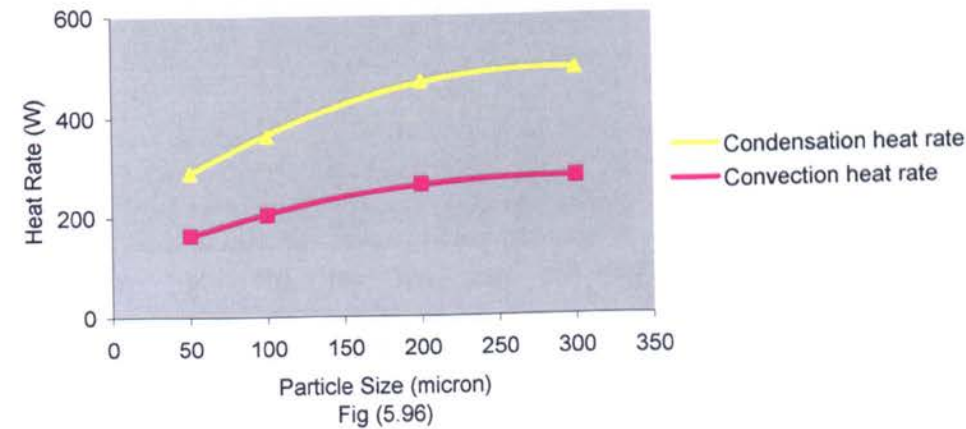
Analytical Boiling, Condensation & Convection Heat Rate Vs Particle Size for the 2.0 mm Layer thickness at 1.0 m/s and 25 °C Air velocity and Temperature (O'Neil)



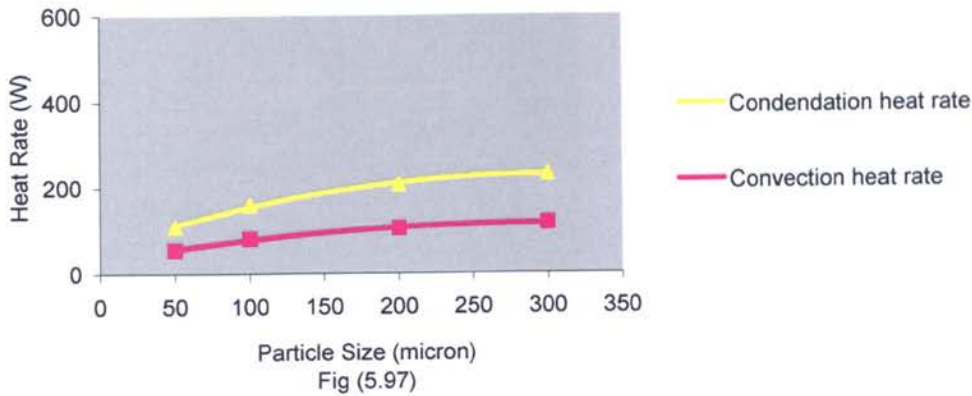
Analytical Boiling, Condensation & Convection Heat Rate Vs Particle Size for the 2.0 mm Layer thickness at 2.0 m/s and 25 °C Air velocity and Temperature (O'Neil)



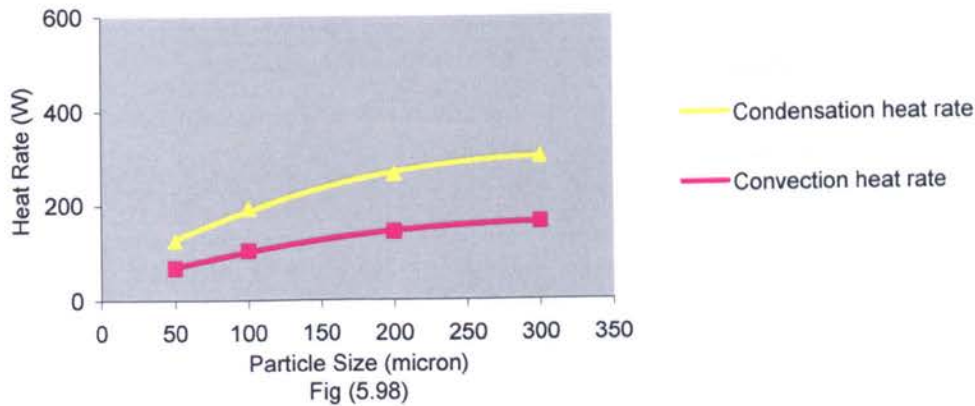
Analytical Boiling, Condensation & Convection Heat Rate Vs Particle Size for the 2.0 mm Layer thickness at 3.0 m/s and 25 °C Air velocity and Temperature (O'Neil)



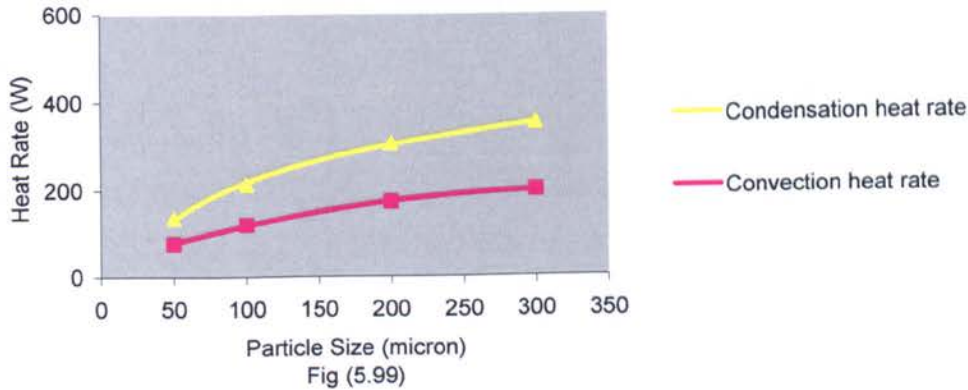
Analytical Boiling, Condensation & Convection Heat Rate Vs Particle Size for the 2.0 Layer thickness at 1.0 m/s and 25 oC Air velocity and Temperature (Rao & Balkrishnan)



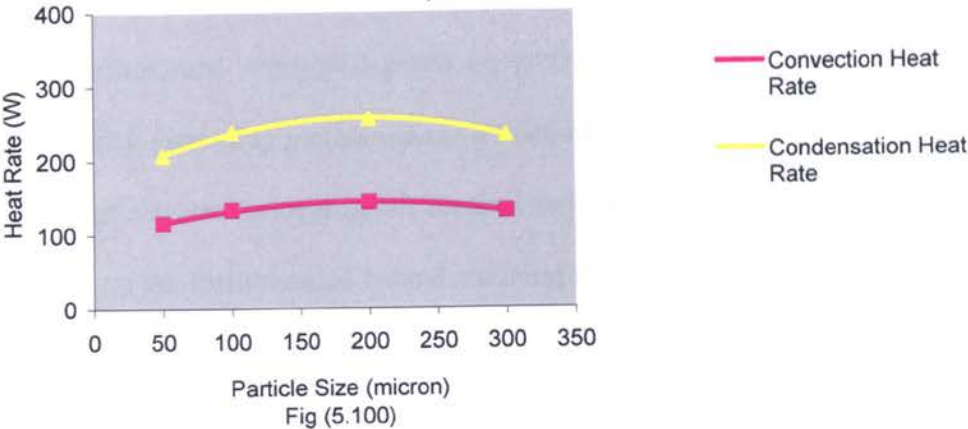
Analytical Boiling, Condensation & Convection Heat Rate Vs Particle Size for the 2.0 Layer thickness at 2.0 m/s and 25 oC Air velocity and Temperature (Rao & Balkrishnan)



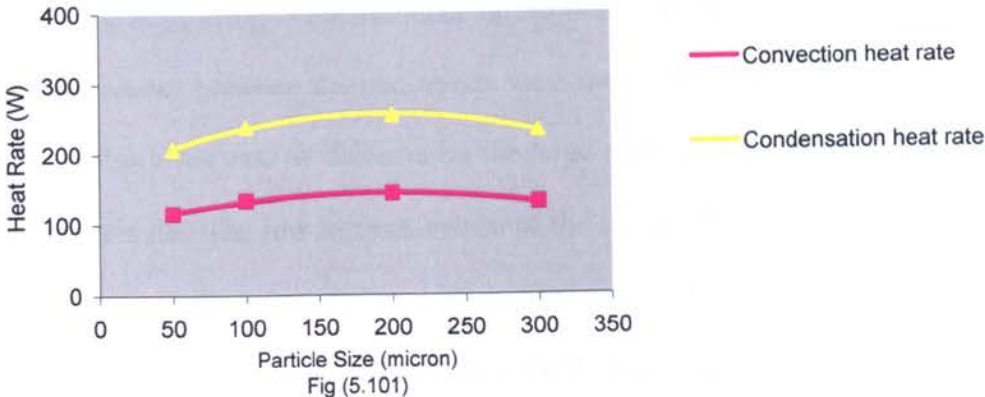
Analytical Boiling, Condensation & Convection Heat Rate Vs Particle Size for the 2.0 Layer thickness at 3.0 m/s and 25 oC Air velocity and Temperature (Rao & Balkrishnan)



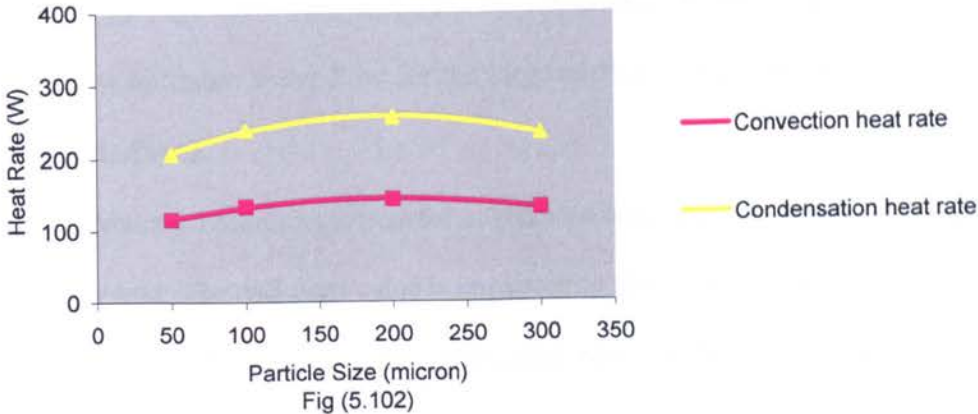
Experimental Condensation & Convection Heat Rate Vs Particle Size for the 2.0 Layer thickness at 1.0 m/s and 25 oC Air velocity and Temperature



Experimental Condensation & Convection Heat Rate Vs Particle Size for the 2.0 Layer thickness at 2.0 m/s and 25 oC Air velocity and Temperature



Experimental Condensation & Convection Heat Rate Vs Particle Size for the 2.0 Layer thickness at 3.0 m/s and 25 oC Air velocity and Temperature



Chapter 6**Conclusion**

In conclusion, it is stated that for the range of particle size tested in this research the boiling performance strongly depends on particle size. Experimental boiling heat rate increases with increasing particle size to a maximum and then decreases. Low liquid flow, difficulty of vapour removal, short menisci length and excessive capillary pressure are thought to be the main reasons behind attaining low boiling heat rates from small particle size evaporators. With increase in vapour generation rates for large particle sizes the viscous forces in the vapour region and chocking due to vapour velocity reaching that of sound limit the increase of boiling heat rate and in most cases, reverse the upward trend of heat rate.

Analytical results using O'Neil formula agreed fairly well with the experimental data. The main differences between the two trends were the lower average values of boiling heat rates and the lower rate of decrease on the large particle sizes' side of the curve for the analytical results. The low average values of the boiling heat rates are attributable to the inaccuracies of all the formulae used in the computational iterative model. The low steepness on the decreasing curves in O'Neil results is thought to be due to under estimation of the flooding of some nucleation sites due to increased water flow associated with larger particle sizes. This highlights the importance of designing the porous layer in a way to have optimum water flow for the large particle size evaporators to avoid flooding the nucleation sites.

The experimental boiling heat transfer coefficient was found to follow the same trend as that of heat rate. The optimum value is consistently maintained by the 200 μm particle size and 2 mm layer thickness evaporator. Boiling heat transfer coefficients obtained using O'Neils boiling formula agreed in trend with the experimental ones for particle sizes 50, 100 and 200 μm and disagreed for larger particle sizes. The disagreement is reflected by the fact that O'Neil results showed monotonous increase for particle sizes greater than 200

Chapter 6: Conclusion

μm . It is evident from, both analytical and experimental results that the discrepancy resulted from the fact that experimental wall superheats were actually higher than those predicted analytically. In explanation to this, the deterioration in boiling performance due to flooding¹ and the formation of thin film of vapour separating the wick from the tube wall are thought to be possible causes of this increased experimental wall superheats in large particle sizes' evaporators.

The boiling heat rate obtained using Rao and Balkrishnan's is relatively low and showed monotonous increase with particle size. It is not known, for sure whether there will be a maximum followed by a fall down at larger particle sizes or not. However, the rate of increase seems to slow down indicating a possible approach to a maximum. Nevertheless, this trend appear to confirm the explanation given earlier that high liquid pressure drops, difficulty of vapour removal, short thin films and excessive capillary pressure seem to be major constraints of boiling associated with small particle sizes. The use of Darcy's law in deriving Rao and Balkrishnan's boiling formula might have contributed to the discrepancy. This is due to the failure of the authors to verify that the velocity of the vapour leaving the porous layer is high enough to justify using Darcy's law. The analytical boiling heat transfer coefficient, using Rao and Balkrishnan boiling formula, was found to be low. The low boiling heat rate obtained from this formula and the use of Clapeyron equation in deriving this model for boiling in porous structures are thought to be behind the low value of boiling heat transfer coefficient. Whilst the change in pressure in Clapeyron equation is due to the phase change from liquid to vapour, Rao and Balkrishnan dealt with it as a pressure drop due to vapour flow across the porous layer.

The change in boiling performance with varying layer thickness is found to be relatively mild. Whilst some curves (on both, the analytical and experimental results) are seen to decrease monotonically with increasing layer thickness, others act differently and show monotonous increase in performance with increasing particle size. This could be an

¹ Flooding of nucleation sites is over feeding them with water flow greater than the optimum flow and at a temperature less than the saturation temperature.

Chapter 6: Conclusion

indication that the general trend, if larger layer thickness ranges are to be tested, is one of peaks and troughs. Contradicting factors are thought to be behind this wavy trend. On one hand, increased layer thickness increases thermal resistance and reduces vapour core diameter. Both factors decrease boiling performance. On the other hand, the thicker the layer, the larger the number of nucleation sites and the better the mass flow rate due to better ejection by the larger (due to coalescence) vapour jets. This trend is thought to be useful as it allows flexibility of design, where the performance is not critical and may be optimised at more than one combination of layer parameters.

Neglecting the interfacial temperature, T_i , in predicting the boiling heat transfer coefficient may have contributed to the discrepancies between the experimental and analytical data.

The boiling performance was found to be mildly dependant on air velocity and temperature. This finding agrees well with the results obtained analytically. The dependency on air velocity seems to be slightly stronger than on temperature.

The effect of air inlet relative humidity was found to be significant in determining the cooling capacity of capillary assisted evaporators in a lithium bromide/water cycle. The heat removed from the air by condensing some of its moisture content was found to be more than that removed by forced convection between the air and tube walls. This largely diminishes the sensible decrease in the temperature of the air to be cooled.

Recommendation for Future Work

To better understand boiling in sintered tube evaporators a wider range of particle size and layer thickness should be tested. In particular, thickness ranges with thinner layers than the ones tested in this research should be investigated.

In addition to that the effect of thermo physical properties i.e. layer porosity, permeability and layer material thermal conductivity should be tested.

Using advanced photography methods might be helpful in determining the actual hydrodynamic and thermal processes that take place during boiling in a porous structure. In building an analytical model for boiling in porous structures, such hydrodynamic and thermal processes should be accounted for.

The flooding of nucleation sites associated with large particle sizes should be considered. The porous layer should be designed in a way to avoid excess water flow to the nucleation sites to avoid flooding them. The analytical model should also account for the effect of air inlet relative humidity.

The geometry of the surface to be modified for better boiling by adding capillary structure is of great importance, particularly when high vapour flow rates are involved to avoid limiting the boiling performance by the viscous/sonic limits. The analytical models should look for the optimal geometrical design of the apparatus to be modified along with the optimal design of capillary structure itself.

Appendix A

Iterative Computational Programme Algorithm¹

This algorithm is for a program in FORTRAN 95 language and it calculates the boiling heat rate transported by sintered tubes evaporators as well as the boiling heat transfer coefficient. The influence of heat transfer limits, namely: the capillary, sonic, viscous and boiling limits on boiling performance is taken into account by this program.

Input: D_p, Delta

Output: D_p, Delta, Q_c, Q_b, Q_s, Q_v, M_Dot_w, P_c_max, Delta_P_v, Delta_P_L, Delta_P_i, Q_out, T_sat, Q_boil, Q_conv, Q_cond, T_w, SA

Declaration:

Real: D_p, Delta, Q, Delta_P_v1, Delta_P_v2, Delta_P_v3, P_c_max, R_eff, R_v, d_v, A_v, L_e, h_f4_1, h_f4_2, h_f4_3, h_f3, a, b, c, Q1, Q2, Re_v, Fx, Fx_dash, V_v, V_vi, V_v1, Q_b, k_eff, Delta_P_L1, Delta_P_L2, K, A_W, Delta_P_L, M_Dot_w, Delta_P_v, Delta_P_i, A_i, Mu_v, ROH_v, H_fg, SIGMA, P_sat, k_L, ROH_L, Mu_L, M_Dot_v, VAIR_max, REAIR_max, NUAIR_max, Q_min, T_sat, A_o, Pr_L, h_cond, Q_boil, q_boiling, Q_out, Q_cond, Q_conv, h_conv, PRSA, DELTA_T, T_w, Q_s, Q_v, A1, A2, Delta_P_v4_2, Delta_P_v4_1, Q_new, Ma, Delta_P_v_Lam, Delta_P_L_Lam, d, e, f, i, j, m, Delta_P_i_v, Delta_P_i_i

Constants: k_br=52, D_i=25.3E-3, L_a=2.235, H=0.57, D1=0.075, D2=0.3, R_n=2.54E-7, ETA=0.48, n=9, L_t=0.3, D_o=0.0286, CPL=4200, SL=8.4E-2, ST=56.4E-3, AT=96.1E-3, Gamma=1.33, r_i=0.0127

Constants: V_air= 1, T_air=303.15, NUA=1.59668E-5, PRA=0.70628, kA=2.64704E-2

1. Read input file.
2. As an initial guess take $T_{sat} = 273.16$ and $T_w = 1.0033 * T_{sat}$.
3. Iterate to find the tube wall temperature by starting T_w DO LOOP
 - 3.1. Interpolate to get ROH_L by calling subroutine ROHL
 - 3.2. Interpolate to get ROH_v by calling subroutine ROHV
 - 3.3. Interpolate to get H_fg by calling subroutine HFG
 - 3.4. Interpolate to get Pr_L by calling subroutine PRL
 - 3.5. Interpolate to get K_L by calling subroutine KL

¹ For interpretation of symbols used in this algorithm, refer to the last section of the nomenclature in this thesis.

Appendix A: Iterative Computational Programme Algorithm

- 3.6. Interpolate to get μ_L by calling subroutine MUL
- 3.7. Interpolate to get μ_v by calling subroutine MUV
- 3.8. Interpolate to get SIGMA by calling subroutine SIG_MA
- 3.9. Interpolate to get P_{sat} by calling subroutine PSAT
- 3.10. Interpolate to get PRSA by calling subroutine PR_SA
- 3.11. Interpolate to get CPL by calling subroutine CP_L
- 3.12. Call subroutine Calculate Q_{min}
- 3.13. To calculate Q_{boil} do the following:
 - 3.13.1. Calculate $Ja = (ROH_L * CPL * \Delta T) / (ROH_v * H_{fg})$
 - 3.13.2. Calculate $q_{boiling} = (k_L * \Delta T / (0.044 * D_p^{**2})) * (\Delta T - 9.66 * SIGMA * (T_{sat} - 273.15) / (ROH_v * H_{fg} * D_p))$
 - 3.13.3. Calculate $HTC_{boil} = q_{boiling} / \Delta T$
 - 3.13.4. Calculate $Q_{boil} = q_{boiling} * \pi * d_i * L * n$
- 3.14 To calculate Q_{conv} do the following:
 - 3.14.1. Calculate $VAIR_{max} = (ST * V_{air}) / (ST - d_o)$
 - 3.14.2. Calculate $REAIR_{max} = (VAIR_{max} * D_o) / NUA$
 - 3.14.3. Calculate $NUAIR_{max} = 0.76 * 0.35 * ((ST/SL)^{**0.2}) * (REAIR_{max}^{**0.6}) * (PRA^{**0.36}) * (PRA/PRSA)^{**0.25}$
 - 3.14.4. Calculate $h_{conv} = (NUAIR_{max} * k_A) / D_o$
 - 3.14.5. Calculate $A_o = \pi * D_o * L * n$
 - 3.14.6. Calculate $Q_{conv} = h_{conv} * A_o * (T_{air} - T_w)$
- 3.15. To calculate condensation heat rate, Q_{cond} , do the following:
 - 3.15.1. $h_{cond} = (0.616 * (V_{air} * 3.28083 * 60)^{**0.5}) / 0.17612$
 - 3.15.2. $Q_{cond} = h_{cond} * A_o * (T_{air} - T_w)$
- 3.16. Calculate $Q_{out} = Q_{cond} + Q_{conv}$
- 3.17. IF the following conditions are satisfied, then exit T_w DO LOOP
 - 3.17.1. $(T_w > T_{sat})$
 - 3.17.2. $(T_w < T_{air})$
 - 3.17.3. $ABS(Q_{out} - Q_{boil}) \leq (0.25 * Q_{boil} + 0.06 * Q_{cond} + 0.2 * Q_{conv})$
 - 3.17.4. $Q_{BOIL} \leq Q_{MIN}$
- 3.18. Iterate to find the water saturation temperature by starting T_{sat} DO LOOP
 - 3.18.1. Interpolate to get ROH_L by calling subroutine ROHL.
 - 3.18.2. Interpolate to get ROH_v by calling subroutine ROHV.
 - 3.18.3. Interpolate to get H_{fg} by calling subroutine HFG.
 - 3.18.4. Interpolate to get Pr_L by calling subroutine PRL.

Appendix A: Iterative Computational Programme Algorithm

- 3.18.5. Interpolate to get K_L by calling subroutine KL.
- 3.18.6. Interpolate to get SIGMA by calling subroutine SIG_MA.
- 3.18.7. Interpolate to get P_{Sat} by calling subroutine PSAT.
- 3.18.8. Interpolate to get CPL by calling subroutine CP_L
- 3.18.9. Re-calculate Q_{boil} as following:
 - 3.18.9.1. Calculate $Ja = (ROH_L * CPL * DELTA_T) / (ROH_v * H_{fg})$
 - 3.18.9.2. $q_{boiling} = (k_L * DELTA / (0.044 * D_p^{**2})) * (DELTA_T - 9.66 * SIGMA * (T_{sat} - 273.15) / (ROH_v * H_{fg} * D_p))$
 - 3.18.9.3. Calculate $HTC_{boil} = q_{boiling} / DELTA_T$
 - 3.18.9.5. Calculate $Q_{boil} = q_{boiling} * Pi * d_i * L_t * n$
- 3.18.10. Call subroutine Calculate Q_{min}
- 3.18.11. IF the following conditions are satisfied, then EXIT T_{sat} DO LOOP
 - 3.18.11.1. $(T_w > T_{sat})$
 - 3.18.11.2. $(T_w < T_{AIR})$
 - 3.18.11.3. $|Q_{OUT} - Q_{BOIL}| \leq (0.06 * Q_{COND} + 0.2 * Q_{CONV})$
 - 3.18.11.4. $Q_{BOIL} \leq Q_{MIN}$
- 3.18.12. IF $|T_w - T_{sat}| = 0.1$ then EXIT T_{sat} DO LOOP
- 3.18.13. IF $|T_{air} - T_{sat}| \leq 0.001$ then EXIT T_{sat} DO LOOP
- 3.18.14. If the exit conditions in steps 3.17.10 to 3.17.12 are not satisfied then change the assumption of T-sat as follow: $T_{sat_{new}} = 1.0001 * T_{sat_{old}}$
- 3.19. END DO T_{sat} ITERATION
- 3.20. When a solution is found write SA = 1
- 3.21. IF the following conditions are satisfied, then EXIT T_w DO LOOP
 - 3.21.1. $(T_w > T_{sat})$
 - 3.21.2. $(T_w < T_{AIR})$
 - 3.21.3. $|Q_{OUT} - Q_{BOIL}| \leq (0.06 * Q_{COND} + 0.2 * Q_{CONV})$
 - 3.21.4. $Q_{BOIL} \leq Q_{MIN}$
- 3.22. When no solution is found write SA = 0
- 3.23. IF $(T_w \geq T_{AIR})$, THEN EXIT T_w DO LOOP
- 3.24. CHANGE THE ASSUMPTION OF T_w AS FOLLOWS: $T_{WNEW} = T_{WOLD}$
- 3.25. Put $T_{sat} = 273.16$ o K
4. END DO T_w ITERATION
5. Write output values to output file

7. The programme contains the following subroutines²:

- 7.1. Subroutine HFG
 - 7.2. Subroutine KL
 - 7.3. Subroutine MuL
 - 7.4. Subroutine Muv
 - 7.5. Subroutine PrL
 - 7.6. Subroutine PR_SA
 - 7.7. Subroutine PSAT
 - 7.8. Subroutine CP_L
 - 7.9. Subroutine QMIN
 - 7.10. Subroutine ROHL
 - 7.11. Subroutine ROHV
 - 7.12. Subroutine SIG_MA
- 8. End Programme**

Subroutine Calculate QMIN

This subroutine is part of the main programme for calculating the boiling heat rate transported by the each sintered evaporator under the specific test conditions i.e. air inlet temperature and pressure.

- 1. Calculate vapour core radius $R_v = (d_i/2) - \Delta$
- 2. Calculate vapour core diameter $d_v = 2 * R_v$
- 3. Calculate evaporator effective length radius $L_e = n * L_t$
- 4. Calculate effective pore radius $R_{eff} = 0.41 * (D_p/2)$
- 5. Calculate evaporator tube's inlet cross-sectional area $A_i = \pi * (d_i/2)^2$
- 6. Calculate evaporator vapour core cross-sectional area $A_v = \pi * R_v^2$
- 7. Calculate vapour outlet pipe cross-sectional area after expansion 2: $A_1 = \pi * D_1^2$
- 8. Calculate vapour pressure drop due to friction

$$\Delta P_{v1} = (16 * \mu_v / (2 * ROH_v * H_{fg})) * ((L_e / ((R_v^2) * A_v) + (L_a / (R_i^2) * A_i)))$$

- 9. Calculate the normal hydrostatic vapour pressure drop $\Delta P_{v2} = ROH_v * g * H$

- 10. Calculate vapour velocity $V_v = 1 / (ROH_v * H_{fg} * A_v)^3$

² Detailed algorithm for each subroutine is given on the following pages

Appendix A: Iterative Computational Programme Algorithm

11. Calculate vapour velocity $V_{vi} = V_v * (A_v/A_i)$
12. Calculate vapour velocity after expansion 2: $V_{v1} = V_{vi} * (A_i/A1)$
13. Calculate the friction coefficient $h_{f3} = k_f * (V_{vi}^2)/(2 * g)$ at the right angle elbows
14. Calculate vapour pressure drop at the right angle elbows (5 off)
 $\Delta P_{v3} = 5 * h_{f3} * ROH_v * g$
15. Calculate the friction coefficient due to expansion 1: $h_{f4_1} = ((V_v^2)/(2 * g)) * (1 - (A_v/A_i))^2$
16. Calculate vapour pressure drop due to expansion 1: $\Delta P_{v4_1} = h_{f4_1} * ROH_v * g$
17. Calculate the cross-sectional area of the pipe after expansion 2: $A1 = (\pi/4) * D1^2$
18. Calculate the friction coefficient due to expansion 2: $h_{f4_2} = ((V_{vi}^2)/(2 * g)) * (1 - (A_i/A1))^2$
19. Calculate vapour pressure drop due to expansion 2: $\Delta P_{v4_2} = h_{f4_2} * ROH_v * g$
20. Calculate the friction coefficient due to expansion 3: $h_{f4_3} = ((V_{v1}^2)/(2 * g)) * (1 - (A1/A2))^2$
21. Calculate vapour pressure drop due to expansion 3: $\Delta P_{v4_3} = h_{f4_3} * ROH_v * g$
22. Calculate the total vapour pressure drop due to elbows and expansions 1, 2 & 3
 $\Delta P_v = \Delta P_{v3} + \Delta P_{v4_1} + \Delta P_{v4_2} + \Delta P_{v4_3}$
23. Calculate the permeability of the porous layer $K = \eta * ((0.41 * D_p)^2)/32$
24. Calculate the cross-sectional area of the wick section $A_w = n * L_t * \Delta$
25. Calculate the liquid pressure drop due to friction in the wick and adiabatic sections
 $\Delta P_{L1} = (\mu_L * \pi * (D_i/2)) / (K * A_w * H_{fg} * ROH_L)$
26. Calculate the liquid hydrostatic pressure drop $\Delta P_{L2} = ROH_L * g * D_v$
27. Calculate the maximum capillary rise $P_{c_max} = (2 * \sigma) / R_{eff}$
28. To solve the quadratic equation in Q_c that forms if all vapour and liquid pressure drops are added together and equated with the maximum capillary rise, do the following:
 - 28.1. Let the coefficient of Q_c^2 term be: $a = \Delta P_v$

³ In fact the expression $(1/(ROH_v * H_{fg} * A_v))$ is just a factor that needs to be multiplied by capillary limit heat rate Q_c in order to get the actual vapour velocity. This applies to V_{vi} , h_{f3} , ΔP_{v3} , V_{v1} , h_{f4_1} , ΔP_{v4_2} & ΔP_{v4_2}

Appendix A: Iterative Computational Programme Algorithm

- 28.2. Let the coefficient of Q_c term be: $b = \Delta P_{v1} + \Delta P_{L1}$
- 28.3. Let the constant term be: $c = \Delta P_{v2} + \Delta P_{L2} - P_{c_max}$
- 28.4. Calculate the first root of the quadratic equation $Q1 = (-b + ((b^2) - 4*a*c)^{0.5}) / (2*a)$
- 28.5. Calculate the second root of the quadratic equation $Q2 = (-b - ((b^2) - 4*a*c)^{0.5}) / (2*a)$
- 28.6. Choose the positive root of the quadratic equation as the required solution
29. Calculate Reynolds number $Re_v = 2*R_v*Q/(A_v*Mu_v*H_{fg})$
30. If the vapour flows is laminar then:
- 30.1. Calculate $\Delta P_{v_Lam} = (\Delta P_v * Q_c^2) + (\Delta P_{v1} * Q_c) + (\Delta P_{v2})$
- 30.2. Calculate $\Delta P_{L_Lam} = \Delta P_{L1} * Q_c + \Delta P_{L2}$
- 30.3. Go to step No. 35 in this algorithm
31. If the flow is turbulent calculate the vapour pressure drop in the wick and adiabatic section as follows:
- 31.1. $D = 1 / (Mu_v * H_{fg})^{0.75}$
- 31.2. $E = 2 * Mu_v / (ROH_v * H_{fg})$
- 31.3. $F = (D_v / A_v)^{0.75}$
- 31.4. $I = L_e / ((D_v^2) * A_v)$
- 31.5. $J = (D_i / A_i)^{0.75}$
- 31.6. $m = L_a / ((D_i^2) * A_i)$
- 31.7. $\Delta P_{v1} = D * E * (F * I + J * m)$
32. Calculate the inertial pressure gradient
- 32.1. Pressure gradient in the evaporator section i.e. when $L_a = 0$
- $$\Delta P_{i_v} = n * ((ROH_v * V_v^2) / (2 * g)) * ((28/9) - \& (0.68 * Re_v / (29 * L_e / D_v)))$$
- 32.2. Pressure gradient in the adiabatic section i.e. when $L_e = 0$
- $$\Delta P_{i_i} = ((ROH_v * V_{vi}^2) / (2 * g)) * ((28/9) - \& (0.68 * Re_v * EXP(-60 * L_a / (Re_v * D_i))))$$
- 32.3. The total pressure gradient
- $$\Delta P_i = \Delta P_{i_v} + \Delta P_{i_i}$$
33. Start DO LOOP to solve the equation below formulated by summing up vapour and liquid pressure drops

Appendix A: Iterative Computational Programme Algorithm

$$F_x = ((\Delta P_{v1}) * (Q_c^{**1.75})) + ((\Delta P_v + \Delta P_i) * (Q_c^{**2})) + \Delta P_{L1} * Q_c + (\Delta P_{v2} - P_{c_max})$$

Using Newton Raphson iteration method.

34. Calculate the liquid pressure drop $\Delta P_L = (\Delta P_{L1} * Q_c) + \Delta P_{L2}$

35. Calculate the liquid mass flow rate

$$M_{\text{Dot}_w} = (\Delta P_L * K / \mu_L) * \rho_{H_2O} * A_w * \eta$$

36. Calculate the viscous limit $Q_v =$

$$((d_v^{**2}) * H_{fg} * A_v * P_{sat} * \rho_{H_2O}) / (64 * \mu_v * L_e)$$

37. Calculate the effective thermal conductivity $k_{eff} = (1 - \eta) * K_{br} + \eta * k_L$

38. Calculate the boiling limit

$$Q_b = (2 * \pi * L_e * k_{eff} * T_{sat} / (\rho_{H_2O} * H_{fg} * \log((d_i / R_v))) * ((2 * \sigma / R_n) - P_{c_max})$$

39. Calculate the sonic limit heat rate $Q_s = 0.474 * H_{fg} * A_v * (\rho_{H_2O} * P_{sat})^{**0.5}$

40. IF the vapour flow is laminar, then:

40.1. $\Delta P_i = 0$

40.2. Calculate $\Delta P_{v_Lam} = (\Delta P_v * Q_c^{**2}) + (\Delta P_{v1} * Q_c) + (\Delta P_{v2})$

40.3. Calculate $\Delta P_{L_Lam} = \Delta P_{L1} * Q_c + \Delta P_{L2}$

41. IF the vapour flow is turbulent, then:

41.1. $\Delta P_i = \Delta P_i * Q_c^{**2}$

41.2. $\Delta P_v = (\Delta P_v * Q_c^{**2}) + (\Delta P_{v1} * Q_c^{**1.75}) + (\Delta P_{v2}) + \Delta P_i$

42. Choose the smallest limit heat rate of the four calculated limits i.e. capillary, viscous, boiling and sonic limits and take it as Q_{min}

43. End subroutine Q_{min}

Subroutine HFG

This subroutine is for interpolating to calculate the latent heat of vaporisation depending on the value of water saturation temperature, T_{sat}

1.If $400 > T_{sat} > 273.15$ then $H_{fg} = 1E3 * (3177.7 - (2.4659 * T_{sat}))$

2.Else $H_{fg}=1E3*(3741.5-(3.8422*T_{sat}))$

3.End subroutine HFG

Subroutine KL

This subroutine is for interpolating to calculate the thermal conductivity of the liquid depending on the value of the saturation temperature, T_{sat}

1.If $278.15 > T_{sat} > 273.15$ then $k_L = 1E-3 * ((9/4.99)*(T_{sat}-273.16)+569)$

2.If $283.15 > T_{sat} > 278.15$ then $k_L = 1E-3 * ((9/5)*(T_{sat}-278.15) + 578)$

3.If $288.15 > T_{sat} > 283.15$ then $k_L = 1E-3 * ((8/5)*(T_{sat}-283.15) + 587)$

4.If $293.15 > T_{sat} > 288.15$ then $k_L = 1E-3 * ((8/5)*(T_{sat}-288.15) + 595)$

5.If $298.15 > T_{sat} > 293.15$ then $k_L = 1E-3 * ((8/5)*(T_{sat}-293.15) + 603)$

6.If $303.15 > T_{sat} > 298.15$ then $k_L = 1E-3 * ((8/5)*(T_{sat}-298.15) + 611)$

7.If $308.15 > T_{sat} > 303.15$ then $k_L = 1E-3 * ((7/5)*(T_{sat}-303.15) + 618)$

8.If $313.15 > T_{sat} > 308.15$ then $k_L = 1E-3 * ((7/5)*(T_{sat}-308.15) + 625)$

9. Else $k_L = 0.001*(T_{sat}-273.15) + 0.5941$

10.End subroutine KL

Subroutine MUL

This subroutine is for interpolating to calculate the Dynamic viscosity of the liquid depending on the value of the saturation temperature, T_{sat} .

1.If $278.15 > T_{sat} > 270.16$, then $Mu_L = (71E-6/4.99)*(278.16-T_{sat})+1501E-6$

2.If $283.15 > T_{sat} > 278.15$ then $Mu_L = 1E-6*(1501-(201/5)*(T_{sat}-278.15))$

3.If $288.15 > T_{sat} > 283.15$ then $Mu_L = 1E-6*(1300-(164/5)*(T_{sat}-283.15))$

4.If $293.15 > T_{sat} > 288.15$ then $Mu_L = 1E-6*(1136-(134/5)*(T_{sat}-288.15))$

5.If $298.15 > T_{sat} > 293.15$ then $Mu_L = 1E-6*(1002-(112/5)*(T_{sat}-293.15))$

6.If $303.15 > T_{sat} > 298.15$ then $Mu_L = 1E-6*(890-(93/5)*(T_{sat}-298.15))$

7.If $308.15 > T_{sat} > 303.15$ then $Mu_L = 1E-6*(797-(79/5)*(T_{sat}-303.15))$

8.If $313.15 > T_{sat} > 308.15$ then $Mu_L = 1E-6*(718-(67/5)*(T_{sat}-308.15))$

9. Else $Mu_L = (-1)*5E-06*(T_{sat}-273.15) + 0.0008$

10.End subroutine MuL

Subroutine MUV

This subroutine is for interpolating to calculate the Dynamic viscosity of the vapour depending on the value of the saturation temperature, MU_v

1.If $278.15 > T_{sat} > 270.16$, then $Mu_v = (0.17E-6/4.99)*(T_{sat}-273.01)+8.49E-6$

2.If $283.15 > T_{sat} > 278.15$ then $Mu_v = 1E-6*((0.17/5)*(T_{sat}-278.15) + 8.66)$

3.If $288.15 > T_{sat} > 283.15$ then $Mu_v = 1E-6*((0.17/5)*(T_{sat}-283.15) + 8.83)$

4.If $293.15 > T_{sat} > 288.15$ then $Mu_v = 1E-6*((0.18/5)*(T_{sat}-288.15) + 9.0)$

Appendix A: Iterative Computational Programme Algorithm

- 5.If $298.15 > T_{sat} > 293.15$ then $Mu_v = 1E-6 * ((0.17/5) * (T_{sat} - 288.15) + 9.18)$
- 6.If $303.15 > T_{sat} > 298.15$ then $Mu_v = 1E-6 * ((0.18/5) * (T_{sat} - 293.15) + 9.52)$
- 7.If $308.15 > T_{sat} > 303.15$ then $Mu_v = 1E-6 * ((0.18/5) * (T_{sat} - 303.15) + 9.52)$
- 8.If $313.15 > T_{sat} > 308.15$ then $Mu_v = 1E-6 * ((0.17/5) * (T_{sat} - 308.15) + 9.7)$
9. Else $Mu_v = 3E-08 * (T_{sat} - 273.01) + 8E-06$
10. End subroutine MU_v

Subroutine PRL

This subroutine is for interpolating to calculate Prantl Number of water depending on the value of the saturation temperature, MU_v

- 1.If $280 > T_{sat} > 273.16$, then $Pr_L = -0.4162 * T_{sat} + 126.68$
- 2.If $295 > T_{sat} > 280$, then $Pr_L = -0.27 * T_{sat} + 85.827$
- 3.If $340 > T_{sat} > 295$, then $Pr_L = 9E+16 * T_{sat}^{**}(-6.5275)$
- 4.End subroutine PrL.

Subroutine PR_SA

This subroutine is for interpolating to calculate Prantl Number of air on the evaporator tubes surface depending on the value of the tube's wall temperature, PRSA

- 1.If $T_{sat} < 275$, then $PRSA = (0.007/25) * (275 - T_w) + 0.713$
- 2.300 $T_w < 275$, then $PRSA = (0.006/25) * (300 - T_w) + 0.707$
- 3.320 $T_w < 300$, then $PRSA = (0.006/25) * (325 - T_w) + 0.701$
- 4.Else $PRSA = (0.004/25) * (350 - T_w) + 0.697$
- 5.End subroutine PR_SA

Subroutine PSAT

This subroutine is for interpolating to calculate saturation pressure of water depending on the value of the saturation temperature, T_sat

- 1.If $400 > T_{sat} > 273.16$, then $P_{sat} = 5E-37 * T_{sat}^{**}16.062$
- 2.End subroutine PSAT

Subroutine ROHL

This subroutine is for interpolating to calculate density of water depending on the value of the saturation temperature, T_sat

- 1.If $278 > T_{sat} > 273.01$, then $ROH_L = ((1E-7/4.99) * (278 - T_{sat}) + 0.10001E-2)^{**}(-1)$
- 2.If $283.15 > T_{sat} > 278$, then $ROH_L = ((2E-7/5) * (T_{sat} - 278) + 0.10001E-2)^{**}(-1)$
- 3.If $298.15 > T_{sat} > 283.15$ then $ROH_L = (2E-07 * (T_{sat} - 273.15) + 0.001)^{**}(-1)$
- 4.If $> T_{sat} > 298.15$ then $ROH_L = (3E-07 * (T_{sat} - 273.15) + 0.001)^{**}(-1)$
- 5.If $373.15 > T_{sat} > 323.15$ then $ROH_L = (6E-07 * (T_{sat} - 273.15) + 0.001)^{**}(-1)$

6.End subroutine ROHL

Subroutine ROHV

This subroutine is for interpolating to calculate density of vapour depending on the value of the saturation temperature, T_{sat} .

- 1.If $274.15 > T_{sat} > 270.15$, then $ROH_v = ((13.4/0.99) * (274 - T_{sat}) + 192) ** (-1)$
 - 2.If $305.15 > T_{sat} > 274.15$, then $ROH_v = (197.81 * EXP(-0.0608 * (T_{sat} - 273.15))) ** (-1)$
 - 3.If $323.15 > T_{sat} > 305.15$, then $ROH_v = (-1.0108 * (T_{sat} - 273.15) + 60.748) ** (-1)$
 - 4.If $375.45 > T_{sat} > 323.15$, then $ROH_v = (924754 * (T_{sat} - 273.15) ** (-2.8608)) ** (-1)$
- 5.End subroutine ROHV.**

Subroutine SIG_MA

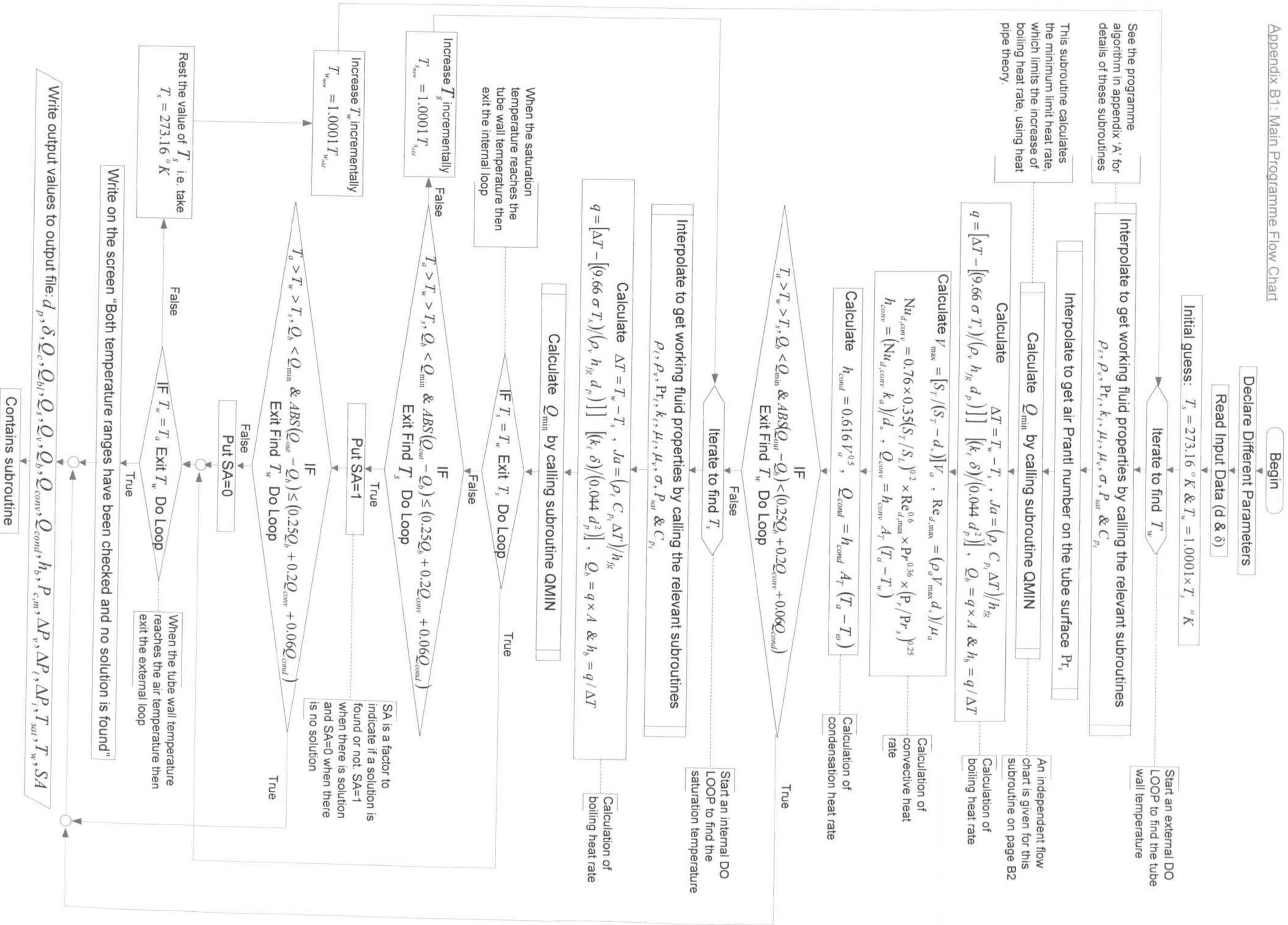
This subroutine is for interpolating to calculate surface tension of water depending on the value of the saturation temperature, T_{sat} .

- 1.If $400 > T_{sat} > 270.15$, then $SIGMA = -0.0002 * T_{sat} + 0.1237$
 - 2.Else $SIGMA = -0.0002 * T_{sat} + 0.1431$
- 3. End subroutine SIG_MA**

Subroutine CP_L

This subroutine is for interpolating to calculate specific heat of water depending on the value of the saturation temperature, T_{sat} .

- 1.If $285 > T_{sat} > 270.15$, then $CPL = 1E+3 * (-0.0027 * T_{sat} + 4.9643)$
 - 2.If $295 > T_{sat} > 285$, then $CPL = 1E+3 * (-0.001 * T_{sat} + 4.474)$
 - 3.If $310 > T_{sat} > 295$, then $CPL = 1E+3 * (2E-05 * T_{sat} ** 2 - 0.0123x + 6.069)$
 - 4.If $400 > T_{sat} > 310$, then $CPL = 1E+3 * (9E-06 * T_{sat} ** 2 - 0.0052 * T_{sat} + 4.9726)$
- 5.End subroutine CP_L.**



Calculate

Start Subroutine QMIN

$$d_v = d_i - 2 \times \delta, R_{eff} = 0.41 \times d_p / 2, L_e = n L_i, A_v = (\pi/4) d_v^2, A_i = (\pi/4) d_i^2, A_1 = (\pi/4) d_1^2, A_2 = (\pi/4) d_2^2, V_v = 1/(\rho_v A_v h_{fg}), V_i = V_v (A_v/A_i) \& V_{v_1} = V_v (A_1/A_i)$$

Vapour pressure drop in the wick and adiabatic section assuming laminar incompressible vapour flow. The pressure drop calculated here is in Pascal per Watt (Pa/W)

Vapour pressure drop at elbows (5 off) in Pa/W^2

$$\text{Calculate } h_{f_1} = K_f (V_v^2 / 2g) \& \Delta P_{v_1} = 5 h_{f_1} \rho_v g$$

Normal hydrostatic vapour pressure drop (in Pascal)

$$\text{Calculate } h_{f_{1-1}} = (V_v^2 / 2g) (1 - (A_i/A_1))^2 \& \Delta P_{v_{1-1}} = h_{f_{1-1}} \rho_v g$$

Vapour pressure drop at expansion 1 (in Pa/W^2)

Vapour pressure drop at expansion 2 & 3 in Pa/W^2

$$\text{Calculate } h_{f_{2-2}} = (V_v^2 / 2g) (1 - (A_i/A_1))^2, \Delta P_{v_{2-2}} = h_{f_{2-2}} \rho_v g, h_{f_{3-3}} = (V_v^2 / 2g) (1 - (A_i/A_2))^2 \& \Delta P_{v_{3-3}} = h_{f_{3-3}} \rho_v g$$

Total Vapour pressure drop in Pa/W^2 i.e. coefficient of Q_c^2

Liquid pressure drop due to viscous friction in the wick section (Pa/W)

$$\text{Calculate } K = \varepsilon D_p^2 / 32, A_w = n L_i \delta \& \Delta P_\ell = \mu_\ell (\pi d_i / 2) / K A_w h_{fg} \rho_\ell$$

Normal hydrostatic liquid pressure drop (in Pascal)

Capillary pressure in Pascal

$$\text{Calculate } \Delta P_+ = \rho_\ell g d_v$$

a, b & c are the coefficients of a quadratic equation in Q_c

$$\text{Calculate } a = \Delta P_v, b = \Delta P_{v_1} + \Delta P_\ell \& c = \Delta P_{v_2} + \Delta P_+ - P_{c,m}$$

$$\text{Calculate } Q_1 = -b + [b^2 - 4ac]^{0.5} / 2c \& Q_2 = [-b - [b^2 - 4ac]^{0.5}] / 2c$$

The maximum capillary pressure generated by the porous layer should be greater than or equal to the summation of all pressure losses occurring throughout the liquid and vapour flow paths. See equation (3.55)

Q_1 & Q_2 are the roots of the quadratic equation and they are in Watt

Nested if-statements for choosing one of the roots as a solution for the quadratic equation

$$Q_c = Q_1$$

$$\text{IF } Q_1 > Q_2 \text{ True}$$

$$\text{IF } Q_1 > 0.001 \text{ True}$$

$$Q_c = Q_2$$

$$\text{IF } Q_2 > 0.001 \text{ True}$$

$$Q_c = Q_2$$

Write on the screen 'There is no mathematical solution'

$$\text{Calculate } Re = (2 r_v Q_c) / A_v \mu_v h_{fg} \& Ma = (4 Q_c / h_{fg} \pi d_i^2) / \sqrt{\gamma R T_v}$$

Actual liquid pressure drop for laminar vapour flow (in Pascal)

Check the validity of the initial assumption of laminar incompressible vapour flow

$$\text{IF } Re < 2300 \text{ and } Ma < 0.3 \text{ True}$$

$$\text{Calculate } \Delta P_\ell = \Delta P_\ell Q_c + \Delta P_+$$

Vapour pressure drop for turbulent vapour flow (Pa/W)

$$\text{Calculate } \Delta P_{v_1} = 0.038 (Q_c / u_h h_{fg})^{3/4} (2 \mu_v Q_c / \rho_v h_{fg}) [(d_v / A_v)^{3/4} (L_e / d_v^2 A_v) + (d_i / A_i)^{3/4} (L_a / d_i^2 A_i)]$$

$$\text{Calculate } \Delta P_\ell = (n \rho_v / 2g) [V_v^2 ((28/9) - (0.68 Re / ((29 L_e / d_v) + Re))) + V_i^2 ((28/9) - 0.68 Exp(-60 L_a / Re d_i))]]$$

$$\text{Calculate } \Delta P_v = \Delta P_{v_1} + \Delta P_{v_{1-1}} + \Delta P_{v_{2-2}} + \Delta P_{v_{3-3}} + \Delta P_\ell$$

$$\text{Calculate } \Delta P_v = (\Delta P_{v_1} + \Delta P_{v_{1-1}} + \Delta P_{v_{2-2}} + \Delta P_{v_{3-3}}) Q_c^2 + \Delta P_\ell Q_c + \Delta P_{v_2}$$

Actual vapour pressure drop for laminar vapour flow (in Pascal)

Total Vapour pressure drop after adding the component of inertial pressure gradient (Pa/W^2)

$$\text{Calculate } F(x) = \Delta P_{v_1}^{0.75} Q_c + (\Delta P_v + \Delta P_\ell) Q_c^2 + \Delta P_\ell Q_c + \Delta P_+ - P_{c,m} \& F'(x) = 1.75 \Delta P_{v_1}^{0.75} Q_c + (2 \Delta P_v + \Delta P_\ell) Q_c + \Delta P_\ell$$

Iterate using Newton-Raphson Method to get Q_c

$$Q_{new} = Q_c - (F(x) / F'(x)) \& Q_c = Q_{new}$$

$$\text{IF } ABS(F(x)) < 0.5 \text{ True}$$

$$\text{Calculate } \Delta P_v = (\Delta P_{v_1} + \Delta P_{v_{1-1}} + \Delta P_{v_{2-2}} + \Delta P_{v_{3-3}} + \Delta P_\ell) Q_c^2 + \Delta P_\ell Q_c^{1.75} + \Delta P_{v_2}, \Delta P_\ell = \Delta P_\ell Q_c^2 \& \Delta P_\ell = \Delta P_\ell Q_c + \Delta P_+$$

Actual values of vapour, inertial and liquid pressure drops for turbulent vapour flow (Pa)

$$\text{Calculate } Q_s = 0.47 h_{fg} A_v (\rho_v P_v)^{1/2}, Q_v = (A_v r_v^2 h_{fg} \rho_v P_v / 16 \mu L_e) \& \dot{m} = (\Delta P_\ell K / \mu_\ell) (\rho_v \varepsilon A_w)$$

Calculate sonic and viscous limit heat rates and water flow rate in the wick section

$$\text{Calculate } k_w = k_s [2k_s + k_\ell - 2\varepsilon(k_s - k_\ell)] / [2k_s + k_\ell + \varepsilon(k_s - k_\ell)] \& Q_{hl} = (2\pi L_e k_w T_v) / (h_{fg} \ln(r_i / r_v)) ((2\sigma / r_n) - P_{c,m})$$

Calculate effective wick thermal conductivity and boiling limit

Nested if-statements for choosing the smallest limit heat rate as the minimum limit

False

$$Q_v < Q_c, Q_v < Q_s \& Q_v < Q_{hl}$$

$$Q_s < Q_c, Q_s < Q_v \& Q_s < Q_{hl}$$

$$Q_c < Q_s, Q_c < Q_v \& Q_c < Q_{hl}$$

$$Q_c < Q_s, Q_c < Q_v \& Q_c < Q_{hl}$$

$$Q_c = Q_{min}$$

$$Q_{hl} = Q_{min}$$

$$Q_v = Q_{min}$$

$$Q_s = Q_{min}$$

$$Q_c = Q_{min}$$

End subroutine

Program Boiling_Heat_Transfer

!This programme is for calculating the boiling heat rate
!and the boiling heat transfer coefficient of a two-row
!staggered tube-bank evaporator. The tubes' inner surface
! are lined with a layer of sintered powder to improve
!evaporator's boiling performance.

Implicit none

Integer ::openstatus,inputstatus,SA

Real ::D_p,Delta,Q_c,Delta_P_v1,Delta_P_v2,Delta_P_v3,P_c_max,R_eff,R_v,d_v,&
 &h_f4_1,h_f4_2,h_f3,a,b,c,Q1,Q2,Re_v,Fx,Fx_dash,V_v,V_v1,Q_b,k_eff,&
 & Delta_P_L1,Delta_P_L2,K,A_W,Delta_P_L,M_Dot_w,Delta_P_v,Delta_P_i,&
 &A_i,Mu_v,ROH_v,H_fg,SIGMA,P_sat,k_L,ROH_L,Mu_L,M_Dot_v,REAIR_max &
 &,NUAIR_max,Q_min,T_sat,A_o,Pr_L ,h_cond, Q_boil,q_boiling,Q_out &
 &,Q_cond,Q_conv,h_conv,PRSA,DELTA_T, T_w,Q_s,Q_v, A1,A2,Delta_P_v4_2&
 &,Delta_P_v4_1,Q_new,Ma, Delta_P_v_lam,Delta_P_L_lam,A_v,L_e, BHTC,&
 &r_i,d,e,f,i,j,m , h_f4_3, V_vi,VAIR_max

Real, parameter:: k_br=52,d_i=25.3E-3,L_a=2.235,H=0.57,D1=0.076&
 &,D2=0.3,R_n=2.54E-7,ETA=0.48,n=9,L_t=0.3,D_o=0.0286,&
 & Gamma=1.33,R=461.5,g=9.81,k_f=0.9,Pi=3.141593&
 &,SL=8.4E-2,ST=56.4E-3,AT=96.1E-3,V_air= 1

! Declare air properties @303 degree Kelvin (30 degree celcius)

Real, parameter::T_air=303.15,CPA=1005.068,NUA=1.59668E-5,&
 &PRA=0.70628,kA=2.64704E-2

! Open input and output files

Open (unit=10,File='particle diameter Data',Form='Formatted',&
 &Iostat=openstatus)

Open (unit=20,File='Heat Transfer Limits.Output',Form='Formatted',&
 &Iostat=openstatus)

!Print headings for the output values

Write (20, FMT=40)'D_p', ' ','Delta', ' ','Q_c', ' ','Q_b', ' ','&

&'Q_s', ' ','Q_v', ' ','M_Dot_w', ' ','P_c', ' ','&

&'Delta_P_v', ' ','Delta_P_L', ' ','Delta_P_i', ' ','&

&'Q_out', ' ','T_sat', ' ','Q_boil', ' ','Q_conv', ' ','&

&'Q_cond', ' ','T_w', ' ','M_Dot_v', ' ','Ma', ' ','BHTC', ' ','SA'

40 FORMAT (2x,A3,5x,A1,2x,A5,1x,A1,5x,A3,4x,A1,4x,A3,5x,A1,5x,A3,&

&4x,A1,5x,A3,4x,A1,3x,A7,2x,A1,3x,A3,8x,A1,3x,A9,8x,A1,3x,A9,&

&2x,A1,2x,A9,2x,A1,2x,A6,2x,A1,2x,A5,2x,A1,2x,A6,2x,A1,2x,A6,&

&2x,A1,2x,A6,2x,A1,2x,A3,2x,A1,2x,A7,2x,A1,2x,A2,7x,A1,2x,A4,2x,A1,2x,A2)

!Read input data

Read_input_Data:Do

Read (unit=10 , FMT=30 , IOSTAT=inputstatus) D_p,Delta

30 FORMAT (F8.6,2x,F6.4)

IF (inputstatus>0) Stop '***input_error***'

IF (inputstatus<0)Exit

!Take an initial guess for T_sat & T_w

T_sat=273.16

T_w=1.0033*T_sat

!Start the outer loop to get T_sat

T_w_ITERATION:DO

!Interpolate to find RHOL

Call ROHL (ROH_L,T_Sat)

!Interpolate to find ROH_v

Call ROHV(ROH_v,T_Sat)

!Interpolate to find HFG

Call HFG(H_fg,T_Sat)

!Interpolate to find ROH_v

Call ROHV(ROH_v,T_Sat)

!Interpolate to find Pr_L

Call PrL(Pr_L,T_Sat)

!Interpolate to find kL

Appendix C: Fortran 95 Programme

Call KL (T_Sat)

!Interpolate to find Mu_v

Call Muv(T_Sat)

!Interpolate to find Mu_L

Call MuL(T_Sat)

!Interpolate to find SIGMA

Call SIG_MA(SIGMA,T_Sat)

!Interpolate to find P_sat

Call PSAT(P_Sat,T_Sat)

!Interpolate to find PRSA

Call PR_SA(PRSA,T_Sat)

!Interpolate to find Q_min

Call QMIN(Q_min,T_Sat)

! Now calculate the boiling heat rate and heat transfer coefficient

DELTA_T=T_w -T_sat

q_boiling=(k_L*DELTA/(0.044*D_p**2))*(DELTA_T-&
&9.66*SIGMA*(T_sat-273.15)/(ROH_v*H_fg*D_p))

Q_boil=q_boiling*Pi*d_i*L_t*N

BHTC= q_boiling/DELTA_T

!Now calculate the convective heat rate using Zhukauskas
!formula

VAIR_max=(ST*V_air)/(ST-d_o)

REAIR_max=(VAIR_max*D_o)/NUA

NUAIR_max=0.76*0.35*((ST/SL)**0.2)*(REAIR_max**0.6)&
&*(PRA**0.36)*(PRA/PRSA)**0.25

h_conv=(NUAIR_max*kA)/D_o

A_o=Pi*D_o*L_t*n

Q_conv=h_conv*A_o*(T_air - T_w)

!Now calculate the condensation heat rate

h_cond=(0.616*(V_air*3.28083*60)**0.5)/0.17612

Q_cond= h_cond*A_o*(T_air - T_w)

!Now calculate the total heat rate on the outside
! of the evaporator tubes

Q_out = Q_cond + Q_conv

!Check if the exit conditions are satisfied

```
IF ( (T_w > T_sat) .and.(T_w < T_air).and. &  
&ABS(Q_out-Q_boil)<=(0.06*Q_cond+0.2*Q_conv)&  
&.and. Q_boil<=Q_min) EXIT
```

!Start the inner loop to get T_sat

T_sat_ITERATION:DO

```
!Interpolate to find kL  
call KL (T_Sat)  
!Interpolate to find Pr_L  
call PrL (Pr_L,T_Sat)  
!Interpolate to find kL  
call KL (T_Sat)  
!Interpolate to find RHOL  
call ROHL(ROH_L,T_Sat)  
!Interpolate to find ROH_v  
call ROHV(ROH_v,T_Sat)  
!Interpolate to find HFG  
call HFG(H_fg,T_Sat)  
!Interpolate to find SIGMA  
call SIG_MA(SIGMA,T_Sat)
```

!Now re-calculate the boiling heat rate and heat transfer coefficient

DELTA_T=T_w -T_sat

```
q_boiling=(k_L*DELTA/(0.044*D_p**2))*(DELTA_T-&  
&9.66*SIGMA*(T_sat-273.15)/(ROH_v*H_fg*D_p))
```

Q_boil=q_boiling*Pi*d_i*L_t*N

BHTC= q_boiling/DELTA_T

!Now re-calculate new heat transfer limits based on
! new T_sat

!Interpolate to find P_sat

call PSAT(P_Sat,T_Sat)

!Interpolate to find Mu_v

call Muv(T_Sat)

!Interpolate to find Mu_L

call MuL(T_Sat)

!Interpolate to find SIGMA

call SIG_MA(SIGMA,T_Sat)

!Get the new value of Q_min

call QMIN(Q_min,T_Sat)

M_Dot_v= Q_boil/H_fg

SA=1 !SA=solution availability

!Check if exit conditions are satisfied

IF ((T_w > T_sat) .and.(T_w < T_air) .and. &

&ABS(Q_out-Q_boil)<=(0.06*Q_cond+0.2*Q_conv) .and. Q_boil<=Q_min) EXIT

IF (ABS(T_w - T_sat)<=0.1) EXIT

IF (ABS(T_air - T_sat)<=0.001) EXIT

!Increase the value to T_sat

T_sat=1.0001*T_sat

END DO T_sat_ITERATION

!Check if exit conditions are satisfied

IF ((T_w > T_sat) .and.(T_w < T_air) .and. &

&ABS(Q_out-Q_boil)<=(0.06*Q_cond+0.2*Q_conv)&

& .and. Q_boil<=Q_min) EXIT

!write a message on the screen if no solution if found

IF (T_w >= T_air)THEN

write (*,*) 'both ranges were checked, and no solution is found'

SA=0 !SA=0 indicates no solution has been found

End IF

IF (T_w >= T_air) EXIT

!Change the guess of T_w

T_w = 1.0001*T_w

!Reset the value of T_sat

T_sat=273.16

END DO T_w_ITERATION

!Print the output values on the output file

Write (20, FMT=70)D_p, ',',Delta, ',',Q_c, ',',Q_b, ','&

&,Q_s,',',Q_v, ',',M_Dot_w,',',P_c_max,',',Delta_P_v,&

&',',Delta_P_L,',',Delta_P_i,',',Q_out,',',T_sat,',',&

&Q_boil,',',Q_conv,',',Q_cond,',',T_w,',',M_Dot_v,',',Ma,',',BHTC,',',SA

70 FORMAT (F8.6,2x,A1,F6.4,2x,A1,F10.2,2x,A1,F10.2,2x,A1,&

&F10.2,2x,A1,F10.2,2x,A1,F10.8,2x,A1,F10.2,4x,A1,F12.1,8x,&

&A1,F8.1,6x,A1,F6.1,2x,A1,F10.2,2x,A1,F10.2,2x,A1,F7.2,&

&2x,A1,F7.2,2x,A1,F7.2,2x,A1,F6.2,2x,A1,F11.9,2x,A1,1E9.2,2x,A1,1E9.2,2x,A1,11)

END DO Read_input_Data

!This programme contains the following subroutines

Contains

subroutine HFG(H_fg,T_Sat) !Interpolate to find HFG

IF (T_sat>273.15 .and. T_sat<400)THEN

H_fg=1E3*(3177.7-(2.4659*T_sat))

ELSE

H_fg=1E3*(3741.5-(3.8422*T_sat))

END IF

End subroutine HFG

subroutine KL (T_Sat) !Interpolate to find kL

IF (T_sat>273.01 .and. T_sat<278.15)THEN

k_L=(9E-3/4.99)*(T_sat-273.16)+569E-3

ELSE IF (T_sat>278.15 .and. T_sat<313.15) THEN

k_L=0.0016*(T_sat-273.15) + 0.5711

ELSE IF (T_sat>313.15 .and. T_sat<353.15) THEN

$$k_L = 0.001 * (T_{\text{sat}} - 273.15) + 0.5941$$

ELSE IF (T_sat>353.15 .and. T_sat<398.15) THEN

$$k_L = 0.0425 * \text{LOG}(T_{\text{sat}} - 273.15) + 0.4846$$

ELSE IF (T_sat>398.15 .and. T_sat<423.15) THEN

$$k_L = -1\text{E-}05 * (T_{\text{sat}} - 273.15)^2 + 0.4799$$

ELSE

$$k_L = -0.001 * (T_{\text{sat}} - 273.15) + 0.8509$$

END IF

End subroutine KL

subroutine MuL(T_Sat) !Interpolate to find Mu_L

IF (T_sat>270.16 .and. T_sat<278.15) THEN

$$\text{Mu}_L = (71\text{E-}6 / 4.99) * (278.16 - T_{\text{sat}}) + 1501\text{E-}6$$

ELSE IF (T_sat>278.15 .and. T_sat<308.15) THEN

$$\text{Mu}_L = (-1) * 3\text{E-}05 * (T_{\text{sat}} - 273.15) + 0.0016$$

ELSE IF (T_sat>308.15 .and. T_sat<333.15) THEN

$$\text{Mu}_L = (-1) * 1\text{E-}05 * (T_{\text{sat}} - 273.15) + 0.0011$$

ELSE IF (T_sat>333.15 .and. T_sat<368.15) THEN

$$\text{Mu}_L = (-1) * 5\text{E-}06 * (T_{\text{sat}} - 273.15) + 0.0008$$

ELSE IF (T_sat>368.15 .and. T_sat<423.15) THEN

$$\text{Mu}_L = (-1) * 2\text{E-}06 * (T_{\text{sat}} - 273.15) + 0.0005$$

ELSE IF (T_sat>423.15 .and. T_sat<523.15) THEN

$$\text{Mu}_L = (-1) * 8\text{E-}07 * (T_{\text{sat}} - 273.15) + 0.0003$$

ELSE

$$\text{Mu}_L = (-1) * 3\text{E-}07 * (T_{\text{sat}} - 273.15) + 0.0002$$

END IF

End subroutine MuL

subroutine Muv(T_Sat) !Interpolate to find Mu_v

IF (T_sat>270.01 .and. T_sat<278)**THEN**

$$\text{Mu_v} = (0.17\text{E-}6/4.99) * (\text{T_sat} - 273.01) + 8.49\text{E-}6$$

ELSE IF (T_sat>278 .and. T_sat<308.15)**THEN**

$$\text{Mu_v} = 3\text{E-}08 * (\text{T_sat} - 273.01) + 8\text{E-}06$$

ELSE IF (T_sat>308.15 .and. T_sat<373.15)**THEN**

$$\text{Mu_v} = 3\text{E-}08 * (\text{T_sat} - 273.01) + 8\text{E-}06$$

ELSE

$$\text{Mu_v} = 4\text{E-}08 * (\text{T_sat} - 273.01) + 8\text{E-}06$$

END IF

End subroutine Muv

subroutine PrL(Pr_L,T_Sat) !Interpolate to find Pr_L

IF (T_sat>273.01 .and. T_sat<280)**THEN**

$$\text{Pr_L} = -0.4162 * \text{T_sat} + 126.68$$

ELSE IF (T_sat>280 .and. T_sat<295) **THEN**

$$\text{Pr_L} = -0.27 * \text{T_sat} + 85.827$$

ELSE IF (T_sat>295 .and. T_sat<340) **THEN**

$$\text{Pr_L} = 9\text{E+}16 * \text{T_sat}^{**}(-6.5275)$$

ELSE IF (T_sat>295 .and. T_sat<340) **THEN**

$$\text{Pr_L} = 2\text{E+}11 * \text{T_sat}^{**}(-4.2924)$$

ELSE

$$\text{Pr_L} = (0.0001 * \text{T_sat}^{**}2) - 0.1014 * \text{T_sat} + 25.856$$

END IF

End subroutine PrL

subroutine PR_SA(PRSA,T_w)

IF (T_w>250 .and. T_w<450)**THEN**

$$PRSA = (-0.0002) * T_w + 0.7713$$

ELSE IF (T_w>450 .and. T_w<750)**THEN**

$$PRSA = (3E-07 * T_w^{**2}) - 0.0003 * T_w + 0.7675$$

ELSE

$$PRSA = 0.0475 * \text{LOG}(T_w) + 0.3733$$

END IF

End subroutine PR_SA

subroutine PSAT(P_Sat,T_Sat) !Interpolate to find P_sat

IF (T_sat>273.15 .and. T_sat<400)**THEN**

$$P_sat = 5E-37 * T_sat^{**16.062}$$

ELSE

$$P_sat = 2E-19 * T_sat^{**9.253}$$

END IF

End subroutine PSAT

subroutine QMIN(Q_min,T_Sat)

$$R_v = (d_i/2) - \text{Delta}$$

$$d_v = 2 * R_v$$

$$r_i = d_i/2$$

$$L_e = n * L_t$$

$$R_{eff} = 0.41 * (D_p/2)$$

$$A_i = \text{Pi} * (d_i/2)^{**2}$$

$$A_v = \text{Pi} * R_v^{**2} \text{ ! } A_v \text{ is the vapour core area}$$

$$V_v = 1 / (\text{ROH}_v * H_{fg} * A_v)$$

$$V_{vi} = V_v * (A_v/A_i)$$

$$\text{Delta_P_vl} = (16 * \text{Mu}_v / (2^{**} \text{ROH}_v * H_{fg})) * ((L_e / ((R_v^{**2}) * A_v) + (L_a / (R_i^{**2}) * A_i))$$

$$\text{Delta_P_v2} = \text{ROH}_v * g * H$$

$h_{f3} = k_f (V_{vi}^2) / (2g)$!The friction head loss

$\Delta P_{v3} = 5 h_{f3} ROH_v g$

! ΔP_{v3} is the vapour pressure drop due to friction at

! the right-angle elbows (5 off)

! Calculate the vapour pressure drop after expansion 1 of the

! pipe diameter; from d_v to d_i

$h_{f4_1} = ((V_v^2) / (2g)) (1 - (A_v / A_i))^2$

$\Delta P_{v4_1} = h_{f4_1} ROH_v g$

! Calculate the vapour pressure drop at expansion 2 of the

! pipe diameter i.e. from d_i to $D1$

$A1 = (\pi / 4) D1^2$

$h_{f4_2} = ((V_{vi}^2) / (2g)) (1 - (A_i / A1))^2$

$\Delta P_{v4_2} = h_{f4_2} ROH_v g$

! Calculate the vapour pressure drop at expansion 3 of the

! pipe diameter i.e. at entry to the absorber

$A2 = (\pi / 4) D2^2$

$V_{v1} = V_{vi} (A_i / A1)$

$h_{f4_3} = ((V_{v1}^2) / (2g)) (1 - (A1 / A2))^2$

$\Delta P_{v4_3} = h_{f4_3} ROH_v g$

! Vapour pressure drop in terms of Q_c square is:

$\Delta P_v = \Delta P_{v3} + \Delta P_{v4_1} + \Delta P_{v4_2} + \Delta P_{v4_3}$

! Calculate the liquid pressure drop

$K = \eta A ((0.41 D_p)^2) / 32$

$A_w = n L_t \Delta$

$\Delta P_{L1} = (\mu_L \pi (d_i / 2)) / (K A_w H_{fg} ROH_L)$

$\Delta P_{L2} = ROH_L g d_v$

Appendix C: Fortran 95 Programme

! Calculate the maximum capillary pressure

$$P_c_max=(2*\text{SIGMA})/R_eff$$

! Now solve the quadratic equation to find the value of Q

$$a= \Delta P_v \quad \quad \quad \text{! a is } Q^2 \text{ Coefficient}$$

$$b= \Delta P_{v1} + \Delta P_{L1} \quad \quad \quad \text{! b is Q Coefficient}$$

$$c= \Delta P_{v2} + \Delta P_{L2} - P_c_max \quad \text{! c is constant}$$

$$Q1= (-b+((b^2)-4*a*c)^{0.5})/(2*a)$$

$$Q2= (-b-((b^2)-4*a*c)^{0.5})/(2*a)$$

IF (Q1 >= 0.00000001) THEN

$$Q_c= Q1$$

ELSE IF (Q2 > Q1) THEN

$$Q_c=Q2$$

END IF

! Calculate Re_v and Ma to find out whether the assumption of laminar

! incompressible flow is true. Accordingly, if the flow is turbulent, then

! calculate ΔP_{v1} using the equation below otherwise go to 200

$$Re_v= 2*R_v*Q_c/(A_v*\mu_v*H_{fg})$$

$$Ma=(4*Q_c/(H_{fg}*\pi*D_v^2))/(\gamma*R*T_{sat})^{0.5}$$

$$F_x= a*(Q_c^2)+(b*Q_c)+c$$

! Calculate the vapour and liquid pressure drops when

! the vapour flow is laminar and incompressible i.e.

! $Re < 2500$ and $Ma \ll 0.3$

IF (Re_v <= 2300 .and. Ma <= 0.05) THEN

$$\Delta P_{v_lam}= \Delta P_v *(Q_c^2)+(\Delta P_{v1}*Q_c)+(\Delta P_{v2})$$

$$\Delta P_{L_lam}= \Delta P_{L1}*Q_c + \Delta P_{L2}$$

GO to 440

ELSE IF (Ma>=0.3)THEN

WRITE (*,*)'MAch No is greater than 0.3'

END IF

! In case of turbulent vapour flow use the formula below

! to calculate the vapour viscous pressure drop

$$D=1/(\text{Mu}_v \cdot H_{fg})^{**0.75}$$

$$E=2 \cdot \text{Mu}_v / (\text{ROH}_v \cdot H_{fg})$$

$$F=(D_v/A_v)^{**0.75}$$

$$I=L_e/((D_v^{**2}) \cdot A_v)$$

$$J=(D_i/A_i)^{**0.75}$$

$$m=L_a/((D_i^{**2}) \cdot A_i)$$

$$\text{Delta_P_v1}=D \cdot E \cdot (F \cdot I + J \cdot m)$$

!Iterate using Newton-Raphson Method to find Q when the effect

!of turbulence is taken into account

FIND_Q_TUR:DO

$$F_x = ((\text{Delta_P_v1}) \cdot (Q_c^{**1.75})) + (\text{Delta_P_v}) \cdot (Q_c^{**2}) \&$$

$$\& + \text{Delta_P_L1} \cdot Q_c + (\text{Delta_P_v2} + \text{Delta_P_L2} - P_{c_max})$$

$$F_{x_dash} = (1.75 \cdot \text{Delta_P_v1} \cdot Q_c^{**0.75}) + (2 \cdot (\text{Delta_P_v} \&$$

$$\&) \cdot Q_c) + \text{Delta_P_L1}$$

IF (ABS (Fx) <= 0.1)EXIT

$$Q_{new} = Q_c - (F_x/F_{x_dash})$$

$$Q_c = Q_{new}$$

END DO FIND_Q_TUR

! Calculate the pressure drop due to inertia. Note that

!this pressure gradient is calculated for the evaporator

!length only i.e. adiabatic section not included

$$\text{Delta_P_i} = ((\text{ROH}_v \cdot V_v^{**2}) / (2 \cdot g)) \cdot ((28/9) - (0.68 \cdot \text{Re}_v / ((29 \cdot L_e / D_v) + \text{Re}_v^{**2} \cdot \text{EXP}(-60 \cdot L_a / (\text{Re}_v \cdot D_v))))))$$

FIND_Q_TUR_INERT:DO

$F_x = ((\Delta P_v) * (Q_c^{**1.75})) + (\Delta P_v + \Delta P_i) * (Q_c^{**2}) \&$
 $\& + \Delta P_{L1} * Q_c + (\Delta P_{v2} + \Delta P_{L2} - P_{c_max})$

$F_{x_dash} = (1.75 * \Delta P_v * Q_c^{**0.75}) + (2 * (\Delta P_v + \Delta P_i) \&$
 $\&) * Q_c + \Delta P_{L1}$

IF (ABS (Fx) <= 0.1)EXIT

$Q_{new} = Q_c - (F_x / F_{x_dash})$

$Q_c = Q_{new}$

END DO FIND_Q_TUR_INERT

! Calculate the viscous limit

440 $Q_v = ((D_v^{**2}) * H_{fg} * A_v * P_{sat} * ROH_v) / (64 * \mu_v * L_e)$

! Calculate the boiling limit

$k_{eff} = (1 - \eta) * K_{br} + \eta * k_L$

$Q_b = (2 * \pi * L_e * k_{eff} * T_{sat} / (ROH_v * H_{fg} * \log(D_i / R_v))) * \&$
 $\& ((2 * \sigma / R_n) - P_{c_max})$

! Calculate the sonic limit

$Q_s = 0.474 * H_{fg} * A_v * (ROH_v * P_{sat})^{**0.5}$

IF (Re_v <= 2300) THEN

$\Delta P_v = \Delta P_{v_Lam}$

$\Delta P_i = 0$

$\Delta P_L = \Delta P_{L_Lam}$

$M_{Dot_w} = (\Delta P_L * K / \mu_L) * ROH_L * A_w * \eta$!In terms of Darcy's velocity

ELSE

$\Delta P_i = \Delta P_i * (Q_c^{**2})$

$\Delta P_v = \Delta P_v * (Q_c^{**2}) + \Delta P_{v1} * Q_c^{**1.75} \&$
 $\& + \Delta P_{v2} + \Delta P_i$

$\Delta P_L = \Delta P_{L1} * Q_c + \Delta P_{L2}$

M_Dot_w=(Delta_P_L*K/Mu_L)*ROH_L*A_w*ETA

END IF

!Again find out the new smallest/minimum heat transfer limit

IF (Q_c<Q_s .and. Q_c<Q_v .and. Q_c<Q_b)THEN

Q_min=Q_c

ELSE IF(Q_s<Q_c .and. Q_s<Q_v .and. Q_s<Q_b)THEN

Q_min=Q_s

ELSE IF(Q_v<Q_c .and. Q_v<Q_s .and. Q_v<Q_b)THEN

Q_min=Q_v

ELSE

Q_min=Q_b

END IF

End subroutine QMIN

subroutine ROHL (ROH_L,T_Sat) !Exterapolate to find RHOL

IF (T_sat>273.01 .and. T_sat<278)THEN

ROH_L=((1E-7/4.99)*(278-T_sat)+0.10001E-2)**(-1)

ELSE IF (T_sat>278 .and. T_sat<283.15)THEN

ROH_L=((2E-7/5)*(T_sat-278)+0.10001E-2)**(-1)

ELSE IF (T_sat>283.15 .and. T_sat<298.15)THEN

ROH_L=(2E-07*(T_sat-273.15) + 0.001)**(-1)

ELSE IF (T_sat>298.15 .and. T_sat<323.15)THEN

ROH_L=(3E-07*(T_sat-273.15) + 0.001)**(-1)

ELSE IF (T_sat>323.15 .and. T_sat<373.15)THEN

ROH_L=(6E-07*(T_sat-273.15) + 0.001)**(-1)

ELSE IF (T_sat>373.15 .and. T_sat<423.15)THEN

ROH_L=(9E-07*(T_sat-273.15) + 0.001)**(-1)

ELSE

ROH_L=(2E-06*(T_sat-273.15) + 0.0008)**(-1)

END IF

End subroutine ROHL

subroutine ROHV(ROH_v,T_Sat) !Interpolate to find ROH_v

IF (T_sat>270.15 .and. T_sat<274.15)THEN

$$\text{ROH_v} = ((13.4/0.99) * (274 - T_{\text{sat}}) + 192) ** (-1)$$

ELSE IF (T_sat>274.15 .and. T_sat<305.15)THEN

$$\text{ROH_v} = (197.81 * \text{EXP}(-0.0608 * (T_{\text{sat}} - 273.15))) ** (-1)$$

ELSE IF (T_sat>305.16 .and. T_sat<323.15)THEN

$$\text{ROH_v} = (-1.0108 * (T_{\text{sat}} - 273.15) + 60.748) ** (-1)$$

ELSE IF (T_sat>323.15 .and. T_sat<375.45)THEN

$$\text{ROH_v} = (924754 * (T_{\text{sat}} - 273.15) ** (-2.8608)) ** (-1)$$

ELSE IF (T_sat>375.45 .and. T_sat<412.05)THEN

$$\text{ROH_v} = (2\text{E}+07 * (T_{\text{sat}} - 273.15) ** (-3.533)) ** (-1)$$

ELSE IF (T_sat>421.05 .and. T_sat<457.25)THEN

$$\text{ROH_v} = (9\text{E}+07 * (T_{\text{sat}} - 273.15) ** (-3.8328)) ** (-1)$$

ELSE IF (T_sat>457.25 .and. T_sat<485.95)THEN

$$\text{ROH_v} = (3\text{E}+08 * (T_{\text{sat}} - 273.15) ** (-4.0397)) ** (-1)$$

ELSE

$$\text{ROH_v} = (7\text{E}+08 * (T_{\text{sat}} - 273.15) ** (-4.2294)) ** (-1)$$

END IF

End subroutine ROHV

subroutine SIG_MA(SIGMA,T_Sat) !Interpolate to find SIGMA

IF (T_sat>270.15 .and. T_sat<400)THEN

$$\text{SIGMA} = -0.0002 * T_{\text{sat}} + 0.1237$$

ELSE

$$\text{SIGMA} = -0.0002 * T_{\text{sat}} + 0.1431$$

END IF

End subroutine SIG_MA

End Program Boiling_Heat_Transfer

Read input data

$$AAA = ||Q_b| - |Q_{out}||$$

Iterate to find T_w

Calculate J_a, q, h_b, Q_b & h_{cond} using equations (3.7), (3.4), (4.2), (4.3) and (3.31)

Calculate $h_{out} = h_{conv} + h_{cond}$

$$\mathbb{Q}_b^{\text{IF}} = \mathbb{Q}_{\text{ONI}}$$

Initialise T_1, T_2 & BBB

<

Iterate to find T_w

Interpolate to find air, water and vapour properties

Interpolation is done using if statements

$$\text{Calculate } \omega_m = \frac{0.622 \Phi_m P_{sat,m}}{P_{atm} - \Phi_m P_{sat,m}}$$
$$\omega_{out} = \frac{P_{out} - \omega_{out} P_{sat,out}}{P_{in} - \omega_{out} P_{sat,out}}, \quad H_{in} = C_{p_a} T_{a,in} + \omega_{in} H_{out} = C_{p_a} T_{a,out} + \omega_{out} H_{sat,out}, \quad m_{\omega} = \omega_{out} - \omega_{in} \quad \text{and}$$
$$\mathcal{Q}_{\text{hyg}} = m_{\omega} (H_{\text{out}} - H_{\text{in}}) + m_{\omega} H_{\omega}$$

True IF

Calculate

$$R_{in} = \frac{1}{h_{conv}} + \frac{0.5d_o}{k_{cu}} \ln\left(\frac{d_o}{d_i}\right) + \frac{0.5d_o}{k_w} \ln\left(\frac{d_i}{d_{ii}}\right) + \frac{d_o}{d_{ii}h_b} + \frac{1}{h_{cond}} \quad \& \quad h_{all} = \frac{1}{R_{th}}$$

Calculate $T_{out} = T_{in} - Q_b / m_a C_{p,a}$

Take $\tilde{Q}_{out} = \tilde{Q}_{conv}$ and $h_{out} = h_{conv}$

~~IF $T_{out} > T_w$. and. $T_w > T_s$ False~~

Write $d_p, T_{out}, T_w, q, Q_b, Q_{conv}, Q_{cond}, h_b, h_{conv}, h_{out}, h_{cond}$ & h_{all}

Write d_p

Appendix E: Tables of Experimental Results

Table (E.1): 50 μm Particle size and 1.0 mm Layer Thickness Evaporator

V_a (m/s)	T_a ($^{\circ}\text{C}$)	T_w ($^{\circ}\text{C}$)	T_s ($^{\circ}\text{C}$)	ΔT_s ($^{\circ}\text{C}$)	\dot{m}_v (kg / s)	Q_b (kW)	h_s (kW/m ² K)
1	25	4.58	2.55	2.03	0.000257	0.64	1.3
1	30	5.81	4.5	1.31	0.00018	0.45	1.41
1	35	8.15	4.09	4.06	0.000301	0.75	0.76
2	25	7.02	3.31	3.71	0.000246	0.61	0.68
2	30	5.93	3.99	1.94	0.000244	0.61	1.29
2	35	5.56	2.76	2.8	0.000255	0.64	0.94
3	25	6.84	4.32	2.52	0.000246	0.61	1.01
3	30	9.92	5.94	3.98	0.000335	0.83	0.86
3	35	7.61	3.81	3.8	0.000307	0.76	0.83

Table (E.2): 50 μm Particle size and 1.5 mm Layer Thickness Evaporator

V_a (m/s)	T_a ($^{\circ}\text{C}$)	T_w ($^{\circ}\text{C}$)	T_s ($^{\circ}\text{C}$)	ΔT_s ($^{\circ}\text{C}$)	\dot{m}_v (kg / s)	Q_b (kW)	h_s (kW/m ² K)
1	25	7.64	3.65	3.99	0.000228	0.57	0.57
1	30	4.94	2.72	2.22	0.00022	0.55	1.01
1	35	7.82	3.41	4.41	0.000271	0.68	0.63
2	25	7.08	2	5.08	0.000258	0.64	0.52
2	30	6.91	3.74	3.17	0.000245	0.61	0.79
2	35	8.09	4.05	4.04	0.000331	0.82	0.84
3	25	5.97	1.71	4.26	0.000194	0.48	0.47
3	30	8.22	3.49	4.73	0.000286	0.71	0.62
3	35	9.1	4.34	4.76	0.00032	0.8	0.69

Table (4.3): 50 μm Particle size and 2.0 mm Layer Thickness Evaporator

V_a (m/s)	T_a ($^{\circ}\text{C}$)	T_w ($^{\circ}\text{C}$)	T_s ($^{\circ}\text{C}$)	ΔT_s ($^{\circ}\text{C}$)	\dot{m}_v (kg / s)	Q_b (kW)	h_s (kW/m ² K)
1	25	7.15	4.37	2.78	0.000218	0.54	0.81
1	30	5.34	2.83	2.51	0.000242	0.6	0.99
1	35	6.84	2.13	4.71	0.000359	0.89	0.78
2	25	7.39	3.64	3.75	0.000268	0.67	0.73
2	30	7.25	2.68	4.57	0.000359	0.9	0.81
2	35	6.59	2.75	3.84	0.000346	0.86	0.93
3	25	7.53	2.75	4.78	0.000352	0.88	0.76
3	30	8.33	2.95	5.38	0.000226	0.56	0.43
3	35	8.14	3.94	4.2	0.000325	0.81	0.8

Table (E.4): 50 μm Particle size and 2.5 mm Layer Thickness Evaporator

V_a (m/s)	T_a ($^{\circ}\text{C}$)	T_w ($^{\circ}\text{C}$)	T_s ($^{\circ}\text{C}$)	ΔT_s ($^{\circ}\text{C}$)	\dot{m}_v (kg / s)	Q_b (kW)	h_s (kW/m ² K)
1	25	7.34	3.89	3.45	0.00019	0.47	0.57
1	30	6.72	2.88	3.84	0.000232	0.58	0.62
1	35	6.95	3.56	3.39	0.000234	0.58	0.71
2	25	8.03	3.04	4.99	0.000301	0.75	0.63
2	30	8.68	3.96	4.72	0.0003	0.75	0.65
2	35	8.18	3.47	4.71	0.000268	0.67	0.58
3	25	8.93	2.96	5.97	0.000247	0.62	0.43
3	30	8.81	3.36	5.45	0.000379	0.95	0.72
3	35	11.6	4.32	7.28	0.00032	0.8	0.45

Appendix E: Tables of Experimental Results

Table (E.5): 100 μm Particle size and 1.0 mm Layer Thickness Evaporator

V_a (m/s)	T_a ($^{\circ}\text{C}$)	T_w ($^{\circ}\text{C}$)	T_s ($^{\circ}\text{C}$)	ΔT_s ($^{\circ}\text{C}$)	\dot{m}_v (kg / s)	Q_b (kW)	h_s (kW/m ² K)
1	25	4.06	1.96	2.1	0.00045	1.13	2.05
1	30	3.9	1.83	2.07	0.00042	1.05	2.37
1	35	5.01	2.45	2.56	0.00035	0.88	1.42
2	25	4.89	2.82	2.07	0.000329	0.82	1.63
2	30	5.22	3.16	2.06	0.000316	1.05	1.44
2	35	4.34	2.71	1.63	0.000304	0.76	1.92
3	25	5.08	2.9	2.18	0.000278	0.69	1.31
3	30	5.75	3.55	2.2	0.00096	0.74	1.38
3	35	5.34	2.78	2.56	0.000347	0.87	1.39

Table (E.6): 100 μm Particle size and 1.5 mm Layer Thickness Evaporator

V_a (m/s)	T_a ($^{\circ}\text{C}$)	T_w ($^{\circ}\text{C}$)	T_s ($^{\circ}\text{C}$)	ΔT_s ($^{\circ}\text{C}$)	\dot{m}_v (kg / s)	Q_b (kW)	h_s (kW/m ² K)
1	25	6.1	3	3.1	0.000339	0.85	1.13
1	30	5.7	2.37	3.33	0.000386	0.97	1.21
1	35	5.55	2.19	3.36	0.00045	0.84	1.11
2	25	6.49	2.95	3.54	0.000263	0.66	0.77
2	30	6.15	2.8	3.35	0.000348	0.87	1.32
2	35	6.32	2.71	3.61	0.000346	0.86	1.08
3	25	6.98	2.57	4.41	0.000348	0.87	0.81
3	30	7.61	3.95	3.66	0.000435	1.08	0.77
3	35	7.47	3.76	3.71	0.000328	0.82	0.91

Table (E.7): 100 μm Particle size and 2.0 mm Layer Thickness Evaporator

V_a (m/s)	T_a ($^{\circ}\text{C}$)	T_w ($^{\circ}\text{C}$)	T_s ($^{\circ}\text{C}$)	ΔT_s ($^{\circ}\text{C}$)	\dot{m}_v (kg / s)	Q_b (kW)	h_s (kW/m ² K)
1	25	4.14	2.59	1.55	2.54E-04	0.63	1.69
1	30	5.28	2.96	2.32	3.16E-04	0.79	1.4
1	35	4.5	1.71	2.79	3.64E-04	0.91	1.34
2	25	4.67	2.42	2.25	3.10E-04	0.77	1.41
2	30	6.15	2.8	3.35	0.000348	0.87	1.32
2	35	6.32	2.71	3.61	0.000346	0.86	1.08
3	25	5.62	2.7	2.92	0.000327	0.82	1.15
3	30	6.382	2.462	3.92	0.000285	0.71	0.75
3	35	7.47	3.76	3.71	0.000328	0.82	0.91

Table (E.8): 100 μm Particle size and 2.5 mm Layer Thickness Evaporator

V_a (m/s)	T_a ($^{\circ}\text{C}$)	T_w ($^{\circ}\text{C}$)	T_s ($^{\circ}\text{C}$)	ΔT_s ($^{\circ}\text{C}$)	\dot{m}_v (kg / s)	Q_b (kW)	h_s (kW/m ² K)
1	25	3.58	2.35	1.23	0.000383	0.95	3.22
1	30	3.6	2.18	1.42	0.000144	0.36	1.03
1	35	5.66	2.28	3.38	0.000414	1.03	1.42
2	25	3.48	2.2	1.28	0.000419	1.04	3.38
2	30	4.74	2.73	2.01	0.000385	0.96	1.97
2	35	5.41	2.72	2.69	0.00048	1.2	1.83
3	25	4.2	2.52	1.68	0.000483	1.21	2.96
3	30	5.09	2.73	2.36	0.000444	1.11	1.94
3	35	6.36	3.34	3.02	0.000468	1.17	1.59

Appendix E: Tables of Experimental Results

Table (E.9): 200 μm Particle size and 1.0 mm Layer Thickness Evaporator

V_a (m/s)	T_a ($^{\circ}\text{C}$)	T_w ($^{\circ}\text{C}$)	T_s ($^{\circ}\text{C}$)	ΔT_s ($^{\circ}\text{C}$)	\dot{m}_v (kg / s)	Q_b (kW)	h_b (kW/m ² K)
1	25	3.33	1.86	1.47	0.00061	1.52	4.27
1	30	2.85	1.6	1.25	0.00048	1.2	3.94
1	35	3.33	2.03	1.3	0.000405	1.01	3.23
2	25	3.88	2.68	1.2	0.000484	1.21	4.15
2	30	3.86	2.27	1.59	0.000476	1.19	3.08
2	35	4.79	3.5	1.29	0.000385	0.96	3.06
3	25	5.19	3.63	1.56	0.000447	1.11	2.95
3	30	4.9	3	1.9	0.000486	1.21	2.64
3	35	5.68	3.91	1.77	0.000469	1.17	2.73

Table (E.10): 200 μm Particle size and 1.5 mm Layer Thickness Evaporator

V_a (m/s)	T_a ($^{\circ}\text{C}$)	T_w ($^{\circ}\text{C}$)	T_s ($^{\circ}\text{C}$)	ΔT_s ($^{\circ}\text{C}$)	\dot{m}_v (kg / s)	Q_b (kW)	h_b (kW/m ² K)
1	25	3.63	2.37	1.26	0.00041	1.02	3.36
1	30	4.31	2.74	1.57	0.000552	1.38	2.93
1	35	3.26	1.13	2.13	0.000557	1.39	2.7
2	25	6.65	3.89	2.76	0.000737	1.84	2.75
2	30	4.27	1.96	2.31	0.000529	1.32	2.36
2	35	4.23	2.03	2.2	0.000466	1.16	2.18
3	25	5.13	2.79	2.34	0.000619	1.54	2.72
3	30	5.67	3.51	2.16	0.000444	1.11	2.29
3	35	5.54	2.96	2.58	0.000482	1.2	1.92

Table (E.11): 200 μm Particle size and 2.0 mm Layer Thickness Evaporator

V_a (m/s)	T_a ($^{\circ}\text{C}$)	T_w ($^{\circ}\text{C}$)	T_s ($^{\circ}\text{C}$)	ΔT_s ($^{\circ}\text{C}$)	\dot{m}_v (kg / s)	Q_b (kW)	h_b (kW/m ² K)
1	25	2.57	2	0.57	0.000483	1.21	4.75
1	30	2.13	1.36	0.77	0.000518	1.29	6.89
1	35	2.7	1.72	0.98	0.00051	1.27	5.37
2	25	3.73	2.63	1.1	0.000467	1.17	4.43
2	30	2.28	1.53	0.75	0.000455	1.14	6.25
2	35	2.98	1.68	1.3	0.000484	1.21	3.85
3	25	4.41	3.11	1.3	0.000554	1.38	4.41
3	30	5.83	4.09	1.74	0.000352	0.9	5.26
3	35	6.81	5.23	1.58	0.000476	1.19	3.1

Table (E.12): 200 μm Particle size and 2.5 mm Layer Thickness Evaporator

V_a (m/s)	T_a ($^{\circ}\text{C}$)	T_w ($^{\circ}\text{C}$)	T_s ($^{\circ}\text{C}$)	ΔT_s ($^{\circ}\text{C}$)	\dot{m}_v (kg / s)	Q_b (kW)	h_b (kW/m ² K)
1	25	3.43	1.84	1.59	0.000309	0.77	1.99
1	30	5.8	1.61	4.19	0.00035	0.87	0.86
1	35	3.49	2.29	1.2	0.000353	0.88	3.05
2	25	2.56	1.33	1.23	0.000394	0.98	3.32
2	30	6.54	1.97	4.57	0.000338	0.84	0.76
2	35	4.79	2.48	2.31	0.413E0-3	1.03	2.24
3	25	3.89	1.99	1.9	0.000324	0.81	1.76
3	30	5.18	2.25	2.93	0.000365	0.91	1.29
3	35	5.4	3.5	1.9	0.000534	1.33	2.89

Appendix E: Tables of Experimental Results

Table (E.13): 300 μm Particle size and 1.0 mm Layer Thickness Evaporator

V_a (m/s)	T_a ($^{\circ}\text{C}$)	T_w ($^{\circ}\text{C}$)	T_s ($^{\circ}\text{C}$)	ΔT_s ($^{\circ}\text{C}$)	m_v (kg / s)	Q_b (kW)	h_e (kW/m ² K)
1	25	3.42	1.93	1.49	0.000486	1.21	3.35
1	30	4.01	2.23	1.78	0.000568	1.42	3.28
1	35	4.38	2.85	1.53	0.000441	1.1	2.96
2	25	4.31	2.13	2.18	0.000515	1.28	2.44
2	30	4.58	2.83	1.75	0.000466	1.16	2.73
2	35	5.51	3.64	1.87	0.000482	1.2	2.65
3	25	4.56	2.39	2.17	0.000514	1.28	2.44
3	30	5.27	3.47	1.8	0.000388	0.97	2.11
3	35	6.37	4.37	2	0.000496	1.24	2.56

Table (E.14): 300 μm Particle size and 1.5 mm Layer Thickness Evaporator

V_a (m/s)	T_a ($^{\circ}\text{C}$)	T_w ($^{\circ}\text{C}$)	T_s ($^{\circ}\text{C}$)	ΔT_s ($^{\circ}\text{C}$)	m_v (kg / s)	Q_b (kW)	h_e (kW/m ² K)
1	25	3.82	1.77	2.05	0.000571	1.42	2.87
1	30	3.45	1.3	2.15	0.000466	1.16	2.23
1	35	2.76	1.04	1.72	0.000445	1.11	2.66
2	25	3.77	1.51	2.26	0.000455	1.13	2.08
2	30	4.18	2.3	1.88	0.000377	0.94	2.06
2	35	4.41	1.89	2.52	0.00048	1.21	1.98
3	25	3.82	1.76	2.06	0.000437	1.09	2.19
3	30	4.58	2.41	2.17	0.000405	1.01	1.92
3	35	5.49	2.69	2.8	0.000438	1.09	1.61

Table (E.15): 300 μm Particle size and 2.0 mm Layer Thickness Evaporator

V_a (m/s)	T_a ($^{\circ}\text{C}$)	T_w ($^{\circ}\text{C}$)	T_s ($^{\circ}\text{C}$)	ΔT_s ($^{\circ}\text{C}$)	m_v (kg / s)	Q_b (kW)	h_e (kW/m ² K)
1	25	4.57	1.87	2.7	0.000333	0.83	1.27
1	30	2.6	1.51	1.09	0.000205	0.51	1.95
1	35	3.41	1.41	2	0.000168	0.42	0.86
2	25	5.05	2.06	2.99	0.000317	0.79	1.09
2	30	3.5	1.85	1.65	0.000272	0.68	1.7
2	35	4.74	2.15	2.59	0.000447	1.12	1.77
3	25	6.58	4.14	2.44	0.000583	1.45	1.99
3	30	4.16	2.39	1.77	0.00011	0.28	0.64
3	35	7.2	3.13	4.07	0.00032	0.8	0.81

Table (E.16): 300 μm Particle size and 2.5 mm Layer Thickness Evaporator

V_a (m/s)	T_a ($^{\circ}\text{C}$)	T_w ($^{\circ}\text{C}$)	T_s ($^{\circ}\text{C}$)	ΔT_s ($^{\circ}\text{C}$)	m_v (kg / s)	Q_b (kW)	h_e (kW/m ² K)
1	25	3.82	2.2	1.62	0.000362	0.9	2.29
1	30	3.82	1.61	2.21	0.000317	0.79	1.48
1	35	2.95	1.67	1.28	0.000392	0.98	3.16
2	25	4.07	1.82	2.25	0.000379	0.95	1.73
2	30	5.73	3.58	2.15	0.000349	0.87	1.67
2	35	6.04	2.87	3.17	0.000381	0.95	1.24
3	25	4.86	2	2.86	0.000229	0.57	0.82
3	30	6.74	4.12	2.62	0.000402	1	1.57
3	35	6.8	3.68	3.12	0.000408	1.02	1.35

References

1. Sabir, H.M. and Bwalya, A.C. "Experimental Study of Capillary-assisted Water Evaporators for Vapour Absorption System", Journal of Applied Energy, Vol. 71 (1), PP 45-57, 2002.
2. Faghri, Amir, "Heat Pipe Science and Technology", Taylor & Francis, Washington, D.C.; London, 1995.
3. Dunn, P. & Reay, D.A., "Heat pipes", 4th Edition, Pergamon Press, Oxford, 1994.
4. Kaviany, M., "Principles of Heat Transfer in Porous Media", 2nd Edition, Springer-Verlag, New York, PP 22, 1995.
5. Peterson, G. P., "An Introduction to Heat Pipes: Modelling, Testing, and Applications", Chichester: Wiley, New York, 1994.
6. Tong, L.S. and Tang, Y.S., "Boiling heat Transfer and Two-phase Flow", 2nd Edition, Washington, Taylor & Francis, 1997.
7. Collier, J.G. and Thome, J.R., "Convective Boiling and Condensation", 3rd Edition, Clarendon Press, Oxford, 1994.
8. Lahey, J., "Boiling heat Transfer: Modern Development and Advances", Centre for Multiphase Research: Rensselaer Polytechnic Institute, Troy, ,N Y,USA, Elseveir Science, 1992.
9. Busse, C.A., "Pressure Drop in the Vapour Phase of Long Heat Pipes", Proceedings of the IEEE International Thermionic Conversion Specialist Conference, IEEE, New York, 1967.
10. Chi, S. W., "Heat Pipe Theory and Practice", McGraw-Hill, New York, 1976.
11. V.E. Poznyak, V.K Orlov and V.N. Savel'v, "Intensification of Heat Transfer in a Condenser– Evaporator as a Result of a Porous Coating on The

References

- Boiling Surface”, Chemical and Petroleum Engineering. Vol. 16 (3-4). PP 157-160, 1980.
12. S.A. Kovalev & V.A. Len’Kov, “Mechanism of Burnout with Boiling on a Porous Surface”, Teploenergetika, Vol. 4, PP 8-10, 1981.
13. A.E Bergles & M.C Chyu, “Characteristics of Nucleate Pool Boiling from Porous Metallic Coatings”, Transactions ASME, Journal of Heat Transfer, Vol. 104 (2), PP 56-64, 1982.
14. Niam H. Afgan, Larisa A. Jovic, Sergey A. Kovaber and Victor A. Lenykov, “Boiling Heat Transfer From Surfaces With Porous Layers”, International Journal of Heat and Mass Transfer, Vol. 28 (2), PP 415-422, 1985.
15. X. Zhao and H. Zhang, “Experimental Study of Pool Boiling Heat Transfer from Powder Porous Surface at Higher Heat Fluxes”, Advances in Phase Change Heat Transfer, PP 236–241, 1988.
16. H. J. Zhang and X. B. Zhao, “Experimental Research on Pool Boiling Hot transfer from a Spraying Porous Surface”, Preprints, 7th International Heat Pipe Conference, Minsk, Vol. 1, PP187 – 194, 1990.
17. J. Tekhver, H. Sui and V. Temkina, “Heat Transfer and Hysetersis Phenomena in Boiling on Porous Plasma-Sprayed Surface”, Experimental Thermal Fluid Science, Vol. 5, PP 714-727, 1992.
18. A.D. Pasek, “Pool Boiling on Porous Surfaces in Cryogenic and Refrigerant Liquids”, PhD Thesis, University of Southampton, 1992.
19. P.J. Marto and Lt. V. J. Lepere, “Pool Boling Heat Transfer from Enhanced Surfaces to Dielecric Fluids”, Journal of Heat and Mass Transfer, Transactions of ASME, Series C, Vol. 104 (2), PP 72-80, 1982.

References

20. S. Yilmaz and J. W. Westwater, "Effect of Commercial Enhanced Surfaces on the Boiling Heat Transfer Curve", *Advances in Heat Transfer*, Vol. 18, PP 73-91, 1981.
21. Z. Jon Zuo, Mark T. North, and Lee Ray "Combined Pulsating and Capillary Heat Pipe Mechanisms for Cooling of High Heat Flux Electronics", *Proceedings of ASME Heat Transfer Division; Publ HTD*, Vol. 364 (4), PP 237-243, 1999.
22. J.Y. Chang and S.M. You, "Enhanced Boiling Heat Transfer from Micro-Porous Surfaces: Effects of a Coating Composition and Method", *International Journal of Heat and Mass Transfer*, Vol. 40, (18), PP 4449-4460, 1997
23. M. Fujii, E. Nishiyama and G. Yamanka, "Nucleate Pool Boiling Heat Transfer from Micro- Porous Heating Surface", *Advances in Enhanced Heat Transfer*, PP 45 – 51, 1979.
24. M.N. Ivanovskii, V.V. Privezentsev, Yu. A. Il'in, and E.M. Sidorenko, "Experimental Investigation of Heat Transfer with Evaporation of the Agent from a Corrugated Capillary Structure", *Journal of Engineering Physics and Thermophysics*, Vol. 46 (4), PP 377-381, 1984.
25. K.S. Udell, "Heat Transfer in Porous Media Heated from above with Evaporation Condensation, and Capillary Effects" *ASME Journal of Heat Transfer*, Vol. 105, PP 485-492, 1983.
26. Kent S. Udell, "Heat Transfer in Porous Media Considering Phase Change and Capillarity-The Heat Pipe Effect", *International Journal of Heat Transfer*, Vol. 28 (2), PP 485 – 495, 1985.

References

27. S.A. Kovalev, S.L. Solov'ev and O.A. Ovodkov, "Theory of Boiling Heat Transfer on a Capillary-Porous Surface", Proceedings; 9th International Heat Transfer Conference, Vol. 2, PP 105-110, 1990.
28. I.W. Eames, S. Wu and H. Sabir, "Direct-Heat Exchange Water Evaporator for Vapour Absorption Cycle Refrigeration", Refrigeration Science and Technology, Vol. 4, PP 519-529, 1998.
29. Q. Liao, and T.S. Zhao, "A Visual Study of Phase-change Heat Transfer in a Two-Dimensional Porous Structure with a Partial Heating Boundary", International Journal of Heat and Mass Transfer, Vol. 43 (7), PP 1089-1102, 2000.
30. T.S. Zhao and Q. Liao, "On Capillary-Driven Flow and Phase-Change Heat Transfer in a Porous Structure Heated by a Finned Surface: Measurements and Modelling", International Journal of Heat and Mass Transfer, Vol. 43 (7), PP 1141-1155, 2000.
31. R.J. Raiff and P.C. Wayner, "Evaporation from a Porous Flow Control Element on a Porous Heat Source", International Journal of Heat and Mass Transfer, Vol. 16, PP 1919-1929, 1973.
32. S. Madhusudana Rao and A.R. Blakrishnan, "Analysis of Pool Boiling Heat Transfer Over Porous Surfaces", Journal of Heat and Mass Transfer, Vol. 32, PP 463-469, 1997.
33. Ya. Kh. Tekhver & Kh. N. Sui, "Hysteresis Phenomena in Boiling at a Porous Surface", Izvestiya Akademii Nauk SSSR. Energetika I Transport. (Translation), Vol. 22 (4), PP 157 – 161, 1984.
34. Brautsch and Peter Kew, "Examination and Visualisation of Heat Transfer Processes during Evaporation in Capillary porous Structures", Applied Thermal Engineering, Vol. 22, PP 815-824, 2001.

References

35. O'Neil, P.S., Gotsman, C.F., Tterbot, J.W., "Novel Heat Exchanger Increases Cascade Cycle Efficiency for Natural Gas Liquefaction", *Advances in Cryogenic Engineering*, Vol. 17, PP 420- 437, 1972.
36. L.L. Vasiliev, A.S. Zhuravlev, A.V. Ovsyannik, and M.N. Novikov; "Heat Transfer in Propane Boiling on Surfaces with a Capillary-Porous Structure", *Heat Transfer Research*, Vol. 35 (5 & 6), PP 436-443, 2004.
37. V. K. Orlov & V. N. Savel'ev, "Investigation of Heat Transfer with Boiling of Cryogenic Liquids on Surface with a Capillary-Porous Coating", *Teploenergetika*, Vol. 27(8), PP 66-69, 1980.
38. Ying Zhang and Hongji Zhang, "Boiling Heat Transfer from a thin Power Porous Layer at Low and Moderate Heat Flux", *Multiphase Flow and Heat Transfer*, 2nd International Symposium, PP 358-366, 1992.
39. Kuo-Tong Ma and Chin Pan, "The Effect of Heated Wall Thickness and Materials on Nucleate Boiling at High Heat Flux", *Int. Comm. Heat and Mass Transfer*, Vol. 26 (8), PP 1103-1114, 1999.
40. J.Y. Chang and S.M. You, "Enhanced Boiling Heat Transfer from micro-Porous Surfaces: Effects of a Coating Composition and Method", *International Journal of Heat and Mass Transfer*, Vol. 40, (18), PP 4449-4460, 1997
41. J.R. Thome, "Enhanced Heat Transfer", Hemisphere, New York, 1990.
42. W. Nakayama, T. Daikoku, H. Kuwahara, and T. Nakajima, "Dynamic Model of Enhanced Boiling Heat Transfer on Porous Surfaces. Part II: Analytical Modelling", *Journal of Heat and Mass Transfer, Transactions of ASME*, Vol. 102 (3), PP 451-456, 1980.
43. M. A. Hanlon and H.B. Ma; "Evaporation Heat Transfer in Sintered Porous Media"; *AIAA Paper 2002-3092*, PP 1-11, 2002.

References

44. U. L. Pikhla and Ya. Kh. Tekhver, "Influence of Porous Cooling on Heat Transfer during Boiling", *Izvestiya Akademii Nauk SSSR. Energetika Transport*, Vol. 21 (3), PP 125 - 129, 1983.
45. V.X. Tung and V.K. Dhir, "Experimental Study of Boiling Heat Transfer from a Sphere Embedded in a Liquid-Saturated Porous Medium", *ASME Journal of Heat and Mass Transfer*, Vol. 112, PP 736-743, 1990.
46. Q. Liao and T.S. Zaho, "Evaporative Heat Transfer in a Capillary Structure Heated by a Grooved Block", *Journal of Thermophysics heat transfer*, Vol. 13 (1), PP 126-133, 1999.
47. H. Mustafa and M. Duwairi, "Boundary Layer Analysis of Buoyancy Pressure-Driven Liquid Film, Two-Phase Flow and Heat Transfer in a Capillary Porous Medium", VDI Verlag GmbH. Düsseldorf, 2000.
48. Y.X. Wang and G.P. Peterson; "Analytical Model for Capillary Evaporation Limitation in Thin Porous Layers"; *Journal of Thermophysics and Heat Transfer*, Vol. 17, (2), PP 145-149, 2003.
49. N. P. Pogorelova and V.M. Kiselev; "Boiling Heat Transfer in Highly Porous Cellular Materials of Different Thickness"; *Heat Transfer Research*, Vol. 32 (4-6), PP 187-194, 2001.
50. D. Khrustalev and A. Faghri, "Thick-Film Phenomenon in High-Heat-Flux Evaporation From Cylindrical Pores", *ASME Journal of Heat Transfer*, Vol. 119, PP 272-278, 1997.
51. N. Zhu & K. Vafai, "Analysis of Cylindrical Heat Pipes Incorporating the Effects of Liquid-Vapour and Non-Darcian Transport; A Closed - Form Solution", *International Journal of Heat and Mass Transfer*, Vol. 42, PP 3405-3418, 1999.

References

52. P.C. Wayner, Y.k.. Kao and L.V. Lacroix, "The Interline Heat-Transfer Coefficient of an Evaporating Wetting Film", International Journal of Heat and Mass Transfer, Vol. 19, PP 487-492, 1976.
53. P.C. Stephan and C.A. Busse, "Analysis of Heat Transfer Coefficient of Grooved Heat Pipe Evaporator Walls", International Journal of Heat and Mass Transfer, Vol. 35 (2), PP 383-391, 1992.
54. J.A. Schonberg and P.C. Wayner, "Analytical Solution for the Integral Contact-Line Evaporative Heat Sink", AIAA Thermophysics and Heat Transfer, Vol. 6 (1), PP 128-134, 1992.
55. D. Khrustalev, A. Faghri and John Leland, "Thermal Analysis of Auxiliary-Grooved Heat Pipes", ASME Pet Div Publ PD, Vol. 64 (1), PP 39-54, 1994.
56. D. Khrustalev and A. Faghri, "Heat Transfer during Evaporation on Capillary Grooved Structures of Heat Pipes", Transaction of ASME, Journal of Heat Transfer, Vol. 117, PP 740-747, 1995.
57. J. Wang and I. Catton, "Enhanced Evaporation Heat Transfer in Triangular Grooves Covered with a Thin Fine Porous Layer", Applied Thermal Engineering, Vol. 21, PP. 1721-1737, 2001.
58. J.M. Ha and G.P. Peterson, "Interline Heat Transfer of Evaporating Thin Films along a Micro Grooved surface" New York, ASME International Mechanical Engineering Congress & Exposition, San Francisco, California, Nov.12-17, 1995.
59. Höhmann and P. Stephan, "Microscale Temperature Measurement at an Evaporating Liquid Meniscus", Experimental Thermal and Fluid Science, 2002.
60. D. Khrustalev and A. Faghri, "Fluid Flow Effects in Evaporation from Liquid-Vapour Meniscus", Journal of Heat and Mass Transfer, ASME, Vol. 118, PP 726-730, 1996.

References

61. G. P. Peterson and H. B. Ma, "Theoretical Analysis of the Maximum Heat Transport in Triangular Grooves: A Study of Idealized Micro Heat Pipes", *Journal of Heat Transfer, Transactions of ASME*, Vol. 118, PP731-739, 1996.
62. D. Plesch, W. Bier, D. Seidel and K. Schubert, "Miniature Heat Pipes For Heat Removal from Microelectronic Circuits", *Micromechanical Sensors, Actuators, and Systems*, ASME, DSC Vol. 32, PP 303-313, 1991.
63. D. Khrustalev and A. Faghri, "Thermal Characteristics of Conventional and Flat Miniature Axially Grooved Heat Pipes", *ASME Journal of Heat and Mass Transfer*, Vol. 117, PP 1048-1054, 1995.
64. J. A. Schonberg, S. Das Gupta and P.C. Wayner, Jr., "An Augmented Young-Laplace Model of Evaporating Meniscus in Micro Channels with High Heat Flux", *International Journal of Experimental Thermal and Fluid Science*, Vol. 10, PP 163-170, 1995.
65. Y. Cao and M. Goa, "Experiments and analysis of Flat Miniature Heat Pipes" *Journal of Thermophysics and Heat Transfer*, Vol. 11 (2), PP 158-164, 1997.
66. Y. Cao, J.E. Beam and B. Donovan, "Air-cooling Systems for Metal Oxide Semiconductor Controlled Thyristors Employing Miniature Heat Pipes", *AIAA Thermophysics and Heat Transfer*, Vol. 10 (3), PP 484-489, 1996.
67. R. Hopkins, A. Faghri and D. Khrustalev, "Flat Miniature Heat Pipes with Micro Capillary Grooves", *Journal of Heat Transfer, Transactions ASME*, Vol. 121 (1), PP 102-109, 1999.
68. F.W. Holm and S.P. Goplen, "Heat Transfer in the Meniscus Thin-Film Transition Region", *ASME Journal of Heat Transfer*, Vol. 101 (3), PP 543-547, 1979.
69. J.M. Ha and G.P. Peterson, "Capillary Performance of Evaporating Flow in Micro Grooves: An Analytical Approach for Very Small Tilt Angles", *Journal of Heat Transfer, Transactions ASME*, Vol. 120 (2), PP 452-457, 1998.

References

70. J. M. Ha and G. P. Peterson, "Analytical Prediction of the Axial Dry out Point for Evaporating Liquids in Triangular Microgrooves", Transaction of ASME, Journal of the Heat Transfer, Vol. 116, PP 498 – 503, 1994.
71. A.S. Belonogov and V.M. Kiseev, "Evaporation Problems in Wetting Film Theory", AIChE Symposium Series, Proceeding of the National Heat Transfer Conference, Vol. 91 (306), PP333-336, 1995.
72. G.R. Stores, and I. Catton, "Experimental Investigation of the Capillary Performance" Journal of Heat Transfer, Transactions ASME, Vol. 119 (4), PP 851-853, 1997.
73. M. Goto, N. Inoue, and N. Ishiwatari, "Condensation and Evaporation Heat Transfer of R410A Inside Internally Grooved Horizontal Tubes", International Journal of Refrigeration, Vol. 24, PP 628-638, 2001.
74. P.S Ayyaswamy, I. Catton, and D. K. Edwards, "Capillary Flow in Triangular Grooves", ASME Journal of Applied Mechanics, Vol. 41, 332-336, 1974.
75. H. B. Ma and G. P Peterson, "The Minimum Meniscus Radius and Capillary Heat Transport Limit in Micro Heat Pipes", Journal of Heat Transfer, ASME, Vol. 120, PP 227-233, 1998.
76. V.G. Stepanov, L.D. Volyak, and Yu. Tarlakov, "Wetting Contact Angle of Various Systems", Journal of Engineering Physics and Thermophysics, Vol.32 (6), PP 646-648, 1977.
77. H. B. Ma, G. P. Peterson and X. J. Lu, "The Influence of Vapour-Liquid Interactions on the Liquid Pressure Drop in Triangular Microgrooves", International Journal of Heat and Mass Transfer, Vol. 37 (15), PP 2211-2219, 1994.
78. H.G. Wulz and E. Embacher, "Capillary Pumped Loops for Space Applications, Experimental and Theoretical Studies on the Performance of Capillary Evaporator

References

- Design" AIAA/ASME 5th Joint Thermophysics Conference, Vol. AIAA 90-1739, PP 1-16, 1990.
79. K. Jentung, "Overview of Capillary Pumped Loop Technology", ASME-HTD 29th Heat Transfer Conference, Heat Pipes and Capillary Pumped Loops, Vol. 236, PP 1-17, 1993.
80. Pin-Chih Chen and Wei-keng Lin, "The Application of Capillary Pumped Loop for Cooling of Electronic Components", Applied Thermal Engineering, Vol. 21, PP 1739-1754, 2001.
81. T. Li and M. Ochterbeck, "Effects of Wick Thermal Conductivity on Start-Up of a Capillary Pumped Loop Evaporator", AIAA Paper, Vol. 99-3446, PP 1-12, 1999.
82. Triem Hoang & Jentung Ku, "Hydrodynamic Aspects of Capillary Pumped Loops", SAE Paper 961435, 1996.
83. Triem T. Hoang, "Development of an Advanced Capillary Pumped Loop", SAE Paper -Society of Automotive Engineers- 972325, PP 1-6, 1997.
84. T.J. Dickey and G.P. Peterson, "Experimental and Analytical Investigation of a Capillary Pumped Loop", AIAA Journal of Thermophysics and Heat Transfer, Vol. 8 (3), PP 602-607, 1994.
85. D. Khurstalev, and A. Fagri, "Enhanced Flat Miniature Axially Grooved Heat Pipe", Journal of Heat Transfer Transaction, ASME. Vol. 118 (1). PP 261-264, 1996.
86. Faghri and D. Khrustalev, "Advances in Modelling of Enhanced Flat Miniature Heat Pipes with Capillary Grooves", Journal of Enhanced Heat Transfer, Vol. 4 (2), PP 99-109, 1997.
87. K. Nishikawa and T. ITO, "Augmentation of Nucleate Boiling Heat Transfer by Prepared Surfaces", Heat Transfer in Energy Problems, PP 119-126, 1982.

References

88. S. Fukusako, T. Komoriya, and N. Seki "An Experimental Study of Transition and Film Boiling Heat Transfer in Liquid –Saturated Porous Bed", Transactions of ASME, Journal of Heat Transfer, Vol. 108, PP 117-124, 1986.
89. K.Conrnwell, B.G.Nair and T.D.Paten, "Observation of Boiling in Porous Media", International Journal of Heat Mass Transfer, Vol. 19, PP 236-238, 1976.
90. Tolubinskii, V.I., "Heat Exchange Trough Boiling", Kiev, 1980.
91. A.A. Belyaev, Yu. A. Buevich, and V. M. Kiseev, "Comparative Study of Thermodynamics of Evaporation Schemes in Capillary Structures", Journal of Engineering Physics, Vol. 62 (2), PP 123-127, 1992.
92. Incropera, Frank P., "Fundamentals of Heat and Mass Transfer", 5th Edition, Chichester: Wiley, PP 395-411, 2002.
93. Bryan, W.L., "Heat & Mass Transfer in Dehumidifying Surface Coils", ASHRAE Journal 3/9, PP 51-54, 1961.
94. Douglas, J. F., "Fluid Mechanics", 4th Edition, Harlow: Prentice Hall, 2001.
95. G.S.H. Lock, "Latent Heat Transfer: an Introduction to Fundamentals", Oxford University Press, 1994.